

Area 2: Use Of Engineered Nanoparticle-Stabilized CO₂ Foams To Improve Volumetric Sweep Of CO₂ EOR Processes

CONTRACT NO. DE-FE0005917

FINAL PROJECT REPORT

Reporting Period: January 12, 2011 – January 30, 2015

Prepared by

David A. DiCarlo

Department of Petroleum and Geosystems Engineering
The University of Texas at Austin
1 University Station C0300
Austin, TX 78712-0228
Phone: (512) 471 1283
Email: dicarlo@mail.utexas.edu

Chun Huh

Department of Petroleum and Geosystems Engineering
The University of Texas at Austin
1 University Station C0300
Austin, TX 78712-0228
Phone: (512) 471 3252
Email: chunhuh@mail.utexas.edu

Keith P. Johnston

Department of Chemical Engineering
The University of Texas at Austin
1 University Station C0300
Austin, TX 78712-0228
Phone: (512) 471 4617
Email: johnston@che.utexas.edu

Prepared for

U.S. Department of Energy - NETL
3610 Collins Ferry Road
P.O. Box 880
Morgantown, WV 26508

Acknowledgment: "This material is based upon work supported by the Department of Energy under Award Number DE-DE0005917."

Disclaimer: "This report was prepared as an account of work sponsored by an agency of the United States Government. Neither the United States Government nor any agency thereof, nor any of their employees, makes any warranty, express or implied, or assumes any legal liability or responsibility for the accuracy, completeness, or usefulness of any information, apparatus, product, or process disclosed, or represents that its use would not infringe privately owned rights. Reference herein to any specific commercial product, process, or service by trade name, trademark, manufacturer, or otherwise does not necessarily constitute or imply its endorsement, recommendation, or favoring by the United States Government or any agency thereof. The views and opinions of authors expressed herein do not necessarily state or reflect those of the United States Government or any agency thereof."

Abstract

The goal of this project was to develop a new CO₂ injection enhanced oil recovery (CO₂-EOR) process using engineered nanoparticles with optimized surface coatings that has better volumetric sweep efficiency and a wider application range than conventional CO₂-EOR processes. The main objectives of this project were to (1) identify the characteristics of the optimal nanoparticles that generate extremely stable CO₂ foams in situ in reservoir regions without oil; (2) develop a novel method of mobility control using “self-guiding” foams with smart nanoparticles; and (3) extend the applicability of the new method to reservoirs having a wide range of salinity, temperatures, and heterogeneity.

Concurrent with our experimental effort to understand the foam generation and transport processes and foam-induced mobility reduction, we also developed mathematical models to explain the underlying processes and mechanisms that govern the fate of nanoparticle-stabilized CO₂ foams in porous media and applied these models to (1) simulate the results of foam generation and transport experiments conducted in beadpack and sandstone core systems, (2) analyze CO₂ injection data received from a field operator, and (3) aid with the design of a foam injection pilot test. Our simulator is applicable to near-injection well field-scale foam injection problems and accounts for the effects due to layered heterogeneity in permeability field, foam stabilizing agents effects, oil presence, and shear-thinning on the generation and transport of nanoparticle-stabilized C/W foams. This report presents the details of our experimental and numerical modeling work and outlines the highlights of our findings.

Table of Contents

Abstract	2
Table of Contents	Error! Bookmark not defined.
Executive Summary	5
I. Foam generation and Transport – Experimental Work	7
I.1. Nanoparticle-stabilized CO ₂ -in-brine foams	7
I.1.1. Design of surface-modified silica NPs for foam generation in bead-pack and capillary tube experiments	7
I.1.2. Conditions for generating nanoparticle-stabilized CO ₂ foams in fracture and matrix flow	34
I.2. Surfactant and nanoparticle-stabilized C/W foam systems and synergistic effects	67
1.2.1. Abstract	67
1.2.2. Introduction	67
1.2.3. Materials	71
1.2.4. Methods	71
1.2.5. Results	74
1.2.6. Discussion	83
1.2.7. Conclusions	90
1.2.8. References	90
II. Foam Generation and Transport – Modeling and Simulations	96
II.1. Core-scale NP-C/W foam generation and transport – Full-physics model	96
II.1.1. Abstract	96
II.1.2. Introduction	97
II.1.3. Materials and Methods	100
II.1.4. Foam transport model	101
II.1.4. Results and discussion	104
II.1.5 Conclusions	118
II.1.6. References	118
II.2. Field-scale NP-C/W foam generation and transport – Multi-phase/component model ..	121
II.2.1. Mathematical Model	122
II.2.2. Solution Algorithm	127
II.2.3. Simulations and Results	128
II.2.4. Conclusions	140
II.2.5. References	141

III. Nanoparticle Mobility – Nanoparticle Aggregation and Transport at Elevated Salinity.....	142
III.1. Abstract	142
III.2. Introduction.....	143
III.3. Materials and Methods.....	145
III.4. Results and Discussion	148
III.5. Conclusions.....	160
III.6. References.....	161
IV. Concluding Remarks	164

Executive Summary

Engineered silica nanoparticles have the potential to revolutionize CO₂ enhanced oil recovery (EOR) projects, as these nanoparticles can (a) pass effectively through reservoir rock, and (b) can help create and stabilize CO₂-in-brine foams. When engineered with a proper surface coating, nanoparticles do not aggregate allowing them to stay suspended in brine. Unlike colloidal particles, the extremely small size of the nanoparticles (5-100 nm) allows them to pass through porous without being strained. For analogy, a nanoparticle passing through a typical pore throat of size 5 μm, is similar to a 2 foot stick flowing down the Mississippi river at St Louis, Missouri.

Just as important, with proper treatment, these nanoparticles have been shown to stabilize CO₂-in-brine foams. CO₂ is the most used and most effective EOR injectant, but CO₂ floods suffer from poor sweep efficiency due to CO₂'s low viscosity. Creating and stabilizing CO₂ foam increases the effective viscosity of CO₂ and thus improves the performance of CO₂ floods. The goal of this project was to optimize surface treatment of nanoparticles such that it produces foams at harsh reservoir conditions where other CO₂ foaming agents (surfactants) either break down or are lost due to interaction with the solid phase.

In this final report, we present the results of our coupled experimental and mathematical modeling efforts to understand the underlying processes and mechanisms governing the formation and transport of CO₂-in-brine (C/W) foams stabilized by surface coated silica nanoparticles (NP) in porous rock formations. Here, NP-C/W foams can serve as smart mobility reduction agents targeting high permeability zones in a hydrocarbon reservoir diverting CO₂ flow toward lower permeability streaks thereby improving CO₂ flood conformance and macroscopic sweep efficiency. This report contains four sections: Section I describes NP-C/W generation and transport experiments in beadpacks and consolidated sandstone cores. In Section II, a detailed summary of the numerical modeling approaches is described; this modeling was implemented to simulate and explain the experimental observations presented in Section I. Section III describes experiments and modeling work conducted to characterize the transport and retention of silica NPs, used in Section I, under specific physicochemical conditions of an existing oil reservoir.

Finally, presented in Section IV are concluding remarks and the highlights of our findings during the course of this project.

I. Foam generation and Transport – Experimental Work

This section covers the C/W foam generation and transport experiments on foams stabilized by (i) silica NPs (subsection I.1), and (ii) a mixture of silica NPs and surfactant (subsection I.2).

I.1. Nanoparticle-stabilized CO₂-in-brine foams

In this subsection, first the results of finely textured NP-C/W foams in bead-packs and capillary tubes are presented (subsection I.1.1), and then core-flood experiments are discussed (subsection I.1.2).

I.1.1. Design of surface-modified silica NPs for foam generation in bead-pack and capillary tube experiments

For the first time, opaque white C/W foams with bubble sizes too small to be visible (<100 μm) were generated with either surface-modified silica nanoparticles. Here the HCB (hydrophilic-CO₂philic balance for the nanoparticle) was in the proper range for the adsorption of the nanoparticles at the CO₂-water interface with a desirable contact angle for stabilizing aqueous lamellae between CO₂ bubbles. The HCB for nanoparticles introduced in this work provides a consistent framework for interpreting foam stabilization by nanoparticles. The results of this part of our experimental study on NP-C/W foam generation in beadpack systems were published as an original research paper in the Journal of Colloid and Interface Science:

Worthen, Andrew J., et al. "Nanoparticle-stabilized carbon dioxide-in-water foams with fine texture." *Journal of Colloid and Interface Science* 391 (2013): 142-151.

I.1.1.i. Abstract

The concept of hydrophilic/CO₂-philic balance (HCB) was extended to describe stabilization of carbon dioxide-in-water (C/W) foams (also called emulsions) with silica nanoparticles adsorbed at the CO₂-water interface. Opaque, white C/W foams (bubble diameter <100 μm) were generated with either PEG-coated silica or methylsilyl modified silica nanoparticles in a beadpack with CO₂ densities between 0.2 and 0.9 g mL⁻¹. For methylsilyl modified silica nanoparticles, 50% SiOH modification provided an optimal HCB for generation and stabilization

of viscous C/W foams with high stability. The apparent viscosity measured with a capillary tube viscometer reached 120 fold that of a CO₂-water mixture without nanoparticles, a consequence of the small bubble size and the energy required to deform a high density of aqueous lamellae between CO₂ bubbles. Air-in-water (A/W) foams stabilized with nanoparticles were used to gain insight into the relationship between nanoparticle surface properties and adsorption of the nanoparticles at various types of interfaces. With suitable nanoparticles, A/W foams were stable for at least 7 days and C/W foams were stable for at least 23 hours. The ability to achieve long term stability for nanoparticle stabilized C/W foams could offer an alternative to conventional surfactants, which are known to have much lower adsorption energies.

1.1.1.ii. Introduction

Enhanced oil recovery (EOR) with CO₂ has been practiced on a large scale for over 50 years, yet significant challenges remain to improve volumetric sweep efficiency to improve oil production [1-6]. The volumetric sweep efficiency can be reduced by gravity override caused by the low density of CO₂ as well as by viscous fingering and channeling through high permeability regions [1]. Both of these limitations can be addressed by the formation of C/W foams to increase the effective viscosity of injected CO₂ and thereby provide mobility control [1]. For simplicity, the term “C/W foam” is used in this study to refer to high internal phase volume fraction emulsions of relatively dense supercritical CO₂ in water. An innovative new approach would be to design a “smart” foam that reduces CO₂ mobility in high permeability zones such as in fractures and gravity override regions that contain little oil. In these self-guided smart foams CO₂ mobility would be reduced the most where it is flowing rapidly in regions with low oil content. The smart foam would be designed to break in the presence of residual oil to enable contact with CO₂, leading to increased oil production [7].

CO₂ is an abundant, nonflammable, and essentially nontoxic, nonpolar solvent that has drawn attention for use in various industrial applications because of its tunable properties [8]. CO₂ has a critical temperature of 31°C and a critical pressure of 1070psia. At typical reservoir conditions with temperatures from 30°C to 100°C and pressures above 1000 psia, the density of supercritical CO₂ ranges from 0.2-0.9 g/cm³. The cohesive energy density of CO₂ (also polarizability/volume) is typically less than that of an oil (a nonpolar liquid solvent) and often is

a very weak solvent for even hydrocarbon surfactant tails [9] or ligands on nanoparticle surfaces [10]. Likewise, CO₂ has very weak van der Waals forces and a large free volume leading to low viscosity. Finally, the weak van der Waals forces and the quadrupole moment along with formation of carbonic acid produce a lower CO₂/water interfacial tension of ~20 mN/m at typical reservoir conditions, much lower than for many alkane/water interfaces [8].

A wide number of studies have examined emulsions of CO₂ and water stabilized by surfactants, typically with similar volumes of each phase [4, 6, 8, 11-13]. Given the weak van der Waals forces for CO₂, it is highly challenging to balance the weak solvation of the surfactant tails by CO₂ with the strong solvation of the surfactant head groups by the water phase [8]. The concept of hydrophilic/CO₂-philic balance (HCB) [14] was defined to describe the balance of surfactant and solvent interactions:

$$1/HCB = \frac{A_{TC} - A_{TT} - A_{CC}}{A_{HW} - A_{HH} - A_{WW}} \quad (I.1.1.1)$$

where $A_{\alpha\beta}$ indicates the interaction pair potential between α and β with T = surfactant tail, C = CO₂, H = surfactant head group, and W = water. HCB is very similar to the concept of hydrophilic/lipophilic balance (HLB) used to describe surfactant behavior in oil-water systems [15-17]. The weak solvent strength of CO₂ causes A_{TC} to be very small compared to A_{HW} . Thus, a key to increasing the HCB of a surfactant is to minimize the tail-tail interactions, A_{TT} , which can be achieved by using surfactants that contain “stubby”, low cohesive energy density tails [9, 18-21], e.g. through the use of branching. Tuning the HCB of a surfactant allows control of the curvature of the CO₂-water interface to form emulsions with either CO₂-in-water (C/W) or water-in-CO₂ (W/C) curvature [14]. Other formulation variables such as pH, temperature, pressure, and salinity can also impact the curvature of the CO₂-water interface [14]. However, for a fixed set of reservoir conditions, the HCB of the surfactant becomes the key tunable parameter.

The concept of HCB has also been applied to nanoparticles at CO₂-water interfaces to generate emulsions of W/C [22] or C/W [23]. Similar to Windsor diagrams used to describe the behavior of microemulsions and macroemulsions stabilized by surfactants [16, 24-26], Figure I.1.1.1 illustrates the effect of various formulation variables for a nanoparticle with a coating capable of

lowering the interfacial tension in a CO₂-water system. If the nanoparticle prefers the water phase (high HCB), the interface will bend about CO₂ resulting in a C/W emulsion. According to the Bancroft rule, the continuous phase of the emulsion is the phase preferred by the nanoparticle. The Bancroft rule has been applied to nanoparticle-stabilized CO₂-water macroemulsions (left and right side of Figure I.1.1.1) in previous studies of nanoparticles coated with homopolymers [27] or amphiphilic copolymers [28, 29] in oil-water systems. Solvation of the polymer coating both by CO₂ and water is affected by temperature, pH, pressure, and salinity—each influencing the curvature of the CO₂-water interface in the emulsion.

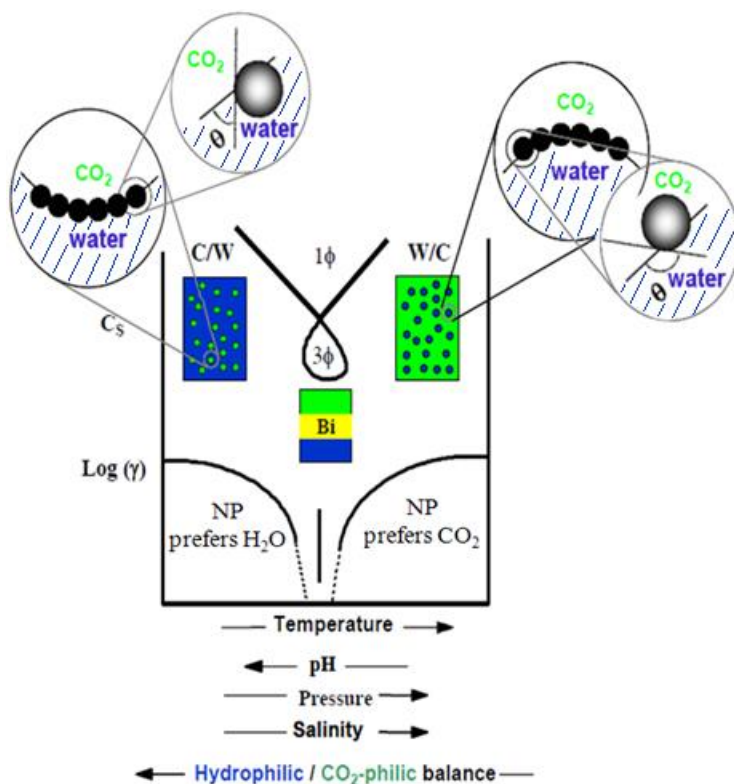


Figure I.1.1.1. Effect of formulation variables on CO₂-water emulsions illustrating contact angle for nanoparticle at the interface.

Various carbosilane ligands have been used to tune the HCB of particles to give the desired emulsion curvature. Silica nanoparticles modified with very hydrophobic (heptadecafluoro-1,1,2,2-tetrahydrodecyl)triethoxysilane to give the particle surface a low HCB (right side of Fig. I.1.1.1) were introduced by Adkins et al. to generate W/C emulsions [22]. In contrast silica nanoparticles that were unmodified or modified with dichlorodimethylsilane (DCDMS) to leave 76% residual SiOH coverage to give the particle surface a high HCB (left side of Fig. I.1.1.1)

were used to generate C/W emulsions [23]. Carbosilane ligands are covalently bound to the silica nanoparticle surface, and are expected to be chemically stable in harsh reservoir environments. In numerous studies, commercially available silica nanoparticles with methylsilyl-modified silanol surface coatings have been designed to stabilize oil-in-water (O/W) emulsions [30], water-in-oil emulsions [30], air-in-water (A/W) foams [31], and even water-in-air (W/A) powders [32], with proper design of the HLB of the particle surface. However, this approach has received relatively little attention for nanoparticles at the CO₂-water interface. Golomb and coworkers report both C/W [33-35] and W/C [34] emulsions depending on material used, where hydrophilic materials created C/W and hydrophobic materials created W/C. The hydrophilic materials used included sand, limestone, and flyash, indicating that interfacially active nanoparticles can be manufactured from extremely low cost materials. In the C/W cases, large droplets in the range of 100-500 μm were reported and a CO₂:water ratio of 1:2+ (by volume) was used, indicating a majority of the C/W emulsion volume was water.

Various particle stabilizers have been used to generate C/W emulsions and foams, but extremely few studies investigated long term stability. In an emulsion, roughly spherical droplets of the internal phase (CO₂) are dispersed in the external phase (water). In foams, the droplets of the dispersed phase (CO₂) become compressed and deformed, resulting in thin lamella of the external phase (water) separating them [36]. The ratio of phases influences the favored continuous phase [37] and the viscosity of the emulsion/foam [36]. Stability is imparted to emulsions and foams with nanoparticles by retarding destabilization mechanisms such as drainage of the liquid in the lamella, coalescence of neighboring bubbles (lamella rupture), and Ostwald ripening [38]. In the work of Dickson [23] discussed above, C/W emulsions with CO₂:water of ca. 1:1 (by volume) were investigated and stability was documented up to 12 h where 20% of the foam volume had resolved. The notable stability of the emulsions was imparted by the silica nanoparticles that were able to prevent coalescence of the creaming CO₂ droplets.

Espinosa and coworkers [39] created C/W emulsions and foams with CO₂: water ratios from 1:1 to 25:1 by shearing CO₂ and water phases in a beadpack. This study contains the only example we know of where high internal phase C/W foams were stabilized with nanoparticles. The small,

5nm colloidal silica particles coated with short-chain PEG [39] were expected to have a high HCB due to the hydrophilicity of the PEG chains and weak solvation of PEG by CO₂ [40]. For the PEG-coated silica stabilized C/W foams [39], the smallest C/W bubbles were on the order of 100µm such that the foams were not opaque white in appearance, and with relatively large polydispersity in bubble size. To achieve high stabilities and viscosities, it would be desirable to design nanoparticles with surface coatings to form opaque white C/W foams with smaller bubble sizes.

The objective of this study was to design silica nanoparticles with the proper HCB to generate viscous, white opaque C/W foams with high stability and bubble sizes smaller than 100 µm for foam qualities (fraction CO₂) from 0.75 to 0.90. Commercial silica nanoparticles with surfaces modified by short methylsilyl ligands provided a wide range of HCB's with 100, 70, 50 and 35% hydrophilic silanol groups (SiOH). CO₂ solvates the very low MW methylsilyl ligands quite effectively relative to hydrocarbon chains because of the low cohesive energy density of CH₃ groups relative to CH₂ groups. The results will show that the HCB of the particles that stabilized C/W foam in a flow apparatus falls between the values shown by Dickson et al. [23] (high HCB for C/W emulsions with 1:1 CO₂:water) and Adkins et al. [22] (low HCB for W/C emulsions with 1:1 CO₂:water). New and previous studies of A/W foams stabilized with nanoparticles [31, 41] were used to gain insight into the relationship between nanoparticle surface properties (silanol fraction, % SiOH) and the adsorption of the nanoparticles at various types of interfaces, A/W, C/W, and O/W [30], in which the cohesive energy density of the nonaqueous phase increases over a wide range from air to oil. Foams stabilized with nanoparticles with 50% residual SiOH coverage and with PEG-coatings were examined in terms of foam viscosity and stability and described in terms of CO₂ and water interactions with the nanoparticle surface. The trends in foam viscosity and stability are discussed in terms of particle size, surface coating, and CO₂ solvation of the tails. Foams were generated by shearing CO₂ and aqueous phases in a beadpack, and the apparent viscosity was measured in a capillary tube. In all experiments, the nanoparticles were introduced with the aqueous phase. Stability is characterized in terms of foam texture change and resolution (by height) from macroscopic observation in a high-pressure view cell after 20-23h. Opaque white foams without any visible discrete bubbles were produced, indicating strong foams with bubble sizes less than 100µm. The use of nanoparticles as foam

stabilizers offers the possibility of generating highly stable C/W foams without the use of surfactants or polymers, which are often not well solvated by CO₂, given its low cohesive energy density. Furthermore, interfacially active nanoparticles provide an alternative to surfactants for stabilization of C/W foams for subsurface applications where surfactants may become lost to adsorption on rock surfaces and to chemical degradation in harsh reservoir conditions, and properly designed nanoparticles can potentially generate more stable foams due to their high adsorption energy at the interface.

I.1.1.iii. Materials

The following amorphous fumed silica with various degrees of hydrophobicity were received in powder form and were gifts from Wacker-Chemie (see Figure I.1.1.2): T30 (unmodified, 100% SiOH coverage), HKSD (30% methylsilyl capped, 70% SiOH), H30 (50% methylsilyl capped, 50% SiOH), and MM038-5 (65% methylsilyl capped, 35% SiOH). The methylsilyl modification was performed by the manufacturer by reaction with dichlorodimethylsilane (see Figure I.1.1.3). The fumed silica particles are fractal-like aggregates [42] of approximately spherical 5-30nm diameter primary particles [30]. Silica nanoparticles with a 5nm diameter silica core and short PEG chains grafted to the surface were a gift from 3M Co., St. Paul, MN as a 19.3% w/v dispersion. These particles are nominally the same as the “Hydrophilic” particles in the work of Espinosa et al. [39]. Nanoparticle dispersions were diluted to desired concentrations with deionized (DI) water (Nanopure II, Barnstead, Dubuque, IA). Where indicated, the salinity and pH were adjusted to the desired level with NaCl (ACS grade, Fisher Scientific, USA) and HCl (ACS grade, Fisher Scientific, USA), respectively.

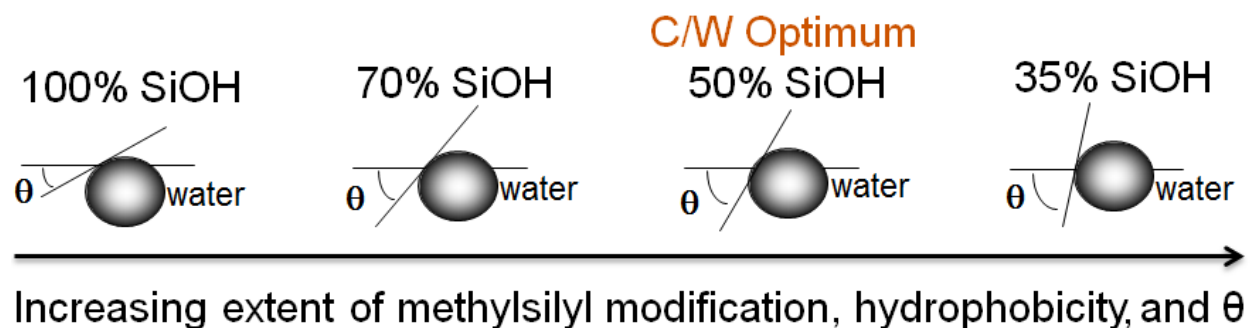


Figure I.1.1.2. Increasing extent of methylsilyl modification increases hydrophobicity and contact angle between water and the nonaqueous phase. We found 50% SiOH to be the optimum for C/W foam generation.

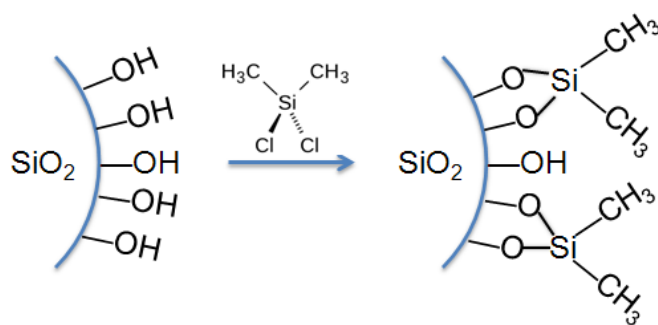


Figure I.1.1.3. Methylsilyl modification of bare silica particles with dichlorodimethylsilane (DCDMS).

Ethanol (ACS/USP grade, Pharmco-Aaper, Brookfield, CT) and CO₂ (research-grade, Matheson, USA) were used as received.

Throughout this work, the given particle and NaCl concentrations are all in % w/v in the aqueous phase, shown simply as “%” for clarity.

I.1.1.iv. Methods

Preparation of dispersions of partially hydrophobic (methylsilyl-modified) nanoparticles.

Since the partially hydrophobic silica particles were not wetted well by DI water, aqueous dispersions were prepared by first dispersing the particles in ethanol, centrifuging the dispersion, decanting the supernatant, and redispersing the particles in DI water using a Branson Sonifier (VWR Scientific, model 250) equipped with a microtip. Centrifugation, decantation, and redispersion in DI water were repeated once to reduce the concentration of ethanol to less than 1% v/v in the 1% w/v particle solutions. Particle hydrodynamic diameters were measured with dynamic light scattering (DLS) with a Brookhaven ZetaPALS instrument at room temperature and are given as mean diameter by volume in Table I.1.1.1. The natural pH of a 1% w/v solution of the particles was ca. pH 9 for the PEG-coated particles and ca. pH 6 for the fumed silica particles in DI water.

Table I.1.1.1. Hydrodynamic diameters of silica particles coated with PEG or various extends of methylsilyl groups

Particle	Coating	Particle Hydrodynamic Diameter ± St. Dev. (nm) in DI water
PEG-coated silica	Short-chain PEG	5.5 ± 0.13

100% SiOH	bare	177 ± 15
70% SiOH	30% methylsilyl modification	190 ± 36
50% SiOH	50% methylsilyl modification	196 ± 19
35% SiOH	65% methylsilyl modification	165 ± 22

A/W foam formation and stability determination. To generate A/W foams, 1.5 mL of aqueous nanoparticle dispersion was loaded into a 1 dram vial (capacity of ca. 3.7mL) and sonicated for 1 minute (67 ± 1 pulses) with the sonicator microtip just below the air-water interface. Digital photographs were taken at intervals and the height of the foam in the vial was measured with ImageJ software, using the known vial outside diameter (1.47cm) as reference.

C/W foam formation, apparent viscosity measurement, and stability determination. A diagram of the apparatus used to generate C/W foams is shown in Figure I.1.1.4, which was adapted from a previous study (Adkins, Chen et al. 2010). Flow rates of the CO₂ and aqueous phases were controlled by separate ISCO syringe pumps with series D pump controllers. The aqueous phase was injected into the apparatus with a feed accumulator (1.73 cm ID, 42 mL capacity) fitted with a piston to segregate the aqueous nanoparticle dispersion from the aqueous phase ISCO pump. The flow rate of CO₂ was set such that the expansion from room temperature to test conditions would provide the proper flow rate in the apparatus. The total flow rate of the CO₂ and aqueous phases was controlled at 1.5 or 3.0 mL/min with CO₂:water from 9:1 to 1:1 by volume. Foam was generated by shearing the aqueous nanoparticle dispersion and the CO₂ in a 0.38 cm ID x 11.3 cm long beadpack filled with 180 μm spherical glass beads (70-100 mesh soda-lime silica glass, Stock Number P-0080, Potters Industries Inc., Valley Forge, PA). Pore throat diameters in the beadpack range from 28-75 μm for hexagonal and cubic packed 180 μm spheres, respectively. Key beadpack parameters are reported in Table I.1.1.2. The temperature was controlled with a water bath and Julabo MP immersion circulator. The desired pressure in the apparatus was maintained at ±25psi with a back pressure regulator (Swagelok model SS-4R3A adjustable relief valve). 23 pore volumes (10mL) of nanoparticle dispersion was pumped through the apparatus before experiments began to condition the beadpack.

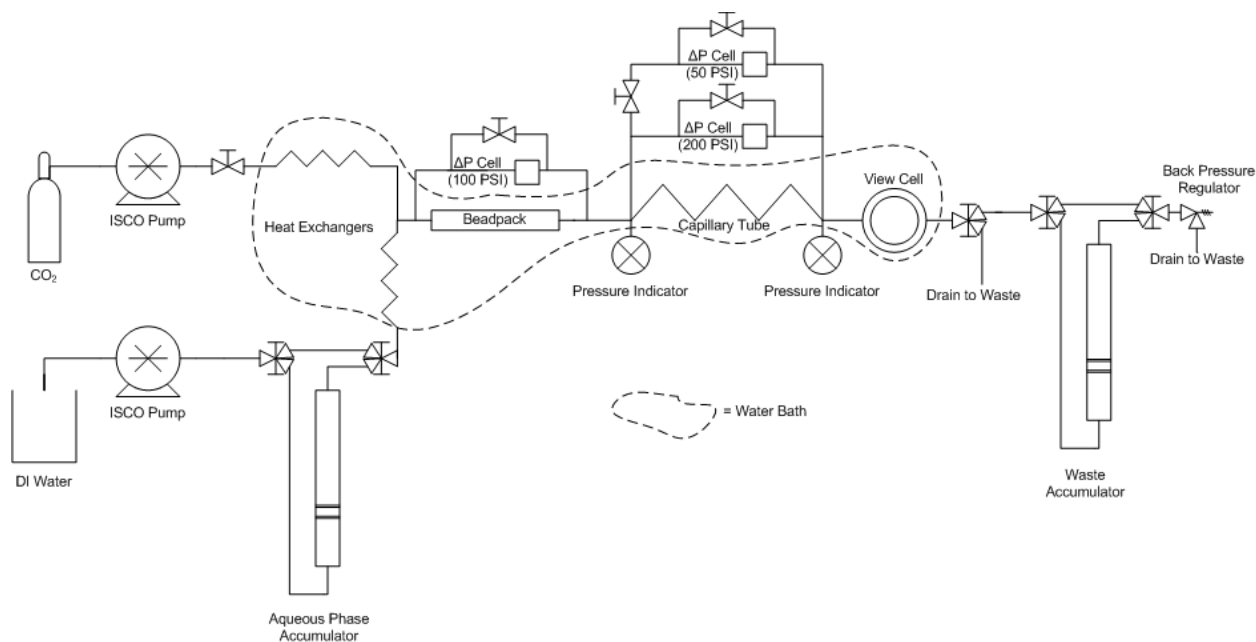


Figure I.1.1.4. Diagram of apparatus for C/W foam generation, measurement of viscosity and long term foam stability.

The apparent viscosity of the foam generated in the beadpack was determined by a method reported elsewhere [43]. Briefly, the pressure drop was measured with a differential pressure cell as the foam flowed through a capillary (0.0762 cm ID x 195 cm long) and the apparent viscosity was calculated with the Hagen-Poiseuille equation. Key capillary tube parameters are reported in Table I.1.1.2. Using this method, the viscosity of a 9:1 volume ratio mixture of CO₂ and water with no nanoparticles was determined to be 0.1 cP.

Table I.1.1.2. Parameters for flow in beadpack and capillary for 1.5mL/min total flow rate

	Permeability, d	Porosity	PV, mL	Superficial velocity, cm s ⁻¹	Residence time, s	Shear rate, s ⁻¹
Beadpack	22.5	0.34	0.436	0.220	17.4	1130
Capillary Tube	-	1	0.889	5.482	35.6	576

The effluent of the capillary flowed into a cylindrical view cell and was observed through a sapphire window. The view cell was fitted with a vertical Teflon channel (0.3 cm wide x 1.4 cm tall x 0.8 cm visual path length) to reduce dead volume. Experiments were typically conducted for 60-80 beadpack pore volumes of total flow. Pressure drop measured in the capillary typically reached a steady value after ca. 40 pore volumes, and at least 30 pore volumes were allowed for flow stabilization in all experiments. After the pressure drop was measured, the differential

pressure (dP) cells were “zeroed” to account for any calibration shift during the experiment. A typical plot of pressure drop vs. beadpack pore volumes injected is shown in Figure I.1.1.5.

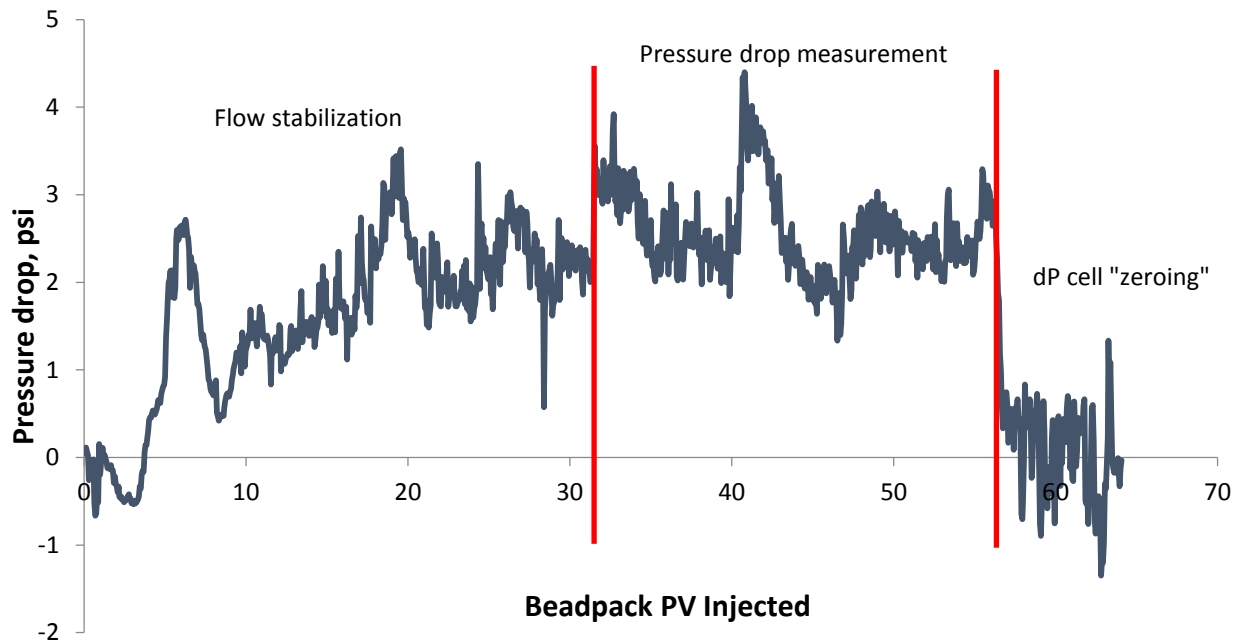


Figure I.1.1.5. Typical plot of pressure drop vs. beadpack pore volumes (PV) injected with demarcated experimental periods. Foam stabilized with 1% PEG-coated silica particles at 50°C and 2000psia with CO₂:water of 9:1 by volume and a total flow rate of 1.5mL/min (Experiment 5).

To determine foam stability, flow was stopped and macroscopic observations of foam height in the high pressure view cell were recorded via digital photography. During stability observations, system pressure was maintained with the CO₂ phase ISCO pump in constant pressure mode and the system temperature was maintained with the water bath and immersion circulator.

I.1.1.v. Results

A/W foam formation and stability. A/W foams were stabilized with 1% silica particles in solution with 0%, 1% and 8% NaCl, and the foams are shown 7 days after emulsion formation in Figure I.1.1.6. The 70% SiOH particles did not stabilize foam without added salt (top left), but stabilized foam with 1% NaCl added (middle left) and a larger volume of foam with 8% NaCl added (bottom left). Adding NaCl caused the particles to aggregate and gravity settle, visible as a layer of particles at the bottom of the vial in the 70% SiOH particle experiments with 1% and 8% NaCl. In the 50% and 35% SiOH samples, adding NaCl resulted in a clear water phase below the foams with 1% and 8% NaCl and increasing foam height from 0% NaCl to 1% NaCl. In the 50%

SiOH samples, adding 1% NaCl also caused the visible bubbles to decrease in size noticeably over the 0% NaCl sample. The 100% SiOH particles did not stabilize foam with up to 8% NaCl (not pictured). The PEG-coated particles stabilized foam with 0%, 1%, and 8% NaCl, but the foams completely resolved in less than 24h (not pictured).

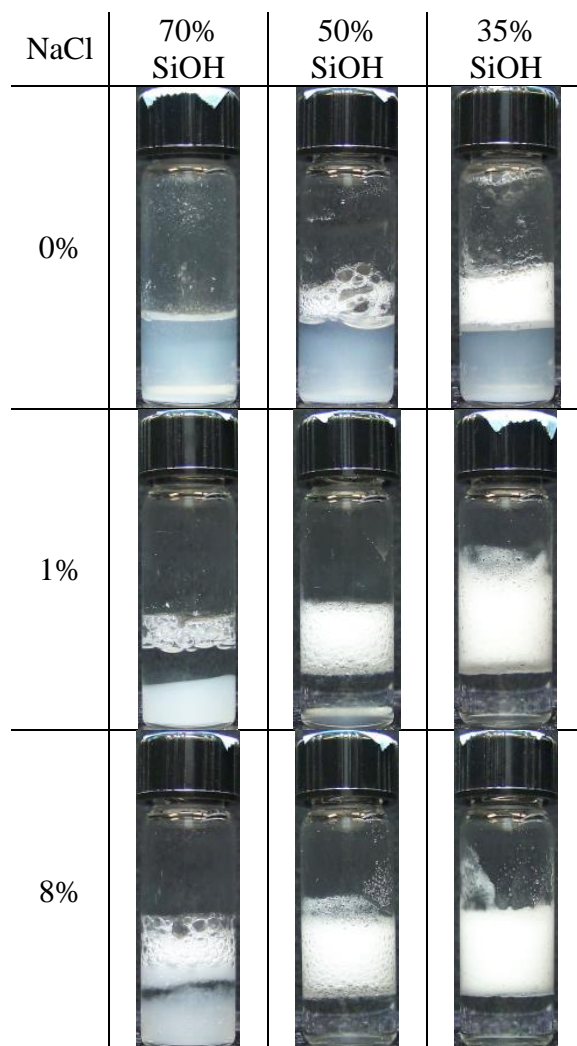


Figure I.1.1.6. A/W foams stabilized with 1% w/v 70%, 50%, and 35% SiOH particles at pH 4 with 0% w/v, 1% w/v, and 8% NaCl w/v, 7 days after foam formation. The outside diameter of the vials is 1.47cm.

Foam heights vs. time of A/W foam stabilized with 1% nanoparticle solution with 1% NaCl at time points up to 7d are shown in Figure I.1.1.7. The initial time point is 30 seconds after sonication. For the partially hydrophobic silica particles, the initial foam height increased from 0.7cm (70% SiOH) to 1.73cm (50% SiOH) to 2.27cm (35% SiOH) indicating a strong

correlation between foam height and particle hydrophobicity. After initially decreasing in height over the first hour, the foams stabilized with modified silica particles remained stable for 7d. For example, the 35% SiOH particles decreased from an initial height of 2.27cm to 1.37cm after 1h, then to 1.36cm after 24h, then to 1.34cm after 7d. The PEG-coated particles initially formed foam with a height of 1.52cm but the foam completely resolved in less than 24 hours, indicating much lower stability of the foams stabilized with PEG-coated particles than foams stabilized with partially hydrophobic silica particles.

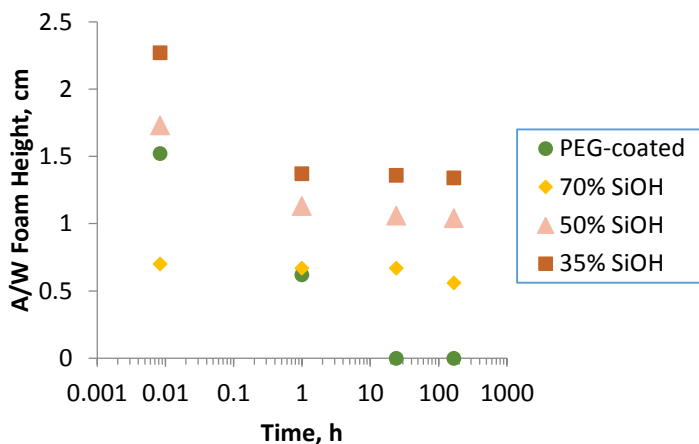


Figure I.1.1.7. Foam height vs. time of A/W foams stabilized with 1% w/v dispersions of 70%, 50%, and 35% SiOH particles and PEG-coated silica at pH 4 with 1% NaCl.

C/W foam formation and viscosity. PEG-coated nanoparticles were used to generate C/W foams with salinities up to 8% NaCl at 50°C at pressures of 1200-3000psia. Here, CO₂ is a supercritical fluid with densities of 0.235g mL⁻¹-0.860g mL⁻¹ (Table I.1.1.3). Experiments 1 and 2 indicate that increased CO₂ density (0.235g mL⁻¹ to 0.792g mL⁻¹) increased PEG-coated silica foam viscosity from 5.48cP to 12.1cP with 3% PEG-coated silica particles. Adding 1% NaCl further increased viscosity to 15.7cP (Experiment 3). Similar to the case for Experiments 1 and 2, increasing CO₂ density (0.506g mL⁻¹ to 0.792g mL⁻¹) increased PEG-coated silica foam viscosity from 2.02cP to 3.58cP with 1% PEG-coated silica particles (Experiments 4-6). However the foam viscosity was lower than in Experiments 1 and 2, as the result of the lower particle concentration. The foam in Experiment 4 had large, visible bubbles (not shown). Experiments 7-9 show that the viscosity of foam stabilized with 1% PEG-coated silica particles increased with the addition of NaCl from 5.68cP with 1% NaCl to over 9.4cP with both 3% and 8% NaCl. The foams in Experiments 2 and 3 (12.1cP and 15.7 cP) are opaque white with bubbles less than

100 μ m in diameter, on the basis of visual observation. To our knowledge, this is the first study to report C/W foams with such fine textures, for foams stabilized solely with nanoparticles.

Table I.1.1.3. C/W foam viscosities with PEG-coated silica particles at 50°C calculated from pressure drops measured in the capillary tube. Total flow rate of 1.5mL/min with CO₂:water of 9:1 by volume.

Experiment	Particle Concentration in Aqueous Phase, % w/v	NaCl Concentration in Aqueous Phase, % w/v	P, psia	ρ_{CO_2} , g mL ⁻¹	μ_{app} , cP
1	3	-	1200	0.235	5.48
2	3	-	3000	0.792	12.1
3	3	1	3000	0.792	15.7
4	1	-	1600	0.506	2.02
5	1	-	2000	0.665	3.01
6	1	-	3000	0.792	3.58
7	1	1	2800	0.776	5.68
8	1	3	2800	0.776	9.42
9	1	8	2800	0.776	9.44

The 50% SiOH particles, with the extremely small methylsilyl ligands, stabilized C/W foam at 50°C (Experiments 10-12) and 35°C (Experiments 13-15) at pressures of 1600 psia to 2800 psia, and densities of 0.506 g mL⁻¹-0.860 g mL⁻¹ (Table I.1.1.4). The foams in Experiments 10-15 had viscosities of 1.36-2.29cP, which were lower than those of the PEG-coated silica particle stabilized foams under the same conditions, except in the case of Experiment 4. For the silica stabilized C/W foams, all of the foams were opaque white with bubbles less than 100 μ m in diameter. We are not aware of any previous studies of C/W stabilized foam with silica nanoparticles and small ligands that had such fine texture.

Table I.1.1.4. C/W foam viscosities with 1% w/v 50% SiOH particles calculated from pressure drops measured in the capillary tube. Total flow rate of 1.5mL/min with CO₂:water of 9:1 by volume.

Experiment	T, °C	P, psia	ρ_{CO_2} , g mL ⁻¹	μ_{app} , cP
10	50	1600	0.506	1.44
11	50	2000	0.665	1.36
12	50	2800	0.776	2.29
13	35	1600	0.745	1.42
14	35	2000	0.798	1.46
15	35	2800	0.860	1.59

The more hydrophilic 100% and 70% SiOH particles did not stabilize foam with 1% particle dispersion at 35°C and 2800 psia, the highest density CO₂ condition tested. Also, the more hydrophobic 35% SiOH particles did not stabilize foam with 1% particle dispersion and aggregated in the presence of CO₂ at 35°C and 2800 psia. The only partially hydrophobic silica particles to stabilize foam were the intermediately hydrophobic 50% SiOH particles.

Figure I.1.1.8 shows the apparent viscosity behavior of the 50% SiOH particles in CO₂-water foams generated at 2800psia and 50°C with foam qualities of 0.5 to 0.975, indicating CO₂:water of 1:1 to 49:1, respectively. Foam quality is given by the CO₂ fraction in the total CO₂-water mixture. Increasing foam quality from 0.5 to 0.75 resulted in an increase in viscosity from 2.01cP to 7.25cP. Further increasing of foam quality caused a decrease in viscosity to 0.65cP at a foam quality of 0.975. These results indicate that the peak foam viscosity in the range of foam quality investigated falls between qualities of 0.5 and 0.9, with a maximum observed value at 0.75. To our knowledge, C/W foams with such a high viscosity have not been reported previously for foams stabilized with silica particles having small ligands.

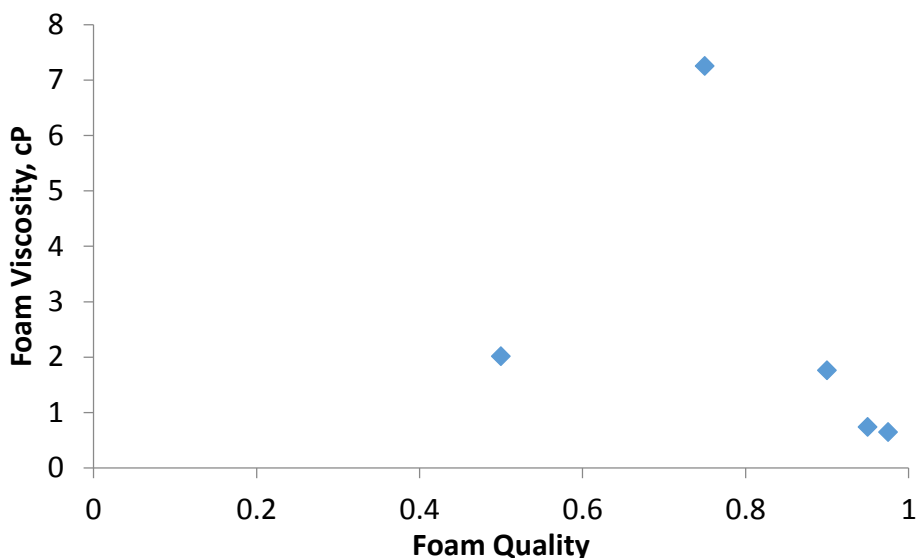
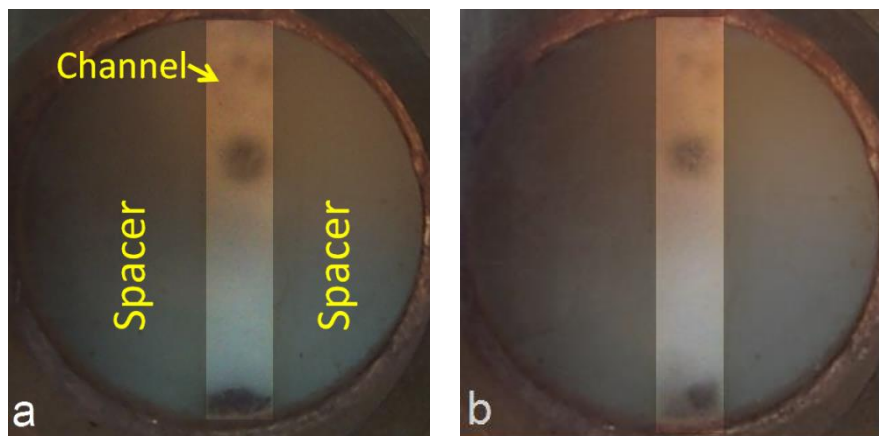


Figure I.1.1.8. Foam viscosity calculated from pressure drop measured in the capillary tube vs. foam quality at 2800psia and 50°C. Foam was generated at a total flow of 3 mL/min using 50% SiOH particles.

C/W foam stability. C/W foams stabilized with 50% SiOH and PEG-coated silica were held quiescent in the high-pressure view cell for 20-23h, with the temperature and pressure maintained at the initial experimental conditions (Figure I.1.1.9). Digital photographs were taken to document the change in foam height and texture over time (results are summarized in Table

I.1.1.5). Foam is visible in the vertical channel in the center of the window between the white Teflon spacers. Fig. 9a shows foam from Experiment 15, stabilized with 50% SiOH particles where initial viscosity was 1.59cP, and Fig. 9b shows the foam after 23h, indicating less than 10% resolution (by height). The unresolved foam remained opaque white. Fig. 9c shows foam at the maximum viscosity given in Fig. 8, stabilized with 50% SiOH at 2800psia and 50°C, where the initial viscosity was 7.25cP, and Fig. 9d shows the foam after 23h, indicating ca. 12% resolution (by height). Again the unresolved foam remained opaque white. Fig. 9e shows foam from Experiment 2, stabilized with PEG-coated silica particles where the initial viscosity was 12.1cP, and Fig. 9f shows the foam after 20h, indicating that ca. 55% of the foam resolved (by height) and the remaining foam was no longer opaque white. Fig. 9g shows foam from Experiment 3, stabilized with PEG-coated silica particles with 1% NaCl where the initial viscosity was 15.7cP, and Fig. 4h shows the foam after 23h, indicating that ca. 75% of the foam resolved (by height) and again the remaining foam was no longer opaque white. The reductions in foam height and opacity after 20-23h indicate lower stability of the PEG-coated particle foams compared to the more stable 50% SiOH particle foams, despite the higher initial viscosities of the PEG-coated particle foams.



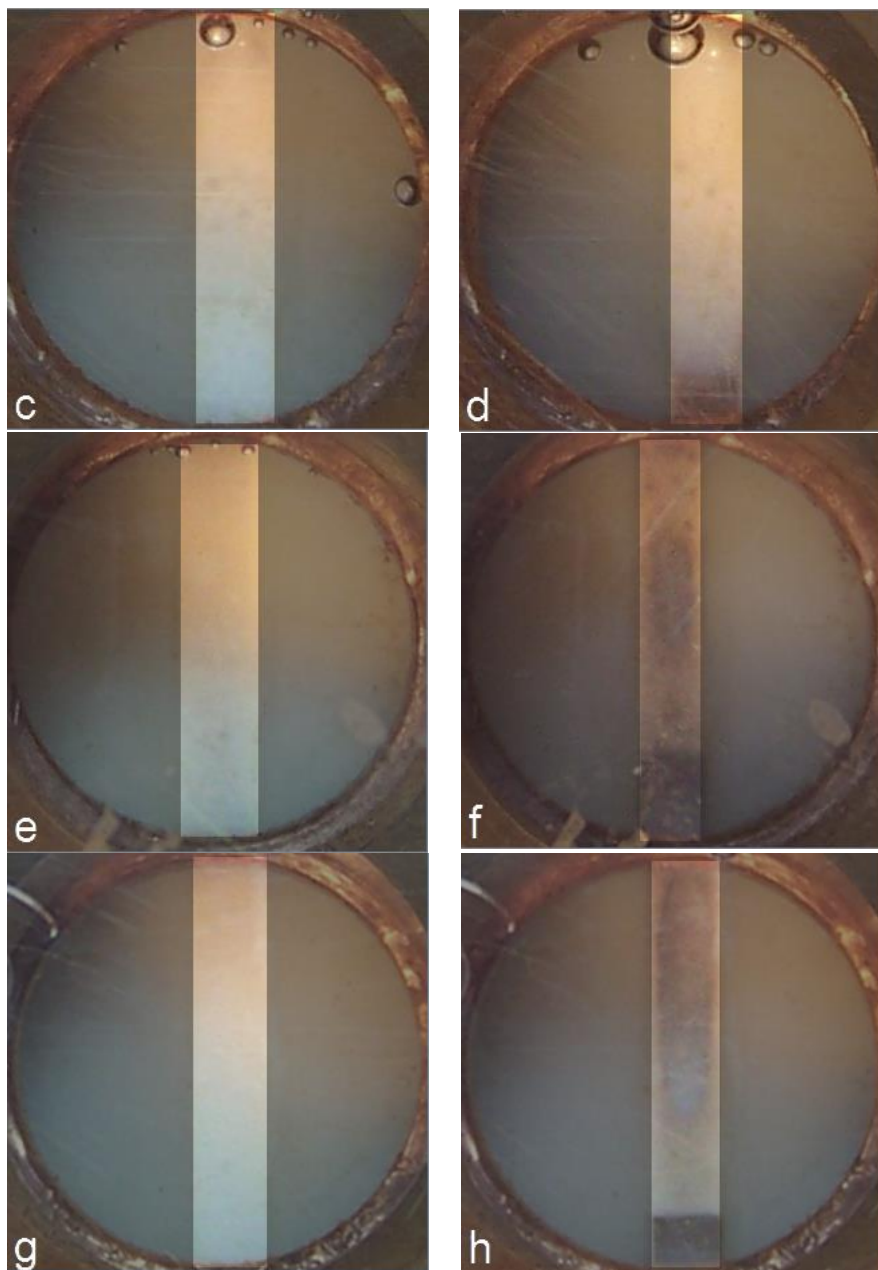


Figure I.1.1.9. Digital photographs of foam in view cell. CO₂:water was 9:1 by volume except in (c) and (d) where CO₂:water was 3:1 by volume. (a) and (b) are 1% w/v 50% SiOH, 2800psia and 35°C, t=0 and 23h, respectively. (c) and (d) are 1% w/v 50% SiOH, 2800psia and 50°C, t=0 and 23h, respectively. (e) and (f) are 3% w/v PEG-coated silica, 3000psia and 50°C, t=0 and 20h, respectively. (g) and (h) are 3% w/v PEG-coated silica, 3000psia and 50°C, with 1% w/v NaCl, t=0 and 23h, respectively. Foam is visible in the center of the window in the vertical channel between Teflon spacers. The Teflon spacers have been darkened with photo editing software to highlight the channel. Dark regions in the channel indicate absence of foam. Window diameter is 1.4cm and visual path length is 0.8cm.

Table I.1.1.5. Measured nanoparticle-stabilized foam resolution from Fig. I.1.1.9.

Particle	Condition	Resolution (by height) in 20-23h
50% SiOH	1% NP, 9:1 C:W, 2800psia, 35°C, no salt	<10%
50% SiOH	1% NP, 3:1 C:W, 2800psia, 50°C, no salt	12%
PEG-coated	3% NP, 9:1 C:W, 2800psia, 50°C, no salt	55%
PEG-coated	3% NP, 9:1 C:W, 2800psia, 50°C, 1% NaCl	75%

1.1.1.vi.Discussion

Nanoparticles adsorbed at the oil-water interface often do not lower interfacial tension for particles modified with low molecular weight ligands [44] and polymeric ligands with low amphiphilicity. However, large interfacial tension reductions at the oil-water interface have been observed for iron oxide nanoparticles coated with amphiphilic copolymers [27, 29]. Whereas the effect of a wide variety of surfactant molecules on the lowering of γ at the CO₂-water interface has been studied in detail [8, 13, 18], analogous studies for nanoparticles have not been reported. At typical reservoir temperatures and pressures, γ is much smaller for the C/W interface, only ~20 mN/m, than the O/W interface. Thus, less shear would be required to form bubbles of the dispersed phase for bulk C/W emulsions or foams relative to O/W emulsions. In each case, it is unclear how much nanoparticles lower the γ , as discussed above. Thus, the unusually low γ for the CO₂-water interface, even without an amphiphile or nanoparticle, may be expected to be beneficial for the formation of nanoparticle-stabilized bubbles.

In a bulk phase, a CO₂ bubble will form when the shear stress exceeds the Laplace pressure of the bubble. The shear rates studied in the beadpack of 1130 s⁻¹-2270 s⁻¹ for flow rates of 1.5 mL/min to 3 mL/min, were sufficient to produce foams as observed by pressure drops in the beadpack of up to 25 psi, where pressure drop in the beadpack at a given flow rate tended to increase with apparent viscosity measured in the capillary. Additional foam formation mechanisms such as leave-behind, snap-off, and lamella division [1] will also be present in the porous media. As the CO₂ bubbles and aqueous lamellae are formed, nanoparticles will be adsorbed at the CO₂-water interface and preserve the foam texture (bubble size) within the beadpack and while it flows through the capillary tube to the view cell. At the slowest flow rate tested, 1.5 mL/min, the foams took less than 1 minute to reach the view cell after leaving the beadpack, so the viscosity measurements and texture observations reflect short-term stability. While in the capillary, the bubbles flow as a bulk foam when the bubble diameter is much less

than the capillary diameter or as individual lamellae when bubble diameter is much greater than capillary tube diameter [45]. Thus, for the foams that appeared opaque white in the view cell (bubble diameters less than 100 μm) bulk foam flow is expected in the capillary tube (diameter of 762 μm).

Models for partitioning of nanoparticles in bulk phases and at the interface. In systematic studies of A/W foams [31] and O/W emulsions [30] stabilized with fumed silica nanoparticles, the hydrophobicity of the particles was tuned from 14% to 100% SiOH. The variation in hydrophobicity controlled the adsorption of the nanoparticles at the interface relative to partitioning into the aqueous phase. The location of the nanoparticle at the interface is quantified by the contact angle measured through the water phase [46] as described by Young's equation

$$\cos(\theta) = \frac{\gamma_{pn} - \gamma_{pw}}{\gamma_{nw}} \quad (1.1.1.2)$$

where γ_{pn} , γ_{pw} , and γ_{nw} are the interfacial energies between particle/nonaqueous phase, particle/aqueous phase, and nonaqueous phase/aqueous phase, respectively, letting $n=A$ (air), O (oil), or C (CO_2). In an air-water system, the adsorption at the interface increases with increased hydrophobicity (increased γ_{pw} and decreased γ_{pA}). In Figure I.1.1.6, hydrophobicity of 50% SiOH or higher, or 70% SiOH with 1%-8% NaCl added to the aqueous solution is necessary to drive the particles to the A/W interface, which is consistent with previous work [31, 41]. The maximum foam height has been observed with 42% SiOH [31]. In oil-water systems, a greater methylsilyl ligand coverage is expected to simultaneously lower γ_{pO} and raise γ_{pw} . Consequently, the maximum O/W emulsion stability was observed by Binks et al. with 67% SiOH [30] over a wide range of oil:water ratios.

In a CO_2 -water system, the influence of interactions between silica, water, and CO_2 on the contact angle of a water droplet has been measured experimentally and described by a thermodynamic model [47]. The interfacial energies between the surface of the particle and CO_2 and water phases may be related to the intermolecular interactions between the surface of the particle and the fluids [48]. Following the definition of HCB for a surfactant at a CO_2 -water

interface (Eqn. I.1.1.1), the equivalent HCB for a nanoparticle with a uniform surface (P) is defined here for the first time as

$$1 / HCB = \frac{A_{PC} - A_{PP} - A_{CC}}{A_{PW} - A_{PP} - A_{WW}} \quad (\text{I.1.1.3})$$

The methylsilyl ligands on the partially hydrophobic silica particles are hydrophobic, have low cohesive energy density, and are thus favorably solvated by CO_2 [18]. Therefore, a decrease in % SiOH simultaneously decreases A_{PW} (increasing γ_{PW}), decreases A_{PP} , and increases A_{PC} (decreasing γ_{PC}). According to Equations I.1.1.2 and 3, controlling the HCB of the particles through the % SiOH allows tuning of θ at the CO_2 -water interface, which influences emulsion curvature (Fig. I.1.1.1).

Silica nanoparticle SiOH level and stabilization of A/W foams, O/W emulsions, and C/W emulsions and foams. The optimum SiOH level for forming a C/W foam may be compared with that for A/W foams and O/W emulsions in terms of the relevant interactions of the surface with the fluid phases. The optimum SiOH level for A/W foam and O/W emulsions were 42% SiOH [31] and 67% SiOH [30], respectively. The fraction of air in the emulsion was approximately 0.7 and the oil fraction in the O/W emulsion was 0.8. In this study, the optimum SiOH level for C/W foam with a CO_2 fraction of 0.9 was 50% SiOH. Thus, the hydrophobicity for optimum particles for CO_2 is intermediate between those for A/W and O/W interfaces. This trend may be expected given that the van der Waals forces of the nonaqueous phase, CO_2 , are intermediate between those for air (essentially none) and an oil. Thus the numerator in Eq. I.1.1.3 is smaller in the case of CO_2 than for oil, but larger than for air. For C/W emulsions with lower qualities, higher HCB particles (100% and 74% SiOH) stabilized the emulsions [23]. For the C/W foams in the current study at higher qualities, a lower HCB was required, which would cause a greater adsorption of nanoparticles at the CO_2 -water interface. Apparently, this higher adsorption was required for stabilization of the lamellae in the high quality C/W relative to the CO_2 droplets at greater spacing in the C/W emulsions at lower quality. At much lower HCB values, e.g. with silica nanoparticles with fluorosilane coatings, W/C emulsions are formed [22] This HCB concept is thus quite useful for designing nanoparticle surfaces for the desired type of emulsion or foam morphology.

Tuning particle HCB to provide lamellae stabilization for viscosity enhancement. Upon formation of the CO₂ bubbles, the nanoparticles must adsorb at the interface, as a function of their HCB, and stabilize the bubbles to stabilize the foam. The apparent viscosity of a foam in a capillary tube is the sum of three possible contributions: slugs of liquid between bubbles, resistance to deformation by the bubbles, and surface tension gradients [45]. As the bubble size decreases, and thus the number of lamellae per unit length increases, the greater resistance to flow raises the apparent viscosity [36, 45, 49]. Viscous C/W foams were generated that raised the apparent viscosity of the CO₂-water mixture over 120 fold with the PEG-modified silica particles (Table 3) and over 70 fold with the 50% SiOH particles (Fig. I.1.1.8). Thus, these coating had HCB values that were in a desirable range for stabilizing foams for high viscosities.

The effects on the viscosity of the C/W foams from the particle concentration, CO₂ density, and NaCl concentration may be related to bubble size and particle HCB (Tables 3 and 4). When the concentration of PEG-modified particles was increased from 1% to 3% in the aqueous phase, smaller bubbles were observed and produced the expected increase in viscosity with the greater number of lamellae [45, 49]. Increasing CO₂ density increased solvation of the PEG chains [40] and the interactions between the CO₂ and the PEG became more favorable [47]. The more favorable interactions decreased the HCB and resulted in improved adsorption at the CO₂-water interface, which resulted in more lamellae and a higher foam viscosity. The same trend in CO₂ density was observed for the 50% silanol surface, as the interactions between CO₂ and the surface became stronger which decreased the HCB of the particles.

Increasing NaCl concentration caused the PEG-modified and 50% SiOH particles to behave more hydrophobically (weakened A_{PW} as observed in the A/W results) which resulted in a lower HCB (Eqn. I.1.1.3) and improved contact angle at the CO₂-water interface (Eqn. I.1.1.2).

Improved contact angle (closer to 90°) favors adsorption of more particles at the CO₂-water interface, greater generation of lamellae, and therefore a higher viscosity. The PEG-modified particles' ability to stabilize foam with up to 8% NaCl present also indicated the low molecular weight PEG-coating can still be solvated by water at high salinity. For PEG-water phase behavior, as the molecular weight of PEG increases, the cloud point where PEG becomes desolvated by water decreases. In contrast, the 50% SiOH particles flocculated in 1% NaCl

aqueous solution (without CO₂), perhaps due to reduced thickness of the double layer [50], and the resulting aggregates were too large to pass through the pores in the beadpack.

Effect of foam quality. As quality is increased from an emulsion with dispersed bubbles in a continuous phase to a foam with compressed bubbles separated by lamellae, the viscosity of the emulsion (foam) is expected to reach a maximum and then drop to gas the phase viscosity as the quality approaches unity [51]. If the foam quality is too low, droplets are spherical and dispersed, without lamellae between them, the viscosities are not expected to be more than a few times that of the solvent, as described by the Krieger-Dougherty equation [50]. When dispersed droplets are far apart, it is not necessary to deform lamellae during flow. Conversely, when the quality is too high, the lamellae are too thin and rupture or, in the most extreme case, the system does not have sufficient liquid to form lamellae. In this study, the highest viscosity of the 50% SiOH particle foam was at a quality of 0.75 (Fig. I.1.1.8), and it decreased markedly for qualities of 0.9 to 0.975. Thus, the quality that gave the highest foam viscosity was lower for these particles at the condition tested than for the PEG-modified particles, which showed a maximum viscosity in the quality range of 0.86-0.92 at a lower pressure of 1400psia and hence a smaller CO₂ density [39]. Further studies of the optimum quality for maximum viscosity would be warranted as a function of temperature, pressure, nanoparticle concentration, and particle HCB.

C/W foam long-term stability. The presence of strongly adsorbed nanoparticles at an interface has the potential to provide long term stabilization of lamellae [52]. Most simply, particles in a foam can organize at an interface in three ways: as (1) a monolayer “bridge” of particles (2) a bilayer and (3) as a gel inside the continuous liquid film [52]. In all three configurations, particles provide a barrier to bubble coalescence. The effectiveness of particles in stabilizing emulsions depends on factors such as particle size, particle shape, particle concentration, contact angle, and interactions between particles [46]. In particular, particles with higher adsorption energy at a fluid-fluid interface, E , are expected to be better long-term stabilizers of lamellae [53]. The adsorption energy is given by

$$E = \pi r^2 \gamma_{\alpha\beta} (1 \pm \cos \theta)^2 \quad (\text{I.1.1.4})$$

where r is the particle radius, $\gamma_{\alpha\beta}$ is the interfacial tension between fluid α and fluid β , and θ is the contact angle of the particle at the interface (as in Eqn. I.1.1.2). The sign in parenthesis

corresponds to a particle center in the nonaqueous phase (+) or in the aqueous phase (-). For example, a particle with $r = 50$ nm and $\theta = 80^\circ$ (putting the particle center slightly on the aqueous side of the interface with a favorable HCB) at a CO₂-water interface ($\gamma_{CW} = 20$ mN/m) has $E = 26,000kT$. Thus, it may be expected that particles can be designed to adsorb irreversibly at a CO₂-water interface, which may favor long term stability. Unlike surfactants which can dynamically adsorb to and desorb from a fluid-fluid interface and partition between the fluid phases, nanoparticles often irreversibly adsorb at the interface [46]. In this case, they will likely be found only at the interface and in the bulk fluid phase where they were initially dispersed. Partitioning of a nanoparticle to a CO₂ droplet from a bulk aqueous phase would require desorption of the nanoparticle from the interface into the CO₂ droplet and solubilization of the nanoparticle in the bulk CO₂ phase. These factors are unlikely given the irreversibility of the adsorption at the interface and weak solvent strength of CO₂, respectively. Typically, fluorocarbon surfaces have been required on nanoparticles for dispersibility in CO₂ [10, 22], although a few exceptions have been observed [10, 54]. The permanence of the adsorption of nanoparticles versus surfactants suggests that properly designed nanoparticles may potentially stabilize foams more effectively than typical surfactants.

Trends in the long-term stability with respect to particle properties that affect E were observed in this study. In particular, the C/W foams were much more stable for the 50% SiOH than the PEG-modified particle stabilizers (Fig. I.1.1.9 and Table I.1.1.5). Assuming a favorable $\theta = 80^\circ$ in each case (contact angles are rarely measured for nanoparticles, given challenges in imaging and capturing micrographs), the 196nm 50% SiOH particles would have an E of over 1200 fold that of the smaller 5.5nm PEG-modified particles given the r^2 dependence of E . Further, the HCB of the PEG-modified particles is expected to be higher than that of the 50% SiOH particles, leading to a smaller θ that causes the particle center to move further into the aqueous phase (closer to $\cos \theta = 1$), potentially leading to an even larger difference in E . This trend is due in part to the greater hydrophilicity of PEG versus 50% SiOH. It is also due to the only moderate solvation of PEG by CO₂ [40] in comparison to greater solvation of the methylsilyl groups. Additionally, the interactions between the low molecular weight methylsilyl ligands on the partially hydrophobic silica particles are small compared to the PEG chains. This could reduce formation of 2D aggregates of particles at the interface [55] that can be present when particles are poorly

solvated. The 2D “islands” of particles can leave large regions of the interfaces without particles to provide a barrier to coalescence, which can result in decreased stability. However, the exact stabilization mechanism and configuration of particles at the C/W interfaces in this study would require further study, as is also the case for O/W interfaces [29, 44, 55].

1.1.1.vii. Conclusions

Opaque white C/W foams with bubble sizes too small to be visible (<100 μm) were generated with either PEG-coated silica or methylsilyl modified silica nanoparticles (50% SiOH.) Here the HCB (hydrophilic-CO₂philic balance for the nanoparticle) was in the proper range for the adsorption of the nanoparticles at the CO₂-water interface with a desirable contact angle for stabilizing aqueous lamellae between CO₂ bubbles. The lamellae increased the foam apparent viscosities up to 120 fold relative to the case of CO₂-water mixtures without nanoparticles. The relatively bare silica nanoparticles, with only 50% short, low cohesive energy density methylsilyl ligands on the surface, favored solvation of the particles surface by CO₂ at the C-W interface. Particles with greater or lesser fraction of methylsilyl coverage did not stabilize C/W foam. The HCB for nanoparticles introduced in this work provides a consistent framework for interpreting foam stabilization by nanoparticles. We illustrated this concept by comparing the influence of different particles on the behavior of A/W foams at ambient conditions, of C/W foams for a wide range of CO₂ densities and of O/W emulsions. The SiOH level that stabilized the C/W foam was 50%, corresponding to a hydrophobicity (and likewise to a HCB) between the optimum values for stabilizing O/W emulsions [30] and A/W foams (this work and [31]). In addition, this HCB was intermediate between values previously shown for C/W [23] and W/C emulsions [22]. For the larger 196 nm 50% SiOH particles, the C/W foam were more stable than for the 5.5nm PEG-coated silica particles, showing four to six times less resolution in a 20-23 hour period. The greater stability for the larger 50% SiOH particles arises from two factors: the much larger adsorption energy ($>10^4 kT$) at the CO₂-water interface, and the more effective solvation of CH₃ groups versus PEG. The ability to achieve long term stability for nanoparticle stabilized C/W foams would offer an alternative to conventional surfactants, which are known to have much lower adsorption energies.

1.1.1.viii. References

- [1] W.R. Rossen, in: R.K. Prud'homme, S.A. Khan (Eds.), *Foams: Theory, Measurements, and Applications*; Marcel Dekker, New York, 1996.
- [2] H.O. Lee, J.P. Heller, A.M.W. Hofer, *SPE Reservoir Engineering* (1991) 421.
- [3] Q.P. Nguyen, W.R. Rossen, P.L.J. Zitha, P.K. Currie, SPE 94764, presented at SPE European Formation Damage Conf., Scheveningen, Norway, May 25-27. (2005).
- [4] W.J. McLendon, P. Koronaios, S. McNulty, R.M. Enick, G. Biesmans, A. Miller, L. Salazar, Y. Soong, V. Romanov, D. Crandall, SPE 154205, presented at SPE Improved Oil Recovery Symp., Tulsa, OK, Apr. 14-18 (2012).
- [5] R.M. Enick, D. Olsen, J. Ammer, W. Schuller, SPE 154122, presented at SPE Improved Oil Recovery Symp., Tulsa, OK, Apr. 14-18. (2012).
- [6] D. Xing, B. Wei, K. Trickett, A. Mohamed, J. Eastoe, Y. Soong, R.M. Enick, SPE 129907, presented at SPE Improved Oil Recovery Symp., Tulsa, OK, Apr. 24-28. (2010).
- [7] F.M. Orr, J.J. Taber, *Science* 224 (1984) 563.
- [8] K.P. Johnston, S.R.P. Da Rocha, *Journal of Supercritical Fluids* 47 (2009) 523.
- [9] K.P. Johnston, D. Cho, S.R.P. da Rocha, P.A. Psathas, W. Ryoo, S.E. Webber, J. Eastoe, A. Dupont, D.C. Steytler, *Langmuir* 17 (2001) 7191.
- [10] J.L. Dickson, P.S. Shah, B.P. Binks, K.P. Johnston, *Langmuir* 20 (2004) 9380.
- [11] J. Eastoe, S. Gold, D.C. Steytler, *Langmuir* 22 (2006) 9832.
- [12] J. Eastoe, S. Gold, *Physical Chemistry Chemical Physics* 7 (2005) 1352.
- [13] J.L. Dickson, P.G. Smith, Jr., V.V. Dhanuka, V. Srinivasan, M.T. Stone, P.J. Rosicky, J.A. Behles, J.S. Keiper, B. Xu, C. Johnson, J.M. DeSimone, K.P. Johnston, *Industrial & Engineering Chemistry Research* 44 (2005) 1370.
- [14] S.R.P. da Rocha, K.L. Harrison, K.P. Johnston, *Langmuir* 15 (1999) 419.
- [15] M. Kahlweit, *Journal of Colloid and Interface Science* 90 (1982) 197.
- [16] M. Bourrel, R.S. Schechter, *Microemulsions and Related Systems: Formation, Solvency, and Physical Properties*. Marcel Dekker, New York, 1988.
- [17] W.C. Griffin, *Journal of the Society of Cosmetic Chemists* 1 (1949) 311.
- [18] S.S. Adkins, X. Chen, Q.P. Nguyen, A.W. Sanders, K.P. Johnston, *Journal of Colloid and Interface Science* 346 (2010) 455.
- [19] V.V. Dhanuka, J.L. Dickson, W. Ryoo, K.P. Johnston, *Journal of Colloid and Interface Science* 298 (2006) 406.
- [20] M.T. Stone, P.G. Smith, S.R.P. da Rocha, P.J. Rosicky, K.P. Johnston, *Journal of Physical Chemistry B* 108 (2004) 1962.
- [21] P.G. Smith, Jr., W. Ryoo, K.P. Johnston, *Journal of Physical Chemistry B* 109 (2005) 20155.
- [22] S.S. Adkins, D. Gohil, J.L. Dickson, S.E. Webber, K.P. Johnston, *Physical Chemistry Chemical Physics* 9 (2007) 6333.
- [23] J.L. Dickson, B.P. Binks, K.P. Johnston, *Langmuir* 20 (2004) 7976.
- [24] J.-L. Salager, R. Antón, D. Sabatini, J. Harwell, E. Acosta, L. Tolosa, *Journal of Surfactants and Detergents* 8 (2005) 3.
- [25] M. Kahlweit, R. Strey, D. Haase, P. Firman, *Langmuir* 4 (1988) 785.
- [26] M. Kahlweit, B. Faulhaber, G. Busse, *Langmuir* 10 (1994) 2528.

- [27] N. Saleh, T. Sarbu, K. Sirk, G.V. Lowry, K. Matyjaszewski, R.D. Tilton, *Langmuir* 21 (2005) 9873.
- [28] N. Saleh, K. Sirk, Y. Liu, T. Phenrat, B. Dufour, K. Matyjaszewski, R.D. Tilton, G.V. Lowry, *Environmental Engineering Science* 24 (2007) 45.
- [29] K.Y. Yoon, Z. Li, B.M. Neilson, W. Lee, C. Huh, S.L. Bryant, C.W. Bielawski, K.P. Johnston, *Macromolecules* 45 (2012) 5157.
- [30] B.P. Binks, S.O. Lumsdon, *Langmuir* 16 (2000) 8622.
- [31] B.P. Binks, T.S. Horozov, *Angewandte Chemie, International Edition* 44 (2005) 3722.
- [32] B.P. Binks, R. Murakami, *Nature Materials* 5 (2006) 865.
- [33] D. Golomb, E. Barry, D. Ryan, C. Lawton, P. Swett, *Environmental Science and Technology* 38 (2004) 4445.
- [34] D. Golomb, E. Barry, D. Ryan, P. Swett, H. Duan, *Industrial & Engineering Chemistry Research* 45 (2006) 2728.
- [35] D. Golomb, S. Pennell, D. Ryan, E. Barry, P. Swett, *Environmental Science & Technology* 41 (2007) 4698.
- [36] Y. Otsubo, R.K. Prud'homme, *Rheologica Acta* 33 (1994) 29.
- [37] E. Paruta-Tuarez, V. Sadtler, P. Marchal, L. Choplin, J.-L. Salager, *Industrial & Engineering Chemistry Research* 50 (2011) 2380.
- [38] D. Langevin, *Advances in Colloid and Interface Science* 88 (2000) 209.
- [39] D. Espinosa, F. Caldelas, K.P. Johnston, S.L. Bryant, C. Huh, SPE 129925, presented at SPE Improved Oil Recovery Symp., Tulsa, OK, Apr. 26-28. (2010).
- [40] M.L. O'Neill, Q. Cao, M. Fang, K.P. Johnston, S.P. Wilkinson, C.D. Smith, J.L. Kerschner, S.H. Jureller, *Industrial & Engineering Chemistry Research* 37 (1998) 3067.
- [41] B.P. Binks, B. Duncumb, R. Murakami, *Langmuir* 23 (2007) 9143.
- [42] J. Nordstrom, A. Matic, J. Sun, M. Forsyth, D.R. MacFarlane, *Soft Matter* 6 (2010) 2293.
- [43] S.S. Adkins, X. Chen, I. Chan, E. Torino, Q.P. Nguyen, A.W. Sanders, K.P. Johnston, *Langmuir* 26 (2010) 5335.
- [44] E. Vignati, R. Piazza, T.P. Lockhart, *Langmuir* 19 (2003) 6650.
- [45] G.J. Hirasaki, J.B. Lawson, *SPE Journal* 25 (1985) 176.
- [46] R. Aveyard, B.P. Binks, J.H. Clint, *Advances in Colloid and Interface Science* 100-102 (2003) 503.
- [47] J.L. Dickson, G. Gupta, T.S. Horozov, B.P. Binks, K.P. Johnston, *Langmuir* 22 (2006) 2161.
- [48] J.N. Israelachvili, *Intermolecular and Surface Forces*. 3 ed., Academic Press, Burlington, MA, 2011.
- [49] A.H. Falls, J. J. Musters, and J. Ratulowski, *SPE Reservoir Engineering* 4 (1989) 155.
- [50] P.C. Hiemenz, R. Rajagopalan, *Principles of Colloid and Surface Chemistry*. 3 ed., Marcel Dekker, inc., New York, 1997.
- [51] S.S. Marsden, Suhail A. Khan, *SPE Journal* 6 (1966) 17.
- [52] T.S. Horozov, *Current Opinion in Colloid & Interface Science* 13 (2008) 134.
- [53] T.N. Hunter, R.J. Pugh, G.V. Franks, G.J. Jameson, *Advances in Colloid and Interface Science* 137 (2008) 57.
- [54] P.W. Bell, M. Anand, X. Fan, R.M. Enick, C.B. Roberts, *Langmuir* 21 (2005) 11608.
- [55] T.S. Horozov, B.P. Binks, *Angewandte Chemie, International Edition* 45 (2006) 773.

I.1.2. Conditions for generating nanoparticle-stabilized CO₂ foams in fracture and matrix flow

In this section, we summarize dozens of foam generation experiments in various media with the goal of understanding the factors that control the formation of NP-C/W foams. The HCB of the nanoparticle's surface, nanoparticle concentration, salinity, presence of surfactant, CO₂:water ratio, and fluid flow rate are each discussed. This work on NP-C/W foam generation and transport was published as an original research paper:

Aroonsri, Archawin, et al. "Conditions for generating nanoparticle-stabilized CO₂ foams in fracture and matrix flow." SPE Annual Technical Conference and Exhibition. Society of Petroleum Engineers, 2013.

I.1.2.i. Abstract

Foams used for mobility control in CO₂ flooding, and for more secure sequestration of anthropogenic CO₂, can be stabilized with nanoparticles, instead of surfactants, bringing some important advantages. The solid nature of the nanoparticles in stabilized foams allows them to withstand the high-temperature reservoir conditions for extended periods of time. They also have more robust stability because of the large adsorption energy required to bring the nanoparticles to the bubble interface.

Silica nanoparticle-stabilized CO₂-in-brine foams were generated by the co-injection of CO₂ and aqueous nanoparticle dispersion through beadpacks, and through unfractured and fractured sandstone cores. Foam flow in rock matrix and fracture, both through Boise and Berea sandstones, was investigated. The apparent viscosity measured from foam flow in various porous media was also compared with that measured in a capillary tube, installed downstream of beadpacks and cores.

The domain of foam stability and the apparent foam viscosity in beadpacks was first investigated with focus on how the surface wettability of nanoparticles affects the foam generation. A variety of silica nanoparticles without any surface coating and with different coatings were tested, and the concept of hydrophilic/CO₂-philic balance (HCB) was found to be

very useful in designing surface coatings that provide foams with robust stability. Opaque, white CO₂-in-water foams (bubble diameter < 100 μm) were generated with either polyethyleneglycol-coated silica or methylsilyl-modified silica nanoparticles with CO₂ densities between 0.2 and 0.9 g/cc. The synergistic interactions at the surface of nanoparticles (bare colloidal silica) and surfactant (caprylamidopropyl betaine) in generating stable CO₂ foams were also investigated.

The common and distinct requirements to generate stable CO₂ foams with 5-nm silica nanoparticles, in rock matrices and in fractures, were characterized by running foam generation experiments in Boise and Berea sandstone cores. The threshold shear rates for foam generation in matrix and in fracture, both in Boise and Berea sandstones, were characterized. The ability of nanoparticles to generate foams only above a threshold shear rate is advantageous, because high shear rates are associated with high permeability zones and fractures. Reducing CO₂ mobility in these zones with foam diverts CO₂ into lower permeability regions that still contain unswept oil.

1.1.2.ii. Introduction

While enhanced oil recovery (EOR) by CO₂ injection is widely practiced in commercial scales in U.S. and elsewhere, the poor sweep efficiency resulting from CO₂'s low viscosity and density is its critical weakness. Improvement in sweep efficiency is one of the most pressing technical challenges for the wider application of CO₂ flooding. As the formation of CO₂ foam lowers the CO₂ mobility, resulting in improved sweep efficiency, extensive research on the use of surfactant-stabilized CO₂ foam has been conducted over the years. A comprehensive literature review of laboratory work on the development of CO₂ foams for mobility control and conformance control, as well as the field tests of CO₂ foams in U. S., was recently made by Enick and Olsen (2012) and Enick *et al.* (2012). Some of the field tests were clearly successful, such as Chevron's North Ward-Estes conformance control test, where foam formation diverted CO₂ from a high-permeability zone and CO₂ recycling was greatly reduced, with incremental oil production (Chou *et al.*, 1992). A short-cycle surfactant-alternating-CO₂ (SAG) injection at Mobil's East Mallet Unit of Slaughter field completely diverted the injection fluids from the problematic top injector perforations, resulting in the oil production increase from the pattern by about 25% (Hoefner and Evans, 1995).

The detailed analysis of the available field test results by Enick and Olsen (2012) shows some notable points: (1) CO₂ foams used after CO₂ flooding could indeed lead to the recovery of incremental oil; (2) a sacrificial surfactant pad should be injected prior to SAG to minimize surfactant loss due to adsorption to rock surfaces, which results in desorption of surfactant from foam's CO₂/water interface and consequent foam destabilization; and (3) against expectation, foams were not as effective in highly heterogeneous formations characterized by fractures and vugs. The last point may be due to the foam's requirement for continuous regeneration as the foam lamella stability is inherently transient (Rossen, 1996). This requirement of continuous regeneration may be difficult to achieve in fractures and vugs (which are present in most of carbonate reservoirs), because they may not have sufficient pore constrictions for repeated foam lamellae generation.

To overcome the undesirable loss of water-soluble surfactant to rock surfaces, efforts to develop CO₂-soluble surfactants for foam generation have recently been made (Le *et al.*, 2008). A single-well injection test was successfully carried out at SACROC unit of the Kelly-Snyder field in 2010 (Sanders *et al.*, 2010) and led to the expansion to a four-well oil recovery pilots. Also, in order to better understand oil recovery during CO₂ foam flooding of fractured reservoir, Fjelde and Zuta (2008) and Zuta and Fjelde (2009) carried out CO₂ foam experiment with fractured model of chalk rock using surfactant. CO₂ foam floods were found to give higher oil recovery after water flooding than injecting CO₂ alone and CO₂ WAG at the same CO₂ volume. Calculated mobility shows that CO₂ foam is very effective in a fractured reservoir as it acts as blocking agent and decreases the mobility of CO₂. Reservoir simulation results were also in good agreement with the laboratory data. Further simulation study by Zuta *et al.* (2010) determined the effect of foam quality and gravity forces on oil recovery. Results indicated increasing oil production rate with decreasing foam quality for both vertical and horizontal injection. In addition, oil recovery with horizontal injection was predicted to be larger than with vertical injection of preformed-foam. Although molecular diffusion was found to be the main oil recovery mechanism in fractured chalk rock, gravity segregation can reduce CO₂ foam flood efficiency in this fractured rock with low matrix permeability.

As foam is proven to be effective in increasing CO₂ sweep efficiency, one solution to the above shortcomings of the surfactant-stabilized foam is to use nanoparticles instead of

surfactants. Among their unique characteristics, stable foam generation using nanoparticles requires a threshold shear rate to force the nanoparticles to the CO₂/water interface, as previously demonstrated in beadpacks (Espinosa *et al.*, 2010; Worthen *et al.*, 2012; Worthen *et al.*, 2013a) and shown here in matrix and fractures. Once the nanoparticles are securely adsorbed on the CO₂/water interface and generate stable foam, the particle desorption generally does not occur easily (unlike surfactant-based foam) even when exposed to the nanoparticle-free reservoir brine, thereby maintaining the good stability of foam. In the reservoirs with CO₂ injection, high shear rates are associated with preferential flow through high-permeability zones. This would be especially true for flow of a CO₂-water mixture through fractures. The characteristics of nanoparticles raise the possibility of selectively reducing CO₂ mobility by generating foam only in regions where CO₂ is flowing rapidly, such as fractures and gravity override regions that contain little oil. The CO₂ would then be diverted to the lower permeability zones where the bypassed oil still exists, thereby achieving the goal of improved sweep efficiency.

Because the nanoparticles adsorbed at the CO₂/water interface generally stay there, the nanoparticle loss to the rock surface could be kept minimal (Zhang *et al.*, 2013). Still another advantage of nanoparticles over surfactants is, their being solid, the silica nanoparticles can also endure the harsh reservoir conditions, such as a high temperature, better than the surfactants. Nanoparticles may be produced from many low cost, chemically stable, abundant, and environmentally benign materials such as silica and clay (Golomb *et al.*, 2006).

The key to nanoparticle (or surfactant) design for CO₂-in-water foams is the hydrophilic/CO₂-philic balance (HCB) (Johnston and Da Rocha, 2009). Analogous to the hydrophilic/lipophilic balance (HLB), the HCB controls the nature of the interface on which the nanoparticles are adsorbed, such as the preferred curvature of the CO₂-water interface and the partitioning of the nanoparticle (or surfactant) to the interface. The HCB has been defined as

$$\frac{1}{HCB} = \frac{A_{AC} - A_{AA} - A_{CC}}{A_{AW} - A_{AA} - A_{WW}} \quad (\text{I.1.2.1})$$

where $A_{\alpha\beta}$ indicates the interaction pair potential between α and β with A = amphiphile, C = CO₂, and W = water (Johnston and Da Rocha, 2009; Worthen *et al.*, 2013a). For surfactants, the tails contribute primarily to A_{AC} and the head primarily to A_{AW} . An important design challenge for

surfactant/CO₂/water systems is the poor solvent properties of CO₂, often leading to very weak solvation of surfactant tails (very small A_{AC}) relative to the strong solvation of surfactant heads by water (large A_{AW}) (Johnston and Da Rocha, 2009). Ultimately, this can result in a surfactant which preferentially stays in the water phase rather than adsorbing at the CO₂-water interface.

In contrast, uniformly coated nanoparticles do not have a “head” nor a “tail”, but rather the surface of the nanoparticle can be designed to have some affinity for both the CO₂ and water phases. By circumventing the problem of solvation of surfactant tails, nanoparticles present an attractive alternative to surfactants for stabilization of CO₂-in-water foams. For example, silica nanoparticles modified with very hydrophobic (heptadecafluoro-1,1,2,2-tetrahydrodecyl) triethoxysilane to give a low HCB can generate water-in-CO₂ (W/C) emulsions ([Adkins *et al.*, 2007](#)) while silica nanoparticles that were unmodified or modified with dichlorodimethylsilane (DCDMS) to leave 76% SiOH coverage to give a high HCB were used by Dickson *et al.* (2004) to generate CO₂-in-water foams.

Properly designed nanoparticles can irreversibly adsorb at an interface, unlike surfactants which typically have an adsorption energy on the order of 1 kT ([Binks, 2002](#)). The adsorption energy E of a particle at a fluid-fluid interface is

$$E = \pi r^2 \gamma_{\alpha\beta} (1 \pm \cos \theta)^2 \quad (\text{I.1.2.2})$$

where r is the particle radius, $\gamma_{\alpha\beta}$ is the interfacial tension between fluid α and fluid β , and θ is the contact angle of the particle at the interface measured through the water phase. The sign in the parenthesis corresponds to a particle center above (+) or below (-) the interface. The above equation gives two tunable parameters: r and θ . Larger particles (larger r) take up more interfacial area and therefore adsorb more strongly at an interface. By properly tuning the HCB of the nanoparticles, θ can be tuned to allow the nanoparticle to adsorb strongly at the interface and impart long term stability to the foam. For example, a nanoparticle with $r = 30$ nm and a favorable contact angle of 80° at a CO₂-water interface ($\gamma_{CW} = 20$ mN/m) has an adsorption energy of nearly 104 kT at 24°C, indicating essentially irreversible adsorption. The presence of nanoparticles at an interface may limit foam destabilization by drainage of lamellae, bubble coalescence, Ostwald ripening, and hole formation ([Worthen *et al.*, 2013b](#)). However, full

coverage by nanoparticles is not needed to generate stable emulsions and foams ([Vignati et al., 2003](#); [Yoon et al., 2012](#)). As little as 5% of a monolayer of nanoparticles may be required to stabilize emulsions, but the reason for this remarkable efficiency is unclear ([Vignati et al., 2003](#)).

Espinosa *et al.* (2010) generated stable CO₂-in-water foams in beadpacks with 5-nm silica nanoparticles whose surface was treated with short-chain polyethylene-glycol (PEG). The domain of foam stability and the normalized mixture viscosity have been measured for a range of values of nanoparticle concentration, water salinity, ratio of CO₂/water flow rates, the overall flow rate and temperature. Worthen *et al.* (2012) and Worthen *et al.* (2013a) investigated the generation of CO₂-in-water foams in beadpacks with focus on how the surface wettability of nanoparticles affects the foam generation. A variety of silica nanoparticles without any surface coating and with different coatings were tested. Worthen *et al.* (2013b) studied the synergistic interactions at the surface of nanoparticles (bare colloidal silica) and surfactant (caprylamidopropyl betaine) in generating stable CO₂ foams. Interestingly, neither species generated CO₂ foams alone. These, and additional foam generation results from beadpack experiments, will be summarized in the next section to set the ground for our investigation of foam generation in unfractured and fractured sandstone cores.

Yu *et al.* (2012) and Mo *et al.* (2012) investigated CO₂ foam generation using commercially available silica nanoparticles. In addition to the characterization of the foam generated in beadpacks, in terms of brine salinity, reservoir pressure and temperature, they also carried out CO₂ foam generation in Berea sandstone core. Stable foam was achieved using nanoparticles concentration of 5000 ppm and phase ratio of 1:4 CO₂:aqueous phase (foam quality = 20%). However, pressure drop across the 10 inch core increased continuously, reaching as high as 870 psi after 9 PV of fluids were injected. Particle concentration, flow rate and phase ratio were found to have effect on foam mobility. Foam could be generated at particle concentration as low as 100 ppm and increasing the concentration resulted in lower foam mobility. Increasing flow rate monotonically decreased the resistance factor, which is defined as the ratio of pressure drop during flow with nanoparticles to pressure drop without nanoparticles at the same phase flow rates. In contrast, relation between foam quality and resistance factor exhibited a maximum between foam quality of 40% and 60%.

In the next Section, the materials and the experimental techniques employed to generate CO₂ foams in beadpacks, and in unfractured and fractured sandstone cores, are described. In the Section, “CO₂ Foam Generation Experiments in Beadpacks”, the effects of nanoparticle concentration, salinity, CO₂/water volume ratio and nanoparticle surface wettability on the foam stability and its apparent viscosity, are described. In the Section, “Foam Generation Results from Sandstone Corefloods”, the foam generation in unfractured and fractured cores, for Boise and Berea sandstones, are described with focus on the role of flow shear rate both in matrix and in fracture. Conclusions follow.

1.1.2.iii. Experimental Methods and Materials

Materials. The nanoparticles used in this study are 5 nm diameter, polyethylene glycol (PEG)-coated silica provided by 3M Co., St Paul, MN as 19.3 wt% dispersion; and silica nanoparticles (~10 nm diameter) modified with a proprietary coating from Nissan Chemical Co., Houston, TX as ca. 20 wt% dispersions with the trade names EOR-5XS and EOR-12. In experiments, the dispersions were diluted with de-ionized (DI) water (Nanopure II, Barnstead, Dubuque, IA) or brine to the desired concentration (1 wt%) before being injected into rock cores or a beadpack. To adjust the salinity of the brine, reagent grade sodium chloride and calcium chloride were added to DI water as required. CO₂ (research-grade, Matheson, USA) was used as received.

Experimental Set-Up. Figure I.1.2.1 shows a schematic of the apparatus for nanoparticle-stabilized CO₂/water foam generation in fracture and matrix. ISCO 500-D Teledyne syringe pump is used to inject the aqueous phase directly to the co-injection system while the Model 1500 HPLC pump injected water displacing CO₂ from the accumulator. The two fluids converge at the T-junction before going through the rock core in the core holder equipped with a Rosemount differential pressure transducer. The effluent from the core flows through the 10 ft. coil of capillary tube (1/16” OD) where the pressure drop is continuously measured using a Rosemount differential pressure transducer. Foam then flows through a high pressure view cell with 1.5 cm window so the visual appearance of the foam can be monitored. Foam effluent is finally collected in a high-pressure accumulator and is subsequently disposed into bulk container. The outlet pressure is adjusted using back pressure relief valve connected to the downstream side of the piston within the waste accumulator and is normally set to 2000 psia. All of the coreflood

experiments reported here were run at room temperature. For experiments with bead packs, the apparatus is similar to the coreflood set up except that core holder is replaced by a 0.38 cm ID \times 11.3 cm long beadpack filled with 180 μm spherical glass beads (70–100 mesh soda-lime silica glass, Stock Number P-0080, Potters Industries Inc., Valley Forge, PA). Pieces of mesh were placed at both ends to prevent glass beads from escaping into the flow system. The beadpack apparatus was maintained at 50°C using a water bath equipped with a Julabo MP immersion heater. Full details of the beadpack apparatus are given in Worthen *et al.* (2013a).

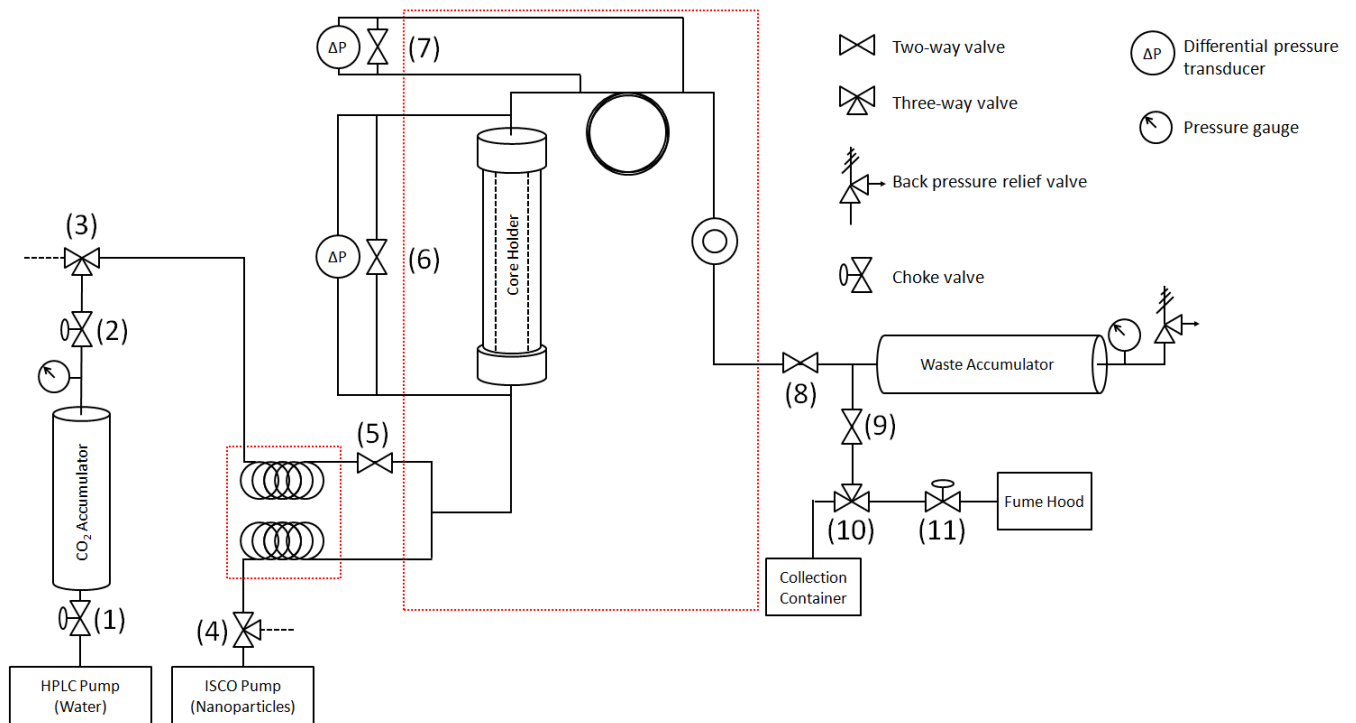


Fig. I.1.2. 1—Schematic of core flood system before three additional intermediate pressure transducers were installed across core holder. Red dotted box represent water bath (left) and oven (right).

Three types of rock were selected for the coreflood study: Boise Sandstone (~1800 mD), Berea Sandstone (~200 mD) and Indiana Limestone (~7 mD). They were cut into either 6-in. or 12-in. long with 1-in. diameter cores and then wrapped with FEP shrink wrap tubing (Geophysical Supply Company, Houston, TX). The shrink wrap not only helps holding 6-inch cores in series with spacers but also help isolate the core holder rubber sleeve from CO₂. Wrapped cores were then vacuumed for a day to removed trapped air before DI water (or brine) was introduced into the vacuumed chamber. The chamber containing the submerged core was

vacuumed again for another 6 hour removing any remaining trapped air before use in the core flood experiment.

Fractured cores are prepared by applying stress onto the shrink-wrapped core using a load frame. Boise sandstone cores fracture at approximately 20 kN of load. Due to the size of the load frame plate, fractured cores are limited to 6 in. long. The two pieces of fractured core were put back together with some offset to keep the fracture open. They were held together with PTFE tape, wrapped by the shrink wrap tubing and saturated with DI water (or brine) using the same procedure as the unfractured cores. Besides the fractured sandstone core, a fractured cement core was also used in one experiment. The cement core was prepared using class H cement, molded in a plastic tube. The cement core was found to fracture at approximately 14 kN of load.

Experimental Methods.

Beadpack Experiments. Experiments were conducted as described elsewhere (Worthen *et al.* 2013a; Worthen *et al.* 2013b). All experiments were done at 2800 psia and 50°C, using a total flow rate of 0.75-3.0 mL/min and a CO₂:water phase ratio of 3:1 by volume. The system pressure was maintained within 25 psi for all experiments. At the typical flow rate of 1.5 mL/min, the shear rate in the beadpack is 1130 s⁻¹, the superficial velocity is 0.220 cm/s, and the residence time is 17.4 s.

Coreflood Experiments. After the core permeability was measured, DI water/brine and CO₂ were co-injected into the core. For most of the experiments, CO₂: aqueous phase volume phase ratio is held constant at 1:1 (CO₂ and aqueous phase are being co-injected at the same volumetric flow rate at coreflood temperature and pressure). All pressure drops across the core and that across capillary tube (located downstream of the core) were recorded at varying total flow rate. These measurements without nanoparticles are used as a baseline. When finished, the core is then flushed with DI water/brine to remove CO₂ and restore permeability to original single phase condition. Once the core is re-saturated with DI water/brine, a foam generation experiment is carried out by co-injecting aqueous phase containing nanoparticle and CO₂ with the same phase ratio as for baseline. Again at varying total flow rate, pressure drops are recorded and pictures of foam in view cell are taken. Pressure drop data with and without nanoparticle are used in

calculating apparent viscosity, normalized viscosity and core mobility reduction factor as defined in the next section.

Apparent Viscosity and Core Mobility Reduction Factor. In the next two sections, the results from the foam generation experiments are reported in terms of the apparent viscosity and the mobility reduction factor. The measured ΔP in the beadpack (or core) allows for calculation of the apparent viscosity of the foam (μ_{app}) using Darcy's Law:

$$\mu_{app,beadpack} = \frac{k_{beadpack} \cdot A \cdot \Delta P}{q \cdot L} \quad (I.1.2.3)$$

where $k_{beadpack}$ is the permeability of the beadpack (or core), A is the cross-sectional area of the beadpack, q is the total volumetric flow rate, and L is the length between the ΔP cells. $k_{beadpack}$ was determined by measuring the pressure drop of water with a known viscosity and flow rate.

In the capillary tube, the apparent viscosity is calculated with the Hagen–Poiseuille equation:

$$\mu_{app,capillary} = \frac{\pi \cdot \Delta P \cdot R^4}{8 \cdot q \cdot L} \quad (I.1.2.4)$$

where R is the capillary tube inner radius.

In coreflood experiments, the core mobility reduction factor (MRF) is the ratio of the apparent viscosity of the foam at a given total flow rate to the apparent viscosity of the CO₂-water mixture at the same total flow rate (baseline):

$$MRF = \frac{\mu_{app} \text{ of foam}}{\mu_{app} \text{ of baseline}} = \frac{\Delta P_{Core} \text{ of foam}}{\Delta P_{Core} \text{ of baseline}} \quad (I.1.2.5)$$

Similarly, the normalized apparent viscosity in the capillary is determined from the ratio of the calculated apparent viscosity of the foam to the apparent viscosity of the pure CO₂-water mixture (baseline):

$$\mu_{norm} = \frac{\mu_{app} \text{ of foam}}{\mu_{app} \text{ of baseline}} = \frac{\Delta P_{capillary} \text{ of foam}}{\Delta P_{capillary} \text{ of baseline}} \quad (I.1.2.6)$$

CO₂ Foam Generation Experiments in Beadpacks

The objective of this section is to describe key findings of several studies of nanoparticle-stabilized CO₂-in-water foams in beadpacks. These lay out the conditions for foam formation. Important findings regarding the effect of nanoparticle concentration and adsorption of surfactant

on nanoparticle surfaces will be discussed from the existing literature and then new results regarding the effects of salinity, CO₂/water ratio, and beadpack shear rate will be discussed.

Factors That Control CO₂ Foam Generation.

Sufficient Nanoparticle Concentration. Espinosa *et al.* (2010) found a minimum of 0.05 wt% PEG-coated silica nanoparticles in deionized water was required for generation of CO₂-in-water foams at 21.1 °C, 1350 psia, and a CO₂/water phase ratio (by volume) of 5:1 (83.3% foam quality) and 11:1 (91.7% foam quality) in a beadpack filled with 180 micron diameter glass beads at a shear rate of ca. 1300 s⁻¹. Smaller nanoparticle concentrations (0.025 wt% and 0.01 wt%) in the aqueous phase were unable to stabilize foams at the same conditions. CO₂/water phase ratios up to 19:1 (95% foam quality) were tested and 0.05 wt% nanoparticles were found to successfully stabilize CO₂-in-water foams. When foam was generated, it had two to eighteen times more resistance to flow than the same fluids without nanoparticles. Foams were generated at temperatures up to 95 °C. Foam generation by co-injection of the fluids requires a threshold shear rate. Worthen *et al.* (2013a) found that bare colloidal silica nanoparticles were unable to stabilize CO₂-in-water foams at 35 °C and 2800 psia even at a large concentration of 1% w/v because the HCB of the nanoparticles was very large and the nanoparticles did not adsorb strongly at the interface. Thus, the PEG coating on the silica nanoparticles imparted the proper HCB for adsorption at the CO₂-water interface (Worthen *et al.*, 2013a), but enough nanoparticles had to be present to successfully stabilize a CO₂-in-water foam.

Adsorption of Surfactant on Nanoparticles. Worthen *et al.* (2013b) used surfactant adsorption on the surface of bare silica nanoparticles to tune the HCB and increase nanoparticle partitioning to the interface. With this technique, nanoparticles that were too hydrophilic to stabilize CO₂-in-water foams were modified through adsorption of caprylamidopropyl betaine to reduce the nanoparticle surface charge and add hydrophobic surfactant tails, increasing the hydrophobicity of the nanoparticles. This technique, known as “in situ surface activation”, may be desirable for CO₂-in-water foams because it is easier and cheaper than covalent grafting of modifiers to the surface of nanoparticles (Cui *et al.*, 2010). Through the proper choice of surfactant modifier, the nanoparticles remained colloidally stable to pass through reservoir rocks (Worthen *et al.*, 2013b). However, some surfactants may cause the nanoparticles to lose colloidal

stability, even at very low surfactant concentrations (Binks and Rodrigues, 2007; Binks *et al.*, 2007). An additional benefit of added surfactant is that free surfactant in solution can lower the CO₂-water interfacial tension, which may further improve foam formation (Worthen *et al.*, 2013b). Together, the 1% w/v nanoparticle and 0.5% surfactant mixture synergistically stabilized very viscous CO₂-in-water foams (>70 cP in the beadpack), while the nanoparticles or surfactant alone was unable to stabilize a CO₂-in-water foam.

1.1.2.iv. Results and Discussions for Beadpack Experiments.

Salinity Effect on C/W Foam Formation and Viscosity. CO₂-in-water (C/W) foams were generated at 50 °C and 2800 psia in a 22.5 darcy beadpack at a shear rate of 1130-2260 s⁻¹, and the apparent viscosity measured in a capillary tube viscometer ($\mu_{\text{app, capillary}}$) is reported in Fig. I.1.2.2 as a function of aqueous phase total dissolved solids. With no salt (TDS = 0), the PEG-coated silica nanoparticles produced a weak foam with viscosity of 3 cP, but the EOR-5XS and EOR-12 silica particles did not produce a foam. As the salinity increased, the viscosity increased for all nanoparticles tested. Significantly, the EOR-5XS and EOR-12 nanoparticles demonstrated a “no foam” to “foam” transition when the aqueous phase was changed from DI water (TDS = 0) to synthetic seawater (TDS = 3.5%).

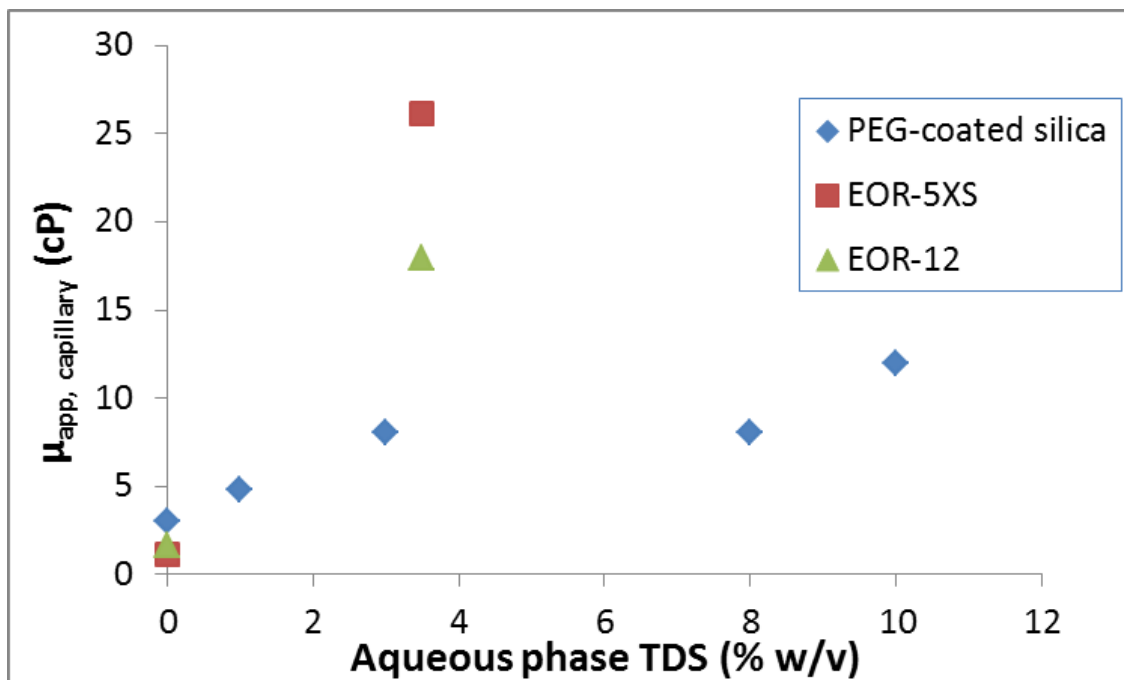


Fig. I.1.2. 2—Apparent viscosity measured in a capillary tube viscometer ($\mu_{app, capillary}$) of C/W foam stabilized with 1% nanoparticles at 50 °C and 2800 psia reported as a function of aqueous phase total dissolved solids (TDS). EOR-5XS and EOR-12 were tested in DI water and synthetic seawater with a 3:1 volume ratio of CO₂ to aqueous phase. PEG-coated silica particles were tested in DI water, NaCl solutions (see full experimental details in Worthen *et al.* 2013a), and API brine (10% TDS; 8% NaCl + 2% CaCl₂) with a 9:1 volume ratio of CO₂ to aqueous phase.

Increasing the salinity caused the nanoparticles to behave more hydrophobically which resulted in a lower HCB and an improved contact angle (closer to 90°) at the CO₂/water/nanoparticle interface (Worthen *et al.*, 2013a). By Eq. (I.1.2.2), increased θ causes a higher adsorption energy which improves adsorption of the nanoparticles at the CO₂-water interface. This process is akin to “salting out” an ionic surfactant, whereby increasing salinity causes the surfactant to behave more hydrophobically (Rosen, 2004). Similarly, Espinosa and coworkers found that increasing salinity from DI water to 2% NaCl at a 0.1 wt% nanoparticle concentration and from 2% to 4% NaCl at 0.5 wt% nanoparticle concentration caused an increase in foam viscosity (Espinosa *et al.*, 2010). However, increasing salinity too much would likely cause the loss of colloidal stability of the nanoparticles, which would cause aggregation and prevent the nanoparticles from flowing through porous media. These results indicate that the salinity of the aqueous phase can be a key parameter for the formation of viscous C/W foams.

C:W Ratio Effect on C/W Foam Formation and Viscosity. C/W foams were generated at 50 °C and 2800 psia in a 22.5 darcy beadpack at a shear rate of 2260 s⁻¹, and the apparent viscosity measured in a capillary tube viscometer ($\mu_{app, capillary}$) is reported in Fig. I.1.2.3 as a function of

foam quality (CO_2 fraction). The shear rate in the capillary tube is 1150 s^{-1} under these flow conditions. Results for partially hydrophobic silica nanoparticles (50% SiOH) are plotted for comparison as they were generated using the same apparatus and under the same operating conditions (Worthen *et al.*, 2013a). By varying the C:W ratio, a maximum viscosity was identified at a quality of 0.75 for C/W foams stabilized with all nanoparticles tested.

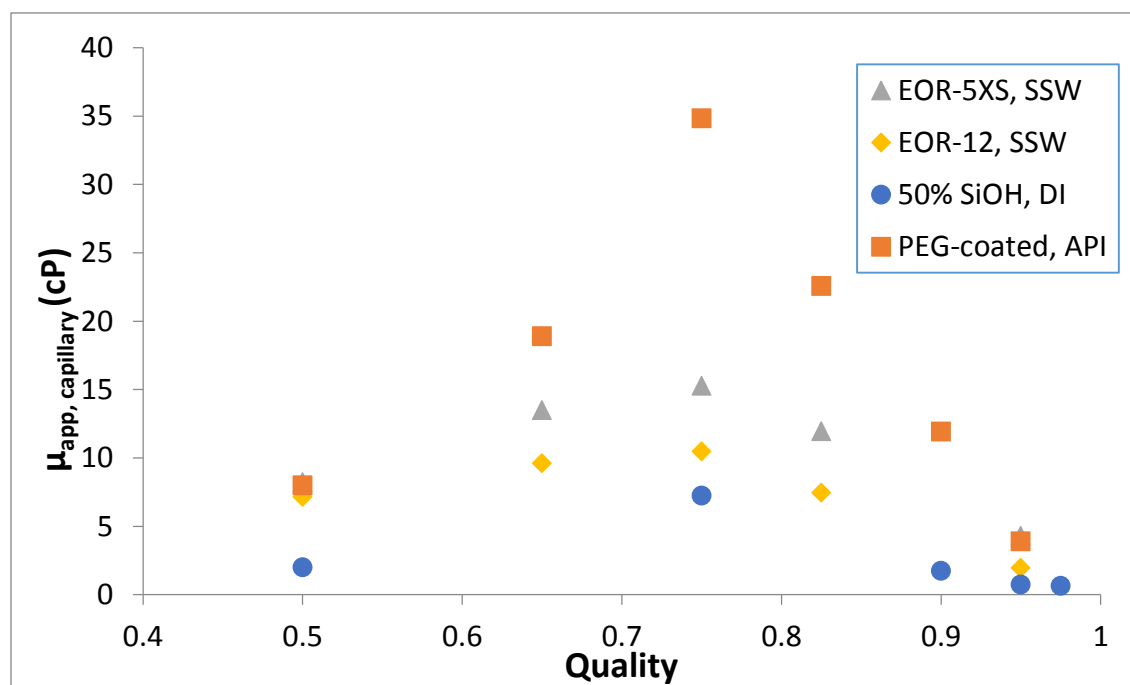


Fig. I.1.2. 3—Apparent viscosity (μ_{app}) of C/W foam stabilized with 1% nanoparticles at $50 \text{ }^\circ\text{C}$ and 2800 psia measured in a capillary tube viscometer as a function of foam quality (CO_2 volume fraction). PEG-coated silica particles were tested in API brine (10% TDS; 8% NaCl + 2% CaCl_2). EOR-5XS and EOR-12 were tested in synthetic seawater (SSW). Wacker 50% SiOH particles are partially modified with dichlorodimethylsilane and were tested in DI water (see full experimental details in Worthen *et al.* 2013a).

The viscosity of the foam is expected to reach a maximum as quality is increased and then drop to the gas phase viscosity as the quality approaches unity (Marsden and Khan, 1966). When the foam quality is too small, the bubbles are very dilute and lack lamellae between them and the viscosities are not expected to be more than a few times that of the solvent. When the quality is too high, the lamellae are very thin and rupture or, in the very extremely high quality regime, the system does not have sufficient liquid to form lamellae. Interestingly, the quality that gave the peak viscosity (0.75) is lower than that found by Espinosa and coworkers (0.86-0.92) with PEG-coated silica nanoparticles when the experiments were conducted at a lower pressure of ca. 1400 psia (Espinosa *et al.*, 2010). However, no foam or very low viscosity foam was formed at qualities above 0.95 in the work presented here and by Espinosa and coworkers. The peak

viscosity at a quality of 0.75 appears to hold true for this beadpack at a shear rate of 2260 s^{-1} , $50 \text{ }^\circ\text{C}$, and 2800 psia , with 1% nanoparticles, regardless of nanoparticle type. The minimum foam quality investigated in beadpacks thus far was 0.5, where a marked reduction in foam viscosity occurred (see Fig. 3 and Worthen *et al.*, 2013a). No foam is expected at very low qualities, but the exact quality where no measurable increase in viscosity occurs has not yet been identified for nanoparticle stabilized foams. Further studies of the optimum quality for maximum viscosity would be warranted as a function of porous media, shear rate, temperature, pressure, and nanoparticle concentration. Overall, these results indicate that the C:W ratio of the foam is a key parameter which can dictate whether a viscous C/W foam is formed.

Effect of Shear Rate. C/W foams were generated with 1% PEG-coated silica nanoparticles in API brine at $50 \text{ }^\circ\text{C}$ and 2800 psia in a 22.5 darcy beadpack at a shear rates of $380\text{-}2260 \text{ s}^{-1}$, and the apparent viscosity (μ_{app}) measured in a capillary tube viscometer and in the beadpack is reported in Fig. I.1.2.4. The apparent viscosity of the foams increased from 12 cP (measured in the capillary tube) at a beadpack shear rate of 380 s^{-1} to a steady value of $\sim 35 \text{ cP}$ at 1130 s^{-1} and 2260 s^{-1} . (The shear rate in the capillary tube is about half the shear rate in the beadpack.) In the beadpack, an apparent peak viscosity of 69 cP was observed at 1130 s^{-1} , which decreased to 46 cP at 2260 s^{-1} .

These results suggest a more subtle interpretation of the concept of a critical shear rate. Very weak foams may be generated at lower shear rates while more viscous foams may be generated at higher shear rates. At very low shear rates, no foam is expected to form as there is not enough shear force provided to form small bubbles (Walstra and Smulders, 1998). Espinosa and coworkers found a “critical shear rate” of ca. 4000 s^{-1} in a similar beadpack when the experiments were done at $95 \text{ }^\circ\text{C}$ and 1350 psia with 0.5% PEG-coated silica nanoparticles in DI water. A larger range of shear rates and experimental conditions need to be investigated to confirm the existence of a “critical shear rate” for foam generation in beadpacks, and to determine any additional non-Newtonian viscosity behavior at very high shear rates. Overall, these results indicate that the shear rate (determined by the porous media properties and the fluid flow rate) is a key parameter which may determine whether a viscous C/W foam is formed.

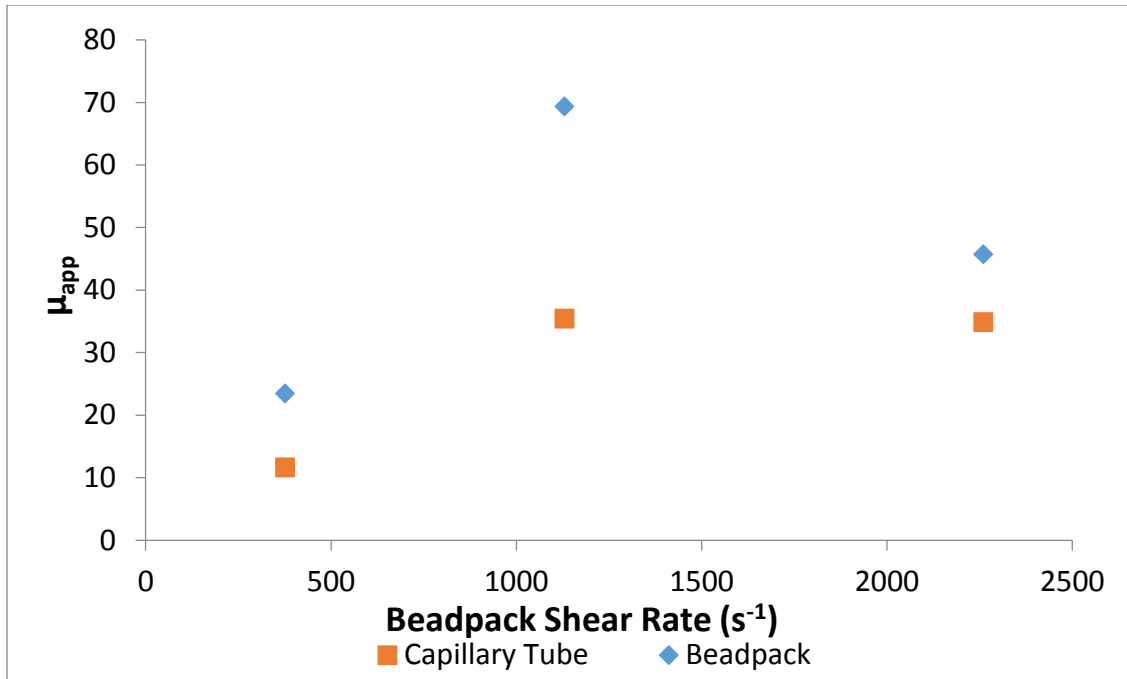


Fig. I.1.2. 4—Apparent viscosity (μ_{app}) of C/W foam stabilized with 1% PEG-coated silica in API brine (8% NaCl + 2% CaCl₂) at 50 °C and 2800 psia measured in a capillary tube viscometer and in the beadpack as a function of beadpack shear rate.

Foam Generation Results from Sandstone Corefloods

Foam generation experiments were carried out both in unfractured and fractured cores of Boise sandstone, Berea sandstone and Indiana limestone. Foam generation in a fractured cement core was also studied. Stable foam was successfully generated in every type of core, but at different experimental conditions. To date, 31 measurements of foam generation and mobility from 7 different corefloods with unfractured rocks (Table I.1.2.1); 15 measurements of generation and mobility from 5 different corefloods with fractured rocks (Table I.1.2.2); and 5 measurements of generation and mobility from a fractured cement core (Table I.1.2.3), have been obtained. In this Section, results of unfractured Boise sandstone corefloods will be first be discussed, followed by results from the fractured cores and other types of rocks.

Foam Generation in Unfractured Boise Sandstone Core. Having porosity of around 22-29%, the permeability of Boise sandstone cores ranged from 1600 to 1900 mD. Figure I.1.2.5 shows, as an example, the foam experiment results from the coreflood B4 (see Table I.1.2.1). Apparent viscosities and MRF (as defined by Eq. I.1.2.5 above) are plotted against the volume of injected

fluid in pore volume unit (PV) for 5 different flow rates. At each injection rate, the pressure drop measured across the core sharply increases, but reaches a steady state, demonstrating that the nanoparticle-stabilized CO₂ foam can be transported in sandstone rock without trapping.

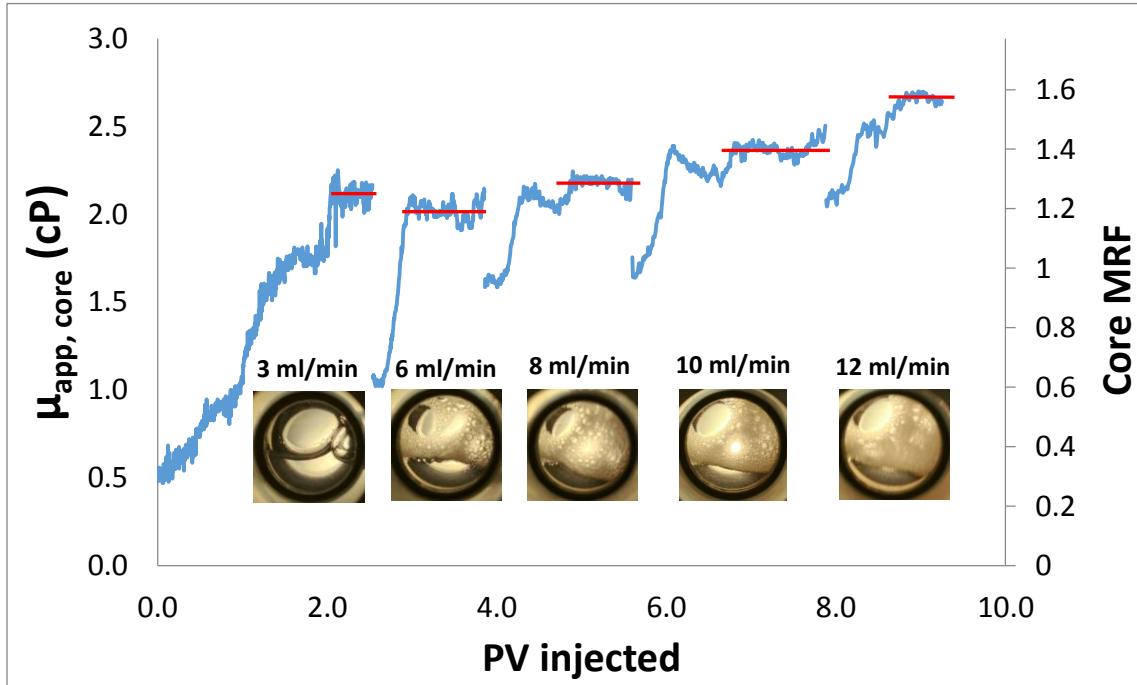


Fig. 1.1.2. 5—Apparent viscosity in unfractured Boise sandstone from coreflood B4. 1% PEG-coated silica in DI water was co-injected with CO₂ using phase ratio of 1:1 at 2000 psia and 23 °C. Using baseline core apparent viscosity of 1.69 cP (without nanoparticle), corresponding core MRF can be read from the secondary axis on the right.

Table I.1.2. 1—Condition and results of foam generation experiments in unfractured sandstone cores at 23 °C and 2000 psia. (1 wt% dispersion of 5nm PEG coated nanosilica was co-injected with CO₂ at varying total injection rate and volume phase ratio.)

Exp name	Medium Type	Matrix K (mD)	Matrix Porosity	Phase Ratio (CO ₂ /AQ)	Salinity (wt%)	Total Flow rate (ml/min)	Shear rate (s ⁻¹)	Foam Visual	Core		Capillary
									μ _{app} (cP)	MRF	Norm. μ
Berea 3	Berea	127	21%	1	2	2	570	Y	2.70	2.23	5.35
Berea 4	Berea	175	21%	1	2	1	240	N	n/a	n/a	1.00
						1.5	370	Y	n/a	n/a	3.92
B1	Boise	1650	22%	1	0	3	230	N	1.61	0.97	1.71
						6	470	Y	1.81	1.01	1.83
						10	780	Y	3.32	1.89	3.13
B2	Boise	1650	22%	1	0	3	230	Y	2.29	1.02	4.46
						6	470	Y	2.58	1.09	3.72
						8	620	Y	3.16	1.37	3.39
						10	780	Y	4.42	1.91	3.35
						12	930	Y	5.36	2.31	3.19
B3	Boise	1720	22%	1	0	3	230	Y	2.09	1.03	3.67
						6	460	Y	2.03	1.00	3.66
						10	760	Y	2.51	1.24	3.17
						15	1100	Y	4.75	2.34	2.63
						20	1500	Y	5.66	2.79	2.70
B4	Boise	1940	29%	1	0	3	190	N	2.11	1.25	1.16
						6	380	Y	2.02	1.19	1.42
						8	500	Y	2.18	1.29	2.00
						10	630	Y	2.37	1.40	2.03
						12	750	Y	2.66	1.58	2.07
B5	Boise	1576	29%	2	2	3	210	Y	1.53	1.05	4.14
						6	420	Y	1.55	1.11	4.12
						9	630	Y	1.60	1.17	4.05
						12	830	Y	1.71	1.28	3.45
B6	Boise	1760	29%	4	2	3	200	N	1.31	1.02	0.99
						6	400	Y	1.56	1.17	1.53
						9	590	Y	1.59	1.18	2.01
						12	790	Y	1.62	1.25	2.08
						15	990	Y	1.68	1.26	2.12

To better understand the foam transport in rock, the foam apparent viscosity was also calculated from pressure drop measured across the capillary tube installed downstream of the core. Results from the coreflood B4 are plotted along with the core apparent viscosity in Fig. I.1.2.6. The apparent viscosity from the capillary tube is, as expected, lower than the corresponding value from the core, because the foam bubble movement is not constrained by the

narrow tortuous passage in rock. We note that the apparent viscosity for the two lower flow rates are distinctly smaller than those for the three higher flow rates, indicating that at those low rates, no foam or only very weak foam was generated (see Fig. I.1.2.7). While the apparent viscosity from core increases with the flow rate, the apparent viscosity from capillary tube remains approximately same for the three high rates. Because the viscometer-measured foam viscosity generally shows shear-thinning behavior, this suggests that, as the flow rate increase, the foam texture may become finer with consequent increase in viscosity, thereby more or less compensating for the viscosity reduction due to shear thinning. This may also explain the MRF increase with flow rate, as further discussed below.

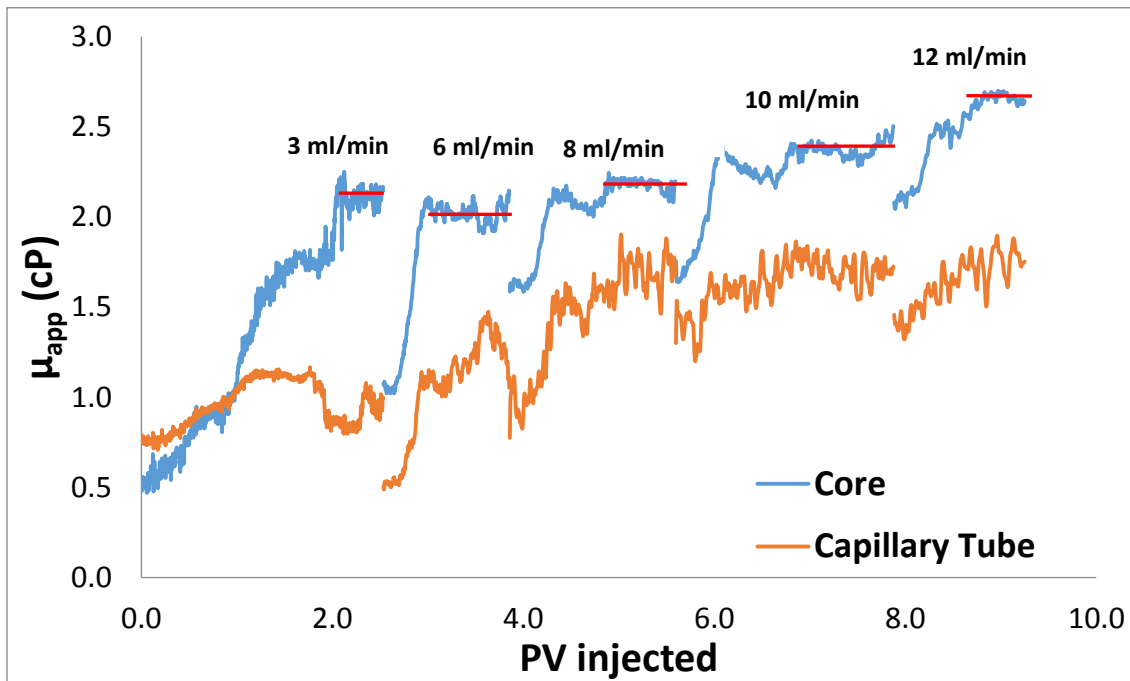


Fig. I.1.2. 6—Comparison of apparent viscosity from stable steady-state coreflood using unfractured Boise sandstone B4 (blue) with those from capillary tube (orange).

With the knowledge of baseline apparent viscosity obtained from CO₂-DI water co-injection, the core mobility reduction factor (MRF) was determined, as shown as secondary Y-axis in Fig. I.1.2.5 for the B4 case. The MRF values from unfractured Boise corefloods are plotted against the effective shear rate calculated for each injection rate, in Fig. I.1.2.7. At low shear rate, core MRF is close to the baseline value of 1, and no significant increase in MRF is observed with increase in shear rate (i.e., injection rate). Once shear rate exceeds a certain value, the core MRF sharply increases with increasing shear rate. This threshold behavior suggests an existence of

critical shear rate for foam generation in Boise sandstone matrix. For these specific cases in Boise sandstone, the critical shear rate for foam generation is estimated to be 460 s^{-1} . We note, however, that very weak foam was sometimes observed below the threshold shear rate.

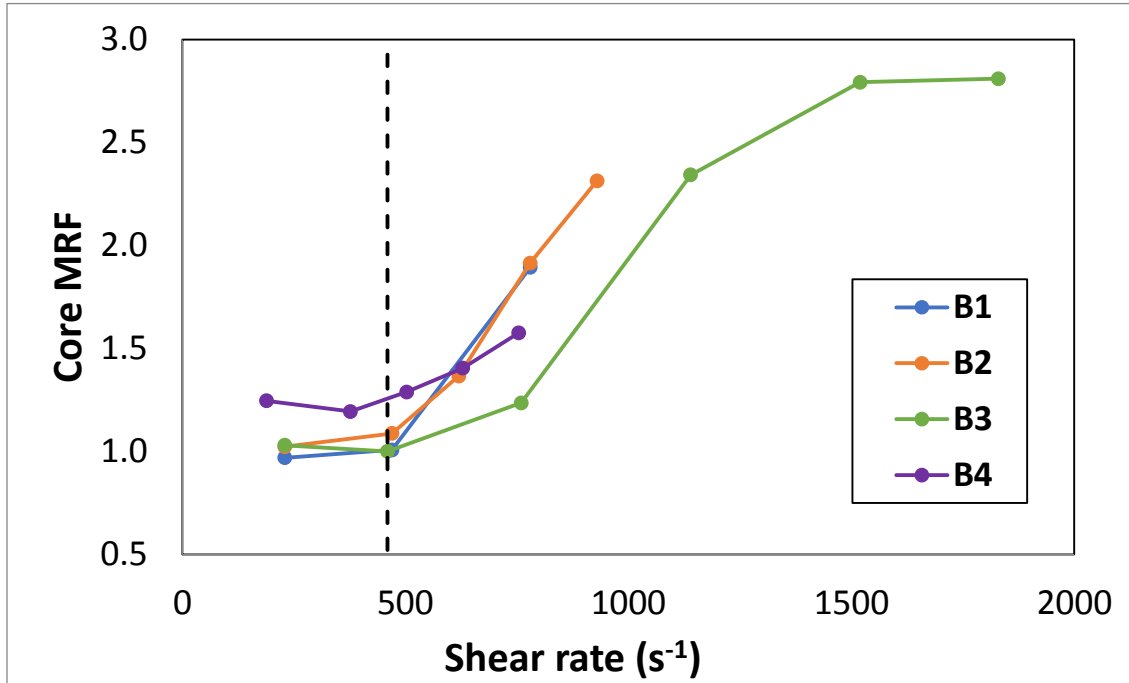


Fig. 1.1.2. 7—Core MRF versus shear rate for unfractured Boise sandstone core flood exhibits critical shear rate for foam generation at 460 s^{-1} . All experiments were carried out at 2000 psia and $23 \text{ }^\circ\text{C}$, using volume phase ratio of 1:1 (CO_2 :nanoparticle dispersion). 1 wt% PEG-coated nanosilica in DI water were used.

The core MRF continues to increase with shear rate, which may be because the foam texture becomes finer as discussed above. Finer foam texture (smaller droplet size) is observed in the view cell as injection rate is increased. According to Ettinger and Radke (1989), foams with finer texture result in a larger resistance to flow through rock, i.e., MRF. During the coreflood B3, MRF continues to rise as high as 2.8 times of the baseline value before leveling off at the shear rate of 1500 s^{-1} . While the reasons for this high plateau value of MRF are not clear, above a certain flow rate, foam bubble generation and coalescence may achieve a balanced state.

Foam Generation in Fractured Boise Sandstone Core. In order to study foam generation in fractured sandstone, a fracture was created in Boise sandstone core, using the procedure discussed in Section, “Experimental Methods”. Figure 1.1.2.8 shows an example of pressure drop

data from foam experiment in the fractured Boise core F1 (see Table 2). Similar to what had been observed in unfractured core flood, the pressure drop both from the core and from the capillary tube showed stabilized trend reaching plateau values relatively quickly. In order to calculate the apparent viscosity of foam *in the fracture* from the overall pressure drop measured, the contribution from the matrix portion of the core needs to be subtracted. This can be done utilizing the MRF data from the above unfractured core floods. The approximate method to calculate the matrix and fracture contributions for foam flow is described in the Appendix. (In the calculation, the simplifying assumption of no crossflow between fracture and matrix zone was made.) The apparent foam viscosity in the fracture *vs.* the effective shear rate in the fracture, accordingly calculated for two fractured Boise sandstone cores with different fracture apertures size (104 and 65 microns; Table 2), are plotted in Fig. I.1.2.9, together with the overall apparent viscosity for the whole core (i.e., without the corrective calculation of the Appendix).

Table I.1.2. 2—Condition and results of foam generation experiments in fractured sandstone cores at 23 °C and 2000 psia. (Boise and Berea sandstone used in these experiments have matrix permeability of 1650 mD and 200 mD respectively. 1 wt% dispersion of 5 nm PEG coated nanosilica dispersion was co-injected with CO₂ at 1:1 volume phase ratio.)

Exp. name	Rock Type	Fracture size (Microns)	Core Avg K (mD)	Matrix Porosity	Salinity (wt%)	Total Flow rate (ml/min)	Shear rate (s ⁻¹)	Foam Visual	Core		Capillary
									μ_{app} (cP)	MRF	Norm. μ
Berea 1F	Berea	165	13360	21%	2	5	1000	N	3.52	0.95	1.09
						10	2100	Y	3.69	1.30	2.24
						16	3400	Y	3.90	1.57	2.21
						20	4200	Y	4.81	2.15	2.13
						24	5000	Y	5.51	2.55	2.08
F1	Boise	104	6425	22%	0	3	800	N	2.15	1.27	2.18
						6	1600	N	2.15	1.26	1.73
						10	2700	Y	2.10	1.23	1.99
						14	3700	Y	2.27	1.34	2.14
						20	4300	Y	5.65	3.32	3.16
F2	Boise	65	2830	22%	0	3	1200	N	1.98	n/a	2.15
						6	2300	Y	2.08	n/a	3.13
						10	4100	Y	1.79	n/a	3.90
						13	5700	Y	1.78	n/a	4.00
						16	6200	Y	3.14	n/a	4.85

Table I.1.2. 3—Condition and results of foam generation experiment in fractured cement core at 23 °C and 2000 psia.

(Fracture aperture is 60.5 microns resulting in 965 mD average core permeability. Cement matrix permeability is considered to be negligibly small. 1 wt% dispersion of 5nm PEG coated nanosilica in DI water was co-injected with CO₂ at 1:1 volume phase ratio.)

Total Flow rate (ml/min)	Shear rate (s ⁻¹)	Foam Visual	Core	Capillary
			μ _{app} (cP)	Normalised μ
3	3400	Y	2.31	3.27
6	6700	Y	1.66	3.83
10	11200	Y	1.30	4.16
14	15700	Y	1.22	3.94
20	22400	Y	1.17	4.05

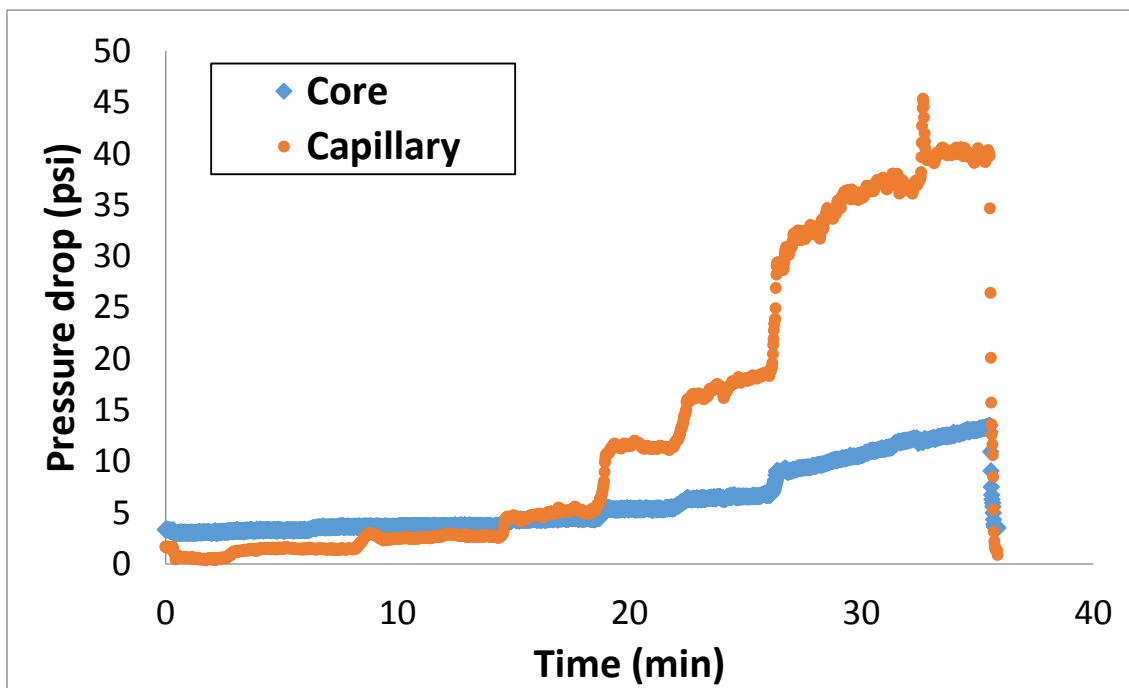


Fig. I.1.2. 8—Pressure difference across core measured from foam experiment in fractured Boise sandstone core flood with core F1. 1% PEG-coated silica in DI water was co-injected with CO₂ using phase ratio of 1:1 at 2000 psia and 23 °C.

As clearly depicted in Fig. I.1.2.9, the concept of threshold shear rate for foam generation applies not only for unfractured rock but also for the fracture in the rock. The fractures in the Boise sandstone cores, F1 and F2, both demonstrate threshold shear rate behavior, but at a different value. Sharp increase in apparent viscosity is observed at the effective shear rate in fracture of around 4000 s⁻¹ for core F1, while for core F2, the critical fracture shear rate was ~6000 s⁻¹. Above the critical shear rate, the apparent viscosity increased drastically from baseline value of 2 cP to as high as 5.65 cP in core F1; and to 3.14 cP in core F2. Similarly to unfractured

rock experiment, even though no increase in apparent viscosity was measured at low shear rate, very weak foam was often observed in the view cell.

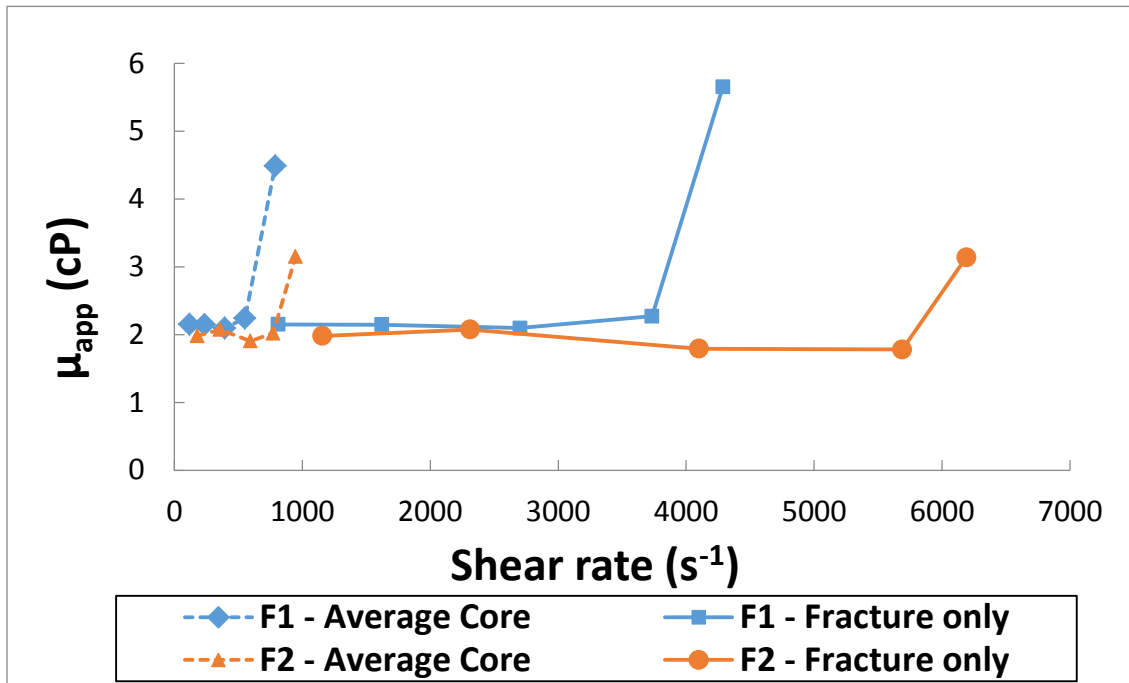


Fig. I.1.2. 9—Core apparent viscosity vs fracture shear rate from the two foam experiments in fractured Boise sandstone core flood under the same experiment condition. Fractured apertures for cores F1 and F2 were 104 microns and 65 microns, respectively. Dash lines are core-average value (combined matrix and fracture flow). The solid lines show the estimated shear rate and viscosity in the fracture.

An interesting aspect of the above calculation of the flow allocation between fracture and matrix zone is that, with the foam generation in the fracture, more of the injected fluid can be *diverted* (allocated) to the matrix zone despite the fact that foam is generated in the matrix zone also. At injection rate of 14 ml/min and lower, shear rate in fracture and matrix are both below the threshold so that no foam would be formed. The calculation given in Table A-1 shows that 75% of the injected fluid is allocated to the fracture. At 20 ml/min, on the other hand, foam would be generated in both matrix and fracture. According to the simple flow allocation calculation (employing the apparent viscosity measured in the fracture for F1), 59% of the injected fluid is now allocated to the fracture. We believe this effect can be enhanced by varying the foam quality, concentration of nanoparticles, salinity, etc.

Foam Generation in Unfractured and Fractured Berea Sandstone Cores. Coreflood experiments with unfractured Berea sandstone cores were carried out, but unfortunately, the state of stabilized plateau pressure drop could not be obtained except when the flow rate is low and no foam is generated in the core. These corefloods are being repeated to see if the large pressure fluctuations and the continual pressure climb are because of the trapping of foam bubbles inside the core, at the core face, or for some other reason. Nevertheless, the apparent viscosity measurements from the capillary tube downstream of the core clearly show a critical shear rate for foam generation, Fig. I.1.2.10. For the Berea 4 experiment (see Table I.1.2.1), co-injection of CO₂ and nanoparticle dispersion at shear rate of 240 s⁻¹ yielded the same apparent viscosity as the baseline experiment in which nanoparticles were not present. When shear rate increases to 366 s⁻¹, a jump in apparent viscosity is observed, and the presence of weak foam is confirmed in the view cell. The peak apparent viscosity is as high as 3.5 cP, almost 5 times of 0.7 cP observed in baseline experiment. Thus, 370 s⁻¹ is approximately the threshold shear rate for the unfractured Berea core used at 2000 psia and 23 C.

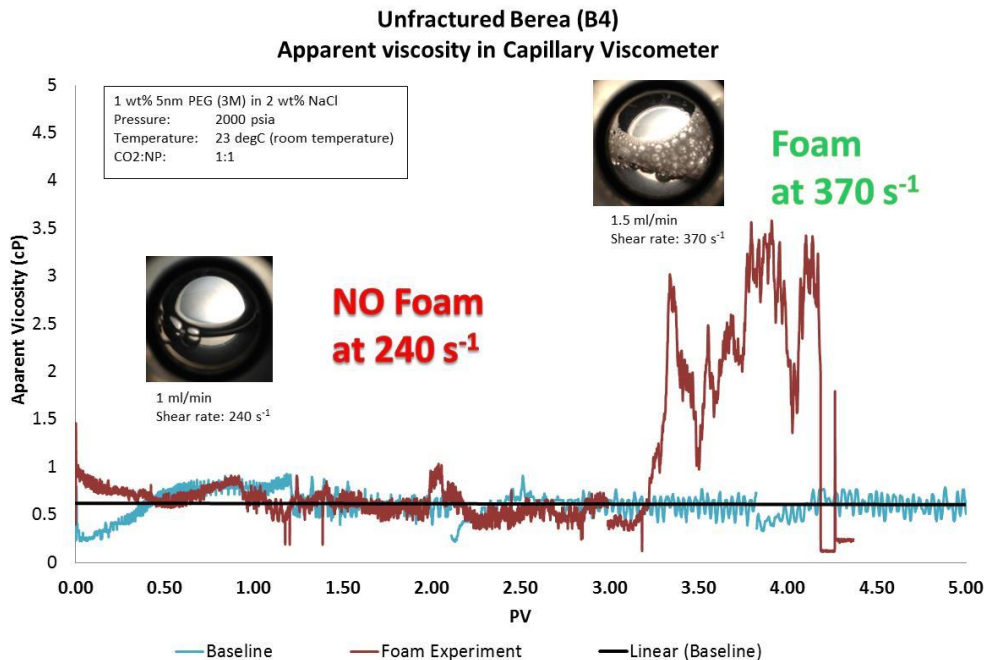


Fig. I.1.2. 10—Apparent viscosity measured in the capillary tube downstream of an unfractured Berea sandstone. 1% PEG-coated silica in 2% NaCl brine and CO₂ were co-injected using phase ratio of 1:1 at 2000 psia and 23 °C. The foam generation threshold falls between shear rates of 244 s⁻¹ and 366 s⁻¹.

As was done with the fractured Boise sandstone case, co-injection of CO₂ and nanoparticle dispersion was also conducted in a fractured Berea sandstone core. The Berea matrix permeability is an order of magnitude lower than Boise sandstone (127-175 md vs. 1800 md), while the fracture gap width is larger (165 μm) than the Boise fracture cases (104 and 65 μm), so almost all of the injected fluid would flow through the fracture. As it was difficult to obtain the apparent viscosity for foam in the matrix of Berea sandstone, we made the simplifying assumption that all fluid went into the fracture, to calculate the apparent viscosity in fracture. Results from the fractured Berea coreflood are shown in Fig. 1.1.2.11. The foam flow in the Berea fracture shows qualitatively a similar behavior to that in the Boise fractures, indicating an existence of a critical shear rate of similar magnitude. The apparent viscosity is about 3.5 cP below the critical shear rate and slowly rises as fracture shear rate increases. When fracture shear rate becomes larger than 3400 s⁻¹, the apparent viscosity increase substantially with the slope five times larger than that below the critical shear rate.

To confirm that foam generation in fracture is possible without the contribution from rock matrix, another coreflood experiment was carried out in fractured cement core with 61 microns aperture. As the matrix permeability of cured cement is on the order of microdarcies, flow in matrix is considered to be negligible. This experiment was successful in generating nanoparticle-stabilized CO₂ foam, yet with different behavior. Unlike the fractured sandstone core cases, fractured cement coreflood did not exhibit the threshold shear rate, even though the foam generation could be observed from the view cell. On the contrary, the fracture apparent viscosity decreased with increase in fracture shear rate, as shown in Fig. 1.1.2.12. In view of the very high shear rate applied, a possible explanation for this phenomenon is shear thinning of the foam when subjected to high shear rate in fracture, as observed with surfactant-stabilized foam in homogenous fracture (Yan *et al.* 2006).

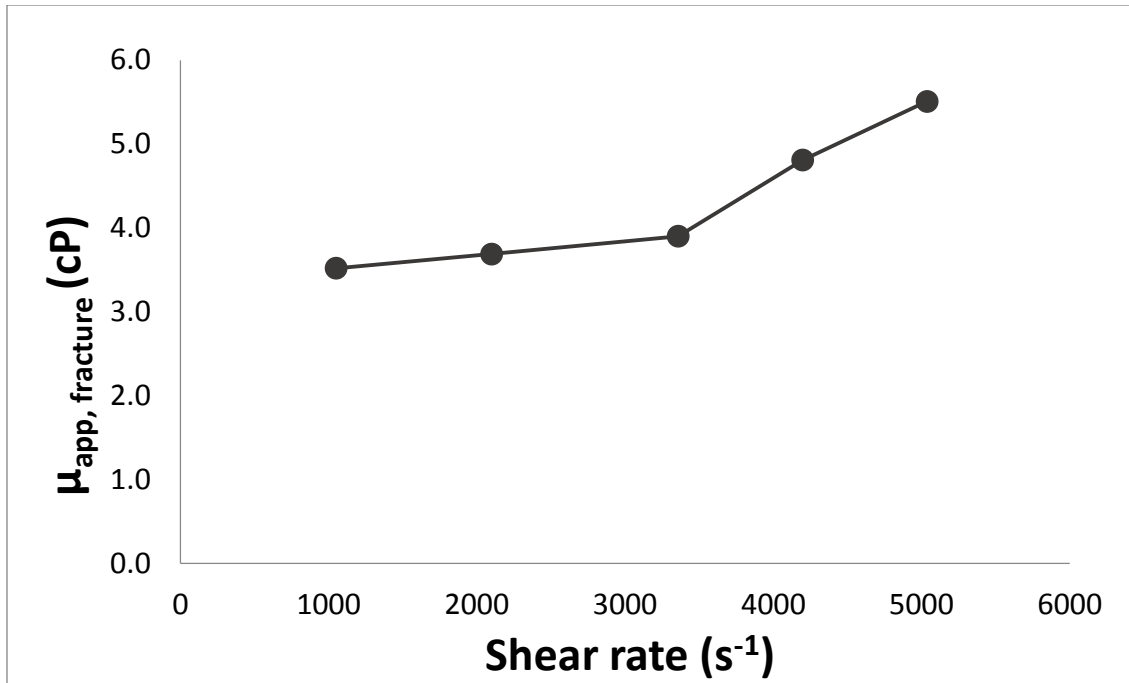


Fig. I.1.2. 11—Apparent viscosity vs. fracture shear rate obtained from a fractured Berea sandstone core flood. Fracture gap size was 165 microns. 1% PEG-coated silica in 2% NaCl brine and CO₂ were co-injected using phase ratio of 1:1 at 2000 psia and 23 °C. Critical shear rate was estimated to be 3400 s⁻¹.

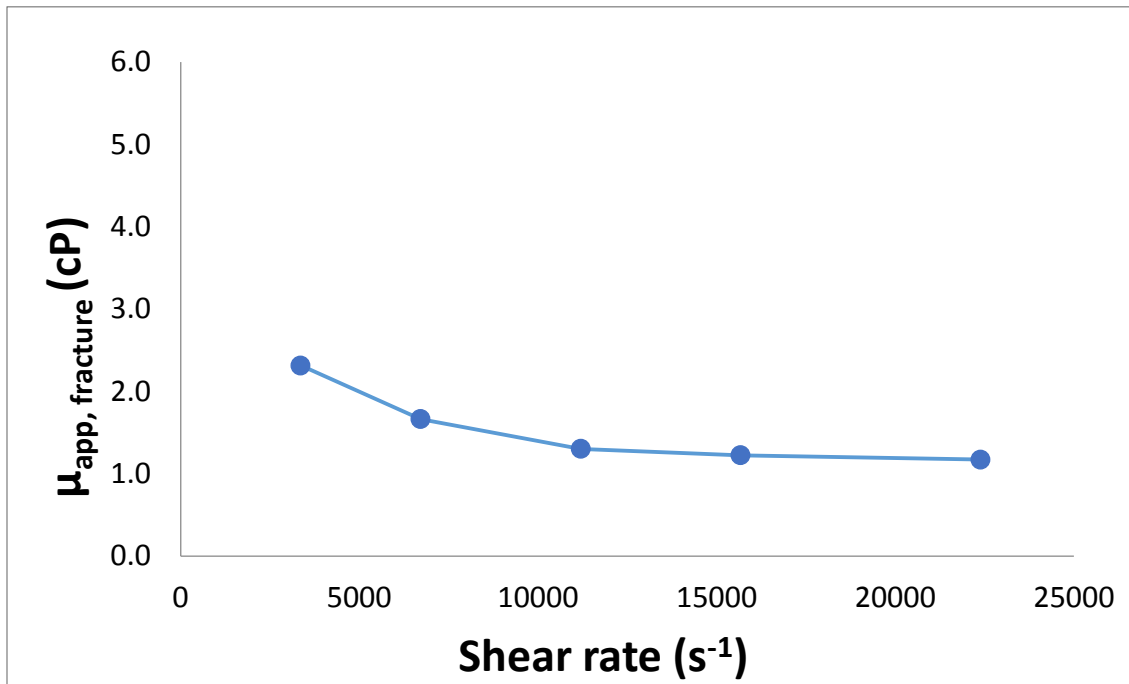


Fig. I.1.2.12—Apparent viscosity vs. fracture shear rate obtained from a fractured cement core flood. Fracture gap size was 60.5 microns. 1% PEG-coated silica in 2% NaCl brine and CO₂ were co-injected using phase ratio of 1:1 at 2000 psia and 23 °C.

Discussions on Factors Affecting Threshold Shear Rate for Corefloods. The shear rate thresholds are evident in every case of nanoparticle-stabilized CO₂ foam generation, but their specific values vary. Taking into account all the available data, the following parameters are believed to have primary effect on the threshold value. A better understanding of these key parameters would allow nanoparticle-stabilized foam to be engineered to form only at desired location where shear rate threshold is satisfied.

Operating Conditions. In beadpacks (permeability ~20 D) the threshold shear rate for foam generation with DI water and 0.5 wt% PEG-coated nanoparticles was less than 1400 s⁻¹ at 1350 psia and 23 °C, but increased to around 2600 s⁻¹ at 1350 psia and 70 °C and increased further to around 4000 s⁻¹ at 1350 psia and 90 °C (Espinosa *et al.*, 2010). This suggests that the threshold increases as the CO₂ density decreases. As Fig. I.1.2.4 indicates, flow in a beadpack can also exhibit a significantly smaller threshold (below 400 s⁻¹) in high salinity brine and 1 wt% PEG-coated nanoparticles at large CO₂ density (2800 psia, 50 °C). Thus factors that influence foam viscosity and stability, such as salinity and nanoparticle concentration, also appear to influence the threshold shear rate.

Matrix Permeability. The threshold shear rates change with rock type even though other experimental conditions are kept the same. The threshold shear rate tends to decrease when the matrix permeability become lower. The shear rate threshold observed in consolidated rock is 470 s⁻¹ in the high permeability Boise sandstone (1700 mD) and about 300 s⁻¹ in the lower permeability Berea sandstone (200 mD). Both values are smaller than the thresholds at similar conditions in beadpacks. This suggests that smaller pore throats facilitate the creation of bubbles and thereby reduce the shear rate needed to generate foam.

Fracture Permeability. The two fractured Boise sandstone corefloods in Fig. I.1.2.6 have fracture aperture sizes of 104 micron and 65 micron and critical shear rates of 3700 s⁻¹ and 5800 s⁻¹, respectively. On the other hand the fractured cement core, with an aperture of 61 micron, exhibits a threshold shear rate smaller than 3000 s⁻¹. These thresholds are all larger than those observed in matrix flow, which supports the contention that smaller constrictions facilitate bubble creation. The absence of a clear trend between threshold shear rate and fracture aperture suggests that the hydraulic aperture (inferred from the flow rate vs. pressure drop measurements

using the classical flow-in-a-slit formula) does not capture the distribution of constriction sizes that control foam generation. This is not surprising, because all the fractured samples used in this work have rough-walled, irregular geometries the entire length of the core.

1.1.2.v. Conclusions

An extensive series of flood experiments on beadpack indicates that:

- Proper hydrophilic-CO₂-philic balance (HCB) of nanoparticle's surface wettability is necessary for generation of viscous CO₂-in-water foams.
- If nanoparticle concentration is too low, no foam is generated regardless of HCB. With deionized water, stable foams could be formed with nanoparticle concentration of as low as 0.05 wt%, while higher particle concentrations were required with increase in salinity, *e.g.*, 0.5 wt% particle concentration for 4% NaCl brine salinity.
- Salinity has a significant effect on the nanoparticle's HCB and thus on the nanoparticle's ability to generate foams and on the viscosity of the resulting foam. Too high salt concentration can cause nanoparticles to lose dispersion stability in brine, preventing the nanoparticles from flowing through the beadpack and thus preventing foam generation.
- By adding a proper surfactant, HCB of nanoparticles can be tuned for generation of stable foams or to increase foam's viscosity.
- If CO₂:water ratio (foam quality) is too high (above 0.95) or too low (below about 0.5), no foam is generated.
- Shear rate higher than a threshold value must be provided to generate a stable foam, when a mixture of CO₂ and nanoparticle-containing brine is co-injected. The threshold shear rate depends on the experimental conditions, *e.g.* foams can be generated at shear rates of <400 s⁻¹ with 1% PEG-coated silica in API brine at 50°C and 2800 psia, but only at shear rates >4000 s⁻¹ with 0.5% PEG-coated silica in DI water at 95°C and 1350 psia.

A set of foam generation in coreflood experiments indicates that:

- In both unfractured and fractured cores, of Boise and Berea sandstones, a critical shear rate for foam generation exists.
- The critical shear rate for foam generation in matrix is believed to be a function of matrix permeability. Lower permeability leads to lower critical shear rate.

- The critical shear rate for foam generation in a fracture is much higher than that in matrix.
- Foam generation in a fracture exhibits a different trend in apparent viscosity vs shear rate than the trend for foam generation in matrix flow. Thus even when foam is generated both in the fracture and the matrix zone in a fractured rock, diversion of flow from the fracture into matrix can occur.

1.1.2.vi. Appendix: Estimation of Flow Allocation into Fracture and Matrix Zone

In order to obtain the apparent viscosity in fracture from the pressure drop measured from fractured core flood, we need to know how much of the injected fluids go into fracture and matrix respectively. Because the permeability of matrix and fracture, and the apparent viscosity in the matrix (from the unfractured core), are known, the fracture apparent viscosity can be approximately calculated, under the simplifying assumption that there is no cross flow between fracture and matrix.

Assuming that the mixture of CO₂ and nanoparticle dispersion flows like a single phase, the flux into the fracture and into the matrix can be calculated using the Darcy's equation, respectively,

$$Q(1 - f) = \frac{K_m(A_{Core} - WH)}{\mu_{m_{app}}} \left(\frac{\Delta P}{L} \right) \quad (I.1.2.A-1)$$

$$Qf = \frac{K_f WH}{\mu_{f_{app}}} \left(\frac{\Delta P}{L} \right) \quad (I.1.2.A-2)$$

where Q is the overall flow rate; f is the fractional flow into fracture; K_f and K_m are fracture and matrix permeabilities, respectively; W and H are fracture length at the core face and fracture gap width, respectively; A_{Core} and L are the core cross-sectional area and core length, respectively; and $\mu_{f_{app}}$ and $\mu_{m_{app}}$ are apparent viscosities in the fracture and in the matrix, respectively.

Summing up the above two equations and re-arranging, we can obtain,

$$\mu_{f_{app}} = \frac{K_f WH}{\frac{Q}{\left(\frac{\Delta P}{L} \right)} - \frac{K_m(A_{Core} - WH)}{\mu_{m_{app}}}} \quad (I.1.2.A-3)$$

To calculate $\mu_{f_{app}}$ from equation (I.I.2.A-3), we need to know $\mu_{m_{app}}$, which however is unknown being a function of the matrix shear rate, which in turn is proportional to $Q(1 - f)$. Therefore, a correlation between the matrix apparent viscosity and the matrix shear rate was developed from the unfractured Boise core flood results, as shown in Fig. I.I.2.A-1. The matrix shear rate is given by (Lake 1989)

$$\dot{\gamma}_{m_{eff}} = \frac{4Q(1 - f)}{(A_{Core} - WH)\sqrt{8K_m\phi_m}} \quad (I.I.2.A-4)$$

By inserting equation (I.I.2.A-1) into (I.I.2.A-4) and utilizing the above correlation, $\mu_{m_{app}}$ can be obtained, and subsequently $\mu_{f_{app}}$ from equation (I.I.2.A-3). The calculations for the case of Fig. I.I.2.9 are summarized in Table I.I.2.A-1.

Table I.I.2.A-1—Table shows decoupling calculation between flow in matrix and fracture of core F1. (% FF is the fraction of flow in fracture. The numbers in red are the shear rate which is above foam generation threshold.)

Q (cc/min)	%FF	Core μ_{app} (cP)		Shear rate (s^{-1})	
		Matrix	Fracture	Matrix	Fracture
3	74.5	2.15	2.15	60	810
6	74.5	2.15	2.15	120	1600
10	74.5	2.10	2.10	200	2700
14	73.5	2.16	2.27	290	3700
20	59.1	2.80	5.65	640	4300

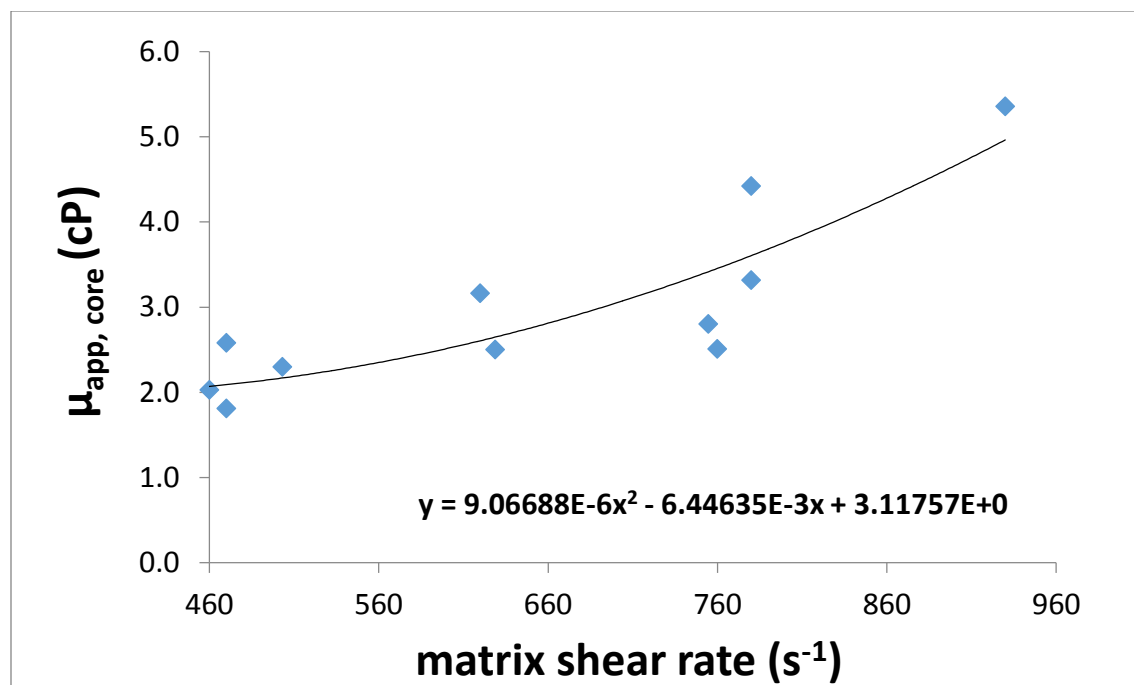


Fig. 1.1.2.A-1—Correlation between apparent viscosity and shear rate in Boise sandstone matrix. The correlation only valid above the critical shear rate of 460 s⁻¹.

1.1.2.vii. References

1. Adkins, S.S., Gohil, D., Dickson, J.L., Webber, S.E., and Johnston, K.P. (2007) "Water-in-carbon dioxide emulsions stabilized with hydrophobic silica particles." *Physical Chemistry Chemical Physics* 9(48): 6333-6343.
2. Binks, B.P. (2002) "Particles as surfactants - similarities and differences." *Current Opinion in Colloid and Interface Science* 7: 21-41.
3. Binks, B.P. and Rodrigues, J.A. (2007) "Enhanced Stabilization of Emulsions Due to Surfactant-Induced Nanoparticle Flocculation." *Langmuir* 23(14): 7436-7439.
4. Binks, B.P., Rodrigues, J.A., and Frith, W.J. (2007) "Synergistic Interaction in Emulsions Stabilized by a Mixture of Silica Nanoparticles and Cationic Surfactant." *Langmuir* 23(7): 3626-3636.
5. Chou, S.I., Vasicek, S.L., Pizio, D.L., Jasek, D.E., and Goodgame, J.A. (1992) "CO₂ Foam Field Trial at North Ward-Estes." SPE 24643, presented at the 67th SPE Annual Technical Conference, Washington, D.C., Oct. 4-7.
6. Cui, Z.G., Cui, Y.Z., Cui, C.F., Chen, Z., and Binks, B.P. (2010) "Aqueous Foams Stabilized by in Situ Surface Activation of CaCO₃ Nanoparticles via Adsorption of Anionic Surfactant." *Langmuir* 26(15): 12567-12574.
7. Dickson, J.L., Binks, B.P., and Johnston, K.P. (2004) "Stabilization of Carbon Dioxide-in-Water Emulsions Using Silica Particles." *Langmuir* 20: 7976-7983.
8. Enick, R.M., Olsen, D., Ammer, J., and Schuller, W. (2012) "Mobility and Conformance Control for CO₂ EOR via Thickeners, Foams, and Gels—A Literature Review of 40 Years of Research and Pilot Tests." SPE 154122, presented at the Eighteenth SPE Improved Oil Recovery Symposium, Tulsa, OK, Apr 14-18.

9. Enick, R.M., and Olsen, D. (2012) "Mobility and Conformance Control for CO₂ EOR via Thickeners, Foams, and Gels—A Detailed Literature Review of 40 Years of Research." Report DOE/NETL-2012/1540, National Energy Technology Laboratory, Department of Energy.
10. Espinosa, D., Caldelas, F., Johnston, K.P., Bryant, S.L., and Huh, C. (2010) "Nanoparticle-Stabilized Supercritical CO₂ Foams for Potential Mobility Control Applications." SPE 129925, presented at SPE Improved Oil Recovery Symp., Tulsa, OK, Apr. 26-28.
11. Ettinger, R.A. and Radke, C.J. (1989) "The Influence of Texture on Steady Foam Flow in Berea Sandstone." SPE 19688, presented at the SPE Annual Technical Conference, San Antonio, TX, Oct 8-11.
12. Golomb, D., Barry, E., Ryan, D., Swett P., and Duan, H. (2006) "Macroemulsions of Liquid and Supercritical CO₂-in-Water and Water-in-Liquid CO₂ Stabilized by Fine Particles." *Industrial & Engineering Chemistry Research* 45(8): 2728-2733.
13. Fjelde, I., and Zuta, J. (2008) "Oil Recovery from Matrix during CO₂-Foam Flooding of Fractured Carbonate Oil Reservoirs." SPE 113880, presented at SPE Europec/EAGE Annual Conference and Exhibition, Rome, Italy, Jun 9-12.
14. Hoefner, M.L. and Evans, E.M. (1995) "CO₂ Foam: Results from Four Developmental Field Trials." *SPE Reservoir Engineering*, Nov. 273–281.
15. Johnston, K.P. and Da Rocha, S.R.P. (2009) "Colloids in supercritical fluids over the last 20 years and future directions." *Journal of Supercritical Fluids* 47: 523-530.
16. Lake, L.W. (1989) *Enhanced Oil Recovery*, Prentice Hall.
17. Le, V.Q., Nguyen, Q.P., and Sanders, A.W. (2008) "A Novel Foam Concept with CO₂ Dissolved Surfactants." SPE 113370, presented at the SPE Improved Oil Recovery Symposium, held in Tulsa, OK, Apr. 19–23.
18. Marsden, S.S. and Khan, S.A. (1966) "The Flow of Foam Through Short Porous Media And Apparent Viscosity Measurements." *SPE Journal* 6(1): 17-25.
19. Mo, D., Yu, J., Liu, N., and Lee, R. (2012) "Study of the Effect of Different Factors on Nanoparticle-Stablized CO₂ Foam for Mobility Control." SPE 159282, presented at SPE Annual Technical Conference and Exhibition, San Antonio, Texas, Oct. 8-10.
20. Rosen, M.J. (2004) *Surfactants and Interfacial Phenomena*. New York, John Wiley & Sons, Inc.
21. Rossen, W.R. (1996) "Foams in Enhanced Oil Recovery." in *Foams. Theory, Measurements, and Applications*, Prud'homme, R. K., and Khan, S. A., eds., Chapter 11, 413-464, Marcel Dekker.
22. Sanders A., Jones, R., Mann, T., Patton, L., Linroth, M., and Nguyen, Q. (2010), "Successful Implementation of CO₂-Foam for Conformance Control." presentation at the CO₂ Conference, Midland Texas, Dec. 9–10.
23. Vignati, E., Piazza, R., and Lockhart, T.P. (2003) "Pickering Emulsions: Interfacial Tension, Colloidal Layer Morphology, and Trapped-Particle Motion." *Langmuir* 19(17): 6650-6656.
24. Walstra, P. and Smulders, P.E.A. (1998) *Emulsion Formation. Modern Aspects of Emulsion Technology*. B. P. Binks. Cambridge, The Royal Society of Chemistry: 56-99.
25. Worthen, A.J., Bagaria, H.G., Chen, Y., Bryant, S.L., Huh, C., and Johnston, K.P. (2012) "Nanoparticle-stabilized Carbon Dioxide-in-water Foams for Enhance Oil Recovery." SPE 154285, presented at the eighteenth SPE Improved Oil Recovery Symp., Tulsa, OK, Apr. 14-18.
26. Worthen, A.J., Bagaria, H.G., Chen, Y., Bryant, S.L., Huh, C., and Johnston, K.P. (2013a) "Nanoparticle-stabilized carbon dioxide-in-water foams with fine texture." *Journal of Colloid and Interface Science* 391(1): 142-151.

27. Worthen, A.J., Bryant, S.L., Huh, C., and Johnston, K.P. (2013b) "Carbon dioxide-in-water foams stabilized with nanoparticles and surfactant acting in synergy." *AIChE Journal* in press.
28. Yoon, K.Y., Li, Z., Neilson, B.M., Lee, W., Huh, C., Bryant, S.L., Bielawski, C.W., and Johnston, K.P. (2012) "Effect of Adsorbed Amphiphilic Copolymers on the Interfacial Activity of Superparamagnetic Nanoclusters and the Emulsification of Oil in Water." *Macromolecules* 45(12): 5157-5166.
29. Yan, W., Miller, C.A., and Hirasaki, G.J. (2006) "Foam sweep in fractures for enhanced oil recovery." *Colloids and Surfaces A: Physicochem. Eng. Aspects*: 348-359.
30. Yu, J., An, C., Mo, D., Liu N., and Lee, R. (2012) "Foam Mobility Control for Nanoparticle-Stabilized Supercritical CO₂ Foam." SPE 153336, presented at the Eighteenth SPE improved Oil Recovery Symp., Tulsa, OK, Apr 14-18.
31. Zhang, T., Davidson, D., Bryant, S.L., and Huh, C. (2010) "Nanoparticle-Stabilized Emulsions for Applications in Enhanced Oil Recovery." SPE/DOE 129885, presented at SPE Improved Oil Recovery Symp., Tulsa, OK., Apr. 26-28.
32. Zhang, T., Murphy, M., Yu, H., Bagaria, H.G., Yoon, K.Y., Nielson, B.M., Bielawski, C.W., Johnston, K.P., Huh, C., and Bryant, S.L. (2013) "Investigation of Nanoparticle Adsorption during Transport in Porous Media." SPE 166346, to be presented at the SPE Annual Technical Conference and Exhibition, New Orleans, LA, USA, Sept. 30-Oct. 2.
33. Zuta, J. and Fjelde, I. (2009) "Transport of CO₂-Foaming Agents during CO₂-Foam Processes in Fractured Chalk Rock." SPE 121253, presented at the EUROPEC/EAGE Conference and Exhibition, Amsterdam, Jun 8-11.
34. Zuta, J., Fjelde, I. and Roman, B. (2010) "Experimental and Simulation of CO₂-Foam Flooding in Fractured Chalk Rock at Reservoir Conditions: Effect of Mode of Injection on Oil Recovery." SPE 129575, presented at the SPE EOR Conference at Oil & Gas West Asia, Muscat, Oman, Apr 11-13.

I.2. Surfactant and nanoparticle-stabilized C/W foam systems and synergistic effects

In this section we present the first example of a combined nanoparticle/surfactant system for the formation of C/W foams. Our experimental observations indicated a strong synergistic effect of the silica NPs for creating viscous C/W foams in presence of trace amounts of caprylamidopropyl betaine surfactant. We argue that the foam formation was aided by interfacial tension reduction from the surfactant, while the foam stability was improved by adsorption of nanoparticles at the CO₂-water interface. The findings of this part of our experimental research were published in AIChE Journal:

Worthen, Andrew J., et al. "Carbon dioxide-in-water foams stabilized with nanoparticles and surfactant acting in synergy." *AIChE Journal* 59.9 (2013): 3490-3501.

1.2.1. Abstract

Synergistic interactions at the interface of nanoparticles (bare colloidal silica) and surfactant (caprylamidopropyl betaine) led to the generation of viscous and stable CO₂-in-water (C/W) foams with fine texture at 19.4 MPa and 50°C. Interestingly, neither species generated C/W foams alone. The surfactant became cationic in the presence of CO₂ and adsorbed on the hydrophilic silica nanoparticle surfaces resulting in an increase in the carbon dioxide/water/nanoparticle contact angle. The surfactant also adsorbed at the CO₂-water interface, reducing interfacial tension to allow formation of finer bubbles. The foams were generated in a beadpack and characterized by apparent viscosity measurements both in the beadpack and in a capillary tube viscometer. In addition, the macroscopic foam stability was observed visually. The foam texture and viscosity were tunable by controlling the aqueous phase composition. Foam stability is discussed in terms of lamella drainage, disjoining pressure, interfacial viscosity, and hole formation.

1.2.2. Introduction

Carbon dioxide has been used for decades for miscible displacement of oil in tertiary enhanced oil recovery (EOR).¹⁻⁴ However, CO₂, as a consequence of its low density (~ 0.05 to 0.5 g/mL) and low viscosity (~ 0.01 cP), often rises too high in the reservoir (gravity override), or fingers

unevenly resulting in poor sweep efficiency.^{5,6} The apparent viscosity of CO₂ in porous media may be increased by a factor of 10 to 100+ by forming foams with surfactants that stabilize the aqueous lamellae separating CO₂ bubbles.⁶ Traditionally, surfactants have been used to generate emulsions and foams of CO₂ and water by designing the proper hydrophilic/CO₂-philic balance of the surfactant, analogous to the hydrophilic/lipophilic balance (HLB).⁷

The HCB influences the interfacial properties of an amphiphile, including the preferred curvature of the CO₂-water interface and the efficiency of the surfactant for lowering the interfacial tension.⁸ The HCB has been defined as

$$1/HCB = \frac{A_{AC} - A_{AA} - A_{CC}}{A_{AW} - A_{AA} - A_{WW}} \quad (1.2.1)$$

where $A_{\alpha\beta}$ indicates the interaction pair potential between α and β with A = amphiphile, C = CO₂, and W = water.^{7,9} For surfactants, the tails contribute primarily to A_{AC} and the head primarily to A_{AW} . A significant challenge to surfactant design for CO₂-water systems is that the low polarizability/volume of CO₂ often results in weak solvation of the surfactant tails resulting in a very high HCB.⁷ Here the surfactant may favor water to such an extent that it adsorbs only weakly at the CO₂-water interface, at a level insufficient for foam formation and stabilization. The presence of surfactant at the interface may limit foam destabilization via multiple mechanisms, including drainage of lamellae, coalescence, and Ostwald ripening.¹⁰ Surfactants with low HCB's have been used to stabilize water-in-CO₂ (W/C) microemulsions¹¹⁻¹³ and emulsions,^{14,15} while surfactants with high HCB's stabilize C/W emulsions^{16,17} and foams.¹⁰ Several studies have focused on nonionic surfactants for C/W emulsions and foams,^{10,16,18,19} especially surfactants with “stubby” branched tails to aid in solubilization by CO₂. Various other classes of surfactants have also been investigated for C/W emulsions and foams, including poly(vinyl acetate) surfactants,^{18,19} ethoxylated sulfonates,^{20,21} sulfobetaines,^{20,22} and amines.

Recently, silica nanoparticles have been used to stabilize emulsions and foams with W/C²³ and C/W^{9,23-25} curvatures. An advantage of nanoparticles for stabilization of CO₂ foams is that they may irreversibly adsorb at CO₂-water interfaces, potentially providing longer term stability than traditional surfactants which dynamically adsorb and desorb at the interface.²⁶ Nanoparticles can be produced from chemically stable, abundant, low cost, and environmentally benign materials

such as silica and clay.²⁷ Changes in the magnitude of A_{AC} with respect to A_{AW} indicate changes in the wettability of the nanoparticle surface by CO_2 and water. The macroscopic manifestation of the relative interactions between the nanoparticles' surface, CO_2 , and water is the contact angle (θ), depicted in Figure 1.2.1. The contact angle is generally considered a key parameter for explaining particle behavior at interfaces.²⁸ However it is typically only measured for flat surfaces such as silica wafers, rather than for nanoparticles at interfaces.²⁹⁻³¹

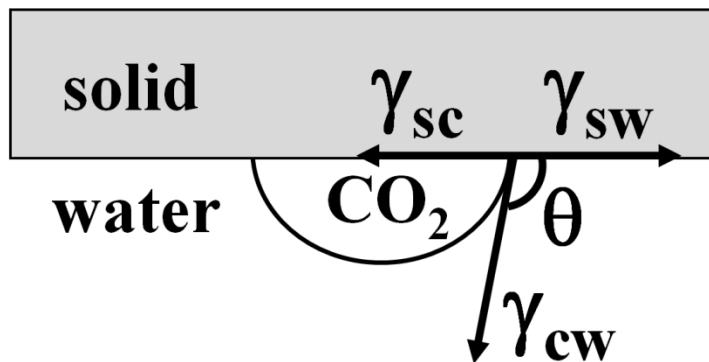


Figure 1.2.1. Schematic illustrating the CO_2 /water/solid contact angle. γ_{cw} , γ_{sc} , and γ_{sw} represent the CO_2 /water, solid/ CO_2 , and solid/water interfacial tensions, respectively.

Generally, bare silica nanoparticles are too hydrophilic to stabilize C/W foams,⁹ but surface modification by formation of covalent bonds has been used to lower the HCB. Silica nanoparticle surfaces have been modified with CO_2 -philic fluorinated ligands for W/C emulsions,²³ hydrophobic dichlorodimethylsilane (DCDMS) for C/W emulsions²⁵ and foams,⁹ and amphiphilic poly(ethylene glycol) (PEG) for C/W foams.^{8,25} While providing permanent attachment to the nanoparticle surface, the covalently modified particles often do not lower interfacial tension significantly at oil-water³² or CO_2 -water interfaces.

In situ surface activation of silica nanoparticles by adsorption of surfactant has been demonstrated as a facile route for formation of O/W emulsions³³⁻³⁶ and A/W foams.³⁷ This method does not require covalent grafting³⁷ and also offers the opportunity for free surfactant to adsorb by itself at the oil-water interface to lower interfacial tension (γ).^{37,38} Additionally, mixed nanoparticle and surfactant amphiphiles can provide novel interfacial phenomena including double phase inversions based on surfactant concentration²⁹ and synergistic emulsion formation.³³ Whereas amine surfactants may be used for *in situ* surface activation of silica nanoparticles, they often cause flocculation of the particles even at low concentrations of

surfactant.^{33,39} Recently, carboxybetaines have been used for wettability alteration of kaolinite clay particles via electrostatic interaction with negatively charge sites on the clay.⁴⁰ Partyka et al.⁴¹ found that carboxybetaines tend to adsorb on silica roughly an order of magnitude lower than protonated amine surfactants of the same tail length at pH 7.5, but their adsorption at lower pH was not investigated. Lower adsorption on silica may be beneficial since higher surfactant concentrations may be used without causing nanoparticle flocculation. Additionally, carboxybetaines are known to have high salinity tolerance and thus are of interest for EOR applications.⁴²⁻⁴⁴

The objectives of this study were to generate viscous and stable CO₂-in-water (C/W) foams with fine texture with a mixture of silica nanoparticles and a surfactant and to explain the behavior in terms of interfacial properties. To our knowledge previous studies have examined either a surfactant or nanoparticle, but not both together. The foam formation is shown to be aided by interfacial tension (γ) reduction from the surfactant, whereas the foam stability may be expected to be augmented by adsorption of nanoparticles at the CO₂-water interface. We utilize a zwitterionic carboxybetaine surfactant (caprylamidopropyl betaine) that becomes cationic upon protonation in the presence of CO₂. Interestingly, neither the surfactant nor the nanoparticles alone stabilized foam. C/W foams were generated in a beadpack and characterized by the apparent viscosity measurements both in the beadpack and in a capillary tube viscometer, as well as the macroscopic foam stability. The mechanism for the form formation and stability is explained qualitatively in terms of γ and carbon dioxide/water/silica contact angle (θ). To more fully characterize the binary amphiphile, *in situ* surface activation of the nanoparticles with the surfactant was characterized in aqueous solution in terms of dynamic light scattering (DLS) and zeta potential measurements. A key challenge was to design a system whereby the surfactant did not cause the nanoparticles to flocculate. The factors that may have contributed to foam stabilization by the nanoparticle/surfactant composite amphiphiles include lack of excessive amphiphile precipitation at the CO₂-water interface, slow lamella drainage, sufficient disjoining pressure, high interfacial viscosity, and resistance to hole formation. The ability to form stable C/W foams with enhanced stabilities with the combination of nanoparticles and surfactant has the potential to aid advancement of CO₂ enhanced oil recovery.

1.2.3. Materials

Bare colloidal silica nanoparticles (NexSil 20, Nyacol Nano Technologies, Inc., USA) were purchased as a 40% aqueous dispersion. Caprylamidopropyl betaine (CAPB) was a gift from Rhodia (Mackam OAB, batch UP1K17X18). Per the certificate of analysis provided by the manufacturer, the solution was 37.6% solids including 6.5% NaCl. The NaCl is a byproduct of the betaine synthesis.⁴⁵ As additional impurities are unknown, a concentration of 30% CAPB was assumed for calculations in this study, based on the typical CAPB concentration per the manufacturer.

HCl (1N solution, Fisher Scientific, USA), NaOH (1N solution, Fisher Scientific, USA), NaCl (ACS Grade, Fisher Scientific, USA), HNO₃ (ACS Plus Grade, Fisher Scientific, USA), NaHCO₃ (ACS Grade, Fisher Scientific, USA), dodecane (99%, Acros Organics, USA), and CO₂ (research-grade, Matheson, USA) were used as received. Deionized (DI) water (Nanopure II, Barnstead, Dubuque, IA) was used for all experiments.

1.2.4. Methods

Preparation and characterization of aqueous dispersions. Dispersions of nanoparticles with surfactant and/or NaCl in water were prepared by adding dilute nanoparticle dispersions to dilute solutions of CAPB, followed by a solution of NaCl in DI water. All nanoparticle, surfactant, and NaCl concentrations are given as % w/v in the aqueous phase. The NaCl concentrations given in this study are based on the added NaCl to the nanoparticle dispersions and surfactant solutions. The NaCl from the stock CAPB solution added an additional 0.002% to 0.1% NaCl for CAPB concentrations of 0.01% to 0.5%, respectively. The additional NaCl was considered insignificant as the nanoparticle/surfactant mixed system behavior was a very weak function of NaCl concentration up to 3% NaCl added to the solution. The nanoparticle and surfactant mixtures were ~ pH 8 before any acid or base was added. Where specified, pH was adjusted to 4, 6, or 8 (within ± 0.05 pH units) by adding 1N HCl or NaOH solution while stirring and monitoring the pH with a pH meter (Oakton pH 11 series with Oakton WD-35801-00 probe, Oakton Instruments, USA). Dispersions of 0.1% colloidal silica with 0% to 0.5% CAPB were characterized at room temperature ($22 \pm 1^\circ\text{C}$) with a Brookhaven ZetaPALS instrument to

determine the zeta potential and the hydrodynamic diameter of the particles. The Smoluchowski equation was used to convert the measured mobility to zeta potential and the CONTIN model was used to fit the dynamic light scattering (DLS) data.

Determination of surfactant isoelectric point. Titration was used to determine the isoelectric point (pI) of the surfactant where 100 mL of 1% CAPB solution was first adjusted to pH 10.09 with 2.4 N NaOH solution and then 5-50 μ L aliquots of 1N HCl solution were added while stirring the surfactant solution. The pH of the surfactant solution was measured with a pH meter (Oakton pH 11 series with Oakton WD-35801-00 probe, Oakton Instruments, USA) and recorded after each aliquot of HCl solution was added.

Interfacial tension and contact angle measurements. Axisymmetric drop shape analysis of a captive bubble was used to determine the CO₂-water interfacial tension (γ) and the contact angle (θ) between CO₂/water/silica wafer. The apparatus and techniques were adapted from previous studies of interfacial tension⁴⁶ and contact angle.³¹ The high-pressure cell that held the stage was pressurized with CO₂ to 6.65 MPa (absolute) and held at room temperature ($22 \pm 1^\circ\text{C}$). The solution was stirred for 30 minutes with excess CO₂ present to ensure the aqueous phase was saturated with CO₂ before measurements were taken. The CO₂ bubble profile shape when captured on the stage was analyzed according to the Laplace equation to calculate γ and θ made with the stage. The average and standard deviation of the calculated interfacial tension or contact angle for 4 bubbles were recorded, where 10 measurements were taken of each bubble every 5 s. For interfacial tension measurements, the stage was cut from a polished quartz wafer (item number SOX101005S2 from MTI Corp., USA). For contact angle measurements, the stage was cut from a silica-coated silicon wafer. To produce the silica coating on the silicon wafer (mirror-polished Si, Wafer World, Inc., USA), it was cleaned with DI water and placed in 15.8 N HNO₃ solution overnight.³³ The resulting silica-coated wafer was then neutralized with NaHCO₃, washed with DI and ethanol, and dried prior to use.

C/W foam formation, apparent viscosity measurement, and stability determination. The C/W foams were formed and characterized in an apparatus described elsewhere.⁹ A diagram of the apparatus used to generate C/W foams is shown in Figure 1.2.2. Nanoparticle dispersions were prepared as described above, without adjusting the pH prior to use. All experiments were done at 19.4 MPa (absolute) and 50°C, using a total flow rate of 1.5 mL/min and a CO₂:water phase ratio of 3:1 by volume. The system pressure was maintained within 0.2 MPa for all

experiments. The apparent viscosity of the foam in the beadpack (0.38 cm ID x 11.3 cm long, filled with 180 μm spherical glass beads, porosity of 0.34, pore volume of 0.436 mL, permeability of 22.5 darcy) was calculated from the pressure drop using Darcy's Law, treating the foam as a single phase.¹ At a flow rate of 1.5 mL/min, the shear rate in the beadpack is 1130 s^{-1} , the superficial velocity is 0.220 cm/s, and the residence time is 17.4 s. The beadpack shear rate and superficial velocity used in this study may be found in field applications near an injection well where most foam generation is expected.⁶ The apparent viscosity of the foam in the capillary tube (0.0762 cm ID x 195 cm long, volume of 0.889 mL, permeability of $\sim 19,000$ darcy) was calculated from the pressure drop across the capillary tube using the Hagen-Poiseuille equation. At a flow rate of 1.5 mL/min, the shear rate at the wall of the capillary tube is 576 s^{-1} , the superficial velocity is 5.482 cm/s, and the residence time is 35.6 s. Per manufacturer's information, the accuracy of the differential pressure reading is $\pm 0.25\%$ of full scale, which is equivalent to ± 0.15 cP in the capillary and ± 0.31 cP in the beadpack.

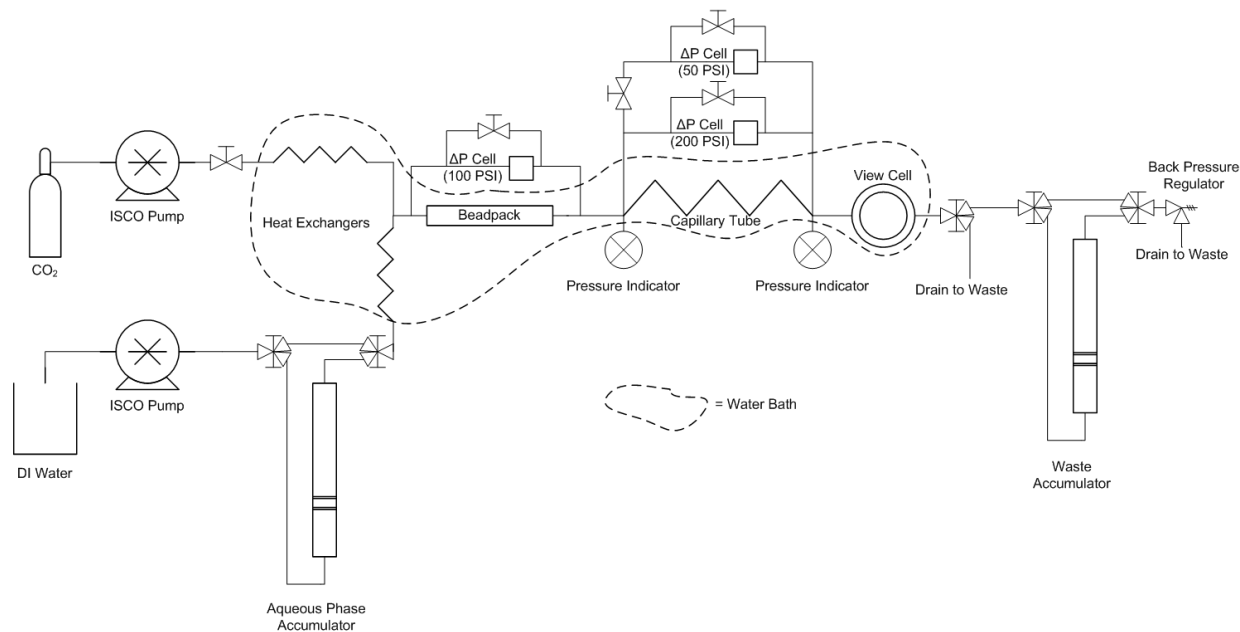


Figure 1.2.2. Diagram of apparatus for C/W foam generation, measurement of viscosity and long-term foam stability.

O/W emulsion formation, stability, and microstructure determination. To generate O/W emulsions, 1.5 mL of nanoparticle dispersion and 1.5 mL of dodecane were loaded into a 1 dram vial (capacity of 3.7 mL) and sonicated for 1 min with a Branson Sonifier (VWR Scientific, model 250) equipped with a microtip. The microtip was held just above the oil-water interface to avoid entraining air during O/W emulsion formation. Digital photographs were taken of the

vials to record macroscopic emulsion behavior. Microstructure was recorded with optical micrographs of the emulsions. The micrographs were taken of 20 μL of O/W emulsion removed from the center of the emulsion phase and placed on a slide with a glass cover slip. Droplet sizes were measured using ImageJ software, using a calibration slide as a standard.

1.2.5. Results

Isoelectric point determination. The caprylamidopropyl betaine (CAPB) surfactant was titrated with HCl to find the isoelectric point (pI) in DI water. Figure 1.2.3 shows the pH of a 1% CAPB sample as a function of added HCl solution, where the pI is indicated by the inflection point at $\text{pH} \sim 6.4$. For the experiments in this study where CO_2 and water are present, the pH will be well below this point and the surfactant will be positively charged (Scheme 1.2.1).

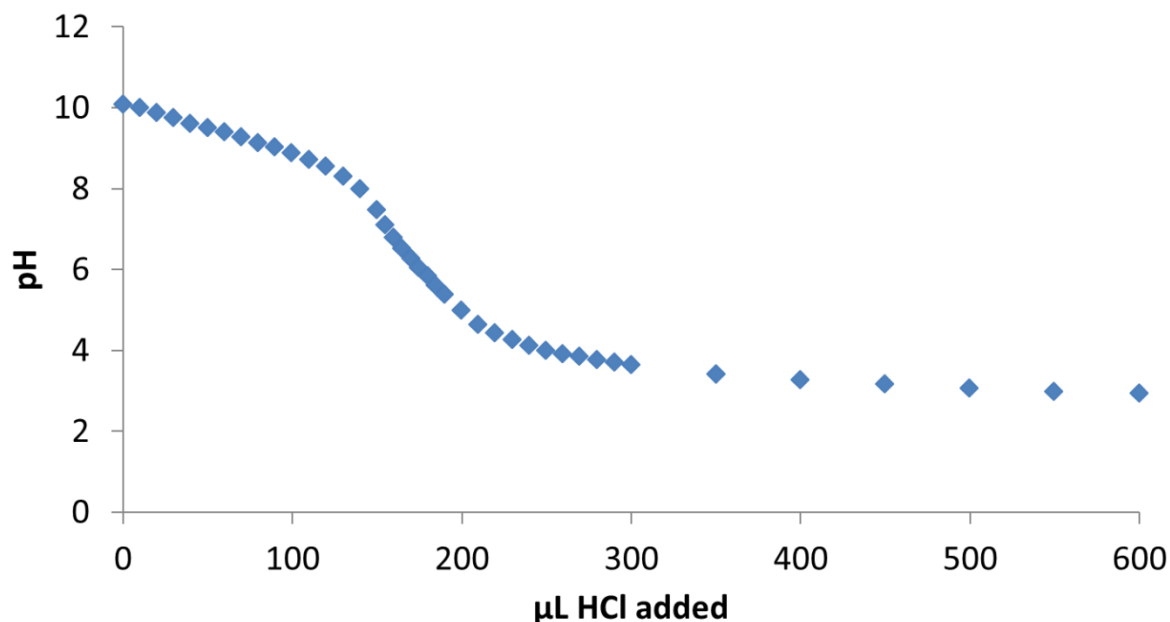
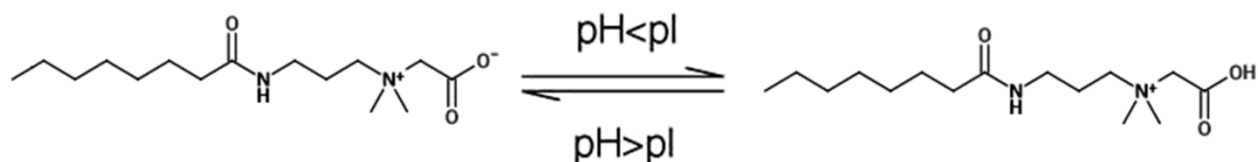


Figure 1.2.3. Titration curve of 100 mL 1% w/v CAPB with 1 N HCl. The inflection point at $\text{pH} \sim 6.4$ indicates the isoelectric point (pI) of the surfactant.



Scheme 1.2.1. CAPB reversibly switches between a zwitterion above the pI and a cation below the pI.

Dynamic light scattering and zeta potential measurements. Dynamic light scattering (DLS) was used to determine the hydrodynamic diameter of the silica particles as a function of CAPB concentration at pH 4 and 6 (Figure 1.2.4a). The results show consistent particle hydrodynamic diameters of ~28 nm at CAPB concentrations up to 0.25%, indicating no detectable particle flocculation occurred after 40 h of aging.

Figure 1.2.4b shows the zeta potential of silica nanoparticles (0.1%) at pH values of 4, 6, and 8 as a function of CAPB concentration. The zeta potential of the nanoparticles was strongly negative without surfactant as expected for silica. As pH 4, where the surfactant is cationic, the zeta potential increased much more strongly than at pH 6 where it was zwitterionic. At pH 8 where it was mildly anionic, the number of negative charges added by the surfactant appeared to be lower than the number negative charges lost from the silica. With the lower local dielectric constant from the adsorbed surfactant and increase in the number of silanol groups with adsorbed hydrophobe from the surfactant tail, the number of dissociated silanol groups appears to have decreased. At pH 4 with 0.5% CAPB, the nanoparticle dispersion became opaque immediately after preparation and showed significant settling in 1-2 minutes as the electrostatic repulsion became small.

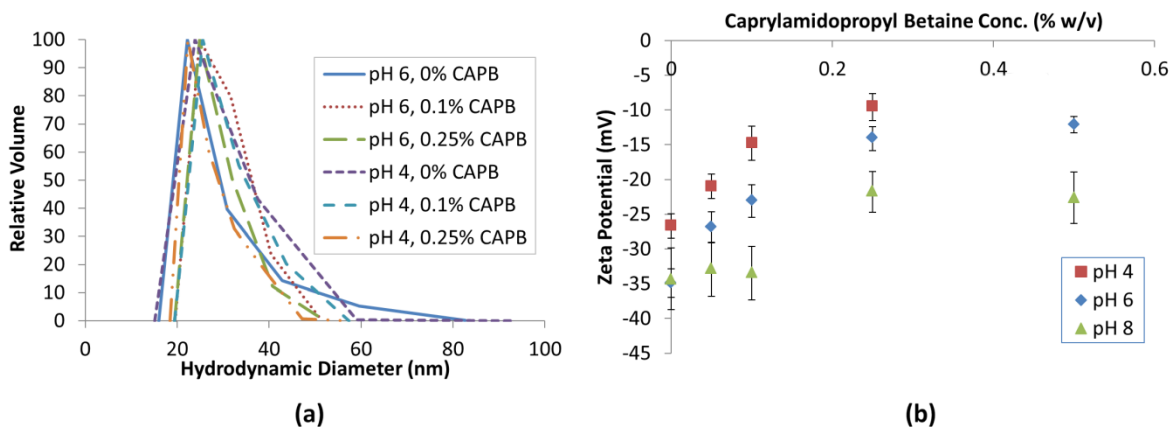


Figure 1.2.4. (a) Size distributions of 0.1% w/v bare colloidal silica measured by DLS at pH 4 and 6 with 0%, 0.1%, and 0.25% CAPB after aging for 40h. The average hydrodynamic diameter for each run was 28 ± 2 nm. (b) Zeta potential of 0.1% w/v bare colloidal silica at pH 4, 6, and 8 as a function of CAPB concentration.

Captive-bubble interfacial tension and contact angle measurements. The results of the CO_2 captive bubble γ and θ measurements are summarized in Table 1. The high pressure cell was held at room temperature (22 ± 1 °C) and 6.65 MPa. A temperature of 22 °C was assumed for fitting the bubble profile. At these conditions, CO_2 is a liquid and has a density of 0.772 g/mL.

As solvation of surfactant tails by CO₂ is known to be a strong function of density,⁷ these conditions were chosen to give a similar CO₂ density to the target foam formation conditions (50°C and 19.4 MPa), where the CO₂ density is 0.776 g/mL. A CAPB concentration of 0.25% in the water phase decreased the CO₂-water interfacial tension by 11.9 mN/m and caused the CO₂/water/silica θ to increase by 11.5°. An attempt was made to determine the solubility of CAPB in CO₂ at a fixed CAPB concentration of 0.15% w/w. Even at 34.6 MPa and 22 °C, it was not soluble. Thus, in the captive bubble and θ measurements the concentration of surfactant in the CO₂ phase may be assumed to be small, such that the surfactant concentration in the water phase remained essentially constant.

Table 1.2.1. Effect of CAPB on γ and θ at 22°C and 6.65 MPa ($\rho_{\text{CO}_2} = 0.772$)

Aqueous phase	$\gamma \pm \text{Std. Dev. (mN/m)}^a$	$\theta \pm \text{Std. Dev. (}^\circ)^b$
DI water	28.3 \pm 1.0	28.1 \pm 1.3
0.25% w/v CAPB	16.4 \pm 1.4	39.6 \pm 1.6

^a Measured using polished quartz wafer

^b Measured using silica-coated wafer

C/W foam texture and viscosity. C/W foams were generated at 50°C and 19.4 MPa with a CO₂:water phase ratio of 3:1 by volume. CO₂ is a supercritical fluid at these conditions with a density of 0.776 g/mL, very similar to the density used for γ and θ measurements.

Representative examples of C/W foam texture are given in Figure 1.2.5, showing a very fine foam (Figure 5a), an intermediate texture (Figure 5b), and a very coarse foam (Figure 5c). The example fine texture foam was generated with 1% silica nanoparticles and 0.05% CAPB with 1% NaCl in solution. The example intermediate texture foam was generated with a lower silica nanoparticle concentration of 0.1%, resulting in large CO₂ bubbles. The example coarse foam was also generated with 0.1% nanoparticles, but with no salt present. These examples demonstrate the texture of the foam may be tuned by adjusting the aqueous phase composition.

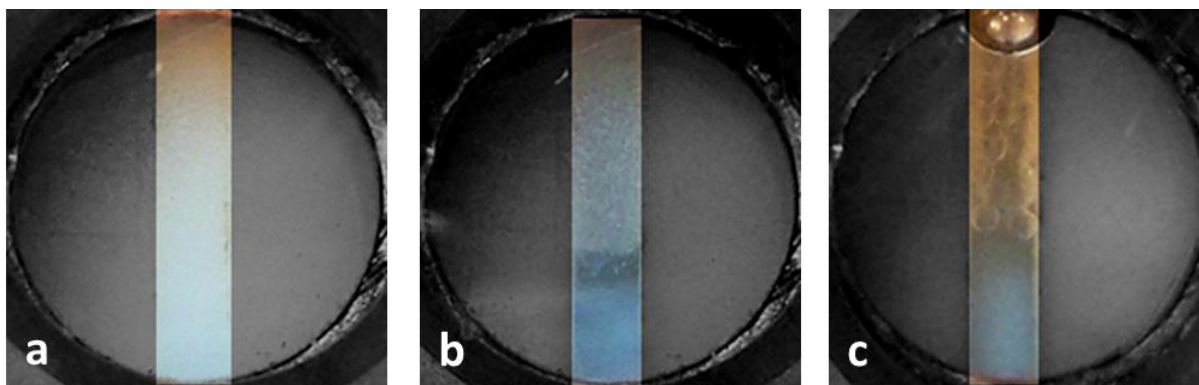


Figure 1.2.5. Representative examples of C/W foam in the view cell at 50°C, 19.4 MPa with a) fine texture, b) intermediate texture, and c) coarse texture. Foam is visible in the center of the window in the vertical channel between Teflon spacers. The Teflon spacers have been darkened with photo editing software to highlight the channel. Dark regions in the channel indicate absence of foam. Window diameter is 1.4 cm and visual path length is 0.8 cm.

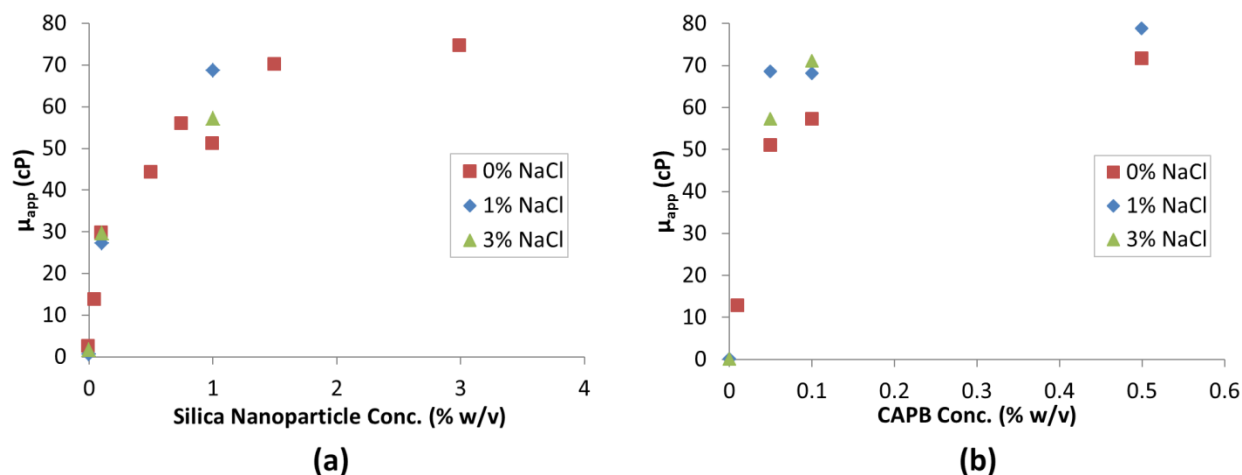


Figure 1.2.6. Particle-surfactant mixture stabilized C/W foam viscosity measured in the beadpack with 0%, 1% and 3% w/v NaCl at 50°C, 19.4 MPa. Viscosity is shown as a function of (a) silica nanoparticle concentration with fixed 0.05% caprylamidopropyl betaine (CAPB) concentration and (b) CAPB concentration with fixed 1% silica nanoparticle concentration.

The apparent viscosity of the CO₂ and aqueous phase mixture in the beadpack and capillary tube are summarized in Figures 1.2.6 and 7, respectively. For all of these foams, the highest viscosity foams (> 10cP in capillary, > 50 cP in beadpack) were very white with fine texture as shown in Figure 1.2.5a. Foams with intermediate viscosities (5-10 cP in capillary, 25-50 cP in beadpack) tended to have intermediate texture as shown in Figure 1.2.5b. Low viscosity foams (2-5 cP in capillary, 10-25 cP in beadpack) had very coarse textures as shown in Figure 1.2.5c. When the mixture viscosity was less than ~2 cP in the capillary and less than ~10 cP in beadpack, at most only single lamellae were visible in the view cell indicating no foam was observed.

Figures 1.2.6 and 7 show the apparent viscosity as a function of silica nanoparticle concentration while holding the CAPB concentration fixed at 0.05% (Figure 1.2.6a and 7a), and as a function of CAPB concentration while holding the nanoparticle concentration fixed at 1% (Figure 1.2.6b and 7b). Salinities of 0%, 1%, and 3% NaCl are shown for both concentration variation methods. When the CAPB concentration was held constant, the salinity did not affect the apparent viscosity. A weak increase in viscosity with increased salinity was observed when the nanoparticle concentration was held constant (Figure 1.2.6b and 7b). In both the beadpack and the capillary, foam was not formed with either surfactant or nanoparticles. However, in each case the foam viscosity increased with increasing nanoparticle concentration or CAPB concentration, while holding the other species constant. The values of viscosity reached 36 cP in the capillary, which is quite large for a surfactant concentration of only 0.05%. The rate of increase of the viscosity as a function of nanoparticle concentration between 1.5% and 3% slowed significantly in both the beadpack (Figure 1.2.6a) and capillary tube (Figure 1.2.7a). The rate of increase as a function of CAPB concentration between 0.1% and 0.5% slowed significantly in both the beadpack and the capillary. Interestingly, the apparent viscosity of the foam was higher in the beadpack than in the capillary for all but the lowest viscosity experiments (Figure 1.2.S1). The nanoparticle dispersions did not visibly flocculate between creation and the end of the foam experiment (2-12 h) at the conditions tested in this study. Periodically, the beadpack permeability was tested with DI water to verify that the beadpack properties had not measurably changed due to filtration or irreversible adsorption of nanoparticle and surfactant aggregates. No decrease in permeability from the initial value of 22.5 Darcy was noted throughout the experiments, indicating the nanoparticles did not appreciably plug the pore throats.

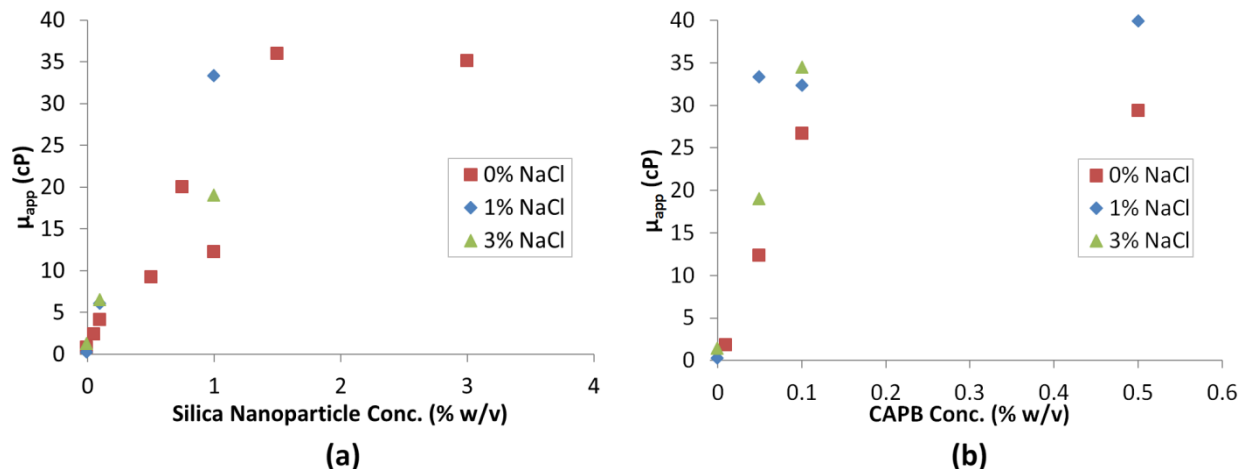


Figure 1.2.7. Particle-surfactant mixture stabilized C/W foam viscosity measured in the capillary tube with 0%, 1% and 3% w/v NaCl at 50°C, 19.4 MPa. Viscosity is shown as a function of (a) silica nanoparticle concentration with fixed 0.05% caprylamidopropyl betaine (CAPB) concentration and (b) CAPB concentration with fixed 1% silica nanoparticle concentration.

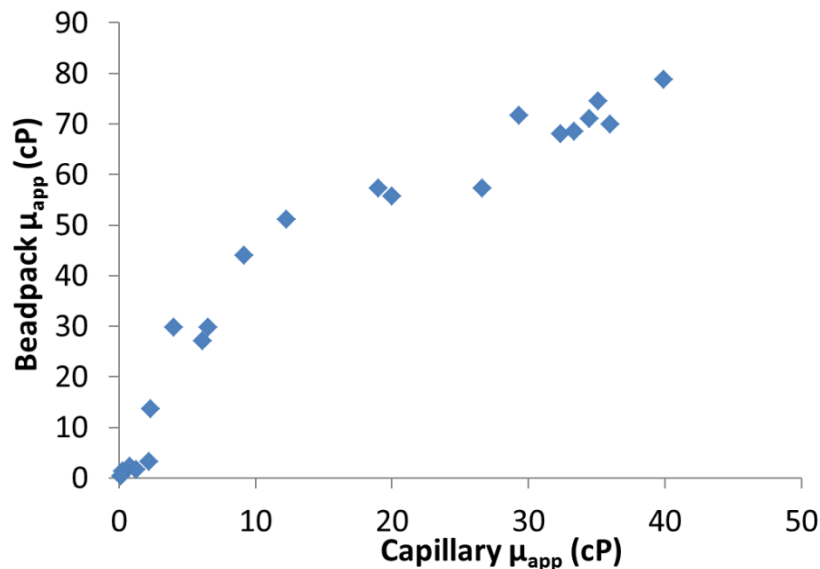


Figure 1.2.S1. Beadpack viscosity vs. capillary viscosity (all data from Figures 1.2.6 and 7) at 50°C, 19.4 MPa.

C/W foam stability. After foam formation and viscosity characterization, two foams were held in the view cell for 20 h to observe their long term stability. Foam generated with 1.5% bare colloidal silica and 0.05% CAPB (0% NaCl) are shown in Figure 1.2.8a and 8b, immediately after the flow experiment was stopped and after 20 h, respectively. The initial viscosity of the foam was 70 cP in the beadpack and 36 cP in the capillary. No foam resolution (by height) was observed, but the foam did become slightly less opaque white. Foam generated with 1% bare colloidal silica and 0.1% CAPB at a salinity of 3% NaCl is shown in Figure 1.2.8c and 8d,

immediately after the flow experiment was stopped and after 20 h, respectively. The initial viscosity of the foam was 71 cP in the beadpack and 34 cP in the capillary. The foam became noticeably less opaque white in the upper 20% of the cell, but remains very opaque white throughout the rest of the volume. Stability observations lasting weeks or months may also be of interest for EOR applications, but were outside the scope of this study.

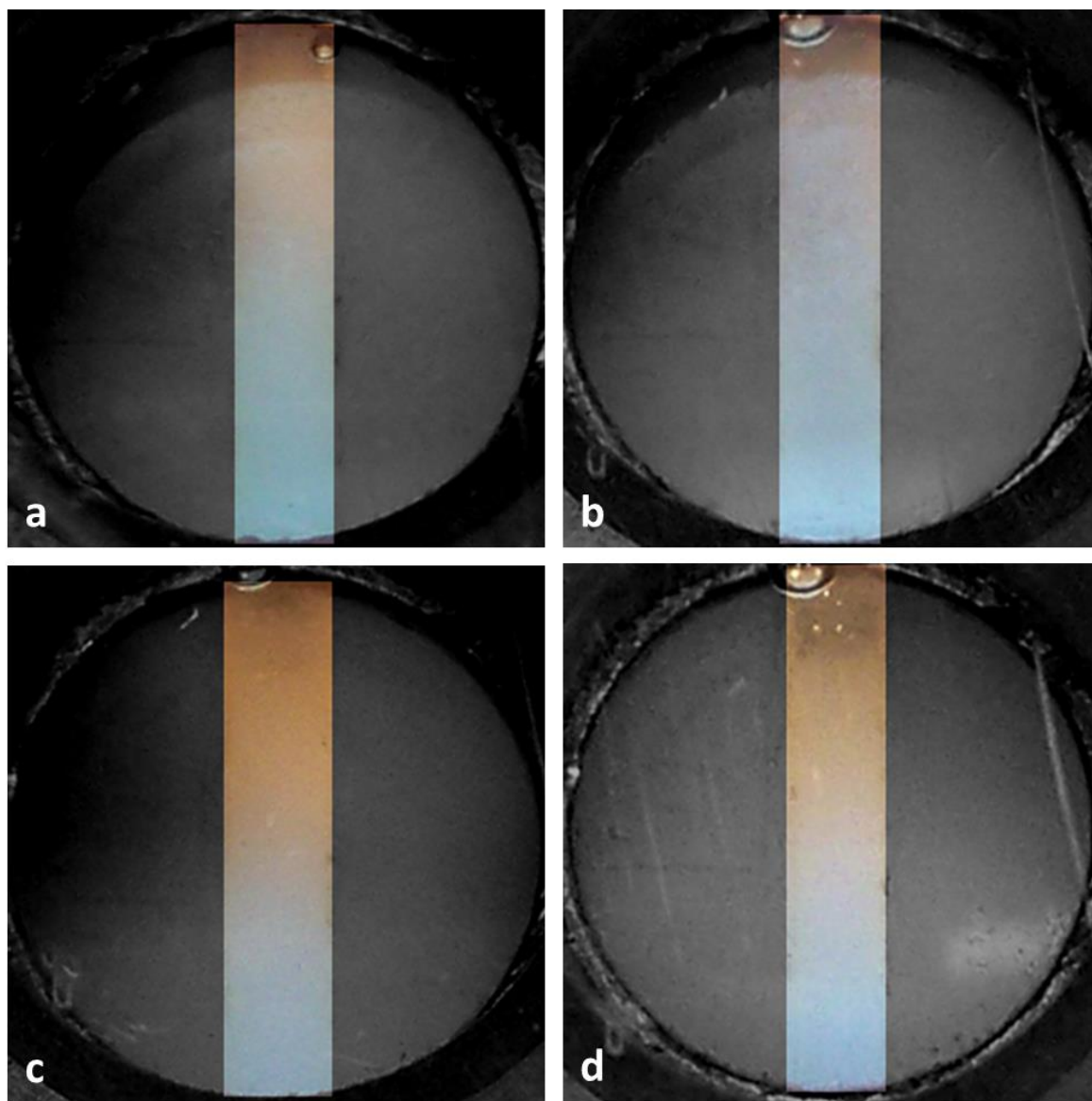


Figure 1.2.8. C/W foam stability in view cell at 50°C, 19.4 MPa. (a) and (b) are 1.5% silica nanoparticles + 0.05% CAPB, $t = 0$ and 20 h, respectively. (c) and (d) are 1% silica nanoparticles + 0.1% CAPB + 3% NaCl, $t = 0$ and 20 h, respectively. Foam is visible in the center of the window in the vertical channel between Teflon spacers. The Teflon spacers have been darkened with photo editing software to highlight the channel. Dark regions in the channel indicate absence of foam. Window diameter is 1.4 cm and visual path length is 0.8 cm.

Effect of pH on interfacial properties. To investigate the effect of pH on the interfacial properties of the nanoparticle/surfactant mixed system, dodecane-in-water emulsions (1:1 dodecane:aqueous phase, by volume) were generated at pH values of 4, 6, and 8. The aqueous phases chosen were 1% bare colloidal silica with 0.05% CAPB, and 1% bare colloidal silica with 0.05% CAPB (concentrations given in aqueous phase). The emulsified volume of dodecane and emulsion macroscopic texture are shown in Figure 1.2.9 after 1 h of aging. In the nanoparticle only emulsions (left column), the amount of dodecane emulsified decreased from pH 4 to pH 6 to pH 8. Also, the emulsions were not opaque white, which indicates that they are likely composed of very large or very disperse droplets. In the surfactant only emulsions (center column), no significant fraction of dodecane was emulsified at any pH tested. In the mixed surfactant/nanoparticle emulsions (right column), no excess dodecane was visible after emulsification at all pH conditions tested. The amount of excess water phase increased from pH 4 to pH 6 to pH 8, and the emulsion also looked less bright white at pH 8, likely indicating larger or more disperse droplets.

To further investigate the microstructure of the surfactant and nanoparticle stabilized emulsions, micrographs were taken of emulsified oil droplets after 1 day (Figure 1.2.10) and 14 days (not shown). The average droplet sizes increased slightly from pH 4 to 6 and significantly increased at pH 8. The oil droplet size distribution is given in Figure 1.2.S2 at pH 4, 6, and 8 at 1 day and 14 days. The average droplet sizes remained constant after 14 days, as did the droplet size distributions (Figure 1.2.S2).

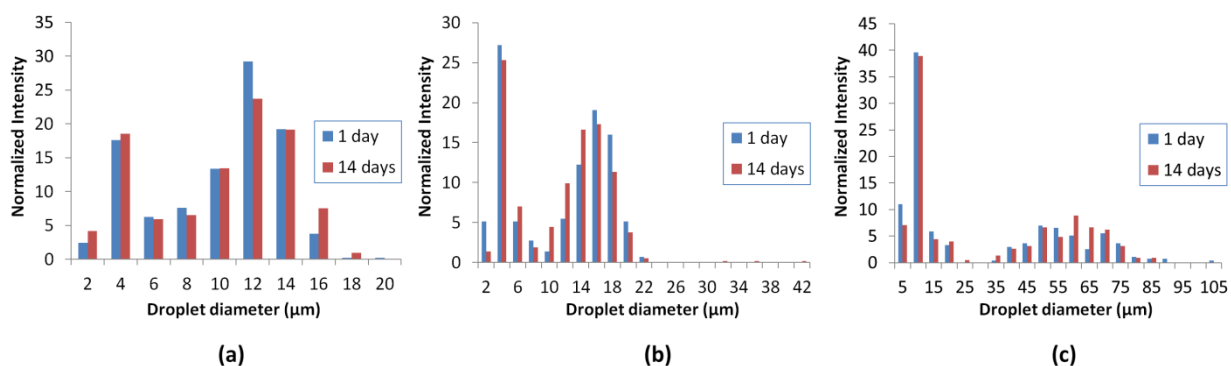


Figure 1.2.S2. Droplet size distributions of emulsions stabilized with 1% bare colloidal silica nanoparticles + 0.05% CAPB at (a) pH 4; (b) pH 6; and (c) pH 8. Droplet distributions were normalized to 100 droplets and the number of droplets in each range is plotted as normalized intensity.

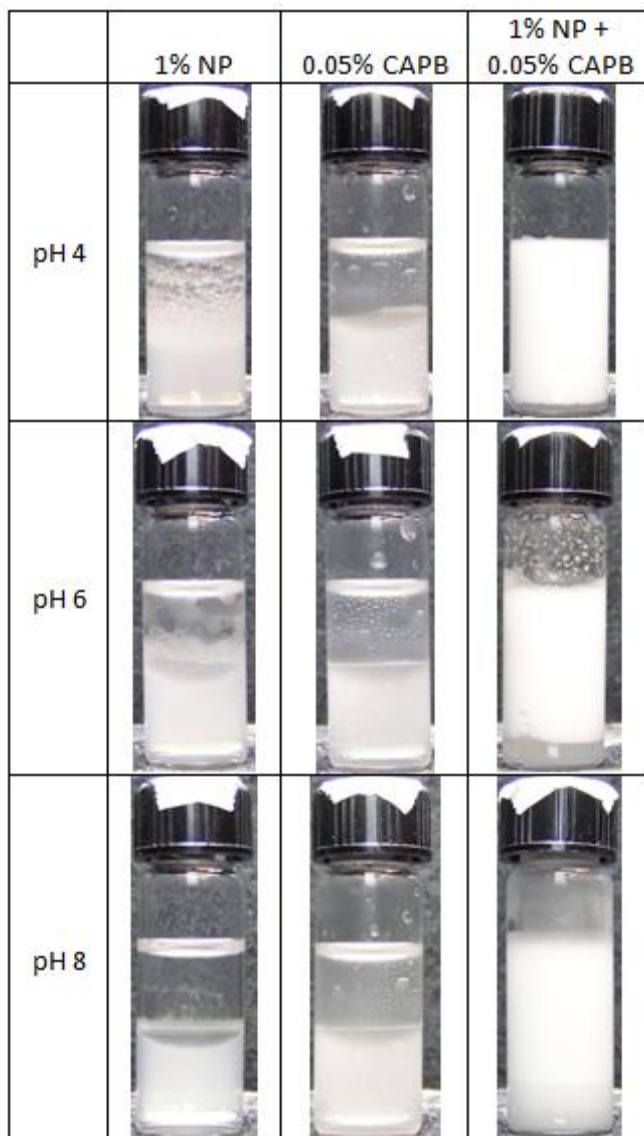


Figure 1.2.9. O/W emulsions prepared with 1:1 dodecane:water (by volume) stabilized at pH 4, 6, and 8 with 1% silica nanoparticles (NP), 0.05% CAPB, and 1% NP + 0.05% CAPB. Photographs taken 1 h after emulsion formation. The outside diameter of the vials is 1.47 cm.

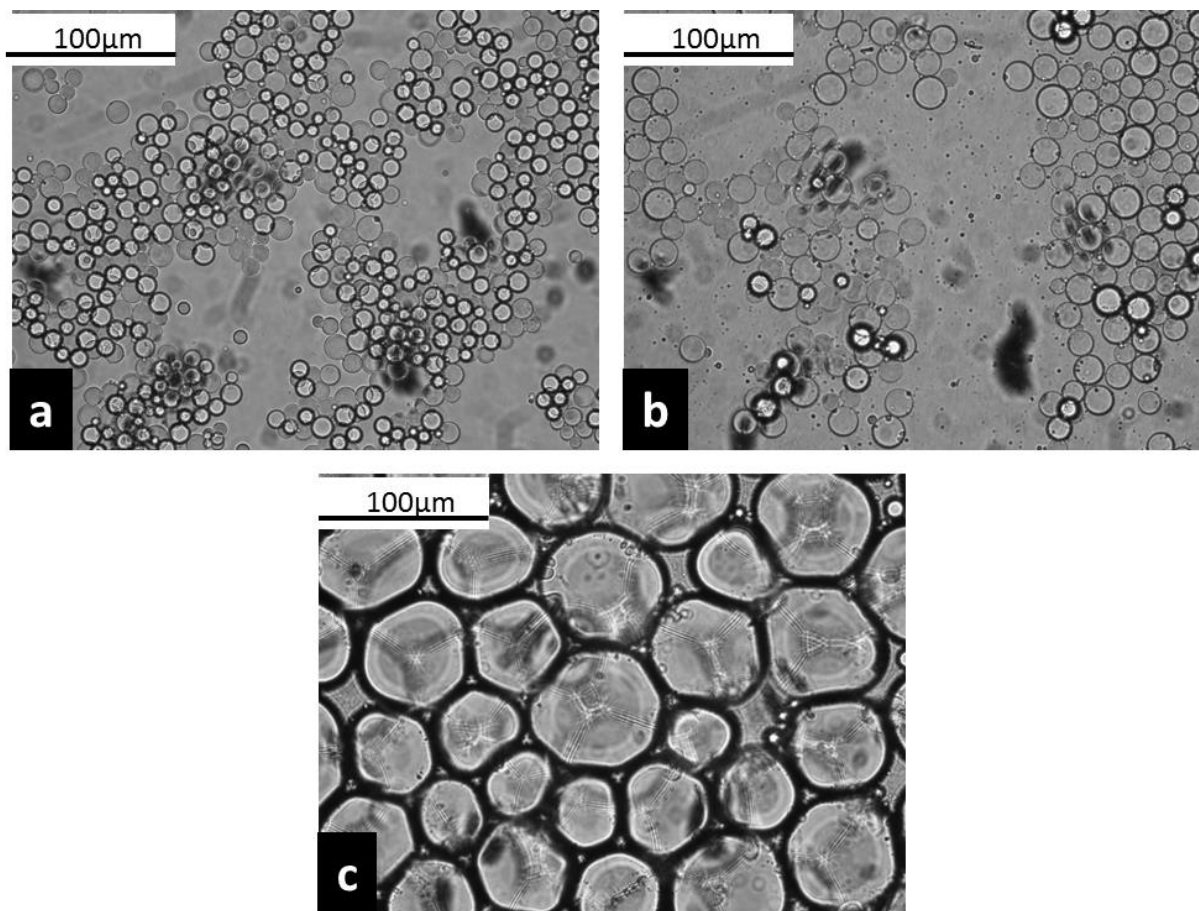


Figure 1.2.10. Optical Micrographs of emulsions stabilized with 1% silica nanoparticles (NP) + 0.05% CAPB at (a) pH 4; (b) pH 6; and (c) pH 8. Micrographs taken 1 day after emulsion formation.

1.2.6. Discussion

Nanoparticle and surfactant effect on CO₂-water IFT

Surfactants with the proper HCB can adsorb at the CO₂-water interface to reduce the interfacial tension. The surface pressure of the surfactant, Π_s , defined by $\gamma_o - \gamma$, where γ_o is the interfacial tension between CO₂ and water without surfactant, may be used to define the surfactant efficiency. In the present study, 0.25% (w/v) CAPB had a moderate surface pressure of 11.9 mN/m at 22°C and 6.65 MPa (CO₂ density of 0.772 g/mL). At CO₂ densities of 0.75~0.78 g/mL, Adkins et al.⁸ and Chen et al.⁴⁶ found Π_s in the range of 18 to 26 mN/m for several ethoxylated nonionic surfactants at concentrations of only 0.01%. The ethoxylated nonionic surfactants had molecular weights of 3x to 4x that of CAPB, which may contribute to greater Π_s values and

surfactant efficiencies. The poor efficiency of CAPB (low Π_s) may be a consequence of a very high HCB, reflecting limited solubilization by CO_2 of the hydrophobic tail compared to strong solubilization by water of the quaternary amine in the head group. The head group interactions include charge-dipole interactions as well as hydrogen bonding with the carboxylic acid. The amide group in the surfactant “tail” also has a hydrogen bond acceptor ($-\text{C}=\text{O}-$) and donor ($-\text{NH}-$)⁴⁷ and thus would also likely prefer to interact with water than CO_2 , contributing further to the high HCB. The efficiency of carboxybetaine surfactants at lowering interfacial tension is expected to be a function of pH, as protonation of the carboxylic acid group in the surfactant head group makes the surfactant cationic⁴⁸ and thus more hydrophilic. In a CO_2 -water saturated system, the pH would naturally fall below the pI of the surfactant for CO_2 /water systems and thus would always be in the higher HCB cationic form. In the presence of an excess CO_2 high pressure supercritical fluid phase, the CO_2 is a strong buffer and it becomes difficult to raise the pH above about 6 even with strong base.⁴⁹

When silica nanoparticles and betaine surfactant are used together in the aqueous phase, intermediate γ lowering is expected compared to a system without nanoparticles present. Bare silica nanoparticles alone are not expected to lower interfacial tension based on previous studies at the oil/water interface. (Vignati), although this phenomena is not fully understood. Nanoparticles coated with amphiphilic polymers may decrease γ , which has been observed in oil-water systems with iron oxide nanoparticles coated with copolymers of poly(acrylic acid) and poly(butyl acrylate)⁵⁰ and silica nanoparticles grafted with poly(styrene sulfonate)⁵¹ and poly(2-(dimethylamino)ethyl methacrylate).⁵² The polymers in these studies had molecular weights between 12 kDa and 30 kDa, and can interact with a large interfacial area to provide γ reduction. In the current work, surfactant that is not adsorbed to the silica nanoparticles would be free to adsorb at the CO_2 -water interface to lower the interfacial tension. The relative affinity of surfactant for adsorption at the CO_2 -water and silica-water interfaces would likely be a function of pH as well, where weak adsorption on the nanoparticles would leave more surfactant free to adsorb at the CO_2 -water interface to lower IFT.

Surfactant effect on contact angle

The contact angle between a nanoparticle surface (P) with CO_2 and water is controlled by the interfacial tensions between the three phases, as described by Young's Equation,

$$\cos \theta = \frac{\gamma_{PC} - \gamma_{PW}}{\gamma_{CW}} \quad (1.2.2)$$

where the nomenclature is shown in Figure 1.2.1. Silica surfaces contain deprotonated silanol groups (SiO⁻) above pH ~2. The surfaces are expected to have a high γ_{PC} and a low γ_{PW} because of the weak and strong solvency for charged species by CO₂ and water, respectively.³¹ If surfactant adsorbs on the silica surface such that the headgroup interacts with the negatively charged surface,^{42,54} the effective surface charge will be reduced and the surfactant hydrophobic tail will add hydrophobicity.

As there is great difficulty in accurately determining nanoparticle contact angles at fluid-fluid interfaces,^{53,54} this study used a flat silica surface as a model for the silica nanoparticle surfaces, following the method reported by Binks and coworkers.^{33,55} The experimentally observed increase in θ between CO₂/water/silica wafer with added surfactant (decrease in $\cos\theta$) indicates that the decrease in the numerator was larger than that in γ_{CW} . The decrease in $\gamma_{PC} - \gamma_{PW}$ with surfactant may be explained from the hydrophilicity. The adsorbed surfactant decreases the hydrophilicity (raises γ_{PW}). This change may be expected to reduce γ_{PC} and raise γ_{PW} as observed, but the individual changes in γ_{PC} and γ_{PW} are unknown.⁵⁶

The observed asymptotic trend in increasing zeta potential (Figure 1.2.4b) suggests that a surfactant bilayer or hemimicelle layer was not formed on the nanoparticle surface under the conditions investigated.²⁹ If so, we would have expected the zeta potential to become positive due to the added cationic surfactant head groups. The observed increase in θ on a flat silica surface and the absence of bilayer or hemimicelle formation suggest that the CO₂/water/nanoparticle surface θ increases monotonically with adsorbed surfactant under the conditions investigated.

Foam formation, texture, and viscosity

To form a CO₂ bubble or droplet, the external (shear) stress applied to the interface must exceed the Laplace pressure (P_c), where $P_c = 2\gamma/R$. The balance between the applied stress and P_c can be described by the Weber number,

$$We = \frac{G\mu_s R}{\gamma} \quad (1.2.3)$$

where G is the shear stress (du/dz), μ_s is the continuous phase shear viscosity, and R is the bubble radius.⁵⁷ Above a critical value of We , the shear breaks up the droplets into smaller ones.⁵⁷ The low γ of CO₂-water binary systems (20-30 mN/m) contributes to a larger We and may aid in the formation of smaller bubbles (fine texture foams) than for oil/water emulsions. The presence of nanoparticles and surfactant may further increase We by increasing μ_s and decreasing γ , respectively. Together, nanoparticle and surfactant mixed systems were shown to favor smaller bubbles (finer foams) than either nanoparticles or surfactant alone in Figure 1.2.5c. Once formed, nanoparticles and surfactant can adsorb on the bubble surfaces to sufficiently stabilize them for viscosity measurement and texture observation (~1 min).

There was a strong correlation between foam texture and viscosity in the present study, which is expected based on the work by several investigators.⁵⁸⁻⁶⁰ The formation of foam increases the apparent viscosity of a dispersed gas phase because of slugs of liquid between bubbles, resistance to deformation by the bubbles, and surface tension gradients across bubbles.⁵⁹ Finer foams have more lamellae and bubbles per unit length than coarser foams, and thus are expected to produce higher viscosities.

Foams tended to show higher viscosities in the beadpack than in the capillary, which may be due to several factors governing the foam rheology. Falls et al.⁶¹ discussed the influence of capillary pressure on the curvature of lamellae in porous media as well as the presence of pore constrictions which can add resistance to lamellae movement through the beadpack. Furthermore, foam formation is expected in the beadpack, where lamellae are continuously created by mechanisms such as leave-behind, snap-off, and lamella division.⁶ The shear rate is higher in the beadpack than in the capillary as well, and shear thickening behavior is often seen in foam flows, and is dictated by quality.⁶²

The viscosity and texture of the foams were influenced markedly by the presence of both the nanoparticles and the surfactant (Figure 1.2.6 and 7). The synergistic behavior of the mixed surfactant and nanoparticle system was evident in that neither the surfactant alone nor the nanoparticles generated foams. Similar synergy has been observed in terms of foam or emulsion formation in A/W³⁷ or O/W^{29,63} systems, respectively. For example, Cui et al.²⁹ used short fatty

acids with cationic CaCO_3 nanoparticles to generate toluene-in-water emulsions, whereas the nanoparticles or the shortest fatty acids alone were poor stabilizers. The synergistic emulsion formation was attributed to the *in situ* surface activation of the nanoparticle with adsorbed fatty acids, demonstrated by decreased zeta potential of the positively charge particles and increased θ of air/water/bulk CaCO_3 surface. The short fatty acids alone were not expected to significantly lower γ , but fine bubbles were generated due to the high G provided by a homogenizer. In the current study, the surfactant was effective at both *in situ* surface activation of the silica nanoparticles, as shown in the zeta potential, and in lowering γ , allowing for generation of finely textured foams with the low G provided by the sandpack.

We propose that the nanoparticle and surfactant adsorbed together at the CO_2 -water interface to allow foams to flow through the beadpack and capillary tube and be observed in the viewcell. A simplified configuration of the adsorbed species at the CO_2 -water interface is given in Figure 1.2.11a, which has been adapted from other investigators.^{29,55} The surfactant may either be free in water, independent of the nanoparticles at the CO_2 -water interface or adsorbed on the nanoparticle surface. The model is consistent with the decreased surface charge of the silica nanoparticles due to adsorption of the protonated carboxybetaine surfactant, increased contact angle of the *in situ* surface activated nanoparticles adsorbed at the CO_2 -water interface, and decreased γ due to surfactant adsorbed at the CO_2 -water interface. The model of the potential positions of the amphiphiles will be utilized below to explain the mechanisms responsible for the stabilization of the CO_2 -water interface.

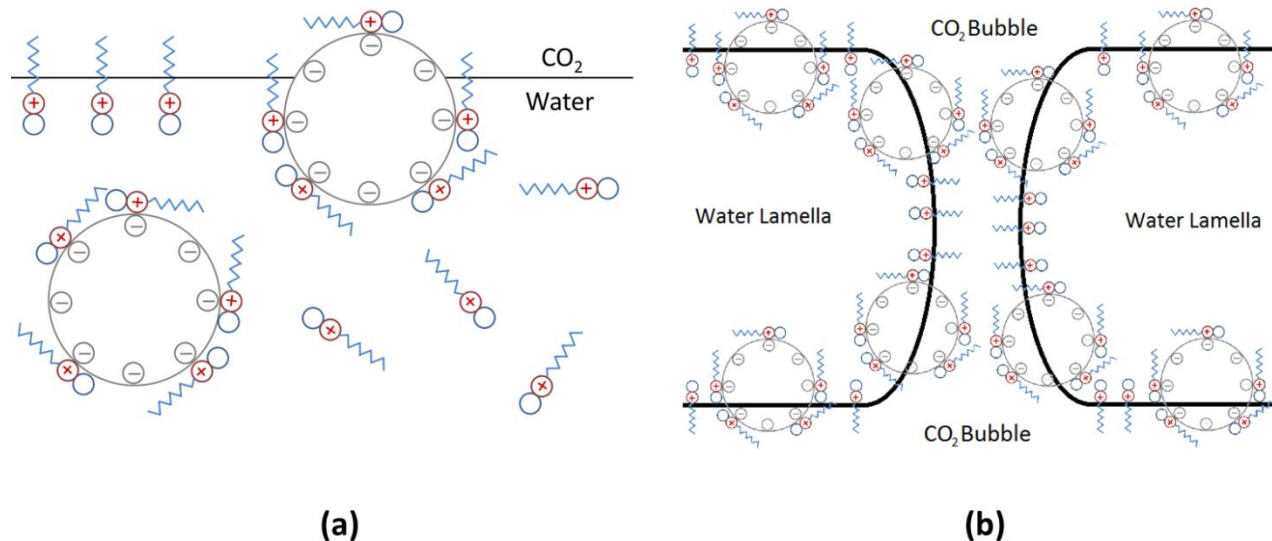


Figure 1.2.11. Simplified schematic of silica nanoparticles with protonated carboxybetaine surfactant at (a) a CO₂-water interface; (b) in an aqueous lamella between CO₂ bubbles connected by a CO₂ hole.

Stabilization mechanisms

Lamella drainage. In a C/W foam, aqueous lamellae separate CO₂ bubbles and prevent the bubbles from coalescing. The lamellae experience a disjoining pressure (Π_d)⁶⁴⁻⁶⁶ due to electrostatic, steric, structural, and additional short-range repulsive forces which counteract the van der Waals attraction between the two film surfaces.^{10,67} The cationic protonated CAPB and the anionic nanoparticles will contribute electrostatic repulsion to Π_d , however the opposite charges for the two amphiphiles will cause some cancellation of charge. The nanoparticles may also contribute to Π_d via structural effects that increase the osmotic pressure due to organization of particles in the lamella^{66,68,69} and contribute mechanical disjoining forces due to nanoparticle flocs “bridging” the lamellae.⁵⁴ The liquid in the lamellae drains due to gravity and capillary forces which reduces lamellae thickness. The contribution due to gravity is ignored in this discussion because of the relatively high density of CO₂ (0.776 g/mL), the small bubble size, and the fact the lamellae are very thin. The drainage due to capillary forces, described by Reynolds for the flow of liquid from between two approaching solid plates, may be expressed as

$$V_{RE} = \frac{-dh_f}{dt} = \left(\frac{h_f^3}{3\mu_c R_{film}^2} \right) \Delta P_{film} \quad (1.2.4)$$

where h_f is the film thickness, R_{film} is the film radius, and $\Delta P_{film} = 2(P_c - \Pi_d(h_f))$.⁷⁰ Thus, a decrease in P_c due to a reduction in γ with surfactant and an increased Π_d due to both nanoparticles and

surfactant may be expected to slow film drainage. Marangoni stabilization, which increases with gradients in γ ,⁷¹ may further provide resistance to flow and contribute to stabilization of lamellae. In the Reynolds Equation (Eqn. 1.2.4), the viscosity of the aqueous lamella (μ_c) is considered constant, which may be an oversimplification. Adsorbed nanoparticles may increase the interfacial viscosity,⁷²⁻⁷⁵ which may further slow lamella drainage and stabilize foams.^{74,76} Murray et al.⁷⁴ measured the interfacial viscosity of n-tetradecane/water interface and found a synergistic increase when both starch particles and sodium caseinate, an interfacially active protein, were adsorbed at the interface. The increase in interfacial viscosity due to adsorbed nanoparticles may slow diffusion of species near the interface, further contributing to stability. For example, an increase in interfacial viscosity could be beneficial in slowing Ostwald ripening, which can be significant in C/W foam destabilization due to the appreciable solubility of CO₂ in water.

Hole formation. Foams may be destabilized by coalescence due to hole formation in the aqueous lamellae separating bubbles. Holes appear because of thermal fluctuations that produce spatial and density variations in the film.^{77,78} Lamellae drainage acts to thin the aqueous lamellae, which reduces the work required to open a hole and increases the probability of hole formation.⁷⁹ If the radius of the hole exceeds a critical value, then the hole will grow and the foam film will rupture. Adkins et al.¹⁰ considered the formation of a CO₂ hole in a C/W/C film stabilized with a surfactant that prefers the aqueous phase. They proposed that the weak solvation of hydrocarbon tails by the CO₂ phase upon the start of hole formation would resist bending of the interface and arrest growth of the hole and prevent coalescence.

The nanoparticles in the present study also prefer the aqueous phase, and are also expected to resist bending of the interface to allow a CO₂ hole to form in lamellae. The adsorption energy, E, for a uniformly coated nanoparticle at a CO₂-water interface is given by

$$E = \pi r^2 \gamma (1 \pm \cos \theta)^2 \quad (1.2.5)$$

where r is the particle radius.²⁸ A 28 nm diameter particle at a CO₂-water interface with surfactant lowering γ to 17 mN/m would have an E = 10³ to 10⁴ kT, depending on θ . This energy would provide essentially irreversible adsorption to the CO₂-water interface and the orientation of the nanoparticle more towards the water side would provide a barrier to resist interface bending to produce a CO₂ channel curved about water on each side of the channel (Figure 1.2.11b). Quantitatively, bending of the interface to expose more nanoparticle surface to the CO₂

phase would be unfavorable, as changing θ by even 1° would require an energy of $10^1 \sim 10^2$ kT. Furthermore, this bending would expose more surfactant tails to CO_2 , which is also unfavorable. Thus, we propose that both the nanoparticles and surfactant would tend to resist hole formation via CO_2 -water interface bending about water.

1.2.7. Conclusions

Viscous and stable C/W foams with fine texture were generated with a nanoparticle (bare colloidal silica) and surfactant (caprylamidopropyl betaine) mixture and described in terms of the relevant interfacial phenomena that influence foam texture, viscosity, and stability. The foam formation was aided by interfacial tension (γ) reduction from the surfactant, while the foam stability may be expected to be augmented by adsorption of nanoparticles at the CO_2 -water interface. Electrostatic interactions between the cationic portion of the surfactant headgroup and the negatively charged silica surface facilitated adsorption of surfactant on the silica nanoparticles, reducing the HCB of the nanoparticles. The lower HCB increased adsorption at the CO_2 -water interface. The *in situ* surface activation of silica with adsorbed surfactant was characterized in terms of an increased zeta potential of the silica nanoparticles and an increased CO_2 /water/silica contact angle. The nanoparticle/ surfactant dispersion remained stable as demonstrated by DLS, as surfactant tail-tail interactions were too weak to cause flocculation of the nanoparticles. The adsorption of surfactant at the CO_2 -water interface did not lower the interfacial tension enough for foam formation. However, in the presence of the silica nanoparticles textured foams were formed with bubbles too small to be visible (<100 μm diameter with a maximum viscosity of 79 cP in the beadpack and 36 cP in the capillary tube. The surfactant and nanoparticles also imparted long term stability to the foam, where no resolution (by height) occurred in 20 h for the most stable foam observed. The stability was favored by various factors including an increase in disjoining pressure and interfacial viscosity, which mitigate lamella drainage and Ostwald ripening, and the unfavorable bending of the interface around the water phase, which resists hole formation.

1.2.8. References

1. Lake L. *Enhanced Oil Recovery*. Englewood Cliffs, NJ: Prentice Hall; 1989.

2. Heller JP. CO₂ foams in enhanced oil recovery. In: Schramm LL, ed. *Advances in Chemistry Series*. Vol 242 (Foams: Fundamentals and Applications in the Petroleum Industry). Washington, DC: American Chemical Society; 1994:201-234.
3. Orr FM, Jr., Heller JP, Taber JJ, Card RJ. Carbon dioxide as solvent for oil recovery. *Chemtech*. 1983;13(8):482-487.
4. Pope GA. The Application of Fractional Flow Theory to Enhanced Oil Recovery. *SPE Journal*. 1980;20(3):191-205.
5. Rossen WR, Gauglitz PA. Percolation theory of creation and mobilization of foams in porous media. *AIChE Journal*. 1990;36(8):1176-1188.
6. Rossen WR. Foams in Enhanced Oil Recovery. In: Prud'homme RK, Khan SA, eds. *Foams: Theory, Measurements, and Applications*. Vol 57. New York: Marcel Dekker; 1996.
7. Johnston KP, Da Rocha SRP. Colloids in supercritical fluids over the last 20 years and future directions. *Journal of Supercritical Fluids*. 2009;47:523-530.
8. Adkins SS, Chen X, Nguyen QP, Sanders AW, Johnston KP. Effect of branching on the interfacial properties of nonionic hydrocarbon surfactants at the air–water and carbon dioxide–water interfaces. *Journal of Colloid and Interface Science*. 2010;346(2):455-463.
9. Worthen AJ, Bagaria HG, Chen Y, Bryant SL, Huh C, Johnston KP. Nanoparticle-stabilized carbon dioxide-in-water foams with fine texture. *Journal of Colloid and Interface Science*. 2013;391(1):142-151.
10. Adkins SS, Chen X, Chan I, Torino E, Nguyen QP, Sanders AW, Johnston KP. Morphology and Stability of CO₂-in-Water Foams with Nonionic Hydrocarbon Surfactants. *Langmuir*. 2010/04/20 2010;26(8):5335-5348.
11. Eastoe J, Gold S, Steytler DC. Surfactants for CO₂. *Langmuir*. 2006;22(24):9832-9842.
12. Eastoe J, Paul A, Downer A, Steytler DC, Rumsey E. Effects of Fluorocarbon Surfactant Chain Structure on Stability of Water-in-Carbon Dioxide Microemulsions. Links between Aqueous Surface Tension and Microemulsion Stability. *Langmuir*. 2002;18:3014-3017.
13. Lee CT, Jr., Psathas PA, Ziegler KJ, Johnston KP, Dai HJ, Cochran HD, Melnichenko YB, Wignall GD. Formation of Water-in-Carbon Dioxide Microemulsions with a Cationic Surfactant: A Small-Angle Neutron Scattering Study. *Journal of Physical Chemistry B*. 2000;104(47):11094-11102.
14. Lee CT, Jr., Psathas PA, Johnston KP, DeGrazia J, Randolph TW. Water-in-Carbon Dioxide Emulsions: Formation and Stability. *Langmuir*. 1999;15(20):6781-6791.
15. Johnston KP, Cho D, da Rocha SRP, Psathas PA, Ryoo W, Webber SE, Eastoe J, Dupont A, Steytler DC. Water in Carbon Dioxide Macroemulsions and Miniemulsions with a Hydrocarbon Surfactant. *Langmuir*. 2001;17:7191-7193.
16. da Rocha SRP, Dickson JL, Cho D, Rossky PJ, Johnston KP. Stubby Surfactants for the Stabilization of Water and CO₂ Emulsions: Trisiloxanes. *Langmuir*. 2003;19:3114-3120.
17. Xing D, Wei B, Trickett K, Mohamed A, Eastoe J, Soong Y, Enick RM. CO₂-Soluble Surfactants for Improved Mobility Control. *SPE 129907, presented at SPE Improved Oil Recovery Symp., Tulsa, OK, Apr. 24-28*. 2010.
18. da Rocha SRP, Psathas PA, Klein E, Johnston KP. Concentrated CO₂-in-Water Emulsions with Nonionic Polymeric Surfactants. *J. Colloid Interface Sci*. 2001;239(1):241-253.
19. McLendon WJ, Koronaios P, McNulty S, Enick RM, Biesmans G, Miller A, Salazar L, Soong Y, Romanov V, Crandall D. Assessment of CO₂-Soluble Surfactants for Mobility

- Reduction using Mobility Measurements and CT Imaging. *SPE 154205, presented at SPE Improved Oil Recovery Symp., Tulsa, OK, Apr. 14-18. 2012.*
20. Lee HO, Heller JP. Laboratory measurements of CO₂-foam mobility. *SPE Reservoir Engineering.* 1990;5(2):193-197.
 21. Kuhlman MI, Falls AH, Hara SK, Monger-McClure TG, Borchardt JK. CO₂ Foam With Surfactants Used Below Their Critical Micelle Concentrations. *SPE Reservoir Engineering.* 1992;7(4):445-452.
 22. Kutay SM, Schramm LL. Structure/Performance Relationships for Surfactant and Polymer Stabilized Foams in Porous Media. *Journal of Canadian Petroleum Technology.* 2004;43(2):19-28.
 23. Adkins SS, Gohil D, Dickson JL, Webber SE, Johnston KP. Water-in-carbon dioxide emulsions stabilized with hydrophobic silica particles. *Physical Chemistry Chemical Physics.* 2007;9(48):6333-6343.
 24. Espinosa D, Caldelas F, Johnston KP, Bryant SL, Huh C. Nanoparticle-Stabilized Supercritical CO₂ Foams for Potential Mobility Control Applications. *SPE 129925, presented at SPE Improved Oil Recovery Symp., Tulsa, OK, Apr. 26-28. 2010.*
 25. Dickson JL, Binks BP, Johnston KP. Stabilization of Carbon Dioxide-in-Water Emulsions Using Silica Particles. *Langmuir.* 2004;20:7976-7983.
 26. Aveyard R, Binks BP, Clint JH. Emulsions Stabilised Solely by Colloidal Particles. *Advances in Colloid and Interface Science.* 2003;100-102:503-546.
 27. Golomb D, Barry E, Ryan D, Swett P, Duan H. Macroemulsions of Liquid and Supercritical CO₂-in-Water and Water-in-Liquid CO₂ Stabilized by Fine Particles. *Industrial & Engineering Chemistry Research.* 2006;45(8):2728-2733.
 28. Binks BP. Particles as surfactants - similarities and differences. *Current Opinion in Colloid and Interface Science.* 2002;7:21-41.
 29. Cui ZG, Cui CF, Zhu Y, Binks BP. Multiple Phase Inversion of Emulsions Stabilized by in Situ Surface Activation of CaCO₃ Nanoparticles via Adsorption of Fatty Acids. *Langmuir.* 2012/01/10 2011;28(1):314-320.
 30. Hunter TN, Wanless EJ, Jameson GJ, Pugh RJ. Non-ionic surfactant interactions with hydrophobic nanoparticles: Impact on foam stability. *Colloids and Surfaces A: Physicochemical and Engineering Aspects.* 2009;347(1-3):81-89.
 31. Dickson JL, Gupta G, Horozov TS, Binks BP, Johnston KP. Wetting Phenomena at the CO₂/Water/Glass Interface. *Langmuir.* 2006;22(5):2161-2170.
 32. Vignati E, Piazza R, Lockhart TP. Pickering Emulsions: Interfacial Tension, Colloidal Layer Morphology, and Trapped-Particle Motion. *Langmuir.* 2003/08/01 2003;19(17):6650-6656.
 33. Binks BP, Rodrigues JA, Frith WJ. Synergistic Interaction in Emulsions Stabilized by a Mixture of Silica Nanoparticles and Cationic Surfactant. *Langmuir.* 2007;23(7):3626-3636.
 34. Lan Q, Yang F, Zhang S, Liu S, Xu J, Sun D. Synergistic effect of silica nanoparticle and cetyltrimethyl ammonium bromide on the stabilization of O/W emulsions. *Colloids and Surfaces A: Physicochemical and Engineering Aspects.* 2007;302(1-3):126-135.

35. Ravera F, Ferrari M, Liggieri L, Loglio G, Santini E, Zanobini A. Liquid–liquid interfacial properties of mixed nanoparticle–surfactant systems. *Colloids and Surfaces A: Physicochemical and Engineering Aspects*. 2008;323(1–3):99-108.
36. Binks BP, Rodrigues JA. Double Inversion of Emulsions By Using Nanoparticles and a Di-Chain Surfactant. *Angewandte Chemie*. 2007;119(28):5485-5488.
37. Cui ZG, Cui YZ, Cui CF, Chen Z, Binks BP. Aqueous Foams Stabilized by in Situ Surface Activation of CaCO₃ Nanoparticles via Adsorption of Anionic Surfactant. *Langmuir*. 2010/08/03 2010;26(15):12567-12574.
38. Akartuna I, Studart AR, Tervoort E, Gonzenbach UT, Gauckler LJ. Stabilization of Oil-in-Water Emulsions by Colloidal Particles Modified with Short Amphiphiles. *Langmuir*. 2008/07/01 2008;24(14):7161-7168.
39. Binks BP, Rodrigues JA. Enhanced Stabilization of Emulsions Due to Surfactant-Induced Nanoparticle Flocculation. *Langmuir*. 2007/07/01 2007;23(14):7436-7439.
40. Jiang T, Hirasaki GJ, Miller CA, Ng S. Wettability Alteration of Clay in Solid-Stabilized Emulsions. *Energy & Fuels*. 2011/06/16 2011;25(6):2551-2558.
41. Partyka S, Lindheimer M, Faucompre B. Aggregate formation at the solid–liquid interface: The calorimetric evidence. *Colloids and Surfaces A: Physicochemical and Engineering Aspects*. 1993;76(0):267-281.
42. Mannhardt K, Schramm LL, Novosad JJ. Effect of Rock Type and Brine Composition on Adsorption of Two Foam-Forming Surfactants *SPE Advanced Technology Series*. 1993;1(1):212-218.
43. Mannhardt K, Novosad JJ, Jha KN. Adsorption of Foam-forming Surfactants In Berea Sandstone. *Journal of Canadian Petroleum Technology*. 1994;33(2):34-43.
44. Lv W, Bazin B, Ma D, Liu Q, Han D, Wu K. Static and dynamic adsorption of anionic and amphoteric surfactants with and without the presence of alkali. *Journal of Petroleum Science and Engineering*. 2011;77(2):209-218.
45. Levinson MI. Surfactant Production: Present Realities and Future Perspectives. In: Zoller U, Sosis P, eds. *Handbook of Detergents Part F: Production*. Boca Raton, FL: Taylor & Francis Group, LLC; 2009:1-36.
46. Chen X, Adkins SS, Nguyen QP, Sanders AW, Johnston KP. Interfacial tension and the behavior of microemulsions and macroemulsions of water and carbon dioxide with a branched hydrocarbon nonionic surfactant. *The Journal of Supercritical Fluids*. 2010;55(2):712-723.
47. Johansson A, Kollman P, Rothenberg S, McKelvey J. Hydrogen bonding ability of the amide group. *Journal of the American Chemical Society*. 1974/06/01 1974;96(12):3794-3800.
48. Lomax EG, ed *Amphoteric Surfactants*. 2nd ed. New York: Marcel Dekker, Inc.; 1996. Surfactant Science Series.
49. Holmes JD, Ziegler KJ, Audriani M, Lee Jr. CT, Bhargava PA, Steytler DC, Johnston KP. Buffering the Aqueous Phase pH in Water-in-CO₂ Microemulsions. *J. Phys. Chem. B*. 1999;103:5703-5711.
50. Yoon KY, Li Z, Neilson BM, Lee W, Huh C, Bryant SL, Bielawski CW, Johnston KP. Effect of Adsorbed Amphiphilic Copolymers on the Interfacial Activity of Superparamagnetic

- Nanoclusters and the Emulsification of Oil in Water. *Macromolecules*. 2012/06/26 2012;45(12):5157-5166.
51. Saleh N, Sarbu T, Sirk K, Lowry GV, Matyjaszewski K, Tilton RD. Oil-in-Water Emulsions Stabilized by Highly Charged Polyelectrolyte-Grafted Silica Nanoparticles†. *Langmuir*. 2005/10/01 2005;21(22):9873-9878.
 52. Saigal T, Dong H, Matyjaszewski K, Tilton RD. Pickering Emulsions Stabilized by Nanoparticles with Thermally Responsive Grafted Polymer Brushes. *Langmuir*. 2010/10/05 2010;26(19):15200-15209.
 53. Binks BP, Murakami R. Phase inversion of particle-stabilized materials from foams to dry water. *Nature Materials*. 2006;5(11):865-869.
 54. Hunter TN, Pugh RJ, Franks GV, Jameson GJ. The role of particles in stabilising foams and emulsions. *Advances in Colloid and Interface Science*. 2008;137(2):57-81.
 55. Binks BP, Kirkland M, Rodrigues JA. Origin of stabilisation of aqueous foams in nanoparticle-surfactant mixtures. *Soft Matter*. 2008;4(12):2373-2382.
 56. Binks BP, Clint JH. Solid Wettability from Surface Energy Components: Relevance to Pickering Emulsions. *Langmuir*. 2002;18:1270-1273.
 57. Walstra P, Smulders PEA. Emulsion Formation. In: Binks BP, ed. *Modern Aspects of Emulsion Technology*. Cambridge: The Royal Society of Chemistry; 1998:56-99.
 58. Otsubo Y, Prud'homme RK. Rheology of oil-in-water emulsions. *Rheologica Acta*. 1994;33(1):29-37.
 59. Hirasaki GJ, Lawson JB. Mechanisms of Foam Flow in Porous Media: Apparent Viscosity in Smooth Capillaries. *Society of Petroleum Engineers Journal*. 1985:176-190.
 60. Pal R. Effect of droplet size on the rheology of emulsions. *AIChE Journal*. 1996;42(11):3181-3190.
 61. Falls AH, J. J. Musters, and J. Ratulowski. The Apparent Viscosity of Foams in Homogeneous Bead Packs. *SPE Reservoir Engineering*. 1989;4(55):155-164.
 62. Alvarez JM, Rivas HJ, Rossen WR. Unified Model for Steady-State Foam Behavior at High and Low Foam Qualities. *SPE Journal*. 2001;6(3):325-333.
 63. Midmore BR. Preparation of a novel silica-stabilized oil/water emulsion. *Colloids and Surfaces A: Physicochemical and Engineering Aspects*. 1998;132(2-3):257-265.
 64. Derjaguin BV, Churaev NV. Structural component of disjoining pressure. *Journal of Colloid and Interface Science*. 1974;49(2):249-255.
 65. Aronson AS, Bergeron V, Fagan ME, Radke CJ. The influence of disjoining pressure on foam stability and flow in porous media. *Colloids and Surfaces A: Physicochemical and Engineering Aspects*. 1994;83(2):109-120.
 66. Stubenrauch C, von Klitzing R. Disjoining pressure in thin liquid foam and emulsion films—new concepts and perspectives. *Journal of Physics: Condensed Matter*. 2003;15(27):R1197-R1232.
 67. Aveyard R, Binks BP, Esquena J, Fletcher PDI, Bault P, Villa P. Flocculation Transitions of Weakly Charged Oil-in-Water Emulsions Stabilized by Different Surfactants. *Langmuir*. 2002;18(9):3487-3494.
 68. Chengara A, Nikolov AD, Wasan DT, Trokhymchuk A, Henderson D. Spreading of nanofluids driven by the structural disjoining pressure gradient. *Journal of Colloid and Interface Science*. 2004;280(1):192-201.

69. Wasan D, Nikolov A. Thin liquid films containing micelles or nanoparticles. *Current Opinion in Colloid & Interface Science*. 2008;13(3):128-133.
70. Langevin D. Influence of interfacial rheology on foam and emulsion properties. *Advances in Colloid and Interface Science*. 2000;88(1,2):209-222.
71. Lucassen-Reynders EH, Cagna A, Lucassen J. Gibbs elasticity, surface dilational modulus and diffusional relaxation in nonionic surfactant monolayers. *Colloids and Surfaces, A: Physicochemical and Engineering Aspects*. 2001;186(1-2):63-72.
72. Wasan DT, Gupta L, Vora MK. Interfacial shear viscosity at fluid-fluid interfaces. *AIChE Journal*. 1971;17(6):1287-1295.
73. Lishchuk SV, Halliday I. Effective surface viscosities of a particle-laden fluid interface. *Physical Review E*. 2009;80(1):016306.
74. Murray BS, Durga K, Yusoff A, Stoyanov SD. Stabilization of foams and emulsions by mixtures of surface active food-grade particles and proteins. *Food Hydrocolloids*. 2011;25(4):627-638.
75. Wijmans CM, Dickinson E. Simulation of Interfacial Shear and Dilatational Rheology of an Adsorbed Protein Monolayer Modeled as a Network of Spherical Particles. *Langmuir*. 1998/12/01 1998;14(25):7278-7286.
76. Pugh RJ. Experimental techniques for studying the structure of foams and froths. *Advances in Colloid and Interface Science*. 2005;114–115(0):239-251.
77. Kabalnov A, Wennerstrom H. Macroemulsion Stability: The Oriented Wedge Theory Revisited. *Langmuir*. 1996;12:276-292.
78. Vrij A, Overbeek JTG. Rupture of thin liquid films due to spontaneous fluctuations in thickness. *Journal of the American Chemical Society*. 1968/06/01 1968;90(12):3074-3078.
79. Babak VG, Stebe M-J. Highly concentrated emulsions: Physicochemical principles of formulation. *Journal of Dispersion Science and Technology*. 2002;23(1-3):1-22.

II. Foam Generation and Transport – Modeling and Simulations

This section outlines our modeling work on (i) simulating core-scale NP-C/W foam generation and displacement experiments, and (ii) predictive modeling of foam formation and its effect on the volumetric sweep efficiency and CO₂ flood conformance in field scale problems.

II.1. Core-scale NP-C/W foam generation and transport – Full-physics model

The results of this mathematical modeling study were incorporated in a technical manuscript that was submitted to the Journal of Transport in Porous Media:

Prigiobbe, Valentina et al. “Transport of nanoparticle-stabilized CO₂-foam in porous media” (2015) – Transport in Porous Media – *In review*.

II.1.1. Abstract

Foam is injected in the subsurface to improve mobility control through the increase of the effective gas viscosity, e.g., in CO₂-based enhanced oil recovery processes. As fine textured foam has higher viscosity, it is envisaged to achieve an optimal foam texture and to maintain it for the entire period of an application. However, mechanisms of foam formation and destruction, which affect texture, are difficult to regulate.

In this study, we investigate the synergic effect of nanoparticles and surfactant on the foam texture and the effective gas viscosity (μ_{fg}) during transport in a porous medium. Experiments using glass-bead packs were performed injecting CO₂ and a solution containing either only surfactant or surfactant and nanoparticles. During each experiment the pressure drop (Δp) through the porous medium was measured to follow the generation of the foam. A two-phase flow mechanistic model combining the mass conservation law for water and CO₂ and the population balance equation (PBE) of the lamellae

was used to analyze the experiments and predict foam transport under the investigated conditions. The constitutive equations for foam generation and destruction were based on the dominant role of pressure gradient on lamella division and of capillary pressure on bubble coalescence and their parameters were estimated using pressure drop measurements. The

experiments compare well with the theory showing that a foam stabilized with nanoparticles and surfactant can be modeled as a surfactant-stabilized foam. Overall, Δp increases smoothly while the foam forms and, upon breakthrough, it stabilizes around a constant value while approaching steady state. During this phase oscillations occur, particularly when high quality foam is generated as the system is close to its critical conditions of capillary pressure and water saturation. When steady state is reached, the effective gas viscosity varies with f_g and solution composition and significantly increases when surfactant and nanoparticles are added. The maximum value of μ_{fg} is 0.110 Pa·s for $f_g = 0.75$, which is almost two-folds of the maximum value attained when only a surfactant is used, corresponding to 0.067 Pa·s at $f_g = 0.4$. This suggests that when nanoparticles and surfactant are employed, they can favor the formation of a strong high-quality CO₂-foam.

II.1.2. Introduction

Foam is a complex fluid, where a gas phase is dispersed within a liquid phase as bubbles, which are separated by thin films (called lamellae). The density of the lamellae gives to the foam its texture (n_f) and its flow properties. The larger the n_f the finer the foam texture and the lower is the gas mobility [26]. A foam is thermodynamically unstable, but its spontaneous decay can be reduced using either surface-tension reducing substances, such as surfactant, or coalescence-preventing substances, such as nanoparticles, making it metastable within the purpose of the application.

Foam injection into the subsurface is employed principally in enhanced oil recovery (EOR) [27,36] and contaminated aquifer remediation [17,30,49,28], where the mobility control of a gas is critical for the performance of the overall operation. In comparison to a gas, a foam has higher viscosity and higher density and penetrates more uniformly into low permeability layers mitigating the effect of reservoir heterogeneity [37]. Generally in EOR, carbon dioxide (CO₂) is used because allows high oil recovery efficiency through swelling and viscosity reduction of the oil [32,27]. However, the injection of CO₂ has the drawback of high buoyancy, viscous fingering, and channeling through high permeability layers, which determine low process efficiency. To overcome these problems, CO₂ is injected as a foam [36].

During the transport in porous media, gas bubbles in a conventional surfactant-stabilized foam undergo a continuous formation and destruction, which are regulated by mechanisms at the pore scale. As a fine textured foam (large n_f) is desired, techniques have been tested to enhance foam generation and reduce foam destruction. At this aim, surfactant are added to the liquid phase. They adsorb at the gas-liquid interface reducing the interfacial tension, increasing the disjoining pressure in the lamellae, and slow drainage to maintain thicker films [26,7,8]. Thus, surfactants increase the stability of foams by mitigating processes such as coalescence and Ostwald ripening. Nevertheless, even the best formulation has the disadvantage that the surfactant can desorb from the interface and adsorb onto the porous medium surface, leaving behind a coarse foam.

Studies have shown that by adding particles to a bulk foam its stability can be considerably increased [34]. Experiments of transport of CO₂-foam in a porous medium have also demonstrated that nanoparticles enhance foam stability [15,46,4,47]. Upon foam generation, nanoparticles are adsorbed at the CO₂-liquid interface preserving the foam texture (bubble size) [42]. They form layers creating an armor which reduces the drainage within the lamella and the gas diffusion through the thin film [10,38,19], and simultaneously increase the maximum capillary pressure (P_c , difference between the gas and the liquid phase at the bubble interface) providing a barrier for bubble coalescence [23, 20,8]. The effect of particle stabilization is influenced by particle size, particle shape, particle concentration, contact angle, and interactions between particles. These properties affect the adsorption energy which can reach several thousand kT , where k is the Boltzmann constant and T is the absolute temperature, making the adsorption of the nanoparticle practically irreversible, in contrast to surfactant [10,7]. Another factor particular to nanoparticle-stabilized foams is the potential for particles to aggregate, increasing their size, and therefore reducing their effect as they can be retained due to straining within of the porous medium [45,4]. Key factors are the hydrophobicity of the nanoparticles surface and the solution composition [40]. Negatively charged nanoparticles behave more hydrophobically in high salinity water, resulting in larger adsorption, however they might also aggregate due to the reduced inter-particle repulsive forces [14,46,47]. Recent research has therefore focused on the use of particles at the nanoscale with engineered surface coating to enhance particle adsorption and minimize particle aggregation. Moreover, combination of nanoparticles with surfactant has shown to mitigate this effect in emulsion and CO₂-foam creating even in the presence of particle

aggregation stable fine bubbles [11,48,43,44]. A schematic representation of geometrical configurations for particles and surfactant at the bubble interface is given in Figure II.1.1.

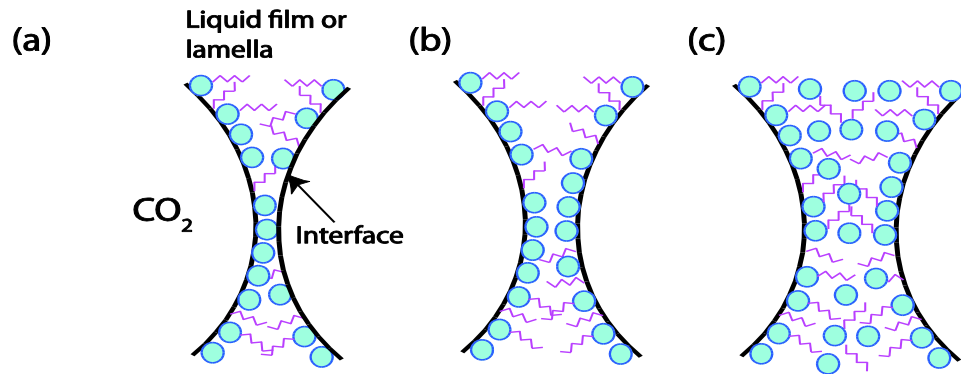


Fig. II.1.1 Scheme of nanoparticles (blue circles) and surfactant (red line segments) at the CO₂-liquid interface. The picture shows the synergy between nanoparticles and surfactant, i.e., surfactants attaching to the nanoparticles enhance their adsorption at the interface. (a) Monolayer, (b) bilayer, and (c) particle network. The curvature of the interface has been exaggerated for the sake of the illustration.

In this paper, we present an experimental and modeling work to study the synergic effect of nanoparticles and surfactant on the transport of a foam through porous media. Upon optimization of pressure difference measurements through the columns, we determined the effective gas viscosity and the behavior of the CO₂-foam. We analyzed the evolution of its texture and the change of the effective gas viscosity as a function of solution composition and foam quality (fg, defined as the ratio between the gas flux and the total flux). A two-phase flow mechanistic model coupling population balance equation (PBE) of lamellae density with the fractional flow equations was used to analyze the experiments. The modeling approach was chosen on earlier fundamental studies (e.g., [25,22,5,6]) aimed at understanding the effect of surfactant formulation and concentration in various foam systems. They all implemented PBE models to gain a physical insight into the mechanisms underlying the generation and the destruction phenomena. Through the inversion of pressure drop measurements, model parameters were estimated and the evolution of the foam texture and effective gas viscosity were calculated.

The article is divided in five sections. In section 2, the materials and the methods to perform the experiments are described. In section 3, the foam transport model is explained. In section 4, the experimental results are reported, and then discussed within the mathematical framework of the model. Finally, in section 5, the conclusions are drawn.

II.1.3. Materials and Methods

Surface-modified colloidal silica nanoparticles (EOR-5XS, Nissan Chemical Co., U.S.A.) were provided as a 20 % by weight aqueous dispersion. The measured average diameter with dynamic light scattering was 6 nm. The surfactant solution provided by Rhodia (Mackam DAB-ULS, U.S.A.) was approximately 35 % betaines (i.e., 24 % lauramidopropyl betaine (LAPB), 9.5 % myristamidopropyl betaine, 1 % palmitamidopropyl betaine, and < 1 % capramidopropyl betaine). This composition was used for surfactant concentration calculations. The solution also contained < 0.5 % NaCl, which is a byproduct of the betaine synthesis. Carbon dioxide (Coleman-grade, 99.99 % purity, Matheson, U.S.A.) and deionized (DI) water (Nanopure II, Barnstead, U.S.A.) were used for all experiments. The suspension of nanoparticles was added to the system through an accumulator (HiP, U.S.A.). All materials were used without further purification. The dispersions of nanoparticles with surfactant in water were prepared by adding nanoparticle dispersions to dilute solutions of LAPB. The NaCl from the LAPB solution added a maximum of 0.0006 % NaCl (ca. 0.1 mM NaCl) to the nanoparticle dispersions for a surfactant concentration 0.04 %. The nanoparticle and surfactant mixtures were pH~8 before CO₂ was added. Throughout this work, the surfactant, particle, and NaCl concentrations are all given in % w/v in the aqueous phase and they are shown throughout this article simply as % for brevity. Figure II.1.2 shows a scheme of the set-up used to perform the experiments. Here, mixtures of nanoparticle and surfactant and liquid CO₂ were injected through the system using an accumulator and a pump (Teledyne ISCO Inc., U.S.A.), respectively. Rather than using only one backpressure regulator (BPR) as in our previous studies [43,42], two BPRs (Swagelok model SS-4R3A adjustable relief valve, heated to over 75 °C with water bath) were instead connected in series for controlling the system's pressure (reported by the pressure at the upstream BPR) to prevent CO₂ liquid formation. All experiments were carried out at 2800 psia (19.31 MPa) and 50°C with system pressure maintained within 50 psi (345 KPa). The pressure gradient caused by the flow of foam through the porous medium was measured with a differential pressure transducer (Validyne Engineering Corp., U.S.A.), attached to the upstream and downstream sides of the bead pack. From manufacturer's information, the accuracy of the differential pressure reading is ± 0.25% of full scale. Two types of glass-bead packs were employed. A first one of internal diameter 1.63 cm and length 12.42 cm, filled with 30–50 µm spherical glass beads, with

permeability of 1.2 D ($1.2 \cdot 10^{-12} \text{ m}^2$) and porosity and pore volume of 0.36 and 9.4 mL, respectively. A second one of internal diameter 0.38 cm and length 11.30 cm, filled with 180 μm spherical glass beads, with permeability of 22.5 D ($22.5 \cdot 10^{-12} \text{ m}^2$) and porosity and pore volume of 0.35 and 0.436 mL, respectively. Moreover, in the first type of bead pack, a flow rate of 4.5 mL/min gave a total flux of 102 ft/day ($3.60 \cdot 10^{-4} \text{ m/s}$) and a residence time of 125 s. In the second type of bead pack, a flow rate of 0.5 mL/min gave a total flux of 208 ft/day ($7.34 \cdot 10^{-4} \text{ m/s}$) and a residence time of 52 s. These flow characteristics were selected as they can be found in field applications near the injection well, where most foam generation is expected.

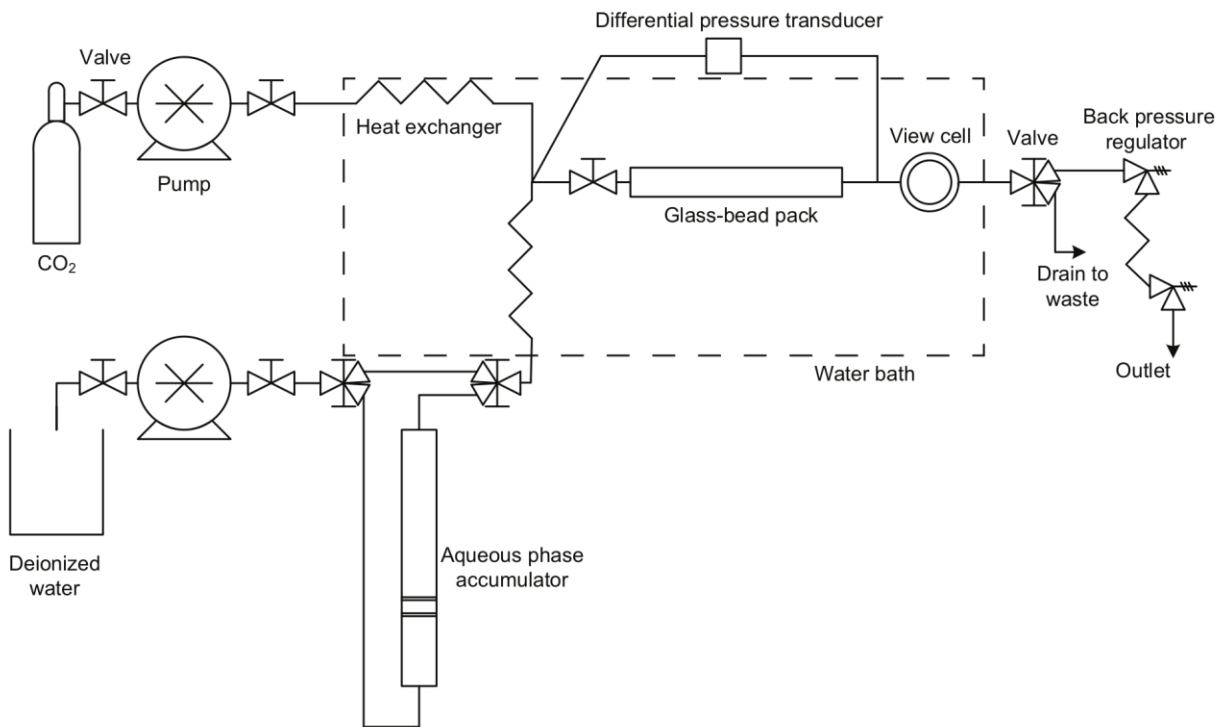


Fig.II.1. 2 Diagram of the experimental set-up.

II.1.4. Foam transport model

Governing equations: Assuming surfactant and nanoparticles do not adsorb onto the surface of the porous medium (i.e., a conservative tracer behavior) and an incompressible isothermal two-phase (CO_2 and water) flow, the fractional flow equation for water saturation (S_w , (-)) and the population balance for the density of the lamellae (n_f , #/m³) are [25,22]

$$\phi \frac{\partial S_w}{\partial t} + u_t \frac{\partial f_w}{\partial x} = 0 \quad (\text{II.1.1})$$

$$\phi \frac{\partial(S_g n_f)}{\partial t} + u_t \frac{\partial(f_g n_f)}{\partial x} = \phi S_g (r_g - r_c) \quad (\text{II.1.2})$$

on $0 < x < L$ and for $t > 0$, where L is the length of the domain (m); Φ is the porosity (-); u_t is the total flux (m/s) given by the sum of the liquid and gas fluxes, i.e., u_w and u_g , respectively; S_g is the gas saturation equal to $1 - S_w$; r_g and r_c are the rates of generation and destruction of the foam lamellae ($\#/(m^3s)$), respectively; f_w is the fractional flow of the liquid phase (-) (with $f_g = 1 - f_w$ indicating the foam quality). Fractional flow is related to the fluid phase mobilities by

$$f_w = \frac{k_{rw}/\mu_w}{k_{rw}/\mu_w + k_{rg}/\mu_g^f} \quad (\text{II.1.3})$$

with k_{rw} and k_{rg} the relative permeability of the liquid and gas phases, respectively, which we assumed of Corey type [27]

$$k_{rw} = c_w \left(\frac{S_w - S_{wc}}{1 - S_{wc} - S_{gr}} \right)^{e_w} \quad (\text{II.1.4})$$

$$k_{rg} = c_g \left(\frac{1 - S_w - S_{gr}}{1 - S_{wc} - S_{gr}} \right)^{e_g} \quad (\text{II.1.5})$$

with the coefficients equal to unity and the exponents equal to 2 applicable for unconsolidate sand packs [13]; S_{wc} and S_{gr} the connate water saturation and the residual gas saturation (-), respectively; μ_w the water viscosity (Pa·s); and μ_g^f the effective gas viscosity (Pa·s) [18]

$$\mu_g^f = \mu_g^0 + C_f \frac{n_f}{\sqrt[3]{u_g/\phi S_g}} \quad (\text{II.1.6})$$

where C_f is a model parameter (Pa·m³). The liquid and gas fluxes, u_w and u_g , are given by the Darcy's law for the liquid and gas phases

$$u_w = - \frac{k k_{rw}}{\mu_w} \nabla P_w \quad (\text{II.1.7})$$

$$u_g = - \frac{k k_{rg}}{\mu_g^f} (\nabla P_w - \nabla P_c) \quad (\text{II.1.8})$$

where k is the permeability of the porous medium (m^2); ∇P_w is the pressure gradient of the liquid phase (Pa/m); and ∇P_c is the gradient of the capillary pressure (Pa/m), which was neglected as it is much smaller than ∇P_w . Therefore, throughout this article ∇p_w is identified as ∇p for simplicity. The constitutive equations for r_g and r_c , which account for the mechanisms of foam generation and destruction at the pore scale, are introduced under constitutive equations presented below.

A finite volume scheme was developed to discretize the nonlinear system of eqs. 1 and 2, approximated with a forward upstream-weighted solution, and integrated explicitly [21]. The domain was divided into a grid of N_x cells with length $\Delta x = L/N_x$.

Constitutive equations: Rate of generation. In a bulk foam, a bubble forms when the shear stress exceeds the Laplace pressure of the bubble. When a foam flows through a porous medium, additional mechanisms are present, namely: lamella leave-behind, gas-bubble snap-off, and lamella division [35,36]. While the former creates a coarse foam (small n_f) which is largely controlled by the flow velocity, the latter mechanisms are responsible for the formation of a strong foam (large n_f) and are regulated by the pressure gradient [16,41]. In the application of interest, where strong foam is required, snap-off and lamella division are the most important generation phenomena. Gauglitz et al. [16] observed that a minimum pressure gradient (∇P^{min}) exists for the transition from weak or coarse foam to strong foam, which is inversely proportional to the permeability. However, contrary to a N_2 -foam, a surfactant-stabilized CO_2 -foam presents a negligible ∇P^{min} and can form even at low pressure gradients [16]. Moreover, experiments reported by Yu et al. [47] suggest that in the presence of nanoparticles foam generation is still governed by pressure gradient. On the basis of these observations, we formulated the rate of generation as [22]

$$r_g = C_g \nabla P^m \quad (II.1.9)$$

where C_g and m are two model parameters.

Rate of destruction. In bulk, foam is destabilized due to drainage of liquid within the lamella because of capillary suction (coalescence), which occurs after film thinning to a critical level and hole formation as well as gas diffusion from small to large bubbles [31]. For a foam migrating

through a porous medium, experimental observations suggest that the dominant mechanism is the former [12]. Coalescence is a spontaneous process of thin film rupture, which is regulated by capillary pressure and foam quality. During the displacement of a bubble through the pores, P_c increases reaching its critical value (P_c^*). Therefore, several lamellae rupture within the foam simultaneously, the foam becomes coarser, and P_c decreases. During the displacement of the coarse foam, P_c increases again. It is this process of lamellae rupture and coarse foam displacement which maintains the capillary pressure around its limiting value [24]. In the presence of particles stabilizing a foam, the capillary pressure still controls the coalescence mechanism of a bubble and its value depends on particle properties and particle arrangement within the lamella [23]. Large positive value of P_c^* ensures that a thin liquid film between the bubbles of a foam can withstand a higher pressing force. Considering the Leveret J-function [29] which relates P_c to S_w , the rate of coalescence can be formulated as [1], i.e.,

$$r_c = C_c n_f \left(\frac{S_w}{S_w - S_w^*} \right)^n \quad (\text{II.1.10})$$

where S_w^* is the minimum water saturation value corresponding to P_c^* for which the lamella ruptures, while C_c and n are two model parameters.

II.1.4. Results and discussion

In this section, the experimental results are reported. Initially, preliminary tests were performed to select optimal conditions. Then, the column-flood experiments were carried out systematically changing the concentration of nanoparticles and foam quality to study their effect on foam texture and effective gas viscosity. The geometry of the two glass-bead packs employed in this study together with the physical properties of the system and the general operating conditions applied during the experiments are listed in Table II.1.1.

Table II.1.1 Geometry of the two glass-bead packs, general operating conditions applied during the experiments, and physical properties of the system. Symbols indicate: A, the cross sectional area of the columns; Q, the flow rate; c_s and c_n , the surfactant and nanoparticle concentrations, respectively.

L , m	0.12	0.11
A , m ²	$2 \cdot 10^{-4}$	$1.13 \cdot 10^{-5}$
ϕ , (-)	0.36	0.35
k , m ²	$1.2 \cdot 10^{-12}$ (1.2 D)	$22.5 \cdot 10^{-12}$ (22.5 D)
Q , ml/min	4.50	$3.00^a/0.50$
T , °C	50	50
p at the outlet, MPa	19	19
u_t , m/s	$3.60 \cdot 10^{-4}$	$4.41 \cdot 10^{-3a}/7.34 \cdot 10^{-4}$
u_g , m/s	$1.44-3.24 \cdot 10^{-4}$	$3.31 \cdot 10^{-3a}/3.67-6.97 \cdot 10^{-4}$
u_w , m/s	$0.36-2.16 \cdot 10^{-4}$	$1.10 \cdot 10^{-3a}/0.37-3.67 \cdot 10^{-4}$
c_s , %	0.04	$0-1^a/0.04$
c_n , %	0-4	$0-1^a/0-5$
S_{wc}^b	0.1	0.1
S_{gr}^b	0.0	0.0
μ_w , Pa·s	$1 \cdot 10^{-3}$	$1 \cdot 10^{-3}$
μ_g , Pa·s	$2 \cdot 10^{-5}$	$2 \cdot 10^{-5}$

^a Conditions applied for the experiments shown in Figure II.1.3, carried out to select the optimal surfactant concentration.

^b Value chosen on the basis of the capillary pressure curves measured for distilled water and CO₂ in an unconsolidated sand [33].

II.1.4.1 Preliminary experiments

A series of flow experiments was performed in order to select surfactant concentration. The value was selected on the basis of the best synergy between surfactant and nanoparticles on the effective gas viscosity. Tests were carried out using a glass-bead pack of 22.5 D permeability, changing the concentration of surfactant (c_s) between 0 and 0.1 %, the nanoparticle concentration (c_n) equal to 0, 0.1, and 1.0 %, and maintaining f_g as large as 0.75. The experiments were run until the pressure difference measured through the column stabilized around a constant value (i.e., until steady state). The values of the pressure gradient at steady state are shown in Figure II.1.3. Here, it is possible to see that ∇p increases with c_s and c_n , and reaches its maximum around c_s equal to 0.04 % for c_n 1.0 %. Assuming a similar relative permeability among the tests, the effective gas viscosity increases proportionally to the pressure gradient (eq. II.1.7). Consequently, the highest pressure gradient corresponds to the highest effective gas viscosity. On the basis of these results, a concentration of surfactant equal to 0.04 % was selected and applied in all experiments reported below.

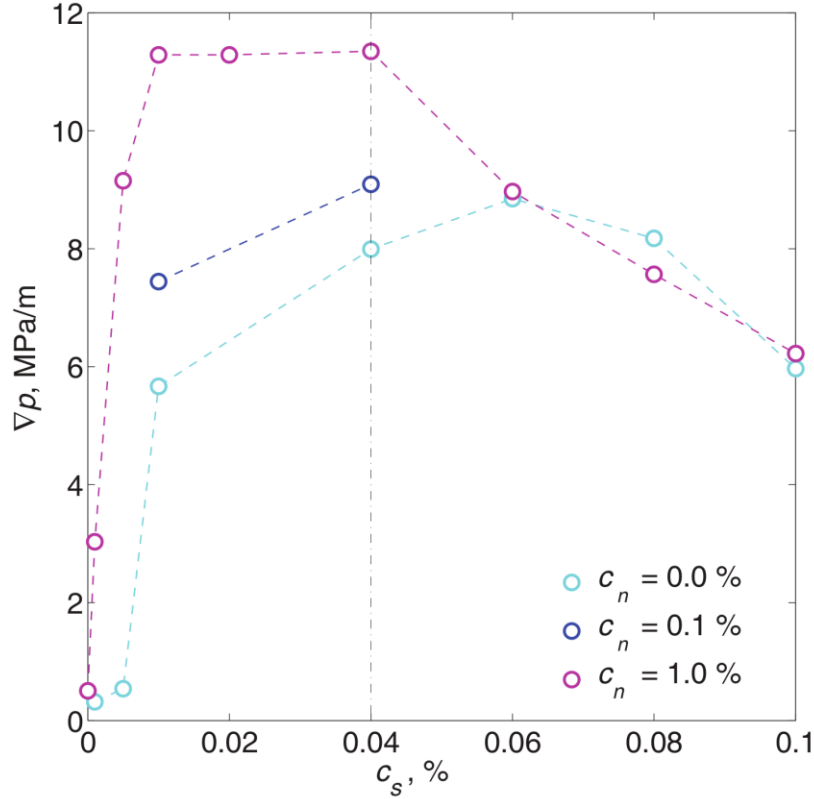


Fig. II.1.3 Pressure gradient (∇p , MPa/m) as a function of surfactant and nanoparticle concentrations. The fluxes, namely u_g and u_w , were 0.0031 and 0.0011 m/s, respectively. The dashed lines are only a visual guide.

II.1.4.2 CO₂-foam transport experiments

The operating conditions applied in the CO₂-foam transport experiments are listed in Table II.1.2. Dataset 1 and Dataset 2 correspond to two groups of experiments run with the column of permeability 1.2 and 22.5 D, respectively. The system geometry and physical properties are correspondingly listed in Table II.1.1. Pressure gradient data at steady state and the calculated effective gas viscosity values upon optimization, as explained in section 4.3, are also reported in Table II.1.2 and the former ones are shown in Figure II.1.4 as a function of foam quality, too.

Table II.1.2 Operating conditions applied during the CO₂-foam transport experiments. The concentration of surfactant was equal to 0.04 %, except in experiments 1 through 3 where no surfactant was added. Dataset 1 and Dataset 2 correspond to two groups of

experiments performed using the columns of 1.2 D and 22.5 D, respectively. The total fluxes were correspondingly $3.60 \cdot 10^{-4}$ and $7.34 \cdot 10^{-4}$ m/s.

Exp.	$f_g, (-)$	$\nabla p, \text{MPa/m}$	$\mu_g^f, \text{Pa}\cdot\text{s}$	$c_n, \%$
Dataset 1				
1	0.40	1.02	~ 0.003	0.00
2	0.60	0.90	~ 0.003	0.00
3	0.80	0.42	~ 0.001	0.00
4	0.40	16.77	0.0655	0.00
5	0.50	18.00	0.0602	0.00
6	0.60	17.86	0.0525	0.00
7	0.70	16.96	0.0450	0.00
8	0.80	14.49	0.0354	0.00
9	0.80	27.52	0.0749	0.05
10	0.50	28.58	0.1065	0.05
11	0.60	30.06	0.0985	0.05
12	0.70	33.23	0.0999	0.05
13	0.40	17.48	0.0691	0.10
14	0.50	25.02	0.0905	0.10
15	0.60	20.77	0.1145	0.10
16	0.70	37.36	0.1004	0.10
17	0.80	35.58	0.0996	0.10
18	0.80	35.31	0.0970	0.10
19	0.90	16.44	0.0408	0.10
20	0.40	24.62	0.1064	1.00
21	0.60	35.95	0.1218	1.00
22	0.80	35.70	0.1008	1.00
23	0.90	25.10	0.0658	1.00
24	0.40	20.74	0.0858	3.00
25	0.60	30.68	0.1010	3.00
26	0.80	40.24	0.1155	3.00
27	0.90	30.10	0.0806	3.00
Dataset 2				
28	0.50	1.23	0.0000	0.00
29	0.60	1.38	0.0331	0.00
30	0.80	1.35	0.0378	0.00
31	0.90	0.01	0.0390	0.00
32	0.50	0.82	0.0241	1.00
33	0.60	0.98	0.0410	1.00
34	0.80	1.61	0.0222	1.00
35	0.90	1.02	0.0253	1.00

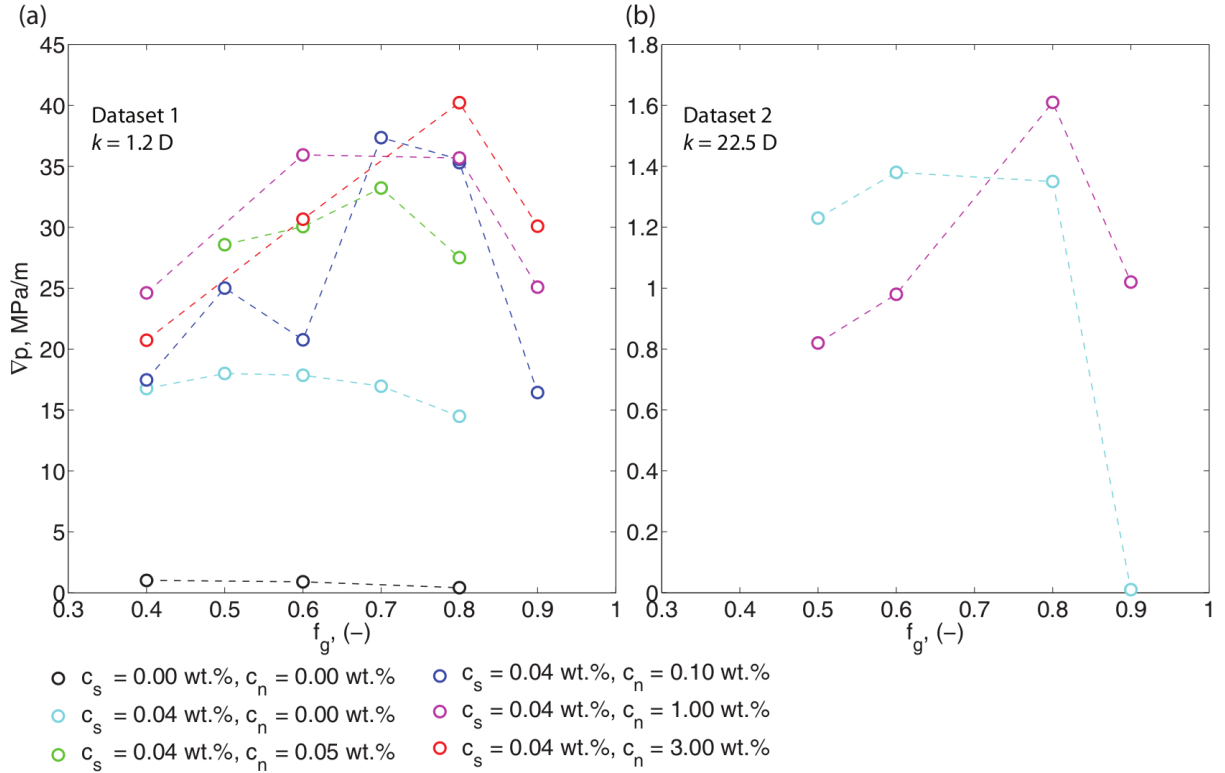


Fig. II.1.4 Pressure gradient (∇p , MPa/m) at steady state as a function of foam quality (f_g , (-)). The dashed lines are only a visual guide.

In the experiments performed using the column of permeability 1.2 D (Dataset 1), the pressure gradient significantly changes with f_g when both surfactant and nanoparticles were used, showing a strong synergy effect of surfactant and nanoparticle on the foam properties. Overall, ∇p increases sensibly when nanoparticles are added, and within the range of tested c_n , already the smallest concentration (0.05 %) has important effects. More in detail, in the experiments where neither surfactant nor nanoparticles were added, the maximum of ∇p is approximately 1 MPa/m for f_g equal to 0.4. In the experiments with only surfactant, the maximum is 17 MPa/m for f_g approximately 0.6, which is 10-folds the value where no surfactant was added. In the experiments with both surfactant and nanoparticles, the maximum of ∇p is 40 MPa/m for f_g between 0.7 and 0.8. Here, the pressure gradient has doubled in comparison to the experiments with only surfactant and, more importantly, the maximum is attained at high quality. This observation indicates remarkable synergy, i.e., a strong high-quality CO_2 -foam can be formed when nanoparticle are used in conjunction with surfactant.

In the experiments performed using the column of permeability 22.5 D (Dataset 2), the overall measured pressure gradient is much lower than in the previous cases and the difference between the tests conducted with and without nanoparticles is negligible. The maximum of ∇p was measured to be approximately 1.6 MPa/m and it was attained at f_g equal to 0.8, indicating that a high-quality CO₂-foam was stabilized effectively with nanoparticles (in the absence of foam, the gradient would have been 0.1 MPa/m). A lower ∇p in these experiments than in those performed with a smaller permeability column should have been expected. In the low-quality regime, large permeability, which corresponds to bigger pore size, determines larger bubbles leading to lower effective foam viscosity and, hence, lower pressure gradient [2]. In the high-quality regime, large permeability reduces instead P^*c weakening the foam and reducing the pressure gradient [37,2]. Moreover, a negligible different behavior between the experiments with and without nanoparticles using this type of column can be observed. The data suggest that the nanoparticles had a small deleterious effect below the optimum foam quality, and a beneficial effect above it. The beneficial effect is most noticeable at a quality of 0.9, where strong foam was formed when nanoparticles were present, and no foam formed without nanoparticles. This suggests that the nanoparticles were effective at stabilizing bubbles at high foam qualities.

In the low-quality regime, the maximum bubble size is approximately equal to the maximum pore size, so larger bubbles must be expected for larger permeability [2]. In the high-quality regime, the bubble size is regulated by P^*c [24] which increases with coverage factor (f , $f = (n_p r^2 \pi) / A_b$, where n_p is the number of particles adsorbed at a bubble wall of surface area A_b (m²)) [23] and decreases with permeability [37,2]. As f decreases and k increases smaller P^*c are expected, which determine a coarser foam with lower resistance and pressure gradient.

Figure II.1.5 shows the pressure gradient measurements during the transient phase of experiments 24 through 27, where a concentration of nanoparticles as large as 3 % was used. Here, ∇p is reported as a function of pore volume injected ($PV = Q \cdot t / (A \cdot L \cdot \phi)$, (-)). In these diagrams, it is possible to see that initially during foam formation the pressure gradient smoothly increases. An exception is for experiment 26 where an accidental opening of the bypass valve caused a sudden pressure drop followed by an increase. Then, when the foam arrives at the outlet of the column, the pressure gradient stabilizes around the maximum value. Similar observation were made by Yu et al. [47]. During this phase, pressure oscillations are present due to

continuous processes of generation and rupture of the bubbles. Oscillations are particularly evident in experiment 27, where the highest foam quality was used. They are due to the vicinity of the system to its critical condition of capillary pressure and water saturation [35,39]. As the foam is displaced, the capillary pressure increases, which might reach its critical value determining the rupture of several lamellae simultaneously. The foam becomes coarser and the pressure through the column decreases. Due to the pressure gradient within the column, new lamellae are generated and P_c increases again [35]. This continuous process of foam generation and destruction might be behind the large oscillations observed in the pressure measurements of experiment 27.

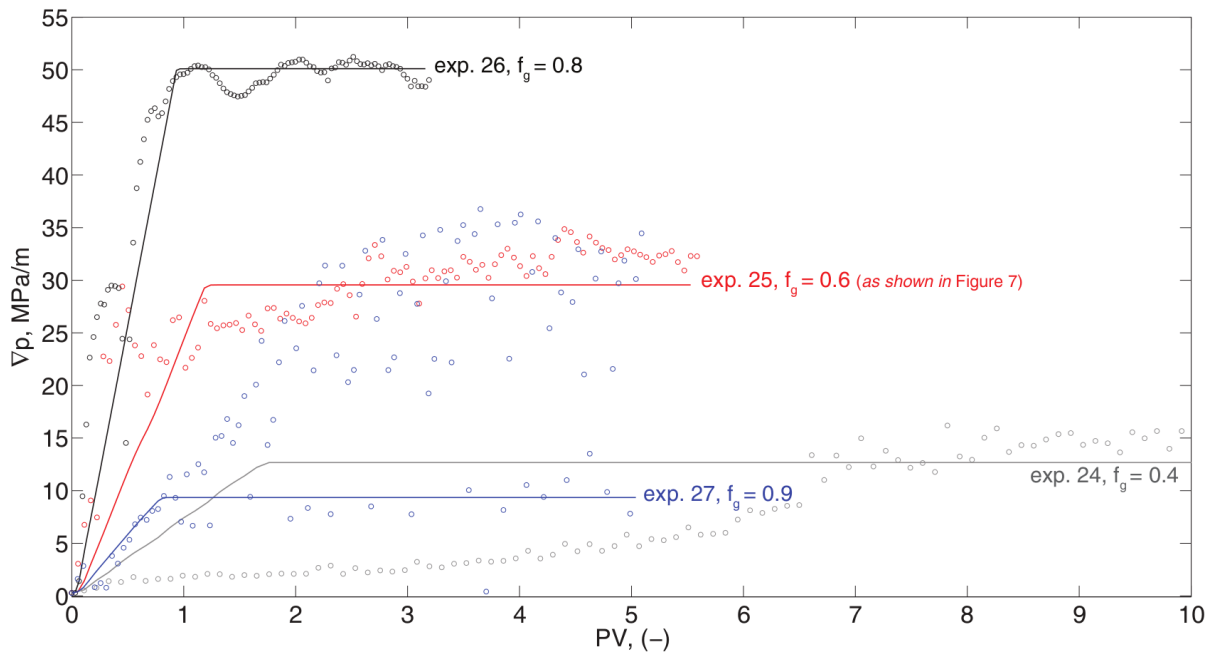


Fig.II.1. 5 Pressure gradient (\bar{V}_p , MPa/m) as a function of pore volume injected (PV, (-)) measured during experiments where a concentration of nanoparticles of 3 % was added. The symbols indicate: circles, measurements; solid lines, model for which the number of grid points was 20.

II.1.4.3 Parameter estimation

In this section, the data collected during the foam transport experiments are analyzed and discussed in the framework of the mathematical model introduced in section 3. Model parameters were estimated inverting pressure difference measurements and then used to calculate the CO₂-foam transport behavior. First, a subset of model parameters was estimated through the optimization of the measurements at steady state and used to calculate the effective gas viscosity at this condition. Then, the pressure measurements taken throughout the entire course of a

transient phase of an experiment were matched to estimate the remaining group of parameters. Upon this optimization, the foam texture and water saturation evolution were determined.

Assuming local equilibrium is reached at steady state, the rate of foam generation equals the rate of foam destruction (i.e., $r_g = r_c$) and therefore combining eqs. 9 and 10, foam texture at steady state is given by

$$n_f = \frac{C_g \nabla p^m}{C_c \left(\frac{S_w}{S_w - S_w^*} \right)^n} \quad (\text{II.1.11})$$

substituting this equation in eq. 6

$$\mu_g^f = \mu_g^0 + \frac{C_f C_g}{C_c} \frac{\nabla p^m}{C_c \left(\frac{S_w}{S_w - S_w^*} \right)^n} \frac{1}{\sqrt[3]{u_g / \phi S_g}} \quad (\text{II.1.12})$$

from which the pressure gradient within the column can be derived through eq. 8. Model parameters and a combinations of them (namely, $\frac{C_f C_g}{C_c}$, n , m , and S_w^*) were estimated by minimizing the least squares of the difference between the measured and calculated ∇p at steady state and the uncertainty within a 95 % confidence interval was determined using the jacobian matrix upon optimization [9]. The measurements were divided in three groups. Two contained results from tests performed using the column of 1.2 D permeability, distinguished by the use of nanoparticles. A third group included all the experiments performed using the column of 22.5 D permeability. The selection was made on the basis of the significant difference in foam behavior due to the change in solution composition and porous medium permeability. The estimated parameter values are given in Table II.1.3 and provide an initial guess for larger scale simulations of foam transport in the subsurface assuming foam has reached steady state. Figure II.1.6 shows the calculated average trends of μ_g^f (eq. 12) upon optimization as a function of f_g . Individual μ_g^f values corresponding to each experiment are listed in Table II.1.2.

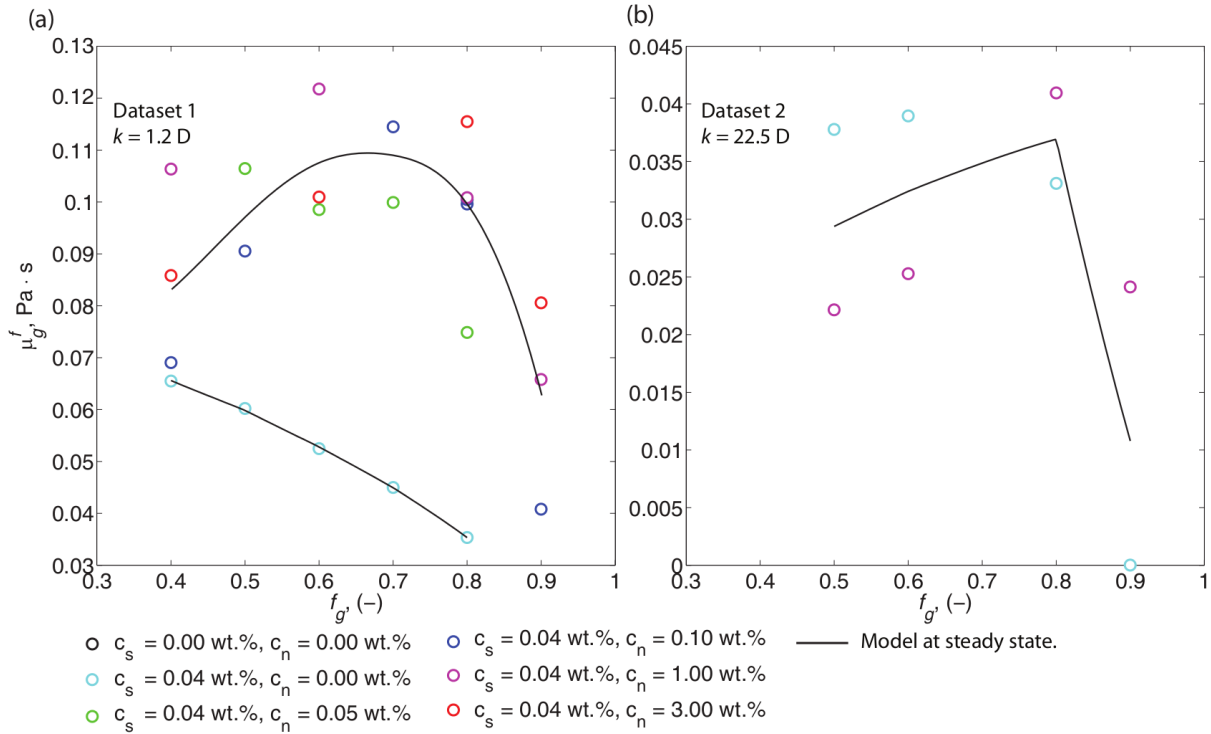


Fig. II.1.6 Effective gas viscosity (μ_g^f) as a function of foam quality (f_g) calculated upon optimization of the pressure gradient at steady state.

Table II.1.3 Estimated values and uncertainty of the model parameters using ∇p at steady state as listed in Table II.1.2.

	$\log_{10}[C_g \cdot C_f/C_e]$	m	$\log_{10}n$	$\log_{10}S_w^*$
Dataset 1				
exp. 4–8	-6.300 ± 5.080	0.588 ± 0.769	-0.139 ± 2.250	-0.916 ± 0.913
exp. 9–27	-9.420 ± 1.320	0.996 ± 0.196	-0.680 ± 2.390	-1.050 ± 0.828
Dataset 2				
exp. 28–35	-9.340 ± 0.903	1.140 ± 0.153	-0.535 ± 0.613	-2.000 ± 1.830
Values in [22]	-11.8	2.4	-0.553	-1.222

Similarly to the trend of the pressure gradient shown in Figure II.1.4, μ_g^f increases with f_g , reaches a maximum, and then decreases as the foam quality approaches unity. At low foam quality, CO₂ bubbles are almost spherical, with thick lamellae between them, the viscosities are not expected more than a few times that of the surfactant solution. As the quality of the foam increases the concentration of the lamellae increases, determining a larger μ_g^f due to the deformation of the bubble through the pores of the medium. At large f_g , namely 0.8–0.95, either the lamellae are too thin and they therefore easily rupture or the water saturation is too low, i.e., there is not enough liquid to support the formation of the lamellae. Consequently, μ_g^f becomes smaller approaching the value of $\mu_0 g$. In the low permeability column, μ_g^f is the largest when

nanoparticles are used. Its maximum is 0.110 Pa·s for $f_g = 0.75$. This value is almost two-folds of the maximum attained when only a surfactant is added, which is ~ 0.067 Pa·s at $f_g \sim 0.4$. Moreover, the maximum moves towards larger foam quality values in the presence of nanoparticles because the nanoparticles by adsorbing at the CO₂-water interface enhance the stability of the thin films present in high lamellae density foam. In the high permeability column, no significant effect of nanoparticles was observed and the calculated maximum of μ_g^f is approximately 0.035 Pa·s for f_g as large as 0.8.

To describe the CO₂-foam behavior during transport, we completed the estimation of the model parameters, inverting the pressure difference measured during the transient displacement of three selected experiments, namely 6, 25, and 34. The estimated values of C_f , C_g , and C_c are given in Table 4 together with the adjusted values of m , n , and S_w^* within their uncertainty.

Table II.1.4 Estimates of C_f , C_g , and C_c determined using pressure drop measurements during experiments 6, 25, and 34.

Exp.	$\log_{10} C_f$	$\log_{10} C_g$	$\log_{10} C_c$	m	$\log_{10} n$	$\log_{10} S_w^*$
6	-14.80 ± 0.008	7.48 ± 0.005	-0.52 ± 0.001	0.588	-0.139	-0.916
25	-15.94 ± 0.001	8.54 ± 0.0003	0.35 ± 0.002	0.78	-1.92	-0.73
34	-16.48 ± 0.05	6.57 ± 0.05	-2.02 ± 0.02	1.140	-0.535	-2.000

The complete set of estimates was used to calculate the evolution of the water saturation, the foam texture, and the pressure gradient during the transport of the CO₂-foam in the two porous media. The results of the inversion of the pressure gradient are shown in Figure II.1.7. The model describes well the period during the formation of the foam, but fails to capture the oscillations of pressure after the breakthrough. This might be ascribed to the assumption behind the model that local equilibrium is attained at steady state. However, the measurements show that this hypothesis is not entirely correct and it might be only a simplification of the overall foam behavior. The set of parameters estimated from experiment 25 was used to predict the pressure evolution of three similar experiments where the same solution composition was used, i.e., experiments 24, 26, and 27. The resulting simulations are shown in Figure II.1.5 as a solid line. Here, it is possible to see that the model predicts well the behavior of experiment 26, which is expected to be governed by the same mechanisms of foam generation and destruction of experiment 25 as a strong high-quality foam is formed. Furthermore, the model prediction of experiment 27 agrees with the measurements, but suggests that the pressure gradient at steady

state equals the minimum measured values; whereas the model entirely misses the pressure gradient of experiment 24. For this, two hypotheses can be formulated. The experiment might have not achieved steady state or a coarse low-quality foam was created, whose generation process was controlled by a different mechanism at the pore scale not account for in the constitutive equations (eqs. 9 and 10) adopted here.

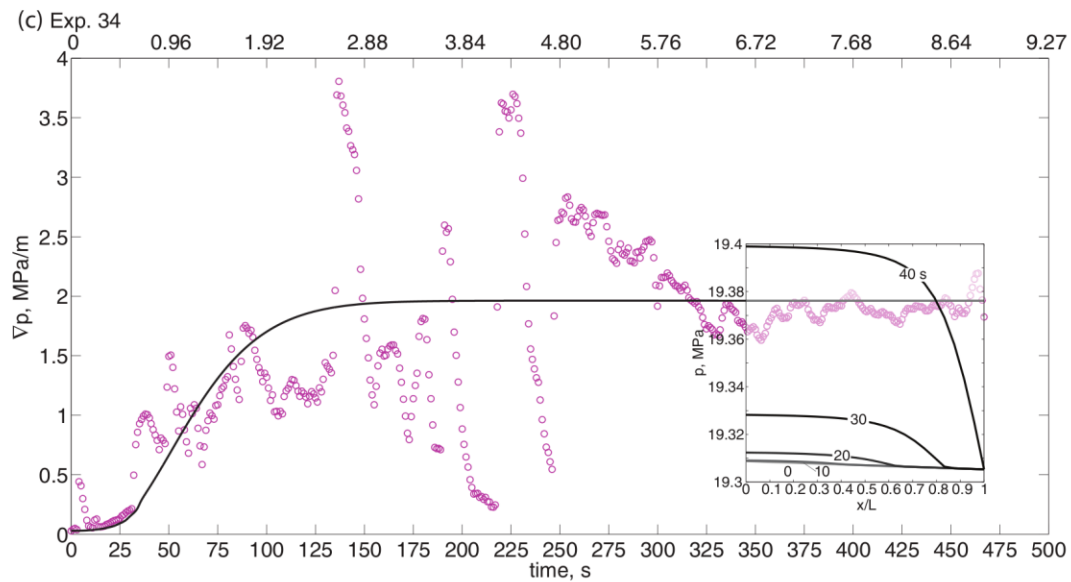
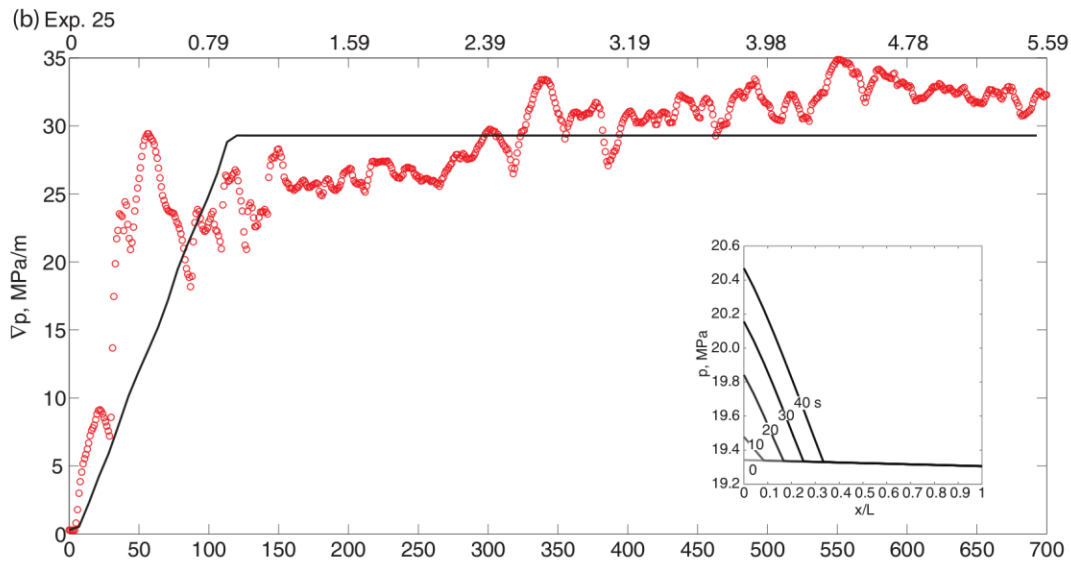
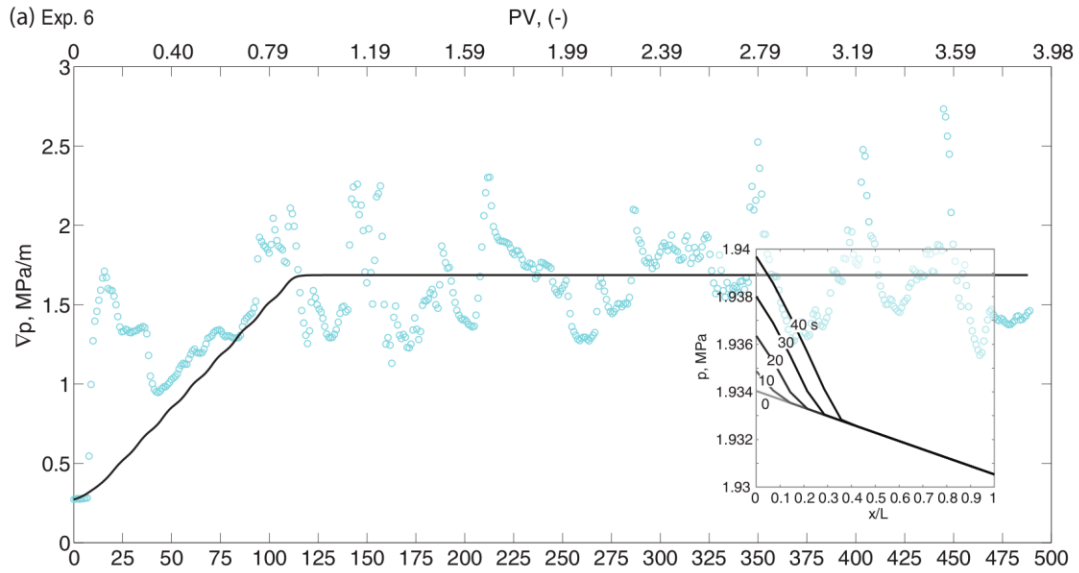


Fig.II.1. 7 Pressure gradient (∇p , MPa/m) as a function of time during the transient foam displacement in: (a) exp. 6, $f_g = 0.6$; (c) exp. 25, $f_g = 0.6$; and (e) exp. 34, $f_g = 0.8$. The symbols indicate: circles, measurements; solid lines, model for which the number of grid points was 20. The inserts show the pressure as a function of normalized distance (x/L) at different times.

Finally, Figure II.1.8 shows model-derived S_w and n_f as a function of normalized distance considering the operating conditions of experiments 6, 25, and 34. In the case of foam displaced in the lower permeability medium (experiments 6 and 25), a large foam bank of almost constant texture forms and when 3 % of nanoparticles are added the highest density of lamellae is generated. In the case of the larger permeability medium (experiment 34), the density of the lamellae increases with distance within the column length indicating that the generation kinetics is much slower than in the previous case. The end of the foam texture allows to predict the viscosity of the foam. Under the conditions of experiments 6 and 25, a large high viscosity foam front at almost stationary flow properties moves through the porous medium. While, under the conditions applied in experiment 34, the effective gas viscosity is growing ahead of the foam front. These two different foam transport behaviors are ascribed to the pressure gradient within the columns, the lower the pressure gradient the slower the generation rate (eq. 9). The pressure gradient measured in experiment 34 was much lower than in experiments 6 and 25.

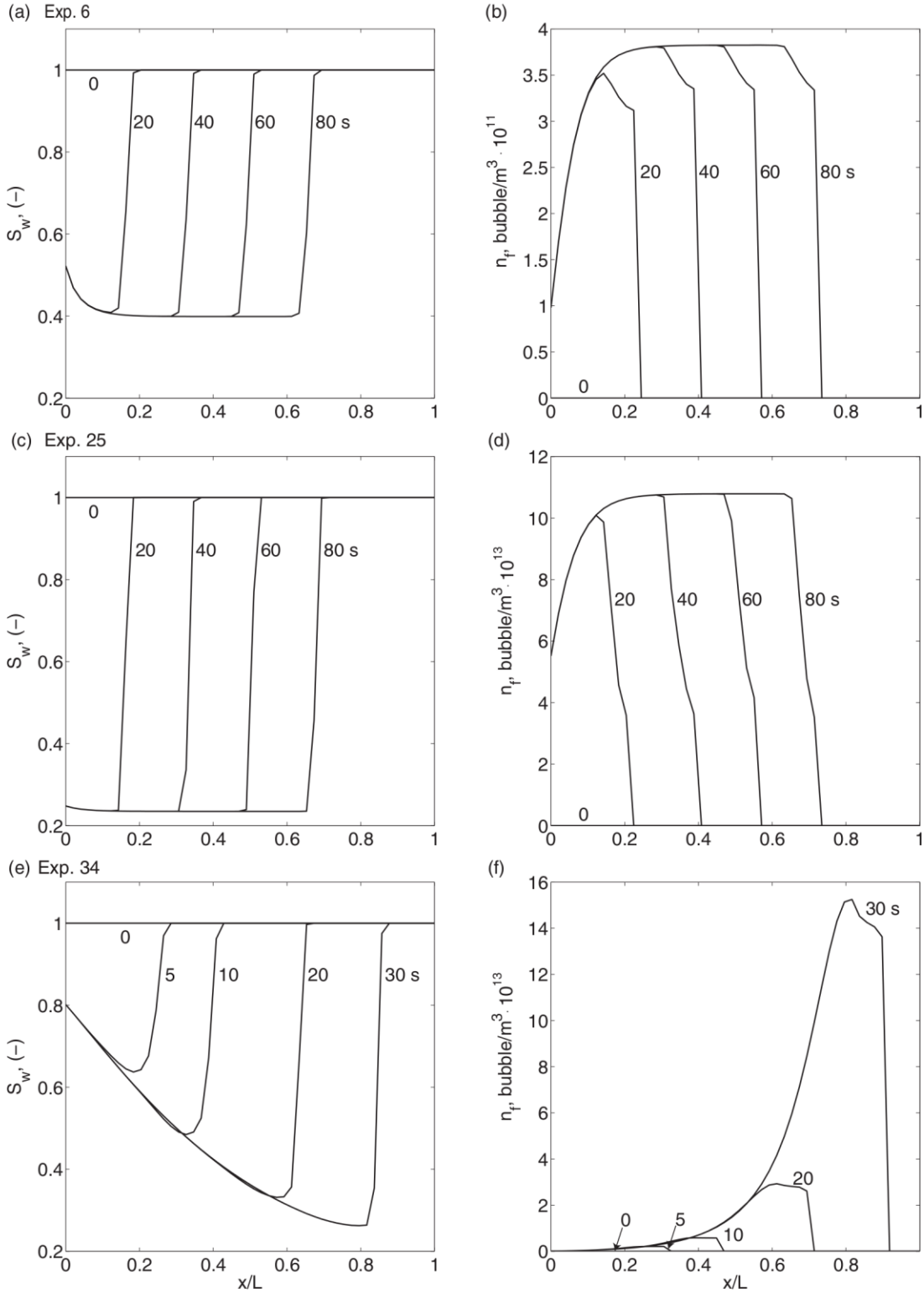


Fig. II.1.8 Water saturation (S_w) and foam texture (n_f) as a function of normalized distance (x/L) calculated using the physical and model parameters listed in Tables 1 and 2. Parts show the evolution during exp. 6, (a) and (b); exp. 25, (c) and (d); and exp. 34, (e) and (f). Number of grid points (N_x) was equal to 50.

II.1.5 Conclusions

In this paper, we have investigated the effect of surfactant and nanoparticles on the transport behavior of a CO₂-foam. Column flood experiments were performed at near-well conditions systematically changing the solution composition and foam quality. A two-phase flow mechanistic model was used to describe the experiments and predict the CO₂-foam evolution under the investigated conditions. A synergic effect was observed between surfactant and nanoparticles on the effective gas viscosity, which doubled in the presence of nanoparticles and more importantly its maximum moved towards high-quality foam regime in contrast to the low-quality foam regime observed in the experiments where only surfactant was used. The model describes well the experiments, particularly where a strong high-quality foam is generated and allows to predict an overall behavior during steady state. A foam stabilized with nanoparticles and surfactant can be described with the same type of model generally used for surfactant-stabilized foam suggesting that the pore level mechanisms controlling the destruction and the generation foam processes are similar with and without nanoparticles as long as sufficient amount of surfactant is employed.

Finally, our results suggest that a strong high-quality CO₂-foam can be formed using nanoparticles and surfactant in conjunction as coalescence-preventing substances, allowing to reduce the water used for the operation, and its transport behavior can be analyzed and predicted within the mathematical framework of the population balance model.

II.1.6. References

1. Afsharpoor, A., Lee, G., Kam, S.: Mechanistic simulation of continuous gas injection period during surfactant-alternating-gas (SAG) processes using foam catastrophe theory. *Chemical Engineering Science* 65(11), 3615–3631 (2010)
2. Alvarez, J.M., Rivas, H.J., Rossen, W.R.: Unified model for steady-state foam behavior at high and low foam qualities. *SPE Journal* SPE 74141 (2001)
3. Aronson, A., Bergeron, V., Fagan, M., Radke, C.: The influence of disjoining pressure on foam stability and flow in porous media. *Colloids and Surfaces A: Physicochemical and Engineering Aspects* 83(2), 109–120 (1994)
4. Aroonsri, A., Worthen, A., Hariz, T., Johnston, K., Huh, C., Bryant, S.: Conditions for generating nanoparticle-stabilized CO₂ foams in fracture and matrix flow. *SPE Annual Technical Conference and Exhibition*, 30 September-2 October, New Orleans, Louisiana, USA SPE 166319 (2013)

5. Ashoori, E., Marchesin, D., Rossen, W.: Roles of transient and local equilibrium foam behavior in porous media: Traveling wave. *Colloids and Surfaces A: Physicochemical and Engineering Aspects* 377(13), 228–242 (2011)
6. Ashoori, E., Marchesin, D., Rossen, W.: Stability analysis of uniform equilibrium foam states for eor processes. *Transport in Porous Media* 92(3), 573–595 (2012)
7. Aveyard, R., Clint, J.H., Nees, D.: Small solid particles and liquid lenses at fluid/fluid interfaces. *Colloid and Polymer Science* 278(2), 155–163 (2000)
8. Azmin, M., Mohamedi, G., Edirisinghe, M., Stride, E.: Dissolution of coated microbubbles: The effect of nanoparticles and surfactant concentration. *Materials Science and Engineering: C* 32(8), 2654–2658 (2012)
9. Beck, J.V., Arnold, K.J.: *Parameter estimation in engineering and science*. John Wiley & Sons, New York (1977)
10. Binks, B.P., Clint, J.H.: Solid wettability from surface energy components: Relevance to pickering emulsions. *Langmuir* 18(4), 1270–1273 (2002)
11. Binks, B.P., Desforges, A., Duff, D.G.: Synergistic stabilization of emulsions by a mixture of surface-active nanoparticles and surfactant. *Langmuir* 23(3), 1098–1106 (2007)
12. C.J. Radke, A.J.: Dynamic stability of foam lamellae flowing through a periodically constrained pore. In *Oil-Field Chemistry, Enhanced Recovery and Production Stimulation*. Ed. John K. Borchardt and Teh Fu Yen. America Chemical Society, Washington, DC. (1961)
13. Collins, R.: *Flow of fluids through porous materials*. Research & Engineering Consultants, Inc., Englewood, CO. (1961)
14. Du, Z., Bilbao-Montoya, M.P., Binks, B.P., Dickinson, E., Ettelaie, R., Murray, B.S.: Outstanding stability of particle-stabilized bubbles. *Langmuir* 19(8), 3106–3108 (2003)
15. Espinosa, D.A., Caldelas, F.M., Johnston, K.P., Bryant, S.L., Huh, C.: Nanoparticle-stabilized supercritical CO₂ foams for potential mobility control applications. in *SPE Improved Oil Recovery Symposium: Proceedings, 24-28 April 2010, Tulsa, Oklahoma, USA, Soc. Pet. Eng., Richardson, Tex.* p. Paper 129925 (2010)
16. Gauglitz, P.A., Friedmann, F., Kam, S.I., Rossen, W.R.: Foam generation in homogeneous porous media. *Chemical Engineering Science* 57(19), 4037–4052 (2002)
17. Hirasaki, G., Jackson, R., Jin, M., Lawson, J., Londergan, J., Meinardus, H., Miller, C., Pope, G., Szafranski, R., Tanzil, D.: Field demonstration of the surfactant/foam process for remediation of a heterogeneous aquifer contaminated with DNAPL, in: Fiorenza, S., Miller, C.A., Oubre, C.L., Ward, C.H. (Eds.). In *NAPL Removal: Surfactants, Foams, and Microemulsions*. Lewis, Boca Raton (2000)
18. Hirasaki, G.J., Lawson, J.B.: Mechanisms of foam flow in porous media: Apparent viscosity in smooth capillaries. *Society of Petroleum Engineers* (1985)
19. Horozov, T.S.: Foams and foam films stabilised by solid particles. *Current Opinion in Colloid & Interface Science* 13(3), 134–140 (2008)
20. Hunter, T.N., Pugh, R.J., Franks, G.V., Jameson, G.J.: The role of particles in stabilising foams and emulsions. *Advances in Colloid and Interface Science* 137(2), 57–81 (2008)
21. Kam, S., Q.P. Nguyen, Q., Rossen, W.: Dynamic simulations with an improved model for foam generation. *SPE journal SPE* 90938, 35–48 (2007)
22. Kam, S., Rossen, W.: A model for foam generation in homogeneous porous media. *SPEJ* 8, 417–425 (2003)
23. Kaptay, G.: Interfacial criteria for stabilization of liquid foams by solid particles. *Colloids and Surfaces A: Physicochemical and Engineering Aspects* 230(13), 67–80 (2003)
24. Khatib, Z.I., Hirasaki, G.J., Falls, A.H.: Effects of capillary pressure on coalescence and phase mobilities in foams flowing through porous media. *SPE Reservoir Engineering* pp. 919–926 (1988)
25. Kovscek, A., Patzek, T., Radke, C.: A mechanistic population balance model for transient and steady-state foam flow in boise sandstone. *Chemical Engineering Science* 50(23), 3783–3799 (1995)

26. Kovscek, A.R., Radke, C.J.: Fundamentals of foam transport in porous media. in: L.I. schramm (ed.), foams: Fundamentals and applications in the petroleum industry. *Advances in Chemistry* 242 (1994)
27. Lake, L.W.: *Enhanced oil recovery*. Prentice Hall, Upper Saddle River, NJ (1989)
28. Lee, S., Lee, G., Kam, S.: Three-phase fractional flow analysis for foam-assisted nonaqueous phase liquid NAPL remediation. *Transport in Porous Media* 101(3), 373–400 (2014)
29. Leverett, M.: Capillary behavior in porous solids. *Transaction of the American Institute of Mining and Metallurgical Engineering* 142, 152–169 (1941)
30. Mulligan, C.N., Eftekhari, F.: Remediation with surfactant foam of pcp-contaminated soil. *Engineering Geology* 70(3–4), 269–279 (2003)
31. Murray, B.S., Ettelaie, R.: Foam stability: proteins and nanoparticles. *Current Opinion in Colloid & Interface Science* 9(5), 314–320 (2004)
32. Orr F.M., J., Taber, J.: Use of carbon dioxide in enhanced oil recovery. *Science* 224(4649), 563–569 (1982)
33. Plug, W.J., Bruining, J.: Capillary pressure for the sand CO₂ water system under various pressure conditions. application to CO₂ sequestration. *Advances in Water Resources* 30(11), 2339–2353 (2007)
34. Ramsden, W.: Separation of solids in the surface-layers of solutions and 'suspensions' (observations on surface-membranes, bubbles, emulsions, and mechanical coagulation). – preliminary account. *Proceedings of the Royal Society of London* 72(477–486), 156–164 (1903)
35. Ransohoff, T.C., Radke, C.J.: Mechanisms of foam generation in glass-bead packs. *Society of Petroleum Engineers* (1988)
36. Rossen, W.: Foams in enhanced oil recovery, in: R.K. Prudhomme, S. Khan (Eds.), *Foams: Theory, Measurements and Applications*. Marcel Dekker, New York (1996)
37. Rossen, W., Lu, Q.: Effect of capillary crossflow on foam improved oil recovery SPE 3831, 579–589 (1997)
38. Sethumadhavan, G., Bindal, S., Nikolov, A., Wasan, D.: Stability of thin liquid films containing polydisperse particles. *Colloids and Surfaces A: Physicochemical and Engineering Aspects* 204(13), 51–62 (2002)
39. Singh, G., Hirasaki, G.J., Miller, C.A.: Dynamics of foam films in constricted pores. *AIChE Journal* 43(12), 3241–3252 (1997)
40. Singh, V., Wang, S., Kool, E.T.: Genetically encoded multispectral labeling of proteins with polyfluorophores on a DNA backbone. *Journal of the American Chemical Society* 135(16), 6184–6191 (2013)
41. Tanzil, D., Hirasaki, G.J., Miller, C.A.: Conditions for foam generation in homogeneous porous media. *Society of Petroleum Engineers* (2002)

II.2. Field-scale NP-C/W foam generation and transport – Multi-phase/component model

Under this task, a mathematical framework for simulating and assessment of the generation and transport of nanoparticle (NP)-stabilized CO₂-in-brine foam in radial multi-layered unfractured rock formations was developed, and was incorporated in a numerical simulator capable of assisting with the analysis and interpretation of field pressure data, design of foam injection schemes, and optimization of the best injection scenario.

The numerical simulator consists of three sub-models: (1) A fractional flow based three phase flow module to address simultaneous flow of water, oil and gas/CW foam in a layered otherwise homogeneous unfractured rock formation, (2) a transport module that accounts for the fate and transport of stabilizing agents (i.e. NPs and surfactant) used for generating and stabilizing CW foam, and (3) an auxiliary foam viscosity module for estimating the gas/foam phase mobility as a function, among other factors, of the shear rate, phase saturations and the concentration of surfactant and NP. The numerical implementation of the mathematical model by the incorporation of:

- (1) A three-phase fractional flow model based on the method of characteristics (MOC) and coherent wave theory (Lake, 1989) for guaranteed high computational performance. Parker et al. (1987) relative permeability-saturation model was employed consistent with approach implemented by the UTCHEM simulator. However, to avoid regions in the saturation triangle with elliptic behavior (a characteristic behavior of models of the flow of three-immiscible incompressible fluids, which results in complex characteristic wave velocities (Juanes and Patzek, 2004)), an algorithm was developed and incorporated to identify and replace the so-called elliptic regions with characteristic velocities obtained from Corey-type relative permeability model based solution of MOC equations (Figure II.2.1).

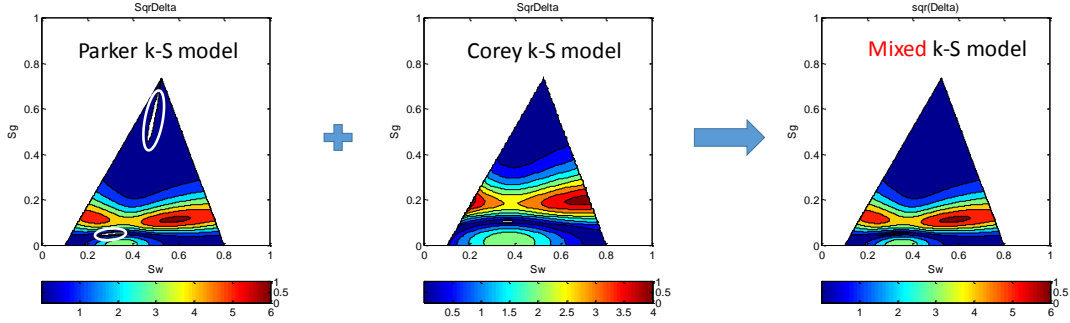


Figure II.2.1. Identifying elliptic regions on the Parker model based characteristic velocities and replacing with characteristic velocities based on Corey-type relative permeability model.

- (2) A multi-component reactive transport model based on the finite differencing method using an upstream-weighting and a generally-weighted scheme for spatial and temporal discretization, respectively. A general form of the colloid filtration theory (Tufenkji and Elimelech, 2004) modified to address the limited NP retention capacity considering velocity dependence and shadow-zone effect (Li et al., 2008) was incorporated to describe NP retention and mobility. A rate-limited Langmuirian-type sorption model was adopted to account for the adsorption and desorption of surfactant.
- (3) A local equilibrium foam viscosity model based on the method proposed by Li et al. (2006) accounting for physicochemical factors including shear-thinning, stabilizing agents (Liu, 2010) and weakening and killing effects due to oil presence (Namdar-Zangeneh et al., 2008).

II.2.1. Mathematical Model

Three-phase radial flow model: Assuming that conditions for isothermal flow of incompressible fluids hold valid, in the absence of chemical reactions and external source/sinks, the conservation of mass for α -phase ($\alpha = w$ (water), g (gas/foam), o (oil)) can be expressed as (Lake, 1989):

$$\phi \frac{\partial}{\partial t} (S_\alpha) + \vec{\nabla} \cdot (f_\alpha \vec{u}) = 0 \quad (\text{II.2..1})$$

which in cylindrical coordinates takes the form

$$\phi \frac{\partial}{\partial t} (S_\alpha) + \frac{1}{r} \frac{\partial}{\partial r} (r f_\alpha u(r)) = 0 \quad (\text{II.2..2})$$

for axisymmetric flow regime near the injection well, given that cross-layer flow and vertical mixing are negligible. Here, S_α [-] is the saturation of α -phase, ϕ [-] is the rock matrix porosity, u [LT^{-1}] is the total surface-area-normalized injection flow rate, and r [L] denotes the radial

distance from the injection well. f_α [-], the fraction of total flow occurring within α -phase, is described as a function of phase saturations and varies with variations in gas/foam phase viscosity. Under horizontal flow conditions and near injection wells, where drag forces dominate capillary effects, f_α is expressed as:

$$f_\alpha = \frac{\lambda_{r\alpha}}{\lambda_{rw} + \lambda_{rf} + \lambda_{ro}} \quad (\text{II.2.3})$$

where $\lambda_{r\alpha} = \frac{k_{r\alpha}}{\mu_\alpha}$ [M^{-1}LT] is the relative α -phase mobility with $k_{r\alpha}$ [-] and μ_α [-] denoting α -phase relative permeability and viscosity, respectively. The relative permeability (Relperm) values can be determined from the three-phase Relperm-Saturation model of *Parker et al.* (1987).

Provided that the confining pressure is large compared to the pressure drop in the proximity of injection well, the incorporation of continuity equation for incompressible fluids (i.e. $r u = r_0 u_0$) into Eq. II.2.2 yields:

$$\phi \frac{\partial}{\partial t} (S_\alpha) + u_0 \frac{r_0}{r} \frac{\partial}{\partial r} (f_\alpha) = 0 \quad (\text{II.2.4})$$

in which, r_0 [L] is the well radius and u_0 [LT^{-1}] is the total injection rate normalized to the surface area of the well. An approach based on the method of characteristics (MOC), fully described in Lake (1989), will be implemented to solve the phase mass balance equations. MOC converts Eq. II.2.4 to a set of hyperbolic ordinary differential equations (ODEs).

Multi-component radial transport model: The aqueous phase is considered as the main carrier of stabilizing agents (SAs) (i.e. NPs and surfactant). A schematic of potential mass transfer mechanisms among existing phases of the system is illustrated in Fig II.2.2. Based on their hydrophilic-lyophobic balance (HLB), some surfactants act as interfacial tracers (considered in this research) that only accumulate at the o/w interface but do not partition into the non-aqueous phases (*Rao, 2000*). Colloidal particles with a broad range of moderately hydrophobic coatings are expected to adhere spontaneously to the interface (*Bishop et al., 2010*), therefore NP partitioning into the non-aqueous phases is considered negligible.

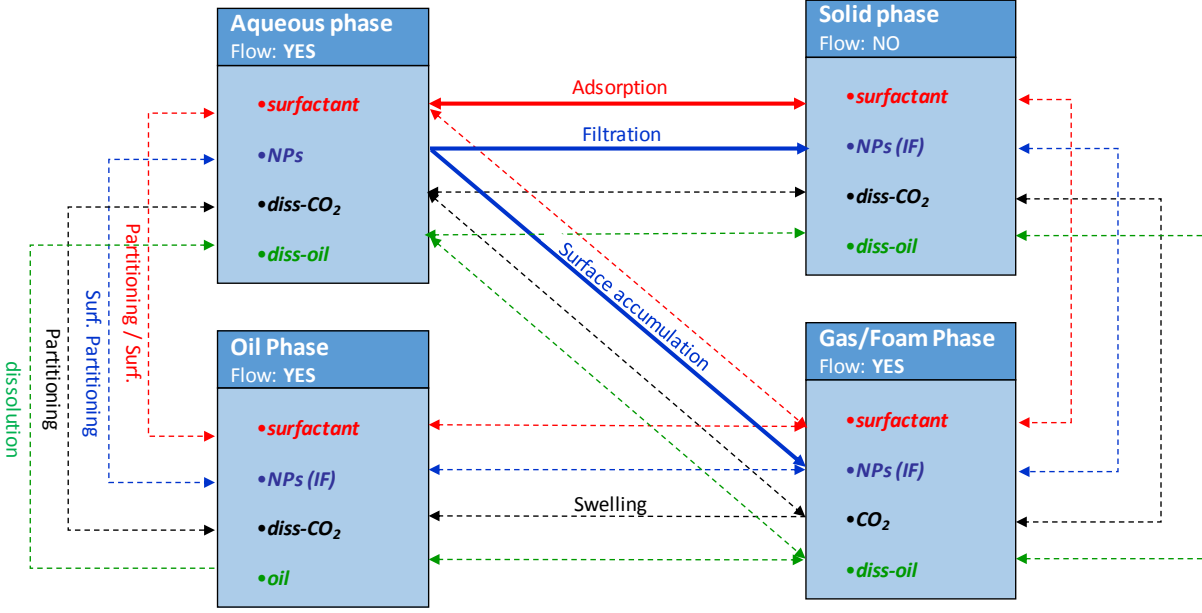


Figure II.2.2. A schematic of interphase mass transfer mechanisms. Solid arrows show the mechanisms that will be implemented in the simulator. The dashed arrows can be incorporated in the future.

A multiphase extension of the transport equation used by *Abriola et al.* (1997) was modified to include a mass accumulation term for sites on g/w interface:

$$\frac{\partial}{\partial t} (\varphi S_w C_c^w + \rho_b \omega_c^s + \varphi S_g \omega_c^{if}) + \nabla \cdot [\varphi S_w (C_c^w v_w - D_{w_c}^h \nabla C_c^w)] = 0 \quad (\text{II.2.5})$$

where, c represents the nanoparticles (NP) and surfactant ($surf$), C_c^w [M/L³ of water], ω_c^s [M/M of dry solid phase], and ω_c^{if} [M/L³ of gas phase] denote the aqueous phase, solid phase, and interfacial concentrations of component c , respectively. ρ_b [kg/m³] is the bulk density of rock, v_w [m/s] is the pore water velocity, and $D_{w_c}^h$ [m²/s] is the hydrodynamic dispersion coefficient of component c in the aqueous phase.

A rate-limited Langmuirian model will be used to describe adsorption and desorption of surfactant. Similarly attachment and re-entrainment of NPs by the solid phase will be represented by a limited-retention-capacity based extension of colloidal filtration theory, which has a mathematical form analogous to the rate-limited Langmuirian adsorption. Hence, a general component kinetic mass transfer between the aqueous and solid phase can be expressed as:

$$\frac{\partial}{\partial t} (\rho_b \omega_c^s) = \varphi S_w k_c^{s,a} \Psi^s C_c^w - k_c^{s,d} \rho_b \omega_c^s \quad (\text{II.2.6})$$

$$\Psi^s = 1 - \frac{\omega_c^s}{\omega_c^{s,max}} \quad (\text{II.2.7})$$

in which Ψ^s [-] is the site-blocking function, and $\omega_c^{s,max}$ [M/M of solid phase] is the maximum retention capacity for component c by solid surfaces, which under variable flow conditions can be scaled according to the model of Li et al. (2008) as:

$$\frac{\omega_c^{s,max}}{\omega_{c,REF}^{s,max}} = \left(\frac{v_p}{v_p^{REF}} \right)^{-0.4} \left(\frac{d_c}{d_c^{REF}} \right)^{-1.6} \quad (\text{II.2.8})$$

$k_{surf}^{s,a}$ [T^{-1}] and $k_{NP}^{s,a}$ [T^{-1}] in Eq. II.2.6 are first-order rate constants for surfactant adsorption and NP attachment, respectively, whereas $k_{surf}^{s,d}$ [T^{-1}] and $k_{NP}^{s,d}$ [T^{-1}] coefficients are rate constants denoting desorption and re-entrainment processes. $k_{NP}^{s,a}$ will be a function of physicochemical properties of system and specifically depends on pore water velocity. It can be estimated at a distance r from injection well by scaling the attachment constant at the well location, $k_{NP}^{s,a}(r_0)$, based on Yao et al. (1971) model of colloidal filtration in porous media:

$$k_{NP}^{s,a}(r) = k_{NP}^{s,a}(r_0) \frac{v_w(r) \eta_s(r)}{v_{w0} \eta_{s0}} \quad (\text{II.2.9})$$

where subscript “0” denotes the injection well location, and η_s [-], the collision contact efficiency of particles with collector surfaces, is calculated from a correlation by Tufenkji and Elimelech (2004).

Gas phase viscosity module: Consistent with previous modeling studies of oil displacement by surfactant-stabilized CO₂ foams (e.g., Namdar-Zangeneh et al., 2009), the viscosity of aqueous phase and oil phase is assumed independent from the foam phase presence. The gas phase viscosity, on the other hand, is a function of foam texture and can increase with lamella density, gas phase saturation (Li et al., 2006), and the concentration of stabilizing agents (Worthen et al., 2013) and may exhibit shear-thinning effects based on the gas phase velocity. An auxiliary relationship for foam viscosity was selected based on the local-equilibrium model of Li et al. (2006) and was modified to include the effect of NPs on the enhancement of the apparent viscosity of foam, as well as foam killing-weakening effect due to the presence of oil. The effective gas phase viscosity, μ_g^f [Pa.s], was expressed as:

$$\mu_g^f = \mu_g^0 F_g k^{3/2} c_f n_f \left(\frac{u_g}{u_g^{ref}} \right)^{n-1} \cdot F_o \cdot F_{surf} \cdot F_{NP} \quad (\text{II.2.10})$$

where μ_g^0 [Pa.s] is the dynamic viscosity of gas phase in the absence of foam, F_g [-] is a geometric upscaling factor (Li et al., 2006), k [L^2] is the intrinsic permeability, the

term $\left(\frac{u_g}{u_g^{ref}}\right)^{n-1}$ accounts for shear-thinning effects, with u_g [m/s] and u_g^{ref} [L T⁻¹] as the gas phase velocity at a given position and time and from a reference state, respectively. n [-] is a shape parameter, and n_f [L⁻³] is the foam texture, a measure of the density of the lamellae, and is expressed according to Li et al. (2006) as:

$$\left[\begin{array}{ll} n_f = C_{nf} \left(\frac{S_g}{S_{gm}}\right)^m & S_g < S_{gm} \\ n_f = C_{nf} & S_{gm} < S_g < S_g^* - \varepsilon \\ n_f = C_{nf} \left(\frac{S_g^* + \varepsilon - S_g}{2\varepsilon}\right) & S_g^* - \varepsilon < S_g < S_g^* + \varepsilon \\ n_f = 0 & S_g^* + \varepsilon < S_g \end{array} \right. \quad (\text{II.2.11})$$

where C_{nf} [m⁻³] is constant coefficient, and m [-] is a shape parameter. As gas saturation increases from zero, the foam generation rate is greater than foam coalescence rate, which is known as the “lamella density accumulating region”. S_{gm} [-] corresponds to a gas phase saturation above which the foam generation rate and coalescence rate will be equal resulting in a constant lamella density, C_{nf} , until gas saturation reaches the critical saturation, S_g^* [-], signaling an abrupt destruction of the lamellae.

F_o [-], F_{NP} [-] and F_{Surf} [-] are reduction mobility factors denoting, respectively, the effects of oil-saturation, nanoparticles and surfactant on foam viscosity. The model of *Namdar-Zangeneh et al.* (2008) was adopted to address foam killing and weakening effect due to oil presence:

$$\left[\begin{array}{ll} F_o = 0 & S_o^* < S_o < 1 - S_{wr} \\ F_o = \left(\frac{S_o^* - S_o}{S_o^* - S_o^{min}}\right)^{e_1} & S_o^{min} < S_o < S_o^* \\ F_o = 0.5 + \frac{\arctan[e_2(S_o^{min} - S_o)]}{\pi} & S_{or} < S_o < S_o^{min} \end{array} \right. \quad (\text{II.2.12})$$

where S_o^{min} [-] is the lower oil saturation below which oil has a weakening effect on foam viscosity, and S_o^* [-] corresponds to an oil saturation above which foam cannot exist. e_1 [-] and e_2 [-] are shape parameters.

The effect of stabilizing agents on foam viscosity was modeled by incorporating the proposed model of Liu et al. (2010) which expresses the reduction mobility factor due to surfactant concentration, C_{surf} [g/L], as:

$$\left\{ \begin{array}{ll} F_{Surf} = \left(\frac{C_{surf}}{C_{surf}^*} \right)^{epSurf} & 0 < C_{surf} < C_{surf}^* \\ F_{Surf} = 1 & C_{surf} \geq C_{surf}^* \end{array} \right. \quad (II.2.13)$$

in which C_{surf}^* [g/L] is the concentration above which foam exhibits a maximum apparent viscosity, and $epSurf$ [-] is a shape parameter. An analogous model was used to account for stabilizing effect of NPs.

II.2.2. Solution Algorithm

The simulator implements a sequential 4-step call-procedure to model foam transport: (1) the multi-phase flow module, (2) multi-species transport module, (3) the auxiliary gas phase viscosity module, and (4) advancing the time-interval of calculations until the total simulation time is reached. The flowchart of solution algorithm is presented in Fig. II.2.3.

1. The flow module implements an upstream weighing spatial discretization scheme coupled with a generally weighted approach for temporal discretization to solve the phase mass-balance equations sequentially by (1) first solving Eq. 3.a, (2) using the updated S_w and f_w to solve Eq. 3.b, and calculating S_o -values from Eq. 3.c. Phase pressures are then computed using the multiphase extension of Darcy's law.
2. The flow module then passes the updated phase saturation and velocities to the transport module where the new concentrations of surfactant and NPs will be determined at each point in space from the solution to Eq. 5.
3. The gas phase viscosity model then use the updated phase saturation and velocity data, as well as the concentrations of stabilizing agents to compute and update the spatial distribution gas phase viscosity.
4. Computations will proceed to the next time step.

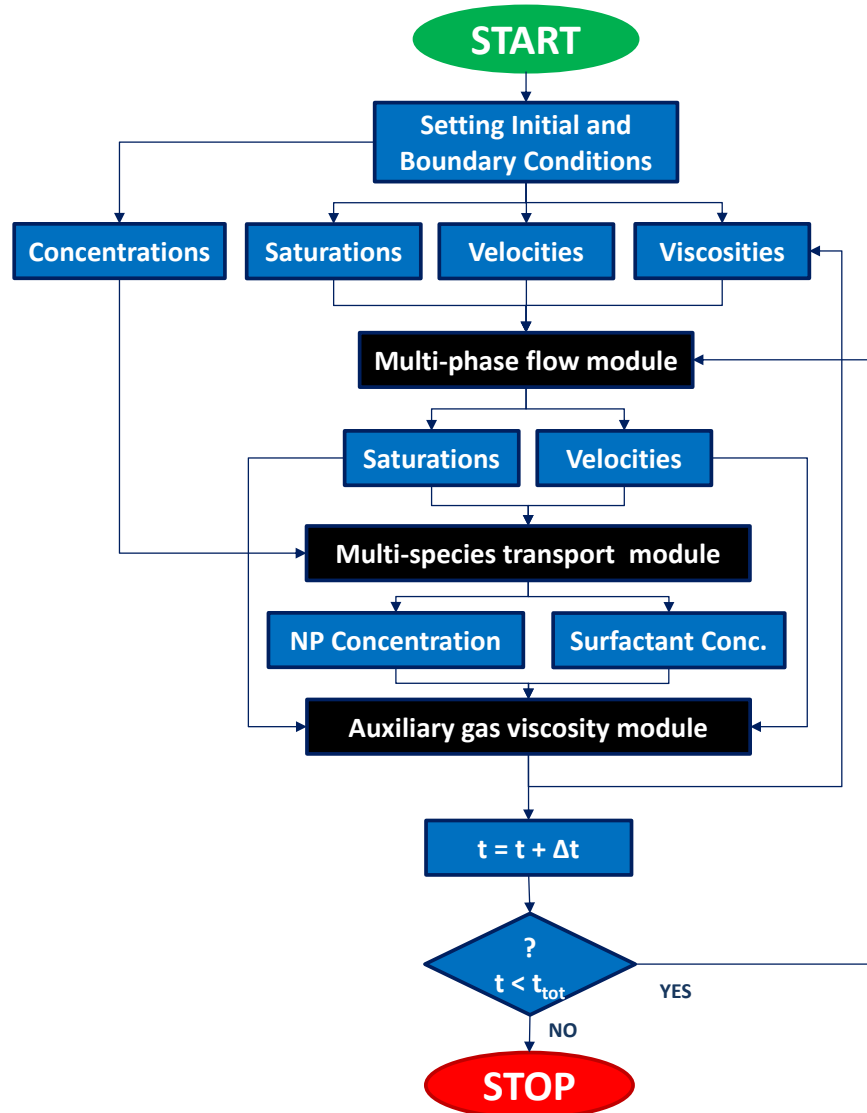


Figure II.2.3. The solution algorithm flow chart.

II.2.3. Simulations and Results

The numerical simulator for the generation and transport of nanoparticle-stabilized CO₂-in-brine (NP-CW) foam in radial multi-layered unfractured rock formations that was developed and presented in the previous project periods, was implemented to explore and compare the effect of (i) formation permeability – foam viscosity relationship, (ii) the transport and retention properties of nanoparticle, and (iii) the injection scheme of nanoparticles and CO₂ (i.e. co-injection versus slug release of NPs) on CO₂ flood conformance and pressure response. The

input parameters were selected consistent with the filed data (due to the agreement of confidentiality between our group at UT and the operator, a generic set of scenarios is employed to demonstrate the capabilities of our numerical simulator in this report). A summary of model inputs is given in Table III.1. Figure III.1 illustrates the generic permeability field used in all simulations ranging uniformly between 50-500 mD. In this section, flow and transport simulations are presented with and without including foam effects.

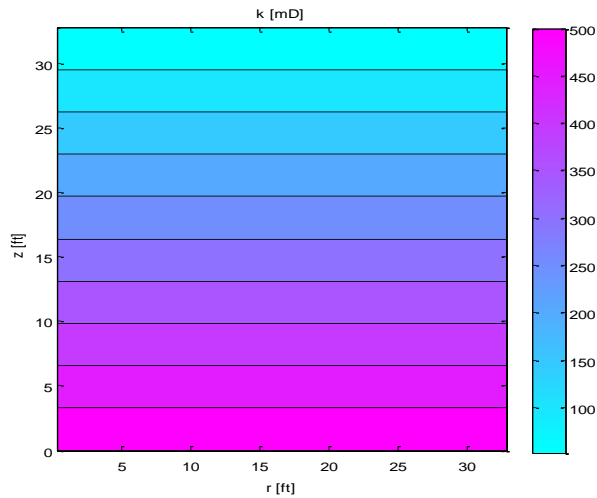


Figure II.2.4. The permeability field implemented in the demonstrative simulations. The examples focus on the near-wellbore region ($r < 10$ m) which strongly influences the injection pressure/rate response.

Table II.2.1. Model input parameters implemented in demonstrative simulations. Selected values are consistent with the field data provided by the involved operator.

<i>Property</i>	<i>Unit</i>	<i>Value</i>	<i>Description</i>
Q_t	bbl/day	500	Total injection rate, reservoir conditions
$f_{g,in}$	-	0.75	Injected gas fraction (foam quality)
P_{re}	psi	2300	Far-field reservoir pressure
S_{wi}	-	0.1-0.7	Initial water saturation
S_{oi}	-	0.05-0.3	Initial oil saturation
S_{wr}	-	0.1	Connate water saturation
S_{gr}	-	0.0	Residual gas saturation
S_{or}	-	0.05-0.2	Residual oil saturation
μ_w	cP	1.0	Dynamic viscosity of water
μ_g^0	cP	0.05	Dynamic viscosity of CO ₂
μ_o	cP	8.1	Dynamic viscosity of oil
$C_{0,NP}$	wt%	0.5	Influent NP concentration
r	m	10	Simulated distance range
ϕ	-	0.3	Formation porosity

Model predictions of flow and distribution of fluid phases with and without foam effects are illustrated in figures II.2.4 and 5, where CO₂ is co-injected with either NP suspension or NP-free brine at a gas volume fraction of 0.75 for 10 hours at a flow rate of 500 bbl/day. Creation of more viscous foam in higher permeability layers results in a significant increase in pressure response at the injection well (>100psi) and reduces gas phase mobility in those regions enough to divert flow toward lower permeability layers (figure II.2.5.a). Another consequence of gas phase mobility reduction in the foam-swept regions is reduction of the residual oil saturation (figure II.2.5.b), which is explained by the dependence of S_{or} on gas phase saturation which in turn increases with the reduction of gas phase mobility due to foam formation.

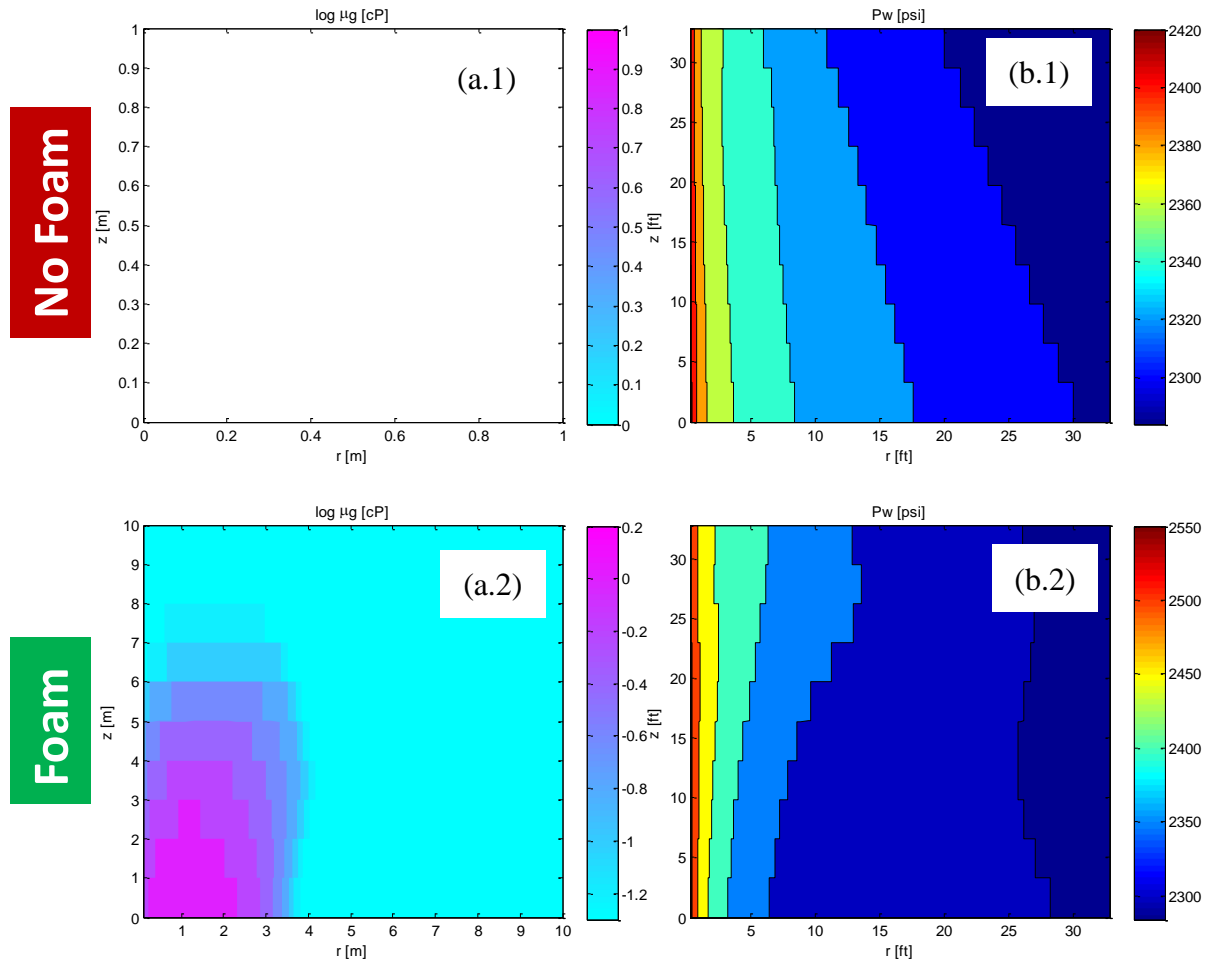


Figure II.2.5. Simulated (a) effective gas viscosity and (b) pressure profiles after 10hr co-injection of (1) CO₂ and reservoir B brine and (2) 0.5% w/v EOR-5XS particles at 0.75 gas fraction at a constant flow rate of 500 bbl/day.

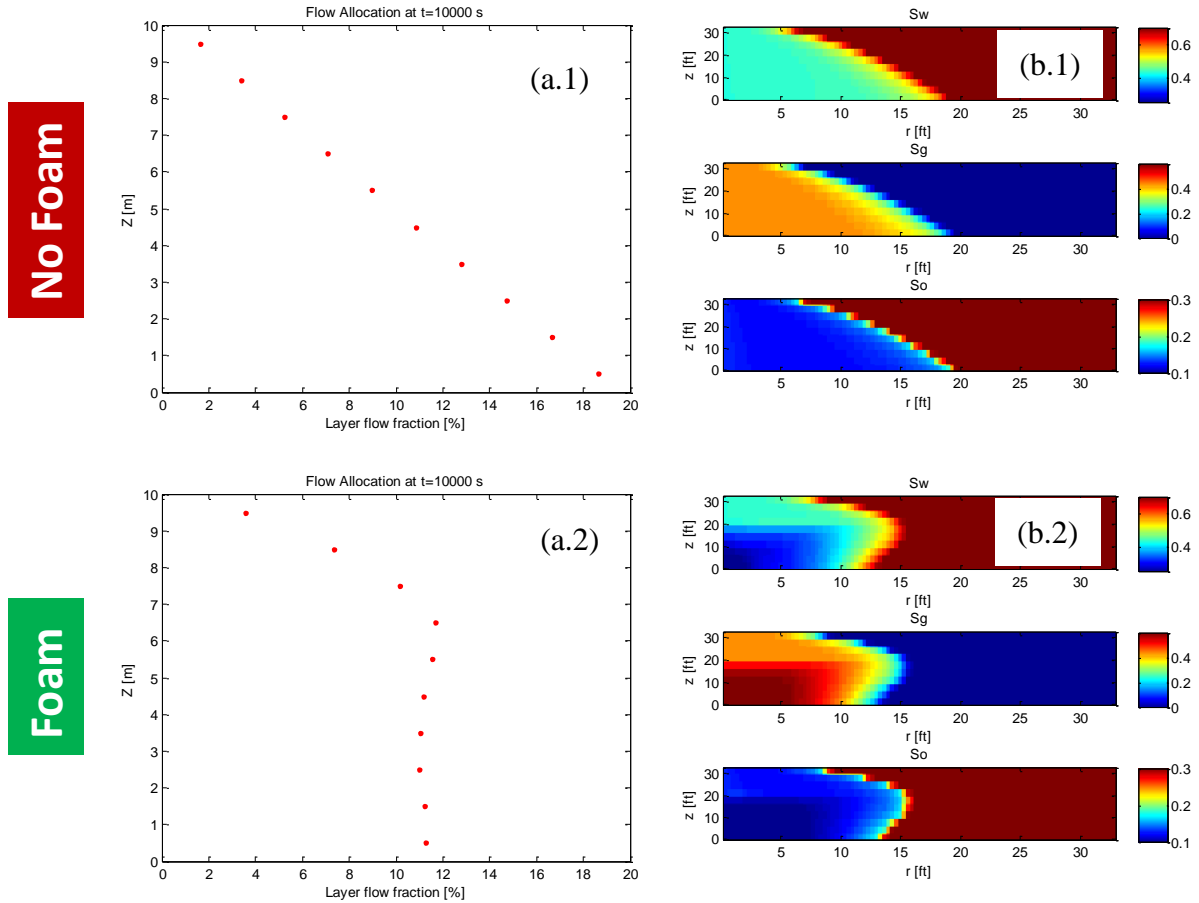


Figure II.2.6. Simulated (a) flow allocation and (b) phase saturation profiles after 10hr co-injection of (1) CO₂ and reservoir B brine and (2) 0.5% w/v EOR-5XS particles at 0.75 gas fraction at a constant flow rate of 500 bbl/day.

II.2.3.1. Intrinsic permeability-foam viscosity relationship effect on flood conformance

If the generated foam exhibit similar strength in all layers, simulation results suggest that should foam be generated in all layers, flood conformance is only slightly improved compared to a no foam scenario (figure III.7) despite the significant pressure response. Improved flood conformance (i.e. flow diversion towards lower permeability streaks) can be achieved if higher permeability layers produce stronger (i.e. more viscous) foam

According to theories which lay the basis of the local equilibrium-based population-balance model of Li and Hirasaki, adapted in this study, the maximum foam viscosity in a heterogeneous porous medium scales with $k^{3/2}$ (Ransohoff and Radke, 1988):

$$\mu_g^f = \mu_g^0 \mathbf{F}_g k^{3/2} n_f \left(\frac{u_g}{u_g^{ref}} \right)^{n-1} \cdot F_o \cdot F_{surf} \cdot F_{NP} \quad (\text{III.1})$$

This $\mu_g^{app} - k$ relationship promotes formation of stronger foam in higher permeability streaks. Several experimental reports support the direct dependence of μ_g^{app} on k . The order of dependence, however, does not always follow theory. For example, the observations of Friedmann et al. (1994) and Gauglitz et al. (2002) suggest a linear relationship between effective viscosity and permeability. In order to better understand the effect of this relationship on model predictions, the sensitivity of flood conformance on the order of dependence of gas viscosity to permeability was analyzed.

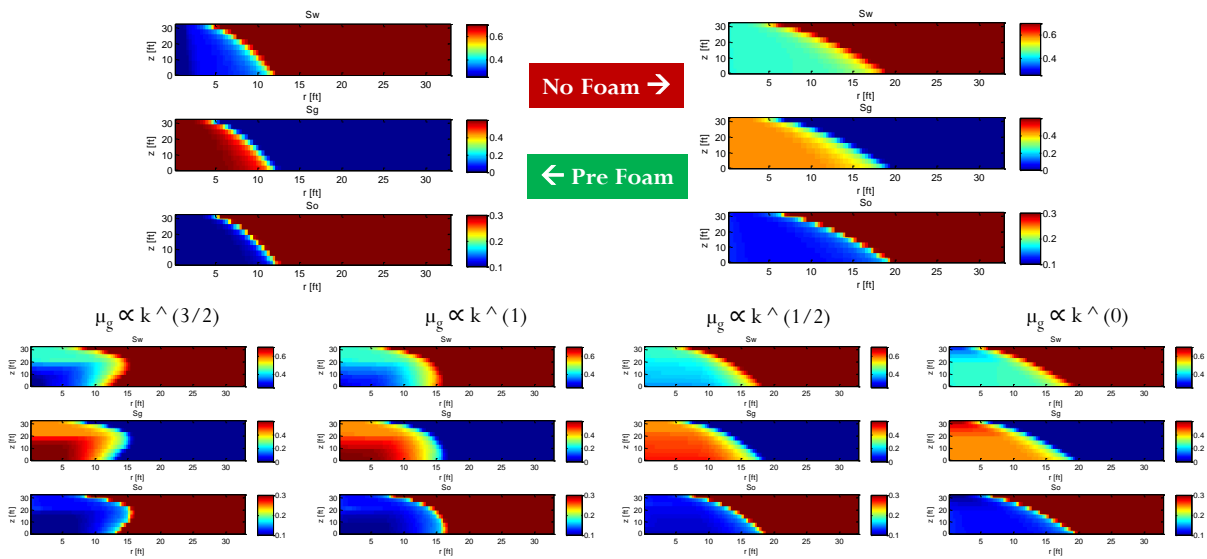


Figure II.2.7. The predicted phase saturation profiles: A comparison of no-foam – pre-generated foam (top row) and sensitivity to the order dependence gas viscosity on permeability (bottom row).

Simulation results suggest that as the power of k in equation III.1 is reduced from $3/2$ to zero the contrast in foam strength induced by variation in permeability decreases (figure II.2.8), and so does the pressure response (figure II.2.9) and the predicted flow diversion toward less permeable layers (figure II.2.10). A linear dependence of μ_g^{app} on k , as suggested in previous reports, results in the gas viscosity contrast required for improved conformance control.

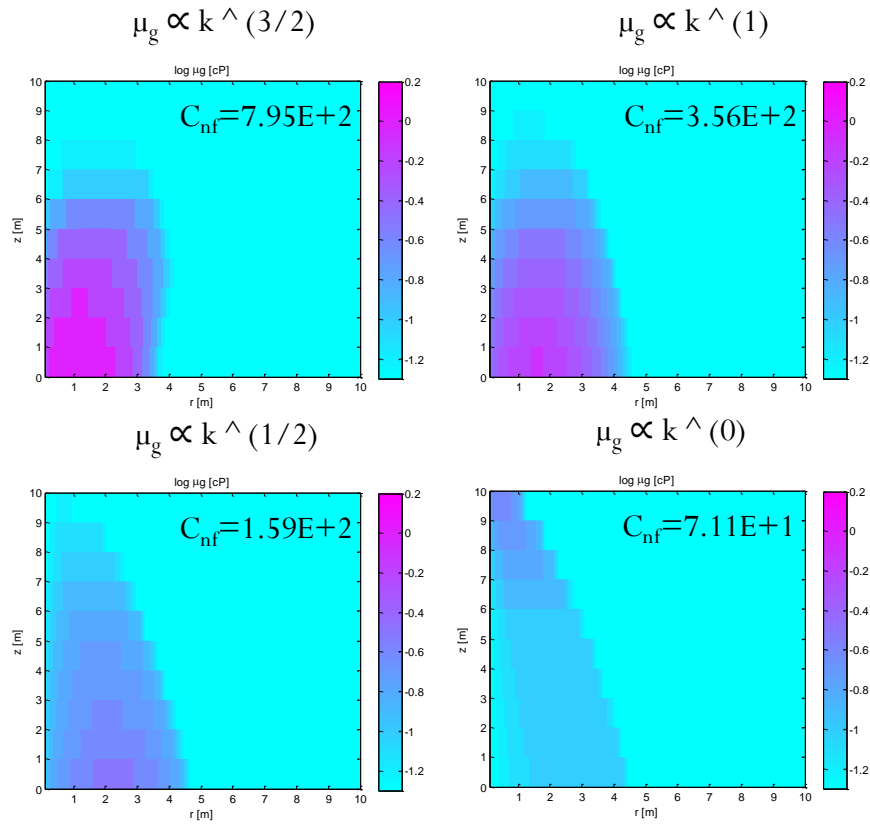


Figure II.2.8. The predicted spatial distribution of effective gas viscosity: Sensitivity to the order dependence gas viscosity on permeability.

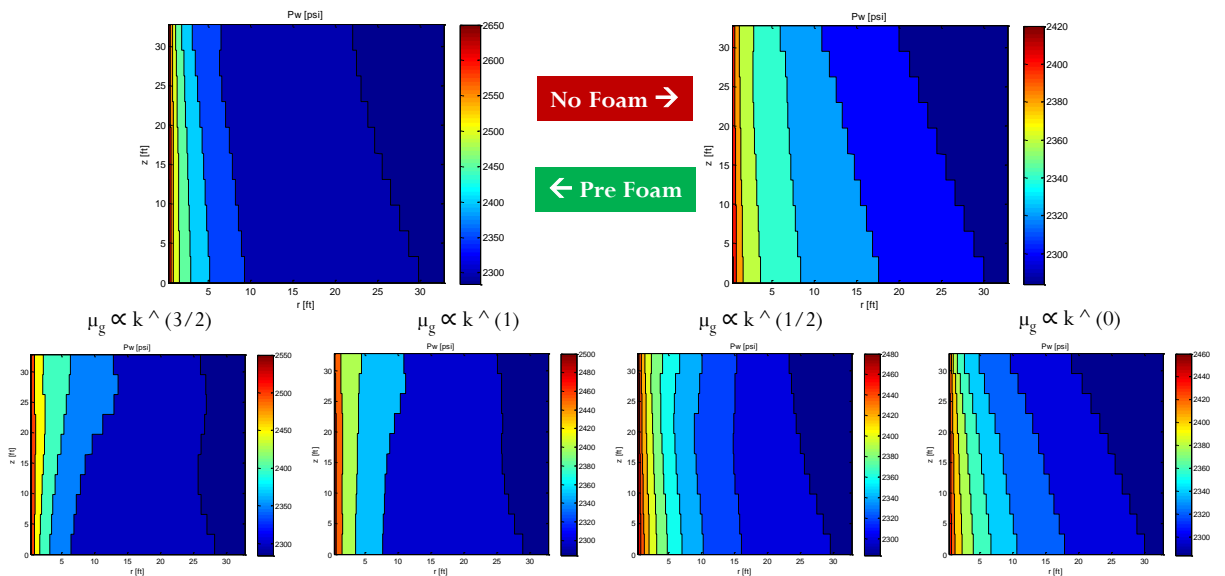


Figure II.2.9. The predicted pressure distribution profiles: A comparison of no-foam – pre-generated foam (top row) and sensitivity to the order dependence gas viscosity on permeability (bottom row).

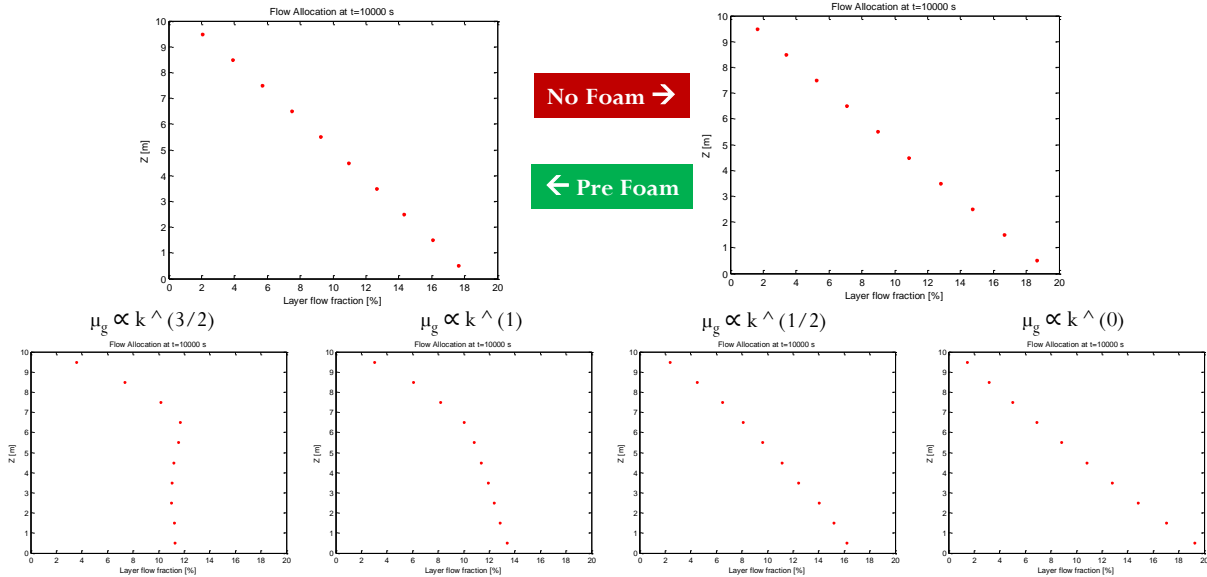


Figure II.2.10. The predicted flow allocation between layers of variable permeability: A comparison of no-foam – pre-generated foam (top row) and sensitivity to the order dependence gas viscosity on permeability (bottom row).

II.2.3.2. Effect of nanoparticle mobility on flood conformance

EOR-5SX and EOR-12 particles have exhibited low to negligible affinity for attachment to solid phase surfaces (figure III.8) in a series of transport sandstone core and sand column experiments described under Task I of this report. The travel length of particles in our bench-top experiments is one foot whereas considerably larger travel distances at significantly lower pore velocities are conceivable in field-scale problems. Hence, we incorporated the particle-solid phase attachment efficiencies estimated from experimental data in the upscaled foam injection simulations to explore the effect of NP retention on the efficacy of NP-CW foam for flood conformance.

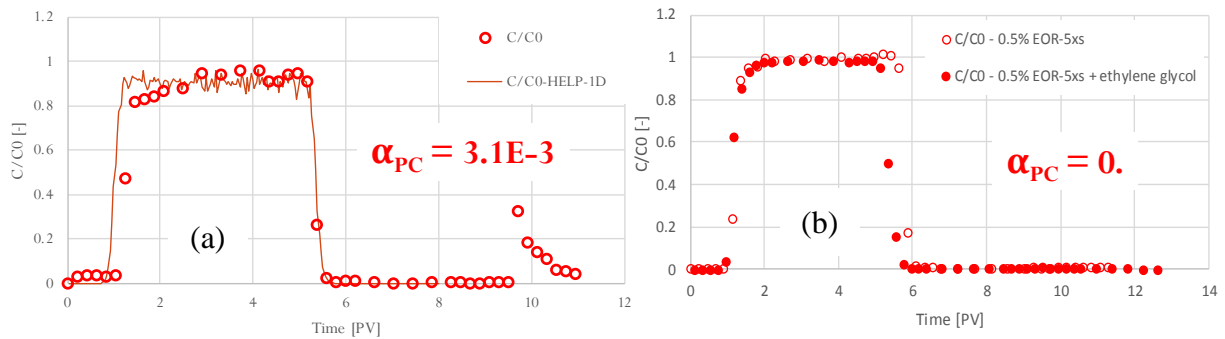


Figure II.2.11. Measured effluent EOR-5XS NP concentrations transported through 1-ft long Ottawa sand columns in (a) synthetic seawater and (b) API brine.

Two scenarios of foam generation and transport for (i) tracer (i.e. non-attaching) NPs and (ii) particles that can be captured by solid phase were considered. In the latter case, the attachment of NPs was modeled using (i) the clean-bed colloid filtration theory (CFT) and (ii) a modified version of CFT that considers a limited particle capture capacity for solid surface. Simulations suggest that if particle attachment occurs as described by CFT model (i.e. an infinite retention capacity), the effective travel distance of NPs will be limited to ca. 5ft from the injection well (figure II.2.12.b). This loss of NPs to the rock formation results in a reduction in the strength and propagation distance of NP-CW foam (figure II.2.13.a) thereby affecting the predicted improvement of flood conformance. Note that, despite the loss of NPs away from the injection well, the predicted flow diversion toward lower permeability layers is still significant compared to no-foam scenario due to near-well gas phase viscosification in higher permeability zones.

Results based on a generic maximum retention capacity of 0.1 g/kg dry solid, if supported by experiments, suggest effective transport of particles away from the injection well (figure III.9.c) depending upon the capacity of solid surfaces for the capture of particles. This is explained by the saturation of capture sites that would allow for further migration of particles downgradient of upstream regions. Resultantly, a minimal influence of particle deposition on the strength and transport of generated foam is predicted in this scenario.

This part of our modeling study highlights the role of NP mobility as an important factor that can control the efficacy of NP-foam injection for improved flood conformance and emphasizes the need for an accurate characterization of the transport properties of NPs for meaningful prediction of NP-CW foam in upscaled problems.

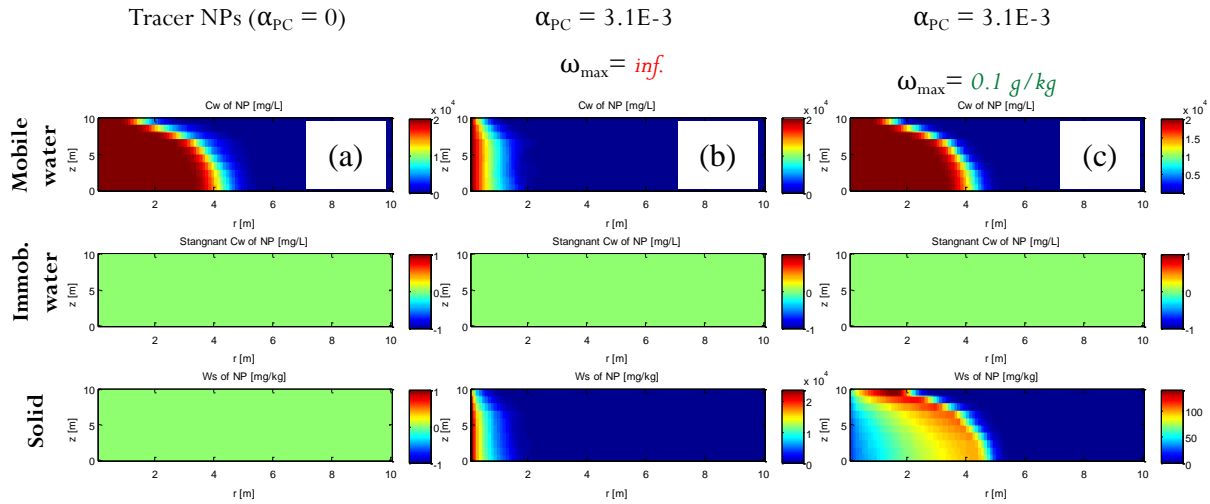


Figure II.2.12. The simulated NP concentration profiles for (a) tracer particles, and particles that attach to the solid phase with (b) an infinite and (c) limited particle retention capacity.

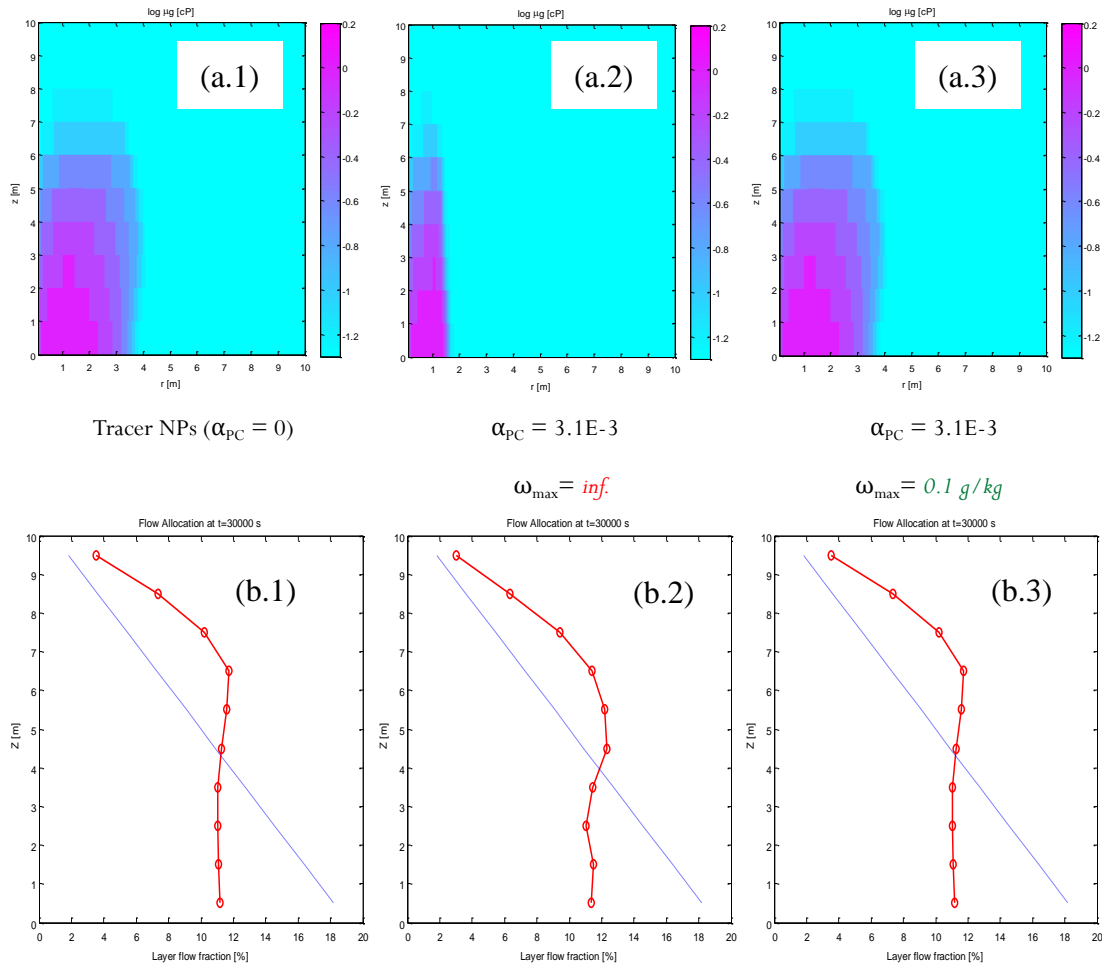


Figure II.2.13. Simulated (a) effective gas viscosity profiles and (b) flow allocation among layers of variable permeability predicted for (1) tracer particles, and particles that attach to the solid phase with (2) an infinite and (3) limited particle retention capacity.

II.2.3.3. Effect of nanoparticle and CO₂ injection on flood conformance

Foam generation and transport experiments conducted in laboratory settings generally involves co-injection of liquid and gas phases at a fixed gas volume fraction. In field practices, however, carrying out a co-injection scheme is rather problematic and impractical, and a successive (sometimes periodic) release of fluid phases is often practiced. Hence, exploring the effect of the injection scheme on foam-induced improvement of CO₂ flood conformance was another part of our modeling efforts in this project period. The multiphase flow module of our numerical simulator was modified to add the capability to address a slug release of nanoparticle suspension during CO₂ flood. The injection scheme was refined to 2.5 hr injection of either (i) NP-free reservoir B brine or (ii) 0.5% w/v EOR-5SX particles followed by 7.5 hr CO₂ flooding at a constant 500 bbl/day flow rate to introduce identical amount of CO₂ and NPs in simulations presented in previous sections of this report.

Simulation results predict the formation of a viscous front in the mixing zone between NP-containing slug and CO₂. Mixing of the two fluids happens because of the larger mobility of the CO₂ phase whose saturation shock front propagates faster than the NP concentration wave, which creates locations where gas phase comes in contact with NP suspension at saturations high enough to promote the division and accumulation of foam lamellae (figure II.2.14.b).

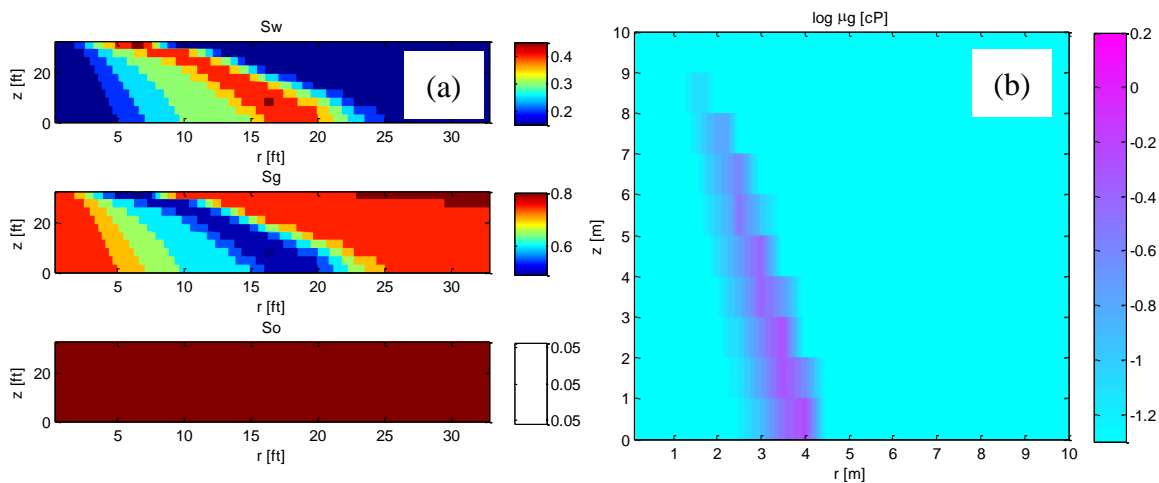


Figure II.2.14. Simulated (a) phase saturation profiles and (b) spatial distribution of effective gas viscosity after 7.5 hours of CO₂ flush subsequent to 2.5 hours of 0.5% EOR-5XS NPs at a constant flow rate of 500 bbl/day.

As a result of the formation of this viscous front, the flow diversion is predicted to occur (comparing figures II.2.15.a-b). Nevertheless, the extent to which the CO₂ flood conformance is improved is small compared to co-injection of NP and CO₂ (figures II.2.6.a and II.2.15.b). The predicted pressure response after the injection of NP-free brine (scenario I) or NP-containing slug (scenario II) (i.e. during the first 2.5 hours of injection) are identical. Upon the introduction of CO₂, however, a greater pressure build-up at the injection well is predicted for the latter scenario (figure III.13), consistent with the expected higher pressure gradient across the viscous front in the mixing zone between gas and liquid phases. Again, the magnitude of pressure difference due to foam viscosification in a slug release scenario is small (<10 psi) compared to that of the co-injection scheme (>100 psi) (figure II.2.5.b).

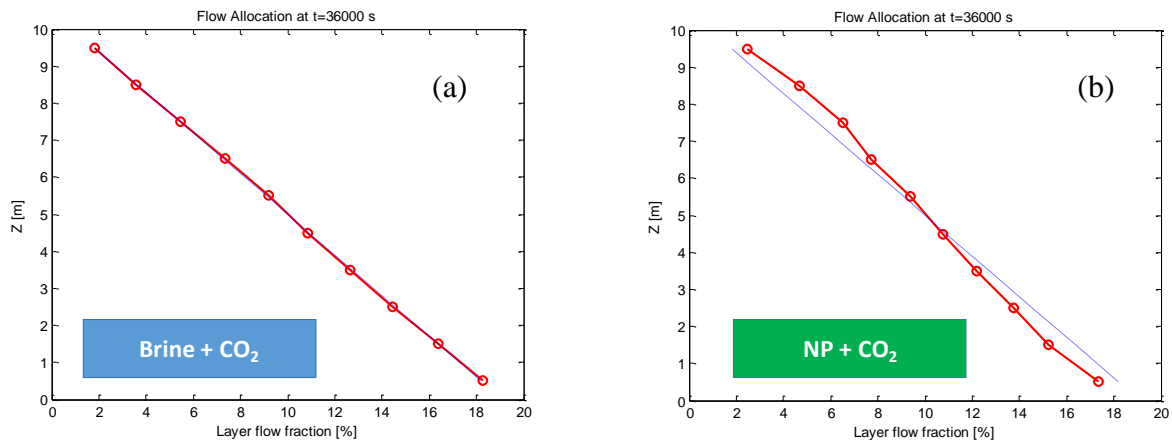


Figure II.2.15. The influence of foam formation on flow allocation between layers of variable permeability subsequent to slug release of (a) NP-free brine and (b) NP suspension followed by CO₂ flooding.

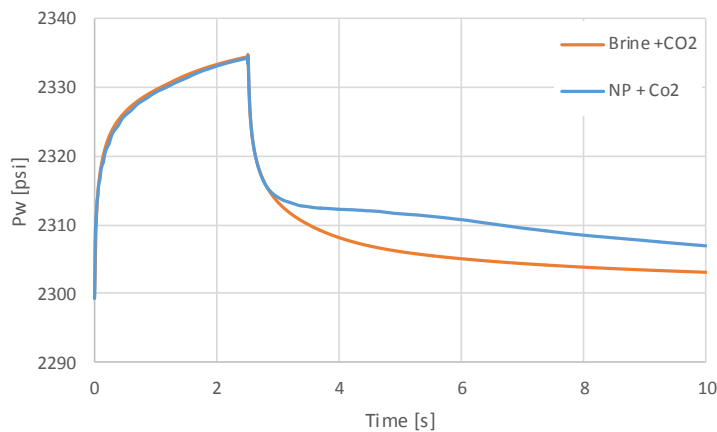


Figure II.2.16. The effect of foam generation on predicted pressure response at injection well during a slug release of brine with or without NPs followed by CO₂ flood.

II.2.4. Conclusions

Under this modeling task, we developed a radial multi-layered foam generation and transport simulator that can be applied to near-injection well field-scale foam problems. Our simulator accounts for the effects due to heterogeneity in permeability field, foam stabilizing agents, oil presence, and shear-thinning on the generation and transport of NP-C/W foams. The foam simulator was implemented in an industry-sponsored experimental-mathematical study to (i) analyze CO₂ injection data received from a field operator and (ii) aid with the design of a foam injection pilot test. The results presented in this section not only demonstrate the capabilities of our model, but also advocate the importance of incorporation and accurate characterization of physicochemical factors such as the viscous behavior of NP-C/W foams, shear rate or pressure gradient necessary for lamella mobilization and division, and the mobility properties of stabilizing agents under representative reservoir conditions.

Simulation results suggest that (i) if foam is created in all layers, regardless of layer permeability, flood conformance can be only slightly improved despite the predicted significant pressure build-up at the injection well. However, (ii) improved conformance can be achieved through selective generation of foam in high-permeability streaks and/or a permeability-dependent viscosification (i.e. stronger foam in higher permeability media at any given interstitial velocity above the minimum velocity required for foam generation). Also, a sensitivity study was conducted to investigate the effect NP mobility on foam generation and transport at field-scale. The results of this study suggest (iii) a slight increase of the NP attachment efficiency (attachment to the solid rock surfaces) can significantly limit the spatial propagation of foam downstream of the injection well, thereby reducing the extent of flow diversion towards low permeability layers.

II.2.5. References

1. Abriola, L.M., J.R. Lang, and K. Rathfelder, Michigan soil vapor extraction remediation (MISER) model, 1997. US Environmental Protection Agency, Research and Development, National Risk Management Research Laboratory.
2. Bishop, E.J., et al., Anionic homopolymers efficiently target zerovalent iron particles to hydrophobic contaminants in sand columns. *Environmental science & technology*, 2010. 44: p. 9069-74.
3. Elimelech, M. and C.R. O'Meila, Kinetics of Deposition of Colloidal Particles in Porous Media. *Environmental Engineering Science*, 1990. 24: p. 1528-1536.
4. Friedmann, Francois, et al. "Steam-foam mechanistic field trial in the midway-sunset field." *SPE Reservoir Engineering* 9.04 (1994): 297-304.
5. Gauglitz, P. A., et al. "Foam generation in homogeneous porous media." *Chemical Engineering Science* 57.19 (2002): 4037-4052.
6. Lake, L.W., Enhanced oil recovery, 1989. Princeton-Hall, Inc. ISBN: 0-13-281601-6.
7. Li, Y., et al., Investigation of the transport and deposition of fullerene (C60) nanoparticles in quartz sands under varying flow conditions. *Environmental science & technology*, 2008. 42: p. 7174-80.
8. Li, B., G.J. Hirasaki, and C.A. Miller, Upscaling of foam mobility control to three dimensions, 2006. SPE 99719.
9. Liu, M.K. Modelling CO2 Foam Displacements for Enhanced Oil Recovery, 2010. Master's Thesis, TU Delft.
10. Ko, Chun-Han, and Menachem Elimelech. "The "shadow effect" in colloid transport and deposition dynamics in granular porous media: measurements and mechanisms." *Environmental science & technology* 34.17 (2000): 3681-3689.
11. Namdar-Zangeneh, M., S.I. Kam, T.C. LaForce, and W.R. Rossen, The method of characteristics applied to oil displacement by foam, 2009. SPE 121580.
12. Parker, J. C., R. J. Lenhard, and T. Kuppusamy, A parametric model for constitutive properties governing multiphase flow in porous media, 1989. *Water Resource Research*, 23, 618-624.
13. Petosa, A.R., et al., Aggregation and deposition of engineered nanomaterials in aquatic environments: role of physicochemical interactions. *Environmental science & technology*, 2010. 44: p. 6532-49.
14. Phenrat, T., et al., Particle Size Distribution, Concentration, and Magnetic Attraction Affect Transport of Polymer-Modified Fe0 Nanoparticles in Sand Columns. *Environmental Science & Technology*, 2009. 43(13): p. 5079-5085.
15. Tufenkji, N. and M. Elimelech, Correlation equation for predicting single-collector efficiency in physicochemical filtration in saturated porous media. *Environmental science & technology*, 2004. 38: p. 529-36.
16. Worthen, A.J., H.G. Bagaria, Y. Chen, S.L. Bryant, C. Huh, and K.P. Johnston, Nanoparticle-stabilized carbon dioxide-in-water foams with fine texture, 2013. *Journal of Colloid and Interface Science*, 391, 142-151.
17. Yao, K.-m., Habibian M.T., and C.R. O'Meila, Water and waste water filtration: concepts and applications. . *Environmental Engineering Science*, 1971. 5: p. 1105-1112.

III. Nanoparticle Mobility – Nanoparticle Aggregation and Transport at Elevated Salinity

The results of this coupled experimental-mathematical modeling study of surface-coated silica NPs transport and retention at high salinity conditions of a specific oil reservoir were incorporated in a technical manuscript that was submitted to the Journal of Petroleum Science and Engineering:

Kim, Ijung et al. “Aggregation of silica nanoparticles and its impact on particle mobility under high salinity conditions” (2015) – J. of Petroleum Sci. Engineering – *Submitted*.

III.1. Abstract

CO₂ foams that are stabilized with nanoparticle have a number of advantages over those stabilized with surfactant, to improve sweep for CO₂ enhanced oil recovery (EOR) processes. Two key advantages in using nanoparticle-stabilized foam are the robust stability of nanoparticles on the gas-liquid interface at high-salinity and elevated temperature conditions and low retention of nanoparticles in reservoir rock. In brines of high salinity with large divalent-ion content, however, nanoparticles are susceptible to aggregation, which can remarkably alter particle mobility. The loss of nanoparticles serving as foam-stabilizing agents can impair foam’s effectiveness for EOR applications.

To better understand the nanoparticle retention/transport under high salinity conditions, the aggregation of the surface-treated silica nanoparticles was studied as a function of salinity and nanoparticle concentration. At pH 8.5, an enhancement in aggregation kinetics occurred with increasing calcium concentration, eventually leading to gel formation in two days at API brine (8% NaCl and 2% CaCl₂) with 4% w/v nanoparticle concentration. However, when the pH was reduced to ca. 3, close to the CO₂ saturated condition, the aggregation was insignificant (~10 nm increase in diameter) regardless of the salinity and the particle concentration over 10 days. At high pH, divalent cations are believed to cause bridging of the nanoparticles with the availability of the negative surface charges on the particle surface.

In the transport test of silica nanoparticles in the sandpack column, negligible amount of nanoparticles was retained (< 7% of injected mass) with non-aggregated nanoparticles and the aggregates less than 235 nm regardless of flow rate. However, the retention of larger aggregates (> ca. 1000 nm) was enhanced as Darcy velocity decreased from 71 to 7.1 m/day. The pressure drop across the column steadily increased due to the increased viscosity of the nanoparticle suspension, suggesting the continuous pore straining as more aggregates were injected to the column. However, the magnitude of the pressure drop changed during the nanoparticle injection period greatly increased as Darcy velocity was decreased. For these high pressure drop column tests, the aggregate sizes in the effluent were less than those in the influent. The viscosity of the nanoparticle aggregates that showed the high pressure drop continuously decreased with shear rate, suggesting their deformation and possibly some breakage. The modeling based on a modified version of clean-bed filtration theory was able to explain experimental breakthrough curves only of the non-aggregated and slightly aggregated particles (e.g., aggregate size < 1000 nm), suggesting further considerations are necessary to understand the physical effect of aggregation on the transport of larger aggregates. These results suggest the possible breakdown of the aggregates due to the hydrodynamic force, therefore recovering the mobility of silica nanoparticles in the porous media.

These observations demonstrate that silica nanoparticle aggregation can be prevented by increasing flow rate and lowering pH. The findings in this study would provide an insight on the behavior of nanoparticle in the reservoirs and the guideline for the application of the nanoparticles on the enhanced oil recovery operation.

III.2. Introduction

Nanoparticles have an important application potential in the oil and gas industry from exploration to production and distribution. Especially for the enhanced oil recovery (EOR) processes, active research efforts are ongoing to employ nanoparticle-stabilized foam and emulsion for mobility control purposes (Aroonsri et al., 2013; Espinoza et al., 2010; Zhang et al., 2009). Since the chemical properties of nanoparticles are nearly unchanged under harsh oil reservoir conditions such as high temperature and high salinity (Zhang et al., 2010), their application would be more promising than the use of surfactants. To take advantage of

nanoparticle-stabilized foams/emulsions, that is, to improve volumetric sweep efficiency, it is critical to understand and control their mobility and long term transport required for successful field-scale displacement of oil. Therefore, an understanding of particle aggregation, and its influence on the retention characteristics of nanoparticles is essential to effectively designing a nanoparticle-mediated CO₂ foam flooding scheme.

To generate the nanoparticle-stabilized foams, the particle concentration needs to be above a certain value to maintain foam stability, especially in a high salinity reservoir condition (Espinoza et al., 2010; Yu et al., 2012). However, when the nanoparticles are concentrated, the collisions between nanoparticles could potentially result in greater aggregation (Holthoff et al., 1996). This change in the stability of nanoparticles would result in a high affinity to other surfaces they can contact with (Solovitch et al., 2010). Aggregation is normally derived by overcoming the energy barrier in electrostatic and entropic interaction between particles. In the case of nanoparticles whose transport behavior is dictated by Brownian motions, the initial particle concentration is a key factor governing the aggregation kinetics (Chen and Elimelech, 2006). For oil reservoir applications, the reservoir brine usually has a high salinity so that the electrostatic characteristic of particles is virtually eliminated (Vandesteeg et al., 1992).

Therefore, the possibility of nanoparticle aggregation, when they are considered for subsurface injection, must be carefully investigated. To prevent the instability of nanoparticles in the aggregation-inducing, high-salinity environment, the surface treatment of nanoparticles should provide steric repulsion between particles keeping them stable along their long travel distance thereby ensuring the longevity of nanoparticle-stabilized foam in the reservoir (Nguyen et al., 2014).

In this study, particle aggregation and its effects on the transport behavior of the surface-treated silica nanoparticles were studied at a range of salinities and particle concentrations representative of practical field conditions. A sand-pack column study was conducted to investigate the coupled effect of flow velocity and aggregation on the retention of silica nanoparticles. Two existing colloidal filtration theory-based models of nanoparticle transport in porous media were adapted and applied to describe the experimental observations, necessary for field application scale-up purposes.

III.3. Materials and Methods

Silica nanoparticles: Spherical silica nanoparticles (nominally 5 nm diameter; see below) were provided by Nissan Chemical (Houston, TX) as a 20% w/v aqueous dispersion. The size distribution of the nanoparticles was measured by dynamic light scattering (DLS, Malvern zetasizer) and transmission electron microscopy (TEM, FEI Tencai). The stock suspension was diluted in the synthetic brine of different composition to obtain the desired nanoparticle concentration for the study of the aggregation, deposition, and transport in sandpacks.

Aggregation test: Silica nanoparticle suspensions varying in concentration (0.5-4.0% w/v) were prepared in three different brines (8% NaCl; 8% NaCl+1% CaCl₂; and 8% NaCl +2% CaCl₂) and two different pH levels (3 and 8.5). The low pH value, created by the addition of HNO₃, is close to the pH of CO₂-saturated water (Peng et al., 2013). The high pH condition was achieved without the addition of any acids or bases. 40 mL of brine was transported to the vials which were kept in a stationary condition without any agitation. The particle aggregate size change over the test period was monitored by sampling 1 mL of dispersion to the cuvette at each sampling time. Sampling was continued until the aggregate sizes became too large (> 1000 nm) to have an accurate measurement.

Deposition test: 2wt% silica nanoparticles were kept in API brine (8% NaCl +2% CaCl₂) for 72 hrs, during which the particle aggregation slowly occurred. While the aggregation was continued, the deposition test was carried out using the quartz crystal microbalance with dissipation (QCM-D, Biolin Scientific) in which silica Q-sensor was mounted. The test was done at three different times of aggregation stage to investigate the effect of aggregate size on the deposition. Before the test, the QCM-D was flushed with DI water until the frequency and dissipation signals were stabilized at zero. For each test, the aggregate suspension was injected for 10 min. The flow rate was fixed at 0.15 mL/min during the entire test period. Based on the frequency data, the mass of the adsorbed silica nanoparticle aggregates onto the silica surface were calculated using the Sauerbrey model embedded in the QCM-D software (QTool). After each test, the silica Q-sensor was rinsed with DI water and immersed in 2% sodium dodecyl sulfate solution for 30 min and rinsed with DI water and dried with nitrogen gas.

Viscosity measurement: The viscosity of the aggregate suspension was measured using the rheometer (ARES-LS1, TA Instruments) with the double-wall couette geometry. Samples of different aggregate size were prepared by keeping different nanoparticle concentrations in API brine for at least 48 hrs. All the measurements were performed in the steady rate sweep test mode between 1 and 1000 s⁻¹ in shear rate and the temperature was controlled by a circulator at 25°C.

Transport test: A glass cylindrical column (2.54 cm in diameter and 30.48 cm in length, Kontes Chromaflex column, Kimble-Chase) was used for the nanoparticle dispersion flow test. The Ottawa sand (U.S. Silica) was used which was sieved using a 300 and 400 µm mesh (mean diameter: 350 µm). Once the column was packed with the sand, it was flushed with the background brine at least 30 pore volumes before the test started. The nanoparticle suspension was stored in a 400 mL floating-piston accumulator and injected from the accumulator to the column by pumping water into the accumulator. The pumping rate (2.5, 5, and 25 mL/min) was controlled to yield a nanoparticle residence time in the column ranging from 2 to 24 min. The nanoparticle was injected for ca. 4.5 pore volumes and followed by rinsing with the background particle-free brine solution for another 4.5 pore volumes. To monitor the pressure drop across the column, pressure transducers were installed at the inlet and outlet of the column. Different aggregate states of silica nanoparticles were tested in API brine (8% NaCl and 2% CaCl₂). The influent and effluent samples were diluted in 3% trace metal grade HNO₃ and analyzed using inductively coupled plasma-optical emission spectrometry (ICP-OES, Varian). The schematic test setup is shown in Figure III.1 and the experimental conditions are summarized in Table III.1.

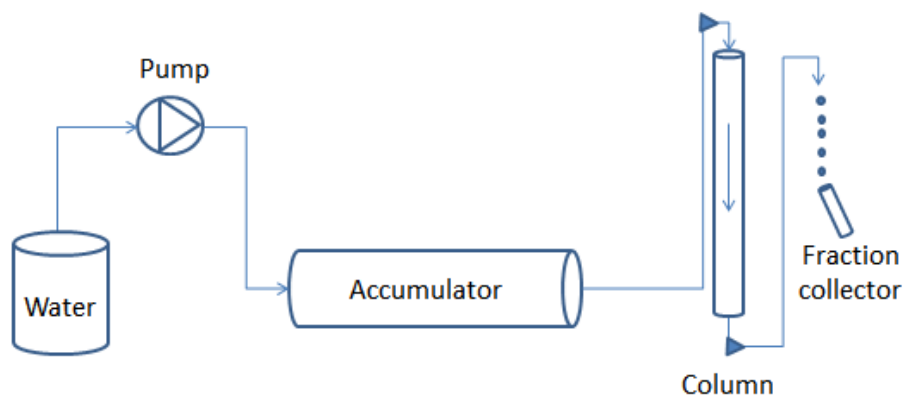


Figure III.1. Schematic view of transport test setup.

Table III.1. Summary of the transport tests with different particle sizes and velocities.

Experiment #	Pre-aggregation	Particle size (nm)	Darcy velocity (m/day)
1	No	5*	71
2	No	25*	71
3	Yes	95	71
4	Yes	235	71
5	Yes	1487	71
6	Yes	2060	71
7	No	5*	7.1
8	Yes	1614	14.2
9	Yes	1554	7.1

* Reported by manufacturer

Modeling Approach: Two commonly used and extensively studied colloidal transport models were adapted and employed to describe the particle retention and transport: (i) a clean-bed colloid filtration theory (CFT) model (Yao et al., 1971) and (ii) a modified version of CFT model (MFT) that incorporates a limited capacity for the attachment of particles to collector surfaces (Elimelech and Omelia, 1990). According to both models, particles are removed from aqueous suspension through the mechanisms of interception, diffusion, and sedimentation. A general mass balance equation for particle transport can be expressed as (Li et al., 2008):

$$\frac{\partial}{\partial t}(\phi C + \rho_b S) + \frac{\partial}{\partial x} \left[\phi \left(v_w C - D_w^h \frac{\partial C}{\partial x} \right) \right] = 0 \quad (\text{III.1})$$

where C [M L^{-3}] and S [M M^{-1}] are the aqueous and retained concentration of particles, respectively, ϕ [-] is porosity, ρ_b [M L^{-3}] is bulk density of porous medium, and v_w [L T^{-1}] and D_w^h [$\text{L}^2 \text{T}^{-1}$] denote interstitial velocity and hydrodynamic dispersion coefficient, respectively. CFT and MFT models consider rate-limited attachment kinetics and a first-order expression for the re-entrainment of the retained particles:

$$\frac{\rho_b}{\theta_w} \frac{\partial S}{\partial t} = k_{att} \psi C - \frac{\rho_b}{\theta_w} k_{det} S \quad (III.2)$$

Here k_{att} [T^{-1}] and k_{det} [T^{-1}] are rate constants representing attachment and detachment processes, where $k_{att} = \frac{3}{2} \frac{(1-\phi)v_w}{d_c} \alpha_{PC} \eta_0$, with d_c [L], mean collector diameter; α_{PC} [-], attachment efficiency; and η_0 [-], single collector contact efficiency. The latter efficiency term was computed from a semi-empirical correlation equation (Tufenkji and Elimelech, 2004) via estimating a number of dimensionless parameters representing the forces and interactions between particles and a single collector. The distinction between CFT and MFT models is in the expression of ψ [-] function in equation (III.2), which is a site blocking function. $\psi = 1$ for unlimited particle attachment (i.e., CFT model) and in case of a limited attachment capacity (i.e., MFT model) $\psi = 1 - \frac{S}{S_{max}}$ with S_{max} [$M M^{-1}$] being the maximum retained concentration.

III.4. Results and Discussion

Nanoparticle characterization: The mean hydrodynamic diameter and the TEM core diameter was 13 nm (Figure III.2(a)) and 9 nm (Figure III.2(b)), respectively. The difference between the two measured diameters is believed to be due to the surface coating thickness which is included in the hydrodynamic diameter (MacCusprie et al., 2011). The zeta potential of the nanoparticles shows that their surface is negatively charged for the entire pH range tested (Figure III.3). As pH was reduced, the magnitude of zeta potential decreased and the point of zero charge was slightly below pH 2. This result demonstrates that the inter-particle electrostatic interaction would be less pronounced at low pH. In API brine, the nanoparticles showed no significant surface charge (~ 0 mV) in the pH range tested. This result supports the negligibility of surface charge at high-salinity conditions due to the suppression of the double layer (Benjamin and Lawler, 2013) and/or the complexation with cations in the dispersion (Jaisi et al., 2008).

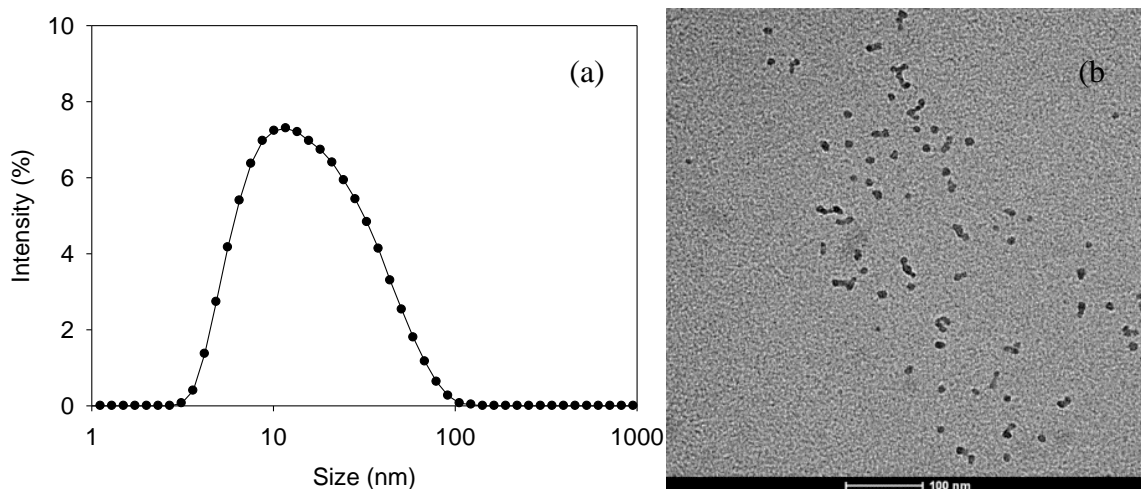


Figure III.2. (a) Particle size distribution measured by DLS, (b) TEM image of silica nanoparticles (when diluted in DI water).

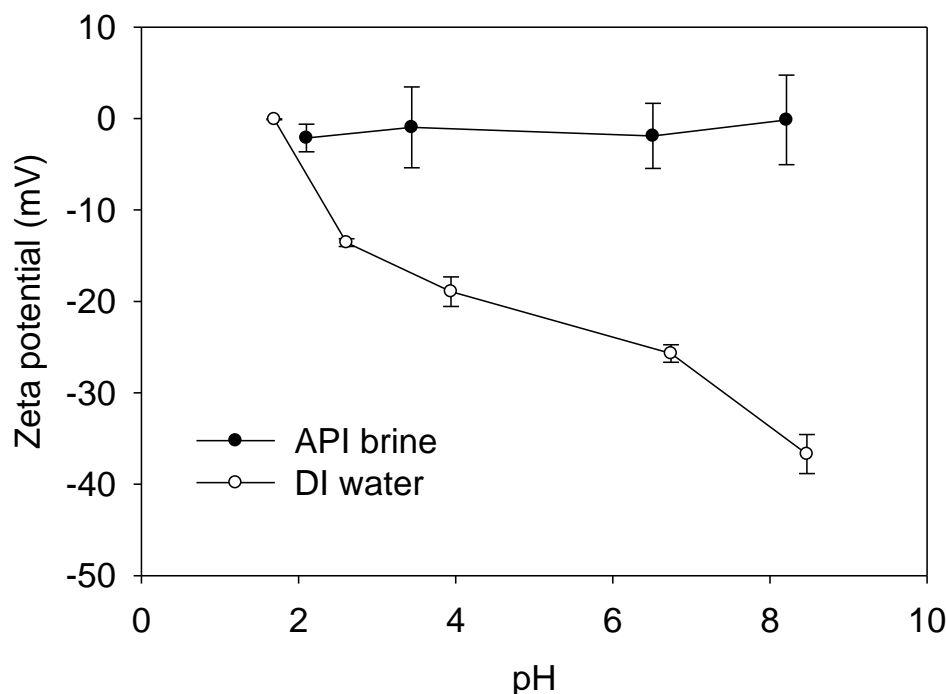


Figure III.3. Zeta potentials of silica nanoparticles diluted in DI water and API brine.

Aggregation of silica nanoparticles: At pH 3, regardless of brine composition and nanoparticle concentration, the aggregation was insignificant over 250 hrs (Figure III.4). Only a few samples showed a tiny increase (e.g., 20 nm to 30 nm) in the particle size when the nanoparticle concentration and the calcium content were increased. The role of calcium is expected to be less pronounced at low pH due to the reduced magnitude of the surface charge hindering the

interaction between calcium ions and the nanoparticle surface. Though the overall surface charge of the nanoparticles was nearly neutralized in API brine, calcium binding might occur due to the surface charge heterogeneity (Bouyer et al., 2001). On the other hand, the aggregation behavior was notably different at pH 8.5, showing a drastic increase in the aggregate size within 100 hrs at conditions identical to the pH 3 experiments (Figure III.5). However, aggregation was negligible in the absence of calcium ions at pH 3 and 8.5, revealing the role of calcium in the aggregation – the bridging of particles via calcium binding onto the surface functional groups (Chen and Elimelech, 2007). The initial nanoparticle concentration was another key parameter controlling the aggregation process (Figure III.6). Considering that Brownian motion is a dominant mechanism controlling nanoparticle transport, more nanoparticles in the same volume space would lead to more collisions, resulting in faster aggregation. In cases with higher than 1% silica nanoparticle concentration in API brine, the aggregation continued until the suspension turned into a weak gel without approaching to a specific aggregate size which was reported as controlled aggregation (Atmuri et al., 2013). The gel formation suggests the aggregation among the smaller aggregates might be possible through the calcium bridging. In other words, the nanoparticles or the aggregates were able to overcome the sterically repulsive energy barrier continuously as a result of the chemical binding on the surface. Though the reason of slow aggregation is unclear, one possible explanation is that neither the steric stabilization nor the calcium bridging can dominate the other mechanism to create a robust dispersion stability or induce rapid aggregation.

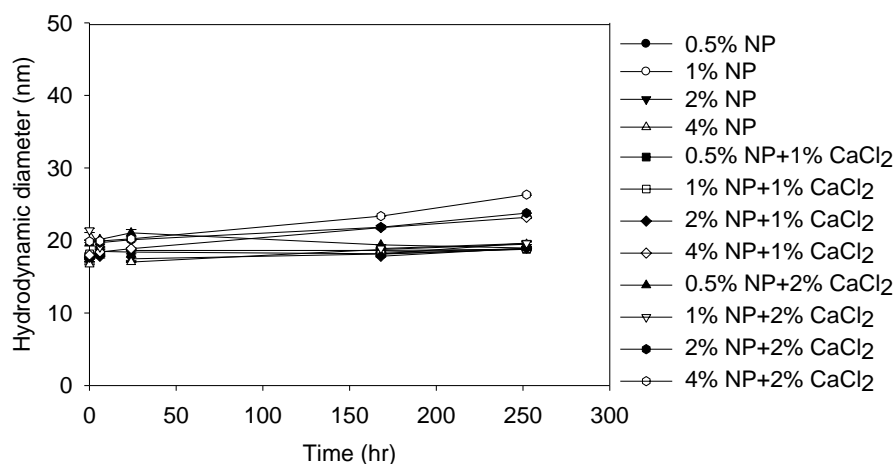


Figure III.4. Effect of calcium cation and nanoparticle concentrations on aggregation at pH 3 and 8% NaCl brine.

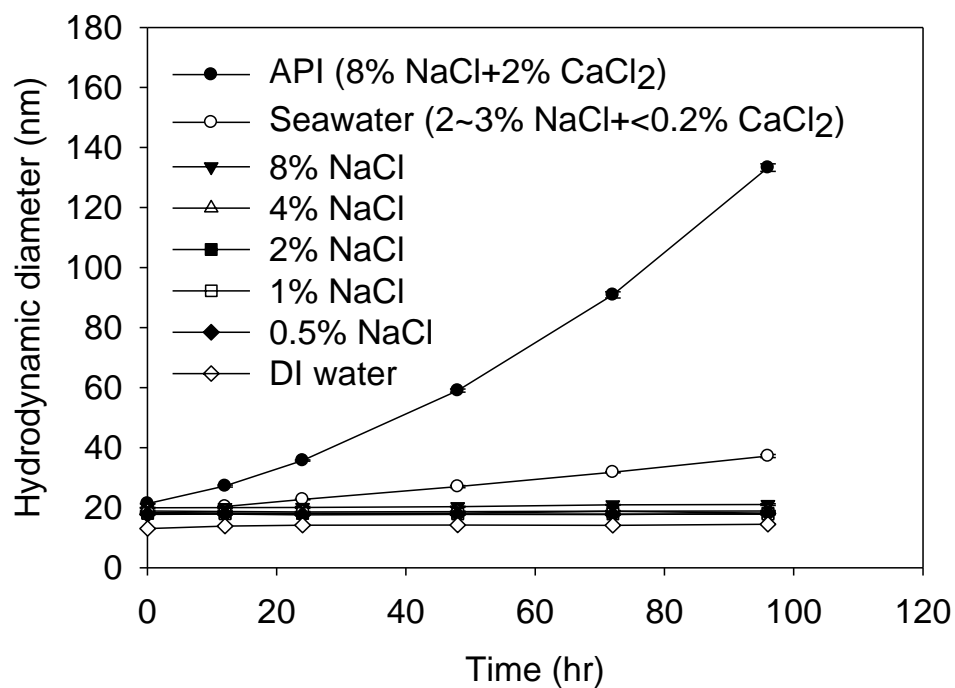


Figure III.5. Effect of salinity on aggregation at pH 8.5.

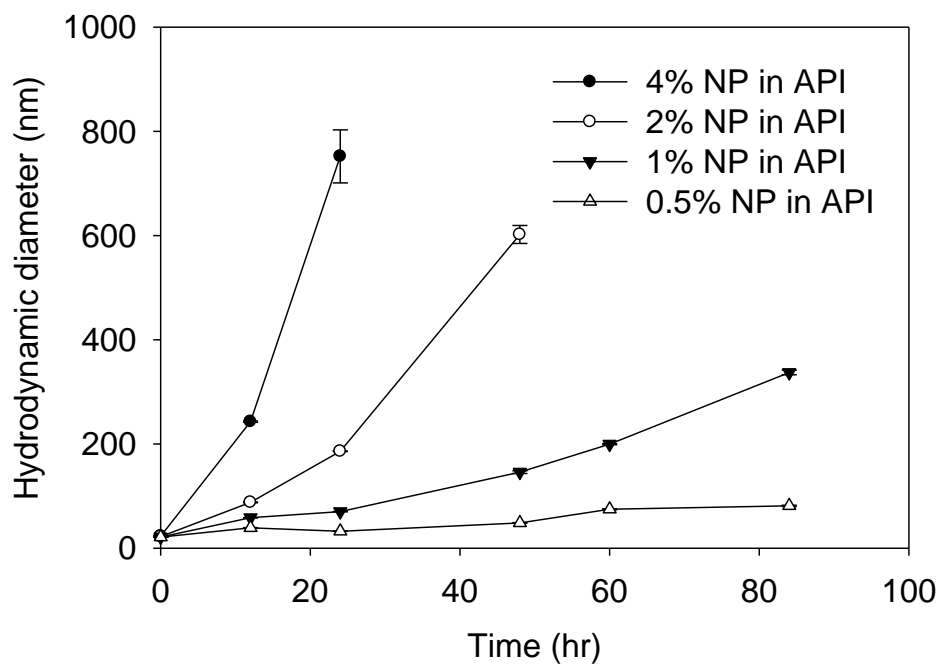


Figure III.6. Effect of particle concentration on aggregation at pH 8.5.

Also, we present the aggregation rate constant (k_s) as a key parameter in the aggregation kinetics using the following equation (Viriden and Berg, 1992).

$$k_s = \frac{1}{r_{mean,o}(\alpha)n_o} \left(\frac{dr_{mean}}{dt} \right)_{t=0} \quad (III.4)$$

k_s is the aggregation rate constant ($[L^3T^{-1}]$), $r_{mean,o}$ is the initial mean radius of the particles ($[L]$), α is the optical factor ($[-]$), n_o is the number concentration of particles ($[L^{-3}]$), $\left(\frac{dr_{mean}}{dt} \right)_{t=0}$ is the change of hydrodynamic diameter at early time of aggregation ($[LT^{-1}]$). The ratio of k_s to $k_{s,max}$ increased as the particle concentration was increased from 0.5 to 4% in API brine (Figure III.7). As the electrolyte concentration was sufficient to eliminate the energy barrier between particles, the particle concentration would play a role of driving the aggregation rate to the limit, providing more opportunities to collide with. This result demonstrates that not only chemical parameters but also physical parameters (e.g., reduced physical distance between particles) can stimulate the aggregation of nanoparticles.

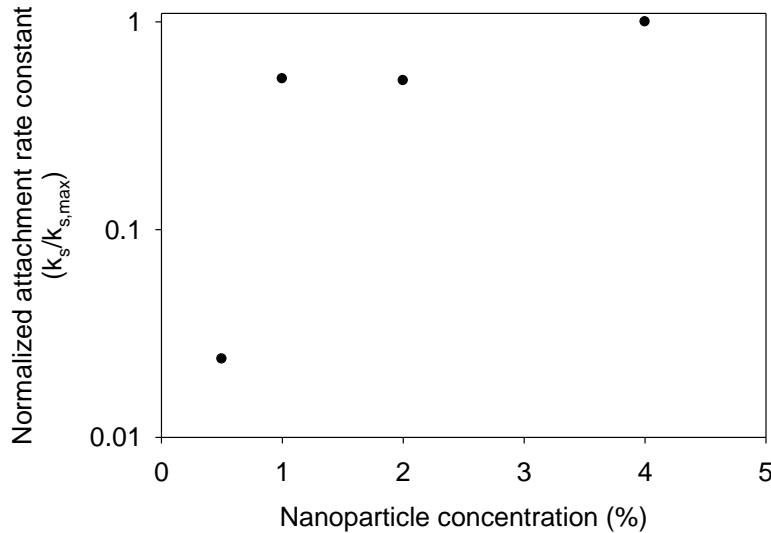


Figure III.7. Normalized aggregation rate constant depending on the particle concentration in API brine.

Deposition of silica nanoparticle aggregates on a well-defined silica surface: The deposition of the silica nanoparticle aggregates flowing above a plane silica surface was measured with three different aggregate sizes (70, 460, and 1200 nm) in API brine. The deposition test was carried out immediately after measuring the aggregate sizes assuming the sizes nearly unchanged

during the test period lasting less than one hour. As shown in Figure III.8, the adsorbed mass of nanoparticles decreased with an increase of aggregate sizes consistent with the simulation results by other researchers (Long and Hilpert, 2009; Ma et al., 2009; Nelson and Ginn, 2011; Tufenkji and Elimelech, 2004; Yao et al., 1971) that the deposition of particles would decrease as particles grow in size up to ~1000 nm due to the reduced Brownian motion. It is anticipated that the size-dependent deposition trend, is valid with surface-treated silica aggregates, in the size range tested here. As long as the experimental conditions are maintained, a similar deposition trend is expected during the transport tests in columns filled with the silica-type packing such as sand or glass bead.

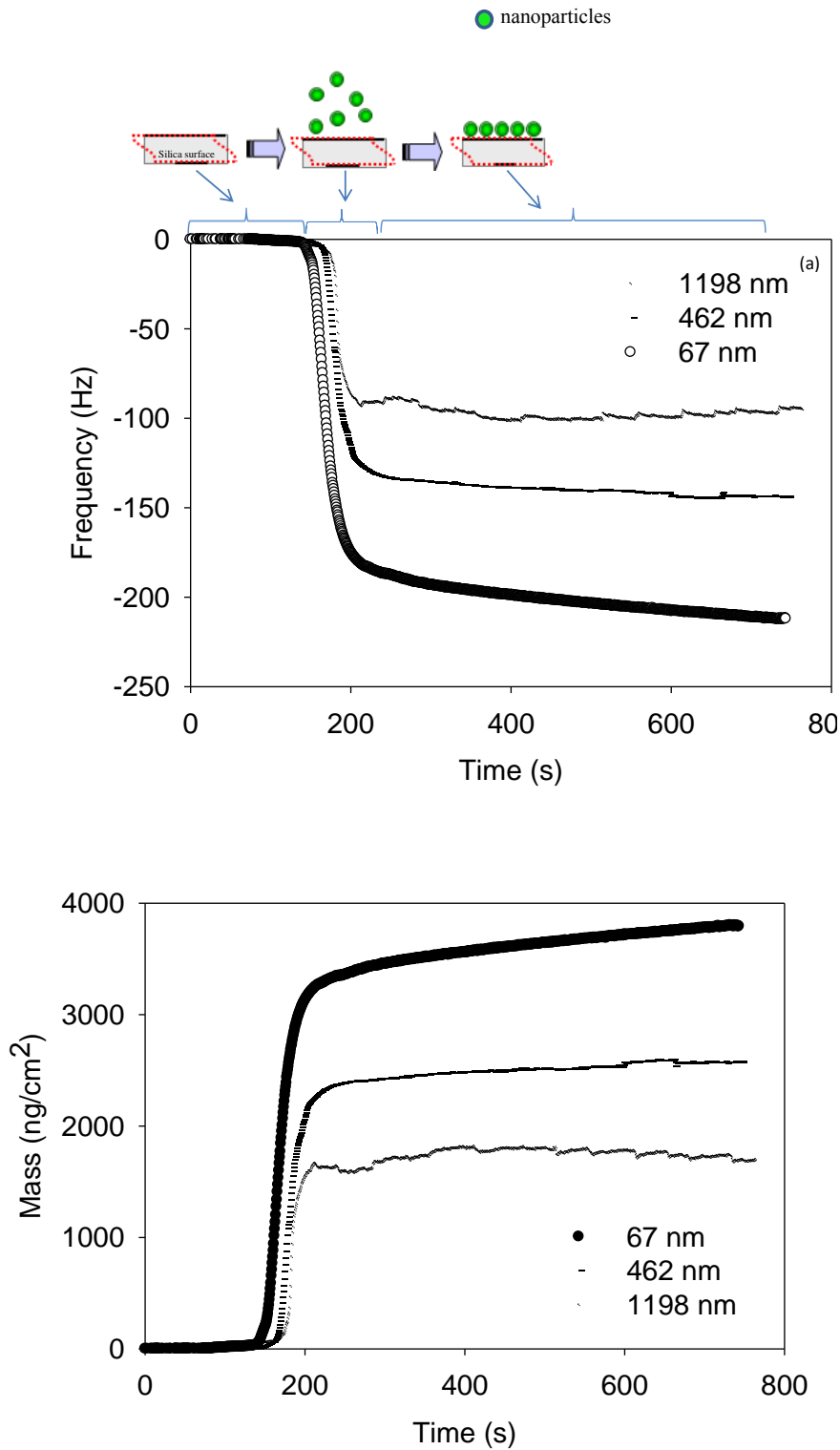


Figure III.8. Variations of (a) frequency and (b) adsorbed mass of silica nanoparticle aggregates onto silica surface during the deposition test (2% silica nanoparticles in API brine). The lag phase at the initial stage represents the time to reach the silica surface from the sample vial.

Transport and retention of silica nanoparticle aggregates in porous media: A series of the column tests was carried out with variable mean aggregate diameter at a fixed Darcy velocity (71 m/day). Here, the nanoparticles were pre-aggregated prior to injection and aggregation during the transport in porous media was neglected consistent with the remarkably larger residence time of particles in the influent chamber (order of hours to days) compared to that of the column (order of minutes). Overall, the retention of the nanoparticle aggregates was insignificant when the average aggregate size was smaller than 235 μm (Figure III.9). However, 24~28% of the injected mass of aggregates larger than 1 μm was retained. Conceivably, the aggregates in this size range attain a significant increase in the viscosity, causing the pore straining (Bradford et al., 2006).

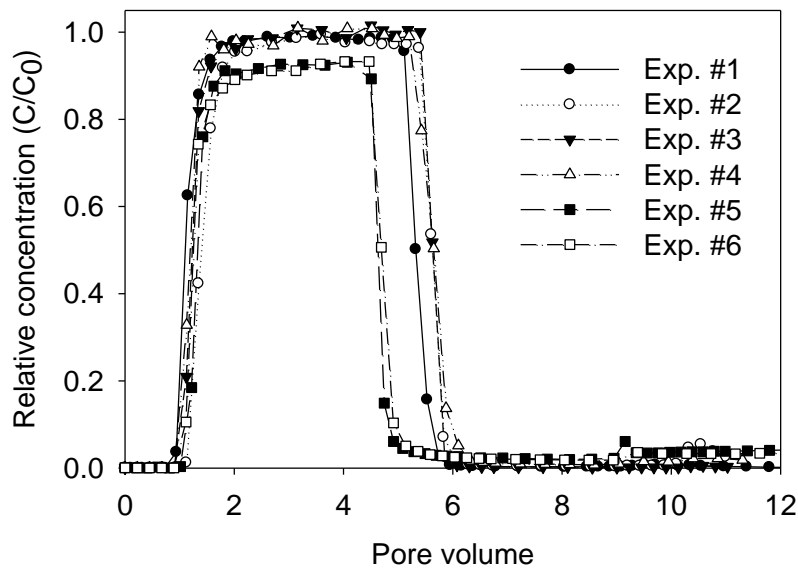


Figure III.9. Effect of nanoparticle (or aggregate) size on transport of nanoparticles (in API brine at pH 8.5)

Another set of the column tests was performed at different Darcy velocities (7.1, 14.2, and 71 m/day). Without pre-aggregation, the nanoparticles were rarely retained showing almost identical result to the high Darcy velocity test. This result suggests that the individual nanoparticles were sterically repulsive enough not to be deposited onto the surface of the sand grains. However, once the nanoparticles were injected after pre-aggregated under high-salinity conditions (which induced the aggregation), the retention was increased upto 88% as Darcy velocity decreased from 71 m/day to 7.1 m/day (Figure III.10). Assuming the steric repulsion of the nanoparticle

aggregates was in effect, this remarkable retention is considered mainly due to the pore straining of the aggregates. The fact that the viscosity was increased as the aggregation continued (Figure III.11) supports the possible pore straining due to the high viscous fluid. The change in the aggregate size distribution between influent and effluent (Figure III.12) indicates the possible breakdown of the aggregates by the applied hydrodynamic force, affecting the retention of the aggregates. Moreover, the fluctuations in the retention profiles at the low velocity tests imply the repeated straining and the breakdown process across the column (Legg et al., 2014). In terms of the pressure drop across the column, the pressure drop steadily increased when the aggregates were injected. However, the increase in the pressure gradient was significantly larger at the low Darcy velocity, implying the continuous pore straining. Overall, the transport of the aggregates revealed irregular effluent profile due to the complicated physical pore straining, and the hydrodynamic force also plays a role by breaking the loosely aggregated particles.

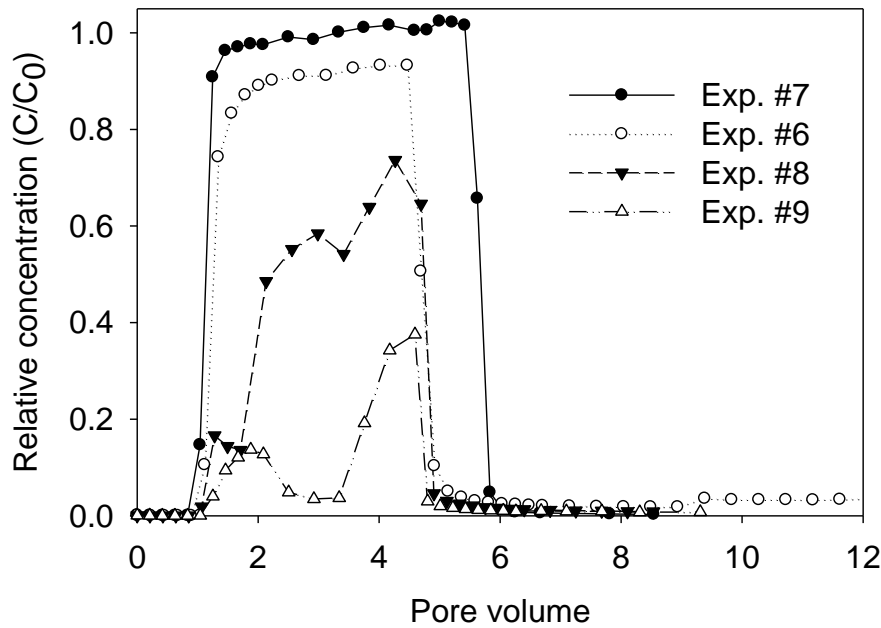


Figure III.10. Effect of flow rate on transport of nanoparticle aggregates (in API brine at pH 8.5)

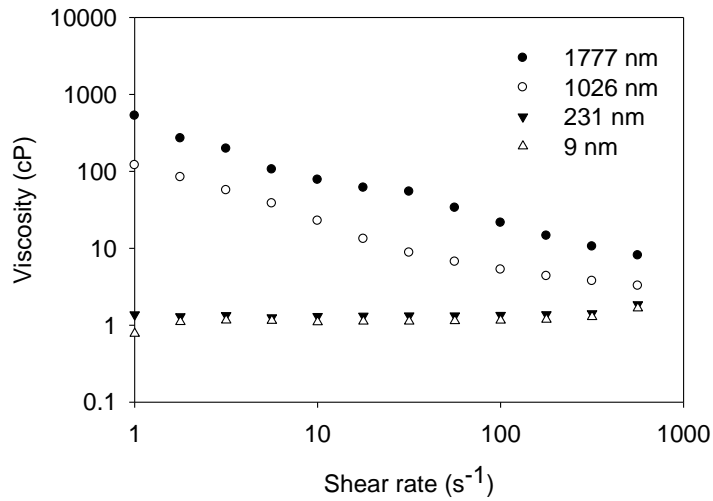
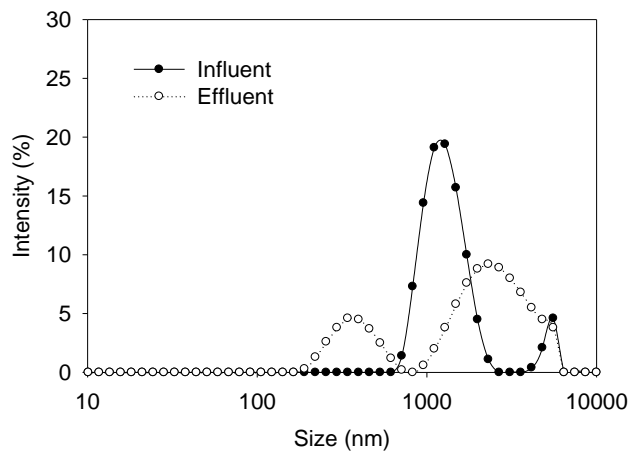
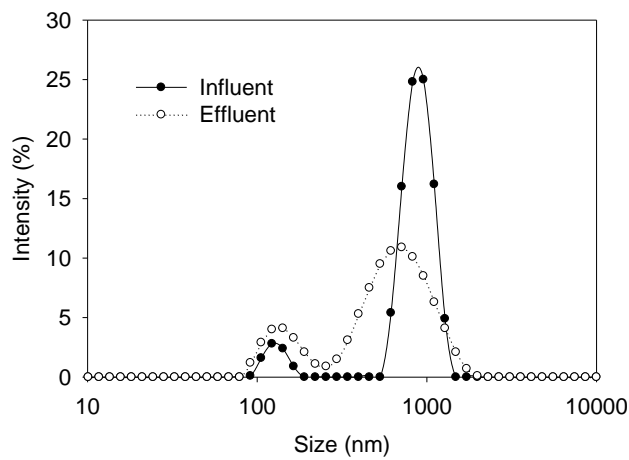


Figure III.11. Variations in viscosity of nanoparticle (or aggregates) suspension.



(a)



(b)

Figure III.12. Aggregate size distribution of influent and effluent (samples from (a) Exp. #5-high velocity (71 m/day) and (b) Exp. #9-low velocity (7.1 m/day) test).

In the literature, the ionic strength increase is known to result in the greater aggregation and deposition of nanoparticles (Petosa et al., 2010). In this study, the nanoparticles we used had a surface coating that provides steric stabilization even at high NaCl salinity; and they showed fairly high mobility regardless of the Darcy velocity when the aggregation was not preceded. However, when pre-aggregated particles were injected to the sand columns, the physical pore straining hampered the transport of the aggregates at the low Darcy velocity, which might be overcome by increasing the hydrodynamic force at higher velocities.

Transport modeling of silica nanoparticle aggregates: The particle transport equations, i.e., equations (III.1) and (III.2), were discretized using a Crank-Nicolson finite difference scheme and parameter estimation was performed employing the least sum of squared residuals technique. The simulation results are shown in Figure III.13, and a summary of model inputs and fitted parameters is provided in Table III.2. The non-aggregated nanoparticles transport similar to a conservative tracer (i.e., C/C_0 values approaching unity). However, the aggregated particles exhibit a significant amount of retention subject to a range of applied Darcy velocities (7.1 to 71 m/day), while in general a gradual increase in the effluent nanoparticle concentration with time was observed in all experiments. The CFT model does not capture the observed increase of effluent particle concentration. However, the MFT model provided better fits to the effluent data of aggregated clusters for higher velocity experiments (i.e., 14.2 and 70.1 m/day). The clean-bed filtration theory cannot explain the scaling of attachment efficiency with velocity (fitted- α_{PC} decreased from 1.06 to 0.079 as v_w was increased from 7.1 to 71 m/day). The reduction in the fitted- S_{max} of MFT model from 47.5 to 4.4 g/kg with the velocity increase, however, is consistent with a phenomenon called as the “shadow zone” effect (Ko and Elimelech, 2000). This effect causes a reduction of particle deposition down-gradient of the collector surface due to an interplay of factors such as approach velocity and electrostatic forces, and thus, S_{max} is expected to inversely correlate with flow velocity (Li et al., 2008).

In addition, in the transport experiments involving pre-aggregates particles, the particle breakthrough curves show slight tailing after the particle injection was stopped, indicating partial re-entrainment of the retained particles. This is consistent with the higher propensity of larger

aggregates (> 1000 nm) to deposit in the secondary energy minima, compared to smaller particles (< 50 nm), making larger particle more likely to detach subsequent to changes in solution chemistry (Petosa et al., 2010) and/or drag forces. The fitted detachment rate constant value increases from 0.16 to 2.52 hr⁻¹ as the flow velocity is increased one order-of-magnitude. This is in line with the increased effect of hydrodynamic drag acting on deposited particles thereby leading to the detachment of particles for which the applied hydrodynamic torque exceeds the adhesive van der Waals torque (Phenrat et al., 2009). At the lowest velocity (7.1 m/day), neither CFT nor MFT model captured the transport behavior of aggregated particles (Figure III.13), clearly demonstrating the need for additional experimental and mechanistic modeling work to glean a thorough understanding of processes that govern the transport and retention of aggregated particles.

Table III.2. Summary of model inputs and fitted retention parameters.

Experiment #		7		6		8		9	
Parameter	Unit	CFT	MFT	CFT	MFT	CFT	MFT	CFT	MFT
α_{pc}	-	3.77×10^{-7}	0.11	1.06	1.32	0.567	0.495	0.089	0.169
S_{max}	g/kg	0.68		47.46		15.54		4.41	
k_{det}	1/hr	0	0	0.16	0.16	0.22	0.22	2.52	2.52
v_w	m/day	7.1		7.1		14.2		71.0	
μ_w	cP				0.95				
μ_{NP}	cP	0.95		30.6		18.3		6.8	

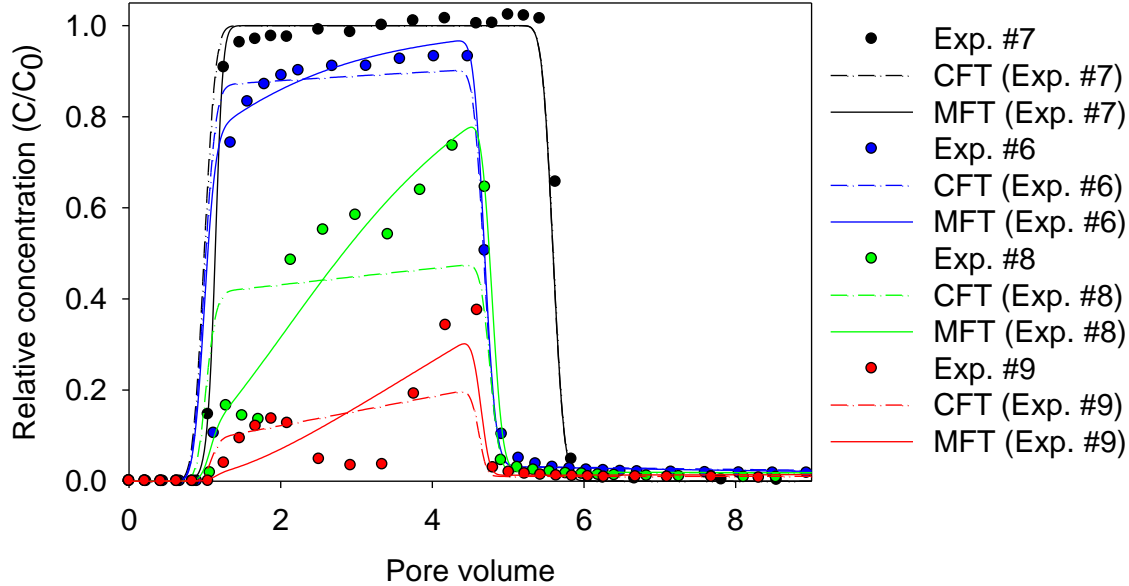


Figure III.13. Experimental and simulated retention profiles in transport test.

III.5. Conclusions

The dispersion stability and transport in sandpack, of a silica nanoparticle whose surface coating was designed to provide steric stabilization even at very high salinity, were studied. Aggregation occurred as calcium concentration and nanoparticle concentration increased at pH 8.5. At calcium concentration higher than 1% and nanoparticle concentration higher than 1%, highly viscous nanoparticle aggregate was generated and retained in the unconsolidated sandpack when there was insufficient hydrodynamic force. However, the comparison of the hydrodynamic diameters of the injected and effluent samples suggests that the breakdown of the aggregates occurred as hydrodynamic force increased. For the whole range of NaCl, CaCl₂, and nanoparticle concentrations tested, remarkably, no aggregation occurred at pH 3, most likely due to the loss of negative surface charge that could bind to the calcium ions. Hence, it is expected that given the low pH levels in CO₂ flooded zones, the tested surface-coated silica nanoparticle dispersion will remain stable over long-distance transport without formation of aggregates.

Because the nanoparticles have the steric repulsion to keep their stability in high-salinity conditions, as the aggregation occurs in the presence of calcium ions, the aggregate structure

appears to be weak and deformable. Therefore, the physical pore straining rather than the chemical attachment is expected to control the transport of aggregated particles. Increasing hydrodynamic force (i.e., higher flow velocity) improved nanoparticle transport. A model that incorporated other mechanisms including physical straining is needed for a more accurate description of the observed transport behavior of silica aggregates in porous media.

When it comes to the field application, the mobility of the silica nanoparticles could be guaranteed under the high flow rate and co-injection with CO₂. The findings in this study would provide an insight on the behavior of nanoparticle in the reservoirs and the guideline for the application of the nanoparticles on the enhanced oil recovery operation.

III.6. References

1. Aroonsri, A. et al., 2013. Conditions for Generating Nanoparticle-Stabilized CO₂ Foams in Fracture and Matrix Flow, SPE Annual Technical Conference and Exhibition 2013. Society of Petroleum Engineers.
2. Atmuri, A.K., Henson, M.A. and Bhatia, S.R., 2013. A population balance equation model to predict regimes of controlled nanoparticle aggregation. *Colloid Surface A*, 436: 325-332.
3. Benjamin, M.M. and Lawler, D.F., 2013. *Water Quality Engineering: Physical and Chemical Treatment Processes*. Wiley.
4. Bouyer, F., Robben, A., Yu, W.L. and Borkovec, M., 2001. Aggregation of colloidal particles in the presence of oppositely charged polyelectrolytes: Effect of surface charge heterogeneities. *Langmuir*, 17(17): 5225-5231.
5. Bradford, S.A., Simunek, J., Bettahar, M., van Genuchten, M.T. and Yates, S.R., 2006. Significance of straining in colloid deposition: Evidence and implications. *Water Resour Res*, 42(12).
6. Chen, K.L. and Elimelech, M., 2006. Aggregation and deposition kinetics of fullerene (C-60) nanoparticles. *Langmuir*, 22(26): 10994-11001.
7. Chen, K.L. and Elimelech, M., 2007. Influence of humic acid on the aggregation kinetics of fullerene (C-60) nanoparticles in monovalent and divalent electrolyte solutions. *J Colloid Interf Sci*, 309(1): 126-134.
8. Elimelech, M. and Omelia, C.R., 1990. Kinetics of Deposition of Colloidal Particles in Porous-Media. *Environ Sci Technol*, 24(10): 1528-1536.
9. Espinoza, D.A., Caldelas, F.M., Johnston, K.P., Bryant, S.L. and Huh, C., 2010. Nanoparticle-Stabilized Supercritical CO₂ Foams for Potential Mobility Control Applications, SPE Improved Oil Recovery Symposium 2010. Society of Petroleum Engineers.
10. Holthoff, H., Egelhaaf, S.U., Borkovec, M., Schurtenberger, P. and Sticher, H., 1996. Coagulation rate measurements of colloidal particles by simultaneous static and dynamic light scattering. *Langmuir*, 12(23): 5541-5549.
11. Hotze, E.M., Phenrat, T. and Lowry, G.V., 2010. Nanoparticle Aggregation: Challenges to Understanding Transport and Reactivity in the Environment. *J Environ Qual*, 39(6): 1909-1924.

12. Jaisi, D.P., Saleh, N.B., Blake, R.E. and Elimelech, M., 2008. Transport of Single-Walled Carbon Nanotubes in Porous Media: Filtration Mechanisms and Reversibility. *Environ Sci Technol*, 42(22): 8317-8323.
13. Ko, C.H. and Elimelech, M., 2000. The "shadow effect" in colloid transport and deposition dynamics in granular porous media: Measurements and mechanisms. *Environ Sci Technol*, 34(17): 3681-3689.
14. Legg, B.A., Zhu, M.Q., Comolli, L.R., Gilbert, B. and Banfield, J.F., 2014. Impacts of Ionic Strength on Three-Dimensional Nanoparticle Aggregate Structure and Consequences for Environmental Transport and Deposition. *Environ Sci Technol*, 48(23): 13703-13710.
15. Li, X.A., Lenhart, J.J. and Walker, H.W., 2010. Dissolution-Accompanied Aggregation Kinetics of Silver Nanoparticles. *Langmuir*, 26(22): 16690-16698.
16. Li, Y.S., Wang, Y.G., Pennell, K.D. and Abriola, L.M., 2008. Investigation of the transport and deposition of fullerene (C60) nanoparticles in quartz sands under varying flow conditions. *Environ Sci Technol*, 42(19): 7174-7180.
17. Long, W. and Hilpert, M., 2009. A Correlation for the Collector Efficiency of Brownian Particles in Clean-Bed Filtration in Sphere Packings by a Lattice-Boltzmann Method. *Environ Sci Technol*, 43(12): 4419-4424.
18. Ma, H.L., Pedel, J., Fife, P. and Johnson, W.P., 2009. Hemispheres-in-Cell Geometry to Predict Colloid Deposition in Porous Media. *Environ Sci Technol*, 43(22): 8573-8579.
19. MacCuspie, R.I. et al., 2011. Challenges for physical characterization of silver nanoparticles under pristine and environmentally relevant conditions. *J Environ Monitor*, 13(5): 1212-1226.
20. Nelson, K.E. and Ginn, T.R., 2011. New collector efficiency equation for colloid filtration in both natural and engineered flow conditions. *Water Resour Res*, 47.
21. Nguyen, P., Fadaei, H. and Sinton, D., 2014. Pore-Scale Assessment of Nanoparticle-Stabilized CO₂ Foam for Enhanced Oil Recovery. *Energ Fuel*, 28(10): 6221-6227.
22. Peng, C., Crawshaw, J.P., Maitland, G.C., Trusler, J.P.M. and Vega-Maza, D., 2013. The pH of CO₂-saturated water at temperatures between 308 K and 423 K at pressures up to 15 MPa. *J Supercrit Fluid*, 82: 129-137.
23. Petosa, A.R., Jaisi, D.P., Quevedo, I.R., Elimelech, M. and Tufenkji, N., 2010. Aggregation and Deposition of Engineered Nanomaterials in Aquatic Environments: Role of Physicochemical Interactions. *Environ Sci Technol*, 44(17): 6532-6549.
24. Phenrat, T. et al., 2009. Particle Size Distribution, Concentration, and Magnetic Attraction Affect Transport of Polymer-Modified Fe-0 Nanoparticles in Sand Columns. *Environ Sci Technol*, 43(13): 5079-5085.
25. Solovitch, N. et al., 2010. Concurrent Aggregation and Deposition of TiO₂ Nanoparticles in a Sandy Porous Media. *Environ Sci Technol*, 44(13): 4897-4902.
26. Tufenkji, N. and Elimelech, M., 2004. Correlation equation for predicting single-collector efficiency in physicochemical filtration in saturated porous media. *Environ Sci Technol*, 38(2): 529-536.
27. Vandesteeg, H.G.M., Stuart, M.A.C., Dekeizer, A. and Bijsterbosch, B.H., 1992. Polyelectrolyte Adsorption - a Subtle Balance of Forces. *Langmuir*, 8(10): 2538-2546.
28. Virden, J.W. and Berg, J.C., 1992. The Use of Photon-Correlation Spectroscopy for Estimating the Rate-Constant for Doublet Formation in an Aggregating Colloidal Dispersion. *J Colloid Interf Sci*, 149(2): 528-535.
29. Yao, K.M., Habibian, M.M. and Omelia, C.R., 1971. Water and Waste Water Filtration - Concepts and Applications. *Environ Sci Technol*, 5(11): 1105-&.
30. Yu, J., Liu, N., Li, L. and Lee, R., 2012. Generation of Nanoparticle-Stabilized Supercritical CO₂ Foams, Carbon Management Technology Conference. Carbon Management Technology Conference.

31. Zhang, T., Davidson, A., Bryant, S.L. and Huh, C., 2010. Nanoparticle-stabilized emulsions for applications in enhanced oil recovery, SPE Improved Oil Recovery Symposium. Society of Petroleum Engineers.
32. Zhang, T., Roberts, M., Bryant, S.L. and Huh, C., 2009. Foams and emulsions stabilized with nanoparticles for potential conformance control applications, SPE International Symposium on Oilfield Chemistry. Society of Petroleum Engineers.

IV. Concluding Remarks

During the course of this project, we conducted research in both experimental and mathematical modeling fronts to glean a more accurate understanding of CO₂ foam creation and destruction processes during its transport through porous media using silica nanoparticles as foam stabilizing agents. We experimented with different particle sizes and surface coating formulations and evaluated foam generation and transport under a variety of physical (e.g., flow velocity, medium permeability, applied shear rates, and temperature) and chemical (e.g., solution and particle surface chemistry) conditions representative of hydrocarbon reservoirs. We implemented mechanistic modeling approaches at different scales (i.e. core-scale to field-scale) to explain our experimental observations at core-scale and developed an upscaled model to serve as a predictive tool for the assessment of NP-C/W foam to improve the volumetric sweep efficiency of field-scale CO₂-flooding practices. Moreover, we implemented the upscaled multiphase flow and multi-component transport simulator to assist with the design of a field trial of NP-stabilized C/W foam technology at a specific oil reservoir.

In brief, some of the selected highlights of our findings are:

- In beadpack systems, we were able to generate stable opaque white C/W foams with bubble sizes too small to be visible (<100 μm) with either PEG-coated silica or methylsilyl modified silica nanoparticles (50% SiOH). By optimizing the hydrophilic CO₂-philic balance (HCB) of the surface coating material, we were able to achieve a more than two orders of magnitude enhancement of foam viscosity compared to the apparent viscosity of CO₂ and brine mixture in absence of foam (see Subsection I.1.1).
- We found that proper HCB of nanoparticle's surface wettability is necessary for generation of viscous CO₂-in-water foams in unconsolidated sandstone cores of variable permeability over a wide range of foam qualities (0.50-0.95). At salinity levels 4% w/v NaCl or higher if NP concentration is too low (< 0.5% w/v), no foam is generated regardless of HCB. Applying a minimum shear rate higher than a threshold value was found essential for generating stable foam in core-flood experiments in both unfractured and fractured cores, of Boise and Berea sandstones (see Subsection I.1.2).

- Addition of a minute amount of caprylamidopropyl betaine surfactant (0.04% w/v) augmented the stability and apparent viscosity of NP-C/W foam producing a fine textured foam (<100 μm diameter with a maximum viscosity of 79 cP in the beadpack and 36 cP in the capillary tube) by reducing the interfacial tension. Electrostatic interactions between the cationic portion of the surfactant headgroup and the negatively charged silica surface facilitated adsorption of surfactant on the silica nanoparticles, reducing the HCB of the nanoparticles thereby increasing NP adsorption at the CO_2 -water interface. The surfactant and nanoparticles also imparted long term stability to the foam by increasing the disjoining pressure and interfacial viscosity, which mitigate lamella drainage and Ostwald ripening, and the unfavorable bending of the interface around the water phase, which resists hole formation (see Subsection I.2).
- A two-phase flow mechanistic model was implemented to describe the experiments and predict the CO_2 -foam evolution under variable flow and foam quality conditions in beadpack columns. A synergic effect was observed between surfactant and nanoparticles on the effective gas viscosity, which doubled in the presence of nanoparticles. The model successfully captures the observed foam viscosification trends in experiments, particularly where strong high-quality foam is generated and yields agreeable predictions of the overall NP-C/W foam behavior at steady state. We found that a foam stabilized with nanoparticles and surfactant can be described with the same type of model generally used for surfactant-stabilized foam suggesting that the pore level mechanisms controlling the destruction and generation of foam are similar with and without nanoparticles as long as sufficient amount of surfactant is employed.
- Simulation results of the upscaled model suggest that if a strong foam is created in all layers with variable permeability, regardless of layer permeability, flood conformance can be only slightly improved despite the predicted significant pressure build-up at the injection well. Improved conformance, however, can be achieved through selective generation of strong foam in high-permeability streaks and/or a permeability-dependent viscosification (i.e. stronger foam in higher permeability streaks). Also, a sensitivity study was conducted to investigate the effect NP mobility on foam generation and transport at field-scale. The results of this study suggest a slight increase of the NP attachment efficiency (attachment to the solid rock surfaces) can impart significant limitation on the

spatial propagation of NP-stabilized foam downgradient from the injection well, thereby limiting the extent of the enhancement of CO₂-flood conformance (see Subsection II.2).

- We studied the dispersion stability and transport in sandpack, of silica nanoparticles with surface coating designed to provide steric stabilization even at very high salinity. Aggregation occurred as calcium concentration and nanoparticle concentration increased at pH 8.5 while no increase in the hydrodynamic radii of NPs was observed (up to 48 hours) at pH 3 at a wide range of NaCl, CaCl₂, and nanoparticle concentrations. This was attributed to the loss of negative surface charge at lower pH that could bind to the calcium ions suggesting long-distance colloidal stability of the surface coated silica NP at the low pH levels associated with CO₂ flooded zones. While a maximum retention capacity-based colloid filtration model explained NP transport behavior at pH 3, at pH 8.5 especially at the lower end of the applied flow velocities, a model that can incorporate other mechanisms including physical straining and filter-ripening is needed for a more accurate description of the observed transport behavior of silica aggregates in porous media. Nonetheless and so far as the field application of the tested particles is concerned, the mobility of the silica nanoparticles could be guaranteed provided high enough injection flow rate and co-injection with CO₂ (see Section III).